Thermo-fluid characteristics of fin-and-tube heat exchangers with various fin details for air conditioning applications

ABDALLA GALAL GOMAA

A thesis submitted in partial fulfilment of the requirements of the University of Northumbria for the degree of Doctor of Philosophy

November 2001

School of Engineering
Faculty of Engineering Science and Technology
University of Northumbria at Newcastle

ABSTRACT

The need for more efficient air conditioning systems requires an in depth understanding about the performance of its components. One of the key components in the air conditioning plant is the fin-and-tube cooling coil, which is investigated here. The main focus of the work is concerned with the analysis of fin-and-tube cooling coils having two classes of passive enhancement techniques known as corrugated and turbulated fins with particular reference of developing flow region.

Initially, two-dimensional modelling was done to establish the scope of later three-dimensional modelling in terms of dominant variables, meshing strategies and convergence criteria. The results gave key insights into required modelling strategies needed for the more complex three-dimensional problem of the composite fin-and-tube cooling coil.

Three-dimensional CFD modelling of fin-and-tube cooling coils having turbulated, corrugated and flat-fin geometries have been investigated with particular reference to the dry-hot arid climate. Five modelling approaches have been considered based on an isothermal fin-and-tube, periodic boundaries, conjugate heat transfer, tube-row temperature gradient and the effect of manufacturing defects. The last three approaches are novel contributions to this field of research. The influences of the key design parameters of fin pitch, fin material, and fin thickness have also been investigated parametrically for all fin types.

To provide confidence in these models, experimental studies on these cooling coils were carried out to acquire data for comparison between the predicted and measured values of heat transfer and friction, and to investigate the effect of range of design conditions on the cooling coils performance.

The detailed results of this work can be used to optimise the air-conditioning coil designs. The turbulated fin coil was found to give the highest values of Nusselt number at given friction factor followed by the corrugated fin coil. At a given pressure drop (ΔP = 52 N/m^2 corresponding to u_{ai} = 2.3 m/s), the heat transfer coefficient of the corrugated and turbulated fin coils was higher than that of flat fin by 16 % and 36 % respectively. For typical operating conditions, the corrugated and turbulated fin coils required core volumes of 19 % and 40 % less than that of flat fin coil respectively for the same performance. The cooling coils employing corrugated and turbulated fin geometries contribute significantly to the energy conservation and volume reduction of the air conditioning plant.

CONTENTS

ACKNOWLEDGEMENT

I would like to express my deep gratitude to my supervision team, Dr T J. Bond, Dr C Underwood and Dr R Penlington for their valuable and continuous guidance, constructive criticism, weekly meetings, and kind advice throughout this research programme.

Great appreciation is also due to Dr. R F Le-Feuvre for his sincere guidance for me at the beginning of this research programme.

I would also like to record my many thanks to Mr A Thompson of Thermal Transfer Technology (3T) Ltd. for manufacturing and supplying the three commercial cooling coils investigated, in addition to a single heating coil used in the experimental rig.

I acknowledge the support of Mr J Brunton, the senior technician at the school of Built Environment, Northumbria University for his kind assistance during the experimental phase of this investigation.

Financial support for this research was awarded by the Government of Egypt for which I am very grateful.

I cannot find words to express my deepest appreciation to my parents who presented me in this life and for their special care to me during all my years of study.

Finally, special thanks, grateful appreciation and love to my wife who helped me during this research. She carried a lot of responsibilities from my shoulders and looked after my children to let me concentrate on this research.

NOMENCLATURE

A_r	aspect ratio, c_p /H	
A_s	heat transfer surface area,	[m^2]
c_p	corrugation pitch	[m]
C_p	specific heat at constant pressure	[J/kg.K]
C_h	corrugated height	[m]
C_v	specific heat at constant volume	[J/kg.K]
D	tube diameter	[m]
D_c	diameter fin-collar	[m]
D_h	hydraulic diameter	[m]
div	divergence of vector (*div* $\mathbf{u} = \partial u/\partial x + \partial v/\partial y + \partial w/\partial z$)	
E	total energy	[J]
E_f	percentage error in friction factor	
E_p	friction power expended per unit of surface area, = $m\ \Delta P/\rho\ A_o$	[W/m^3]
E_R	percentage error in maximum velocity	
f	friction factor	
f_p	fin pitch	[m]
G	mass velocity	[$kg/m^2.s$]
grad	gradient of scalar (*grad* $u = \partial u/\partial x + \partial u/\partial y + \partial u/\partial z$)	
h	average heat transfer coefficient	[$W/m^2.K$]
H	interwall spacing,	[m]
i	internal energy	[J]
j	Colburn factor, $Nu/Re.Pr^{1/3}$	
k	coefficient of thermal conductivity,	[W/m.K]
L	length	[m]
L_f	fin length	[m]
L_p	louvered pitch	[m]

L_h	louvered height	[m]
L_R	geometric parameter, $\sqrt{(S_t/2)^2 + S_L}/2$,	[m]
L_s	streamwise length	[m]
m	mass flow rate,	[kg/s]
M	geometric parameter, $S_t/2$,	[m]
N_R	number of tube rows	
N_x	number of grid nodes in x-direction	
N_y	number of grid nodes in y-direction	
N_t	number of iteration	
Nu	average Nusselt number	
P_f	perimeter of the fin root	[m]
P_p	pumping power,	[W]
Pr	Prandtl number	
Δp	pressure drop,	[N/m^2]
Q	heat transfer rate,	[W]
r	radius of curvature,	[m]
R	universal gas constant	[J/kg.K]
Re	Reynolds number	
R_s	a result	
S	Source term	
S_h	slit height,	[m]
S_L	longitudinal tube pitch	[m]
S_n	number of slits per row per column	
S_t	transverse tube pitch	[m]
S_w	slit width,	[m]
t	fin thickness	[m]
T_b	outlet bulk-fluid temperature,	[K]
T_i	fluid inlet temperature,	[K]

T_w	wall temperature,	[K]
u	average air velocity	[m/s]
u	velocity vector, $(u_{i+}\ v_{j+}\ w_k)$	
U	overall heat transfer coefficient	[W/m^2 K]
u, v, w	velocity components in x, y, and z directions,	[m/s]
V	volume	[m^3]
$\dot{V}$	volume flow rate	[m^3/s]
W	uncertainty	
x, y, z	coordinates	[m]
X_L	longitudinal tube pitch, (S_L/D)	
X_t	transverse tube pitch, (S_t/D)	

Greek symbols

α	surface area density,	[m^2/m^3]
β	corrugation angle	[deg.]
β_L	louvered angle,	[deg.]
ε	heat exchanger effectiveness	
ε_f	maximum fin effectiveness	
η_f	fin efficiency	
η_o	total heat transfer surface efficiency	
θ	logarithmic-mean temperature difference,	[K]
ρ	density,	[kg/m^3]
μ	dynamic viscosity,	[Ns/m^2]
τ	viscous stress	[N/m^2]
λ	second coefficient of viscosity	[Ns/m^2]
δ	boundary layer thickness,	[m]
ϕ	dissipation function	

φ	general flow variable
ζ	under-relaxation factor
σ	contraction ratio, A_{ff}/A_{fr}
Γ	diffusive coefficient

Subscript

a	air
b	base
c	cross section
f	fin
ff	free flow
i	inlet
m	mean
max	maximum
o	outlet
t	tubes
w	water

Abbreviation

2-D	two-dimensional
3-D	three-dimensional
CFD	computational fluid dynamic
conj	conjugate
CPU	central processing unit

CV	control volume
db	dry-bulb
Fig.	figure
HVAC	heating, ventilation and air conditioning
iso	isothermal
LMTD	logarithmic mean temperature difference
NTU	number of transfer unit
OPF	overall performance factor
PDEs	partial differential equations
TRTG	tube-row temperature gradient
wb	wet-bulb

List of Figures

List of tables

CHAPTER -I-

INTRODUCTION

1.1 Introduction

Since the first energy crisis in 1973, there has been great demand to save energy and resources on all levels and related to this there has been a steady increase in heat exchanger research and development. Many workers in this field continue to seek ways of designing fin-and-tube heat exchangers to be more compact, lightweight, with higher effectiveness and lower cost. Fin-and-tube heat exchangers are widely used in refrigeration and air conditioning equipment in addition to automotive applications.

For refrigeration and air conditioning applications that use conventional heat exchangers, the thermal resistance on the airside is about 20 times the thermal resistance on the refrigerant-side [Saber, 1975]. For automotive applications especially on automotive radiators, the thermal resistance on the airside is about 5 to 10 times the resistance of the waterside [Kajino and Hiramatsu, 1985]. Thus, it is very important to enhance the heat transfer coefficient on the airside. A focal point for this work has been heat transfer enhancement which includes the search for special heat exchanger surfaces through which enhancement may be achieved

The need for more effective air-conditioning fin-and-tube heat exchangers has led to the development of a variety of unconventional flow through fin passages to enhance the heat transfer coefficient on the airside. Such passages include the corrugated, louvered and turbulated-fin surfaces as illustrated in Fig. (1.1). Often, manufacturers are forced to design new heat exchanger configurations by trial and error. In addition the designer has limited ability to easily evaluate how different heat exchanger geometries could optimise the performance of heat exchangers in unique application [Mirth and Ramadhyani, 1995].

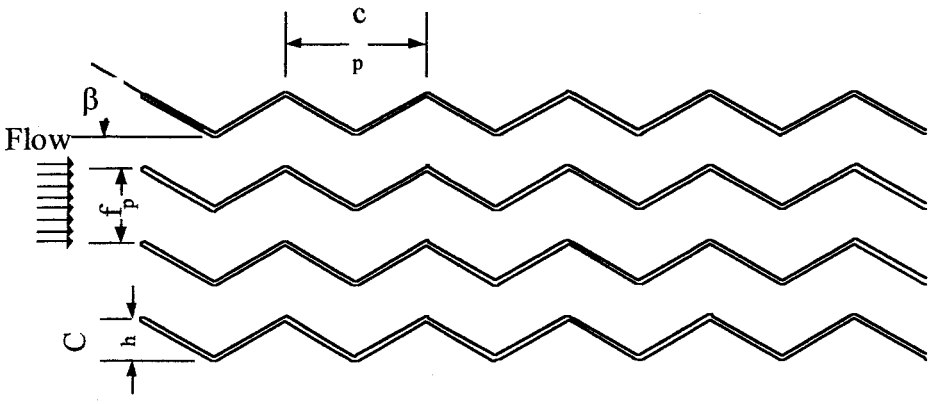

(a) Corrugated fin passage

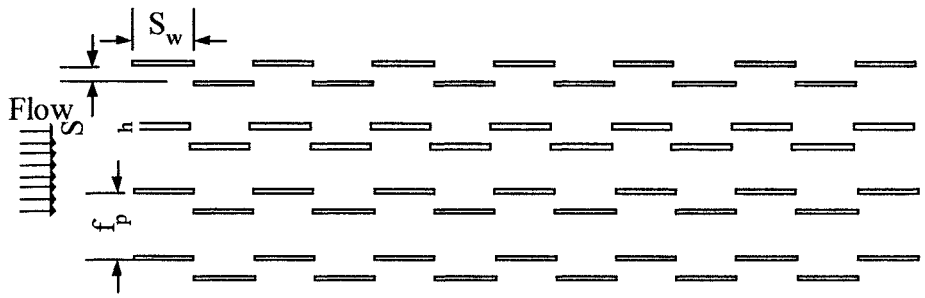

Turbulated (slit) fin passage

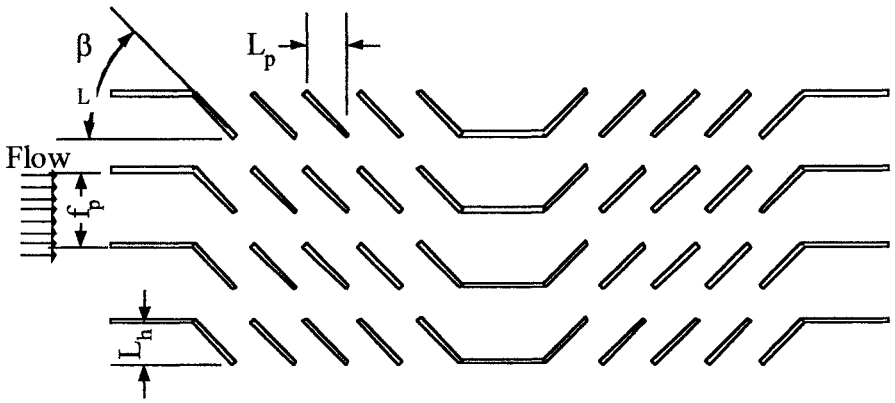

(c) Louvered fin passage

Fig. (1.1) Schematic of the fin passages of fin-and-tube heat exchangers

The various aims of enhancement techniques are to reduce the volume of the heat exchanger for a given duty, to increase the capacity of an existing heat exchanger, or to reduce the approach temperature difference. A combination of these aims is possible. It is important at the outset to recognise that enhancement of heat transfer may lead to an increase in pumping power, due to the greater resistance to flow through the heat exchanger.

The designer of thermodynamic equipment requires an understanding the heat transfer, flow friction and the fluid flow characteristics of flows in complex geometries under certain boundary conditions. These flow characteristics can be obtained by the following methods:

- Measurements. These are performed on full-scale or reduced-scale models. Results are applied to the real flow through the principle of dynamic similarity using dimensionless groups. The transfer characteristics from local flow vectors may be interpreted by laser Doppler anemometer, hot wire anemometer or flow visualisation techniques.
- Theoretical analysis. Appropriate for some simple cases, but in complex geometries it is not always possible to solve the equations for the flow (three-dimensional Navier Stokes equations) which are vital to the energy equation.
- Numerical analysis using computational fluid dynamics techniques. The Navier Stokes equations and the energy equation can be solved in discretised form, obtaining information at discretised node points, using finite difference, finite volume or finite element methods. This method is applicable for laminar flows with steady or transient conditions in addition to the solution of the turbulent flow equations, [Maltson, 1990].

1.2 Compact heat exchangers

A heat exchanger is referred to as a compact heat exchanger if it incorporates a heat transfer surface having a surface area density of about 700 m^2/m^3 on at least one of the fluid sides (usually on the gas side) [Shah, 1992].

In compact heat exchangers, a high heat transfer coefficient is achievable with small hydraulic diameter flow passages with gases and two-phase flows. The constructions for compact heat exchangers are plate-fin heat exchangers and fin-and-tube heat exchangers. Basic flow arrangements for the two fluids are single-pass cross flow, parallel flow, counter flow, and multi-pass cross-counter flow.

In a fin-and-tube heat exchanger, round tubes are most commonly used (although elliptical tubes are also being used) and fins are employed either on the outside or on the inside, (or both). The fins are attached to the tubes by a tight mechanical fit using tension winding, soldering, brazing, welding, bonding or extrusion.

The motivation for using compact surfaces to augment heat transfer may be understood by consideration of the convective equation of heat transfer:

$$Q = U A \Delta T \quad \text{or} \quad \frac{Q}{\Delta T} = U(\alpha . V) \tag{1.1}$$

For a given temperature difference (ΔT) and overall heat transfer coefficient (U), a high surface area density (α) is needed to minimise volume (V) and maximises the surface area (A), resulting in a compact surface. This is usually achieved by extended surfaces in the form of finning which is attached to tubes.

Typical industrial heat exchangers having fin densities that vary from 250 to 630 fins per metre, fin thickness from 0.09 to 5 mm, and fin flow lengths from 25 to 250 mm. A heat exchanger with 400 fins per metre has a surface area density (α) of about 720 m^2/m^3. Current and future applications of compact heat exchangers are used for vehicular, space, aircraft, gas turbine, high temperature waste heat recovery and air-conditioning and refrigeration industries [Shah, 1992].

1.2.1 Enhancement techniques of compact heat exchangers

Substantial energy cost saving can result if the effectiveness of heat exchangers is maximised. One method, which in wide spread use is enhancement. In fact heat transfer enhancement is the most common way of increasing the heat

transfer in heat exchange equipment, typically through the use of extended surfaces or fins. It is believed that many of the mechanisms used or under development for enhancement could be exploited to give heat exchangers even higher effectiveness.

Enhancement techniques are normally concerned with increasing the heat transfer coefficient and may be conveniently divided into two classes. These comprise "passive methods", for example extended surfaces, which require no direct application of external power; and active techniques, such as rotation, which do need external power.

1.3 Work frame

Since most of fin-and-tube air conditioning coils lie in a low-range of Reynolds number (Re < 2000 corresponding to u_{ai} < 4 m/s), then, the airflow may be treated as laminar [Jang *et al*, 1996 and 1997].

In particular, the airflow through the fin-passages is a combination of internal and external flow (internal through arrays of fin plates and external across the tube-bundle). The internal and external laminar flow is characterized by Re ≤ 2300 and Re ≤ 200000 respectively [Young *et al*, 2001]. A laminar flow condition through the fin-passages of louvered fin-and-tube heat exchangers was investigated numerically by Drakulic (1997) and Atkinson *et al* (1998). In their studies, all the louvered fin-and-tube heat exchanger calculations were based on laminar-steady flow conditions within the range 50 ≤ Re ≤ 3200. Consequently the work undertaken here is considered as being laminar.

The Mach number of the airflow in air-conditioning applications is much smaller than 0.2, so analysis can be rationally conducted within the incompressible framework [Sheu and Tsai, 1999].

The developing flow is pertinent in the present work because most of fin-and-tube heat exchangers used for air conditioning applications results in core shapes that have large frontal areas and short channels lengths for the airflow.

Finally, the scope of the present work is investigated by its relevance to hot arid climatic conditions in which only the sensible heat exchange is of interest.

1.4 Research aims

The aims of this research are as follows:

1. To develop a three-dimensional numerical model of the conjugate heat transfer of fin-and-tube air conditioning coils in order to investigate the key variables influencing performance.
2. To develop an understanding of the fluid flow and heat transfer mechanisms associated with airflow through the corrugated and turbulated fin passages.
3. To evaluate the enhancement of heat transfer achieved using corrugated and turbulated fin details.
4. To generate a set of heat transfer and friction data that can be used as a basis for the design and optimisation of a wide range of practical air-conditioning plants.

1.5 Objectives

The performance characteristics of fin-and-tube air conditioning cooling coils are investigated using both modelling and experimental approaches in order to satisfy the following:

1. Two-dimensional CFD modelling of a corrugated wall channel and a staggered tube bundle is initially to be carried out using finite element and finite volume methods. The purpose is to obtain key insights into required

modelling strategies needed for the more complex three-dimensional problem of the composite fin-and-tube heat exchanger. Results from the two contrasting CFD programmes will be compared as a basis for choosing a candidate program for the subsequent three-dimensional analysis.

2. Experimental measurements on a family of air-conditioning cooling coils having flat, corrugated and turbulated-fin geometries will be carried out using a set of boundary conditions relevant to air-conditioning applications in hot arid climates. The experimental results will be used to validate the three-dimensional CFD model results of these cooling coils.

3. Three-dimensional CFD modelling of fin-and-tube cooling coils with various fin details will be carried out using the CFD method identified from two-dimensional work. The Three-dimensional analysis of the fin-and-tube cooling coils will be focused on isothermal fin-and-tube; periodic boundaries; conjugate heat transfer and tube-row temperature gradients in developing flow region.

4. Results from the CFD modelling and experimental investigation will be compared at identical boundary conditions. Any refinements to the modelling methodology will take place at this point in order to establish a valid model.

5. Performance evaluation of fin-and-tube cooling coils with various fin details will be presented. The characteristics of the corrugated and turbulated fin cooling coils will be evaluated and compared with the conventional flat fin coil. Four criteria will be addressed:

   - Relationship between the heat transfer coefficient and pressure drop.
   - Scope for reduction of the transfer surface area.
   - Scope for reduction of the heat exchanger core volume.
   - An overall performance index for the air-conditioning plant.

6. Further parametric studies based on the three-dimensional validated model will be conducted including fin pitch, fin material and fin thickness.

1.6 Thesis organisation

CHAPTER-II- is a review of current literature containing relevant material related to the present work and is subdivided according to the contents of the thesis. Heat transfer and friction data are first discussed for the tube bundle array followed by a review of corrugated-wall channels. Experimental work related to flat, corrugated and interrupted fin-and-tube heat exchangers are reviewed and discussed. A review of the numerical investigation of the fin-and tube heat exchanger is also addressed. Finally the main conclusions of the review and the scope of present work are identified.

CHAPTER –III- gives a review of theory including the fundamental equations of motion and energy and review of the numerical schemes available for the solution of these equations. Since most of the work is conducted using the finite volume method, more details are given. The concept of developing-flow and the role of dimensionless groups are also presented.

CHAPTER –IV- describes a two-dimensional numerical investigation of fluid flow and heat transfer. Preliminary simulation of the fluid flow through a long straight duct is discussed in order to validate the numerical results with a known analytical solution. The performances of corrugated wall channels are simulated using both finite element and finite volume CFD codes following which an analysis of a tube bundle array is similarly conducted. A discussion of results and verification of the various methods are also presented.

CHAPTER –V- describes the experimental investigation of fin-and-tube cooling coils having flat, corrugated and turbulated fin geometries. The measurements of velocity, pressure and temperatures through out the heat exchanger are reported. Details of the test procedures, data reduction, and uncertainty analysis are given.

CHAPTER –VI- is concerned with the three-dimensional modelling of fin-and-tube cooling coils. Mesh generation, computational details and model refinements are discussed. Experimental and numerical results are compared and conclusions are drawn about the validity of the model. Predictions of the corrugated and turbulated-fin efficiencies are conducted and compared with those given in the

literature. Performance evaluation criteria of the cooling coil with various fin details is also discussed.

CHAPTER –VII- using the validated models, the influences of the major parameters affecting the characteristics of cooling coils of fin pitch, fin material and fin thickness are investigated.

CHAPTER –VIII- comprises a summary of the major conclusions, and recommendations for further work.

1.6 Original contributions

The research carried out in this work has resulted in a number of main contributions to knowledge:

- Three-dimensional CFD modelling of the conjugate heat transfer of corrugated and turbulated-fin cooling coils with a particular reference of developing flow region.
- Original modelling of the tube-row temperature gradient.
- Original modelling of the turbulated-fin edge burrs.
- Predication of the corrugated and turbulated fin-efficiency.

These contributions are supported by a number of publications.

CHAPTER –II-

LITERATURE REVIEW

2.1 Introduction

In recent years, considerable interest has been focused on techniques for augmenting convective heat transfer coefficients in air-conditioning equipment to improving the heat transfer performance of plate fin and tube heat exchangers. The most common augmentation techniques are the use of corrugated fins and/or louvered surfaces replacing of flat-plate fins as illustrated in Fig (2.1). Nowadays, experimental investigation and CFD numerical simulation techniques are the two established methods for investigating fluid dynamics in heating and cooling coils.

In this chapter, a summary of previous work is presented considering a brief review of the tube bundle arrays and corrugated wall channels. This is followed by a review of previous work related to experimental investigations into three fin types. A review of the numerical modelling of fin-and-tube heat exchangers is then followed. Finally, the scope of the present work including main points and the reasons of motivation this study is also addressed.

2.2 Tube bundle arrays

There have been a number of studies on the pressure drop and heat transfer characteristics of tube banks in cross flow. Most of previous work has been experimental in nature, and excellent reviews are given in Zukauskas (1978 and 1987). Launder and Massey (1978) performed a numerical prediction of viscous fully developed flow and heat transfer in a staggered tube bundle. It involved the use of a cylindrical network of nodes in the vicinity of the tubes with a Cartesian mesh covering the remainder of the flow domain for $Re \leq 1000$.

(a) Flat fin

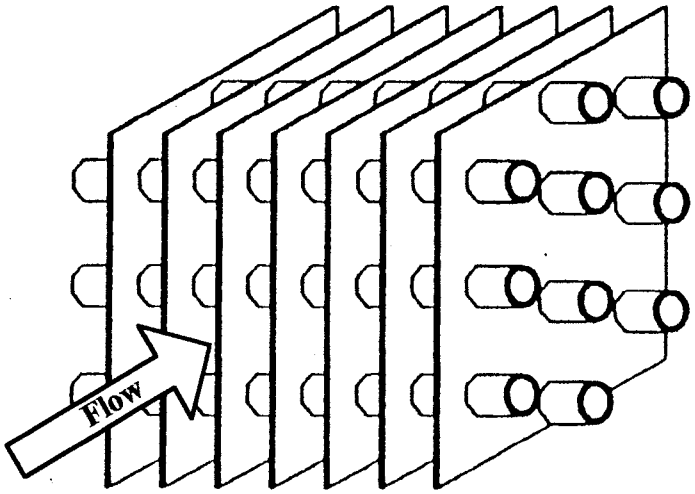

(b) Corrugated fin

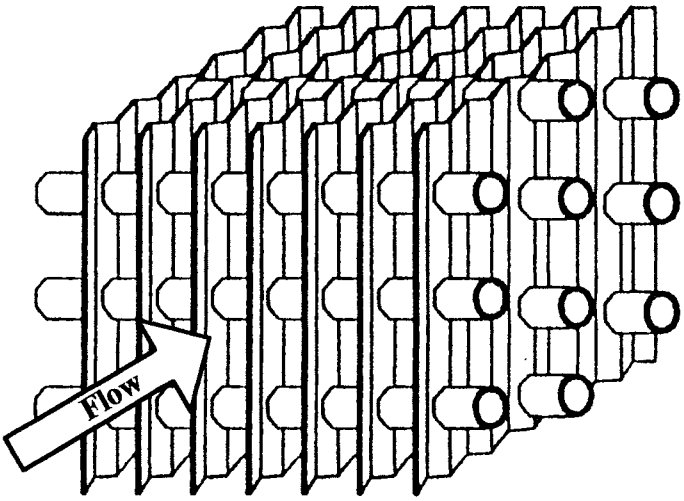

(c) Louvered fin

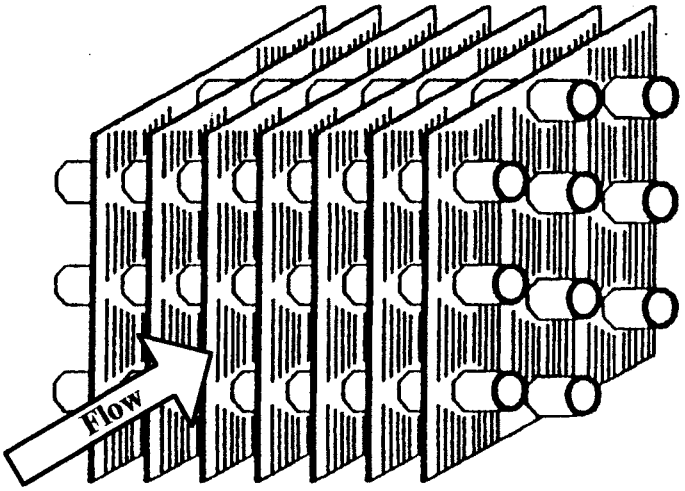

Fig. (2.1) Flat, corrugated and louvered fin-and-tube heat exchangers

Chen and Wung (1989 part I and II) employed a boundary-fitted coordinate system to study fully developed flow and heat transfer for both staggered and in-line tube arrays with a longitudinal and transverse pitch of 2 and $100 \leq Re \leq 1000$. Zdravistch *et al* (1994 & 1995) carried out a numerical study on laminar and turbulent fully developed flow in tube banks. A finite volume method and body fitted coordinate system were used. The calculated outlet values were used as inlet boundary conditions for the next computational element in the tube bank. Laminar and turbulent flow were considered for $400 \leq Re \leq 10^7$. The staggered tube arrangement geometry were $X_t = 1.4$, 2 and $X_L = 2$, representing the transverse and longitudinal tube pitches respectively. Recently, Sorensen *et al* (2001) used a heated gold-film technique to measure the variations in heat transfer in a three-pass inline tube bundle using CFD technique to identify the regions of interest for measurement.

2.3 Corrugated-wall channels

Corrugated surfaces lengthen the path of the fluid flow and produce enhanced flow mixing. Consequently, higher heat transfer performance is expected compared with a plain surface. There was a considerable amount of literature dealing with corrugated surfaces. Sparrow and Comb (1983) carried out an experimental study on the heat transfer and pressure drop of a corrugated-wall channel using water as the working fluid. The corrugation angle was $\beta = 30^o$ and the aspect ratio, $A_r = 2.75$. The flow characteristics were considered for the range of $2000 \leq Re \leq 27000$ and Prandtl number $4 \leq Pr \leq 12$. Flow visualisation was accomplished by the use of the oil-lampblack technique. They concluded that a 31 % decrease in inter-wall spacing gave rise to 30 % increase in Nusselt number but the friction factor was more than doubled.

Sunden, *et al* (1985) carried out an experimental study on heat transfer and pressure drop of a corrugated channel. The investigation was carried out for one corrugated and one smooth channel at $800 \leq Re \leq 5000$. It was found that the heat transfer for the corrugated channel was up to 3.5 times higher than that for the

smooth one, however, the pressure drop was higher by a factor of 5 to 6 and it was suggested that the corrugated height and length should be altered in order to balance the increase in heat transfer and the pressure drop.

The effect of the corrugation angle on the thermohydraulic performance of a plate heat exchanger was investigated by Focke, *et al* (1985). Experimental transfer data were obtained using an electrochemical mass-transfer analogue technique for $0 \leq \beta \leq 90^{o}$ and for $100 \leq \mathrm{Re} \leq 90000$. The results were presented as correlations of Colburn (j) and friction factors (f) against Reynolds number. The effect of inter-wall spacing on the heat transfer and pressure drop in a corrugated-wall channel was investigated by Molki and Yuen (1986). The investigation was conducted via a mass transfer technique in both developing and fully developed regions of corrugation angle $\beta = 30^{o}$, interwall spacing ranging from 4.76 mm to 9.53 mm and $\mathrm{Re} = 4000 \leq \mathrm{Re} \leq 35000$.

The effect of rounding the sharp-edges of corrugations on the heat transfer and pressure drop had been carried out by Sparrow and Hossfeld (1984). The experiments was carried out for $\mathrm{Re} = 2000 \leq \mathrm{Re} \leq 33000$, $4 \leq \mathrm{Pr} \leq 11$, $\beta = 30^{o}$ and $A_r = 0.362$. They concluded that rounding the corrugation peaks in general is a good trade off between heat transfer and pressure drop. At a fixed mass flow rate, the friction factor decreased more than the Nusselt number for the rounded-edge corner compared with that of a sharp-edge corner.

The performance of an advanced corrugated-duct solar air collector compared with five conventional designs was investigated by Metwally *et al* (1997). The air-collector was constructed of corrugated surfaces similar to those used for compact heat exchangers, with the air flowing normal to the corrugations. The comparison revealed that the efficiency of the corrugated duct collector increased by a ratio of 15 % to 43 % over that of the next best conventional design. Heat transfer and flow visualisations were investigated experimentally for laminar and transitional flow in a sinusoidal wavy channel by Rush *et al* (1999) for a channel aspect ratio of 10:1. The inter-wall spacing and wavy pitch were varied during the experiments. Observed instabilities during flow visualisation causing heat transfer enhancement were reported, however pressure drop data were not reported.

Asako and Faghri (1987) presented a finite-volume solution for fully developed laminar flow and heat transfer in a corrugated two-dimensional duct. Representative results were found for uniform wall temperature with $100 \leq Re \leq 1500$, $Pr = 0.7, 4, 8$ and $\beta = 15^{\circ}, 30^{\circ}, 45^{\circ}$. The flow patterns were highly complex including large recirculation zones. Yang *et al* (1995) carried out a numerical prediction of transitional characteristics of fluid flow and heat transfer in periodic fully developed flow in a corrugated duct. $100 \leq Re \leq 2500$, $\beta = 15^{\circ}, 30^{\circ}$ and there were three interwall spacing. Experiments were also performed for pressure drop measurements and flow visualisation where the results were compared with numerical predictions. The predicted transitional Reynolds numbers were lower than the values for the parallel plate duct.

The heat transfer and fluid flow characteristics through a periodic array of wavy passages were studied numerically by Wang and Vanka, (1995). The flow was observed to be steady up to $Re \cong 180$ after which self-sustained oscillatory flow was observed. The self-sustained oscillations led to the destabilisation of the laminar thermal boundary layers, replenishing the near-wall fluid with the fluid from the core region, providing a natural mechanism of heat and mass transfer enhancement. In the steady-flow regime the average Nusselt numbers for the wavy wall channel was only slightly larger than that for a parallel-plate channel. However, the friction factors were about twice those values in the steady-flow region, and remained almost constant in the transitional regime.

Vasudeviah and Balamurugan (2001) undertook an analytical investigation into the heat transfer and pressure drop in the two-dimensional sinusoidal wavy channel (with and without phase shift). The flow was laminar between the two sinusoidal wavy-walls and the maximum heat transfer occurred when the walls were in-phase and were a minimum when they were out of phase.

2.4 Experimental studies of flat fin-and-tube heat exchangers

Most research on flat fin-and-tube heat exchangers has been experimental in nature. Rich (1973) investigated experimentally the effect of the number of tube

rows and fin pitch on the thermofluid characteristics of flat fin coils. They concluded that the heat transfer coefficient was independent of the fin pitch and the pressure drop per row was independent of the number of tube rows. The number of tube rows had a small effect on the average heat transfer coefficient for row numbers greater than four.

Wang *et al* (1996) carried out experiments on sensible heating and friction characteristics of flat fin-and-tube heat exchangers. Fifteen samples with different geometric parameters, including the number of tube rows, fin spacing and fin thickness were tested. Reynolds number was based on the tube collar diameter in the range of $300 \leq Re \leq 7500$. They concluded that the fin spacing did not affect the heat-transfer coefficient for $N_R = 4$, the number of tube rows had negligible effect on the friction factor, and the fin thickness did not affect the heat-transfer or friction.

Wang and Chi (2000 part-I-) studied experimentally the effect of the number of tube rows, fin pitch and tube diameter on the thermofluid characteristics of the flat fin heating coils. They concluded that, the heat transfer characteristics were strongly related to fin pitch. The heat transfer coefficient decreased with increased of fin pitch For $N_R \leq 2$ while for $N_R \geq 4$ and $Re > 2000$, the effect of fin pitch was negligible. The effect of the number of tube rows on the friction factor was very small. In later work of Wang and Chi (2000, part –II-) conducted a heat transfer and friction correlations based on the previously published data including ± 15 % error.

A data reduction for the airside performance of fin-and-tube heat exchangers using the "ε-*NTU* method" was carried out by Wang and Webb (2000). For improved accuracy, they recommended that the temperature drop on the waterside should be higher than 2 K. The heat-transfer performance of cooling and heating coils was modelled by Sauer and Ganesh (1988). The results of the model were compared with manufacturers' catalogue data of three different coil companies. It was observed that the model prediction was slightly lower than that given in the manufacture's data in the case of heating however it was higher in the case chilled-water cooling.

2.5 Experimental studies of corrugated fin-and-tube heat exchanger

There were number of experimental studies on heat exchanger having corrugated or wavy fin surfaces. Giovannoni and Mattarolo (1983) examined the heat transfer coefficient of a corrugated-fin heat exchanger coil compared with the flat fin case for $200 \leq Re \leq 2000$. No friction data were given and also the corrugated fin details (i.e. β, C_h and c_p) were not presented. They concluded that the heat transfer coefficient of the corrugated fin case was enhanced by 20 to 40 % compared with the flat fin case.

Beecher and Fagan (1984) carried out an experimental study on 27 fin-and-tube heat exchangers, 21 of them having corrugated fin geometries. The corrugated fin heat exchangers were all of a three-row staggered arrangement however these geometries were not commonly used in practice. The test apparatus simulated a single-fin passage using a parallel pair of brass plates and the fin collar and tubes were simulated by cylindrical spacers attached to one of the plates. The plates were electrically heated and the electric heaters were adjusted to maintain a constant temperature over the airflow length. All heat transfer data generated was based on 100 % fin efficiency, however no pressure drop data were given. Webb (1990) used a multiple regression technique to correlate Beecher and Fagan's data. Webb's correlation predicted 88 % of the corrugated fin data to within ± 5 %, and 96 % of the data to within ± 10 %.

Ghanem *et al* (1997) carried out an experimental study on five corrugated fin-and-tube heat exchangers. Three of them having corrugation angle (β = 15°, 30°, 45°) with fin pitch (f_p = 6.25 mm) while the other two having (f_p = 3.125, 4.17 mm) and β = 15°. The heat exchangers-tubes were heated electrically using nickel-chrome heaters. The corrugated fin heat exchangers were all of a three-row inline arrangement with S_L = 69.2 mm, S_t = 66.6 mm, D_o = 15.62 mm and t = 0.3 mm, these geometries were not commonly used in practice. All the heat exchangers calculations were based on 100 % fin efficiency. They concluded that the corrugation angle (β = 30°) had the highest ratio of heat transfer Colburn factor to the friction factor (j/f) followed by β = 15° while β = 45° had the lowest ratio.

The modelling of chilled-water cooling coils with corrugated plate fins was carried out by Yik *et al* (1997). This model was developed based on McQuiston's (1978) correlations for flat-plate fins but included the use of Webb's (1990) correlations to determine a correction factor to make the flat-fin coefficients applicable to coils with corrugated fins. They concluded that the prediction of sensible and latent heat-transfer rates could be obtained by applying the correction to the sensible heat-transfer coefficient only. The modelling of the pressure drop and friction of the flat and corrugated fin coils were not reported.

Mirth and Ramadhyani (1993) carried out an experimental study to compare three different methods of modelling the heat and mass transfer in chilled-water wavy fin cooling coils. Five coils were tested for f_p = 3.15 mm, 2.23 mm and 1.6 mm. No details of the wavy fin geometry (i.e β, C_h and c_p) or the friction data were given.

The prediction of the Nusselt number and friction factor for these coils was given in Mirth and Ramadhyani (1994) and a general correlation for the Nusselt number and friction factor were developed. In later work, Mirth and Ramadhyani (1995) developed a model capable of predicting the performance of wavy fin-and-tube cooling coils. The model was tested by comparing its predicted heat transfer rates and pressure drops with previous experimental data. The heat transfer rates were predicted to within ± 5 % of the experimental value for seven wavy-fin coils. Airside pressure drop predictions were less accurate being within ± 25 %. For a given fin surface area, coils with more tube rows tend to perform better than coils with greater fin densities.

Wang *et al* (1997) studied experimentally the heat transfer and friction of the corrugated fin-and-tube heating coil with different configurations. The corrugated-fin configurations were C_h = 2 mm, c_p = 14.7 mm, β = 15.2°, (for in-line arrangement) and C_h = 1.5 mm, c_p = 9.525 mm, β = 17.5° (for staggered arrangement). The corrugated fin heat transfer characteristics were relatively independent of fin pitch and it was found that the friction factor was independent of the number of tube rows. The heat transfer coefficient for corrugated fin geometry was higher than that of the flat fin by 55 % to 70 %. However, the penalty was increased friction factor by 66 % to 140 %.

In the later work of Wang *et al* (1999) the heat transfer and friction data for a corrugated fin-and-tube heating coil were correlated to within ± 15 % of experimental data. Similar results were also experimentally correlated by Kim (1997) and Abu Madi *et al*, (1998).

Kim *et al* (1997) studied heat transfer and friction characteristics for wavy fin-and-tube heat exchangers using plate fins with a herringbone wave configuration. A multiple regression technique was used to correlate the airside heat transfer coefficient and friction factor as a function of flow conditions and geometric variables of the heat exchanger. For the staggered layout, 92 % of the heat transfer data were correlated to within ± 10 % and 91 % of the friction data were correlated to within ± 15 %.

Abu Madi *et al* (1998) carried out an experimental study to correlate the performance characteristics of fin-and-tube heat exchangers with both flat and corrugated fins. The geometric variations included the number of tube rows and fin spacing. Fin type was found to affect the heat transfer and friction factor, but the number of tube rows had a negligible influence on the friction factor. However, There were no results given for corrugated fin configurations (i.e. β, C_h and c_p).

2.6 Experimental studies of heat exchangers having interrupted surfaces

Interrupted fin surfaces often come in two configurations; louvered fin and turbulated fin as illustrated in Fig. (1.1). The most usage of the heat exchanger having louvered fin having flat tube is in the automotive application where the fin was generally brazed to extruded-flat tubes with a cross section of several independent passages. For the air-conditioning application, interrupted fin surface heat exchangers were consisted of mechanically or hydraulically expanded round tubes in a set of parallel continuous fins. Several experimental studies have been reported for heat exchanger with interrupted fin surfaces.

Garimella and Coleman (1998) carried out a study on the design of cross flow condensers for the ammonia-water heat pump. Flat, annular, wavy and

louvered fin geometries were studied. They concluded that the corrugated fin coil had the highest heat transfer coefficient, while the flat fin coil had the lowest pressure drop. The pressure drop of the wavy fin coil was higher than that of flat fin coil by 11.4 %. However all tests were conducted with inconsistent design parameters (D_o, S_t, S_L, f_p, and t) leading to an incomplete comparison between these fin types.

A comparative study of the heat transfer and friction characteristics of a flat, corrugated and louvered-fin heating coils was investigated by Wang *et al* (1998b). They concluded as before in (Wang *et al* 1996 and 1997a) that the heat transfer characteristics were relatively independent of fin pitch and the friction factors were also independent of the number of tube rows. In the later works (Wang *et al*, 1999d) correlations of the heat transfer and friction data were carried out for louvered fin geometries having round and flat tubes resulting in correlations with a ± 15 % error. Heat transfer and pressure drop of flat, wavy and louvered fin coils were also investigated by Yan and Sheen (2000) for $600 \leq Re_{Dc} \leq 3000$. They concluded that the louvered fin was most advantageous from heat transfer point of view when used at the same operating conditions. The louvered fin heat exchanger had about 40 % surface area reduction compared with flat fin and the area reduction increased with fin pitch.

Recently, the effect of the flow inclination angle on the airside thermal hydraulic performance of louvered-fin and flat-tube heat exchangers was investigated by Kim *et al*, (December 2001). The inclination angle from the vertical position ranged from –60° to 60° $100 \leq Re \leq 300$, $\beta_L = 27°$ and $f_p = 1.4$ mm. the inclination angle was found to have a negligible effect on the heat transfer performance, however, pressure drop increase consistently with the inclination angle.

Yun and Lee (1999 & 2000) investigated the heat transfer characteristics of various kinds of heat exchangers with interrupted fin-surfaces. Experiments were conducted for the scaled-up of a prototype by scale ratio of 3:1 of two-row coils for $120 \leq Re \leq 300$. The heat transfer coefficient from the scaled-up experiment was predicted an actual value within an error of 4.5 % while the pressure drop decreased by 10-23 % compared with the prototype. However, all

the heat transfer calculations were conducted by assuming the fin efficiency of 100 %, which is considered an unrealistic assumption.

Wang *et al* (1999c) examined the airside performance of the slit fin geometry (S_h = 0.99 mm, S_w = 2.2 mm and S_n = 4) with different fin pitch and number of tube rows. They concluded that the heat transfer performance increased with decreased of fin pitch however, for $N_R \geq 4$, the effect of fin pitch was reversed. In later work of Wang *et al* (2001) carried out a comparative study on the airside performance of the slit fin-and-tube heat exchangers with $N_R \leq 3$. They concluded that the louvered and slit fin geometries were superior in heat transfer compared with flat fin. For the same frontal area, the heat exchanger volume having interrupted surfaces was 38 % less than that of the flat fin.

Srinivas and John (1998) carried out a study for the design of air-cooled cross-flow condensers for absorption space-conditioning systems. Several alternative fin types (plain, annular, wavy and louvered) were considered. The effect of design variables, such as parallel/serpentine flow arrangements of tubes, fin spacing and core depth were investigated. It was reported that the wavy fin results in the lowest heat exchanger mass among the fin geometries considered for the imposed design objectives and constraints.

Recentely, Lozza and Merlo (2001) investigated experimentally the performance of a two-row air-cooled prototype condenser having flat, corrugated and louvered fin geometries. They concluded that the type of fin strongly influenced the heat exchanger performance and the louvered fin generally provided the best area "goodness factor" (j/f). However a comparison using (j/f) factor could not be fully depicted to give a general criteria of fin configuration.

2.7 Numerical studies on fin-and-tube heat exchangers

A number of mostly recent investigations of fin-and-tube heat exchanger using computational fluid dynamics (CFD) have been reported in the literature. Mendez *et al* (2000) examined the influence of fin pitch on convection in a single-row heating coil using the finite element CFD code "FIDAP" in addition to flow

visualisation. The flow was laminar and developing however conjugate heat transfer and the status of the boundary conditions were not specified. They reported that the fin pitch very strongly influences the overall Nusselt number and the pressure drop. Jang *et al* (1996 & 1997) carried out a three-dimensional numerical study on the fin-and-tube heating coil with flat and wavy fin types. The effects of different geometric parameters, including tube arrangement, tube row numbers and wavy angles β = 8.95, 17.05, 32.21°, were investigated for $400 \leq Re \leq 1200$. They assumed 100 % fin efficiency as well as symmetrical boundaries, which are considered inappropriate assumptions. They concluded that the average heat transfer coefficient of the staggered arrangement was 15 % to 27 % higher than that of the in-line arrangement, while the pressure drop was higher by 20 % to 25 %. The effect of row numbers was less important in a wavy-fin arrangement compared to flat-fin case. The average Nusselt number and pressure drop increased as the wavy angle increased while the highest flow area "goodness factor" (j/f) was obtained at lowest corrugation angle.

A two-dimensional CFD model of a louvered fin passage was carried out by Springer and Thole (1998) to investigate a periodic-velocity field through the fin-passage and observe the development of the boundary layer. The louver fin heat exchanger having flat tube was scaled up of factor 20. The scaled up geometry was $\beta_L = 27°$, $L_p = 27.9$ mm, $t = 2.3$ mm and $f_p = 21.2$ mm. They gave a methodology of measuring the mean velocity between louvers however, the heat transfer and pressure drop data were not specified.

Two-and three-dimensional numerical models of an automotive radiator having louvered-fin and flat-tubes were investigated by Atkinson *et al* (1998). A finite volume CFD code (STAR-CD) was used in the modelling in which the 2-D model dealt with a fin passage without tubes. They concluded that although the computing resource required by the 3-D model was greater than that of the 2-D model, the 3-D results were more accurate.

A three-dimensional numerical analysis of the conjugate heat transfer of a two-row heating coil with flat and slit fin types was presented by Sheu *et al* (1998, 1999a and 1999b). A finite volume discretization method with SIMPLE-based solution algorithm was used for $83 \leq Re \leq 258$. They concluded that perforations

in the fin surface could cause destruction of the boundary layer besides formation of a horseshoe vortex, which wrapped the cylinder surface to flow mixing and, thus, increased heat transfer.

2.8 Scope of the present work

From the literature review of the fin-and-tube heat exchangers, several key areas of investigation have been identified which will support the basis of the Ph.D. programme presented here. It has been observed that, experiments on fin-and-tube heat exchangers with flat, corrugated and louvered fin geometries over the last two decades have yielded valuable insights into the heat transfer and friction characteristics of these heat exchangers. However, there are some omissions identified in the pervious studies, which may be summarised as:

1. There is little published material dealing with turbulated fin heat exchangers.
2. There are inconsistencies in the methods used by some of the previous researchers, such as the 100 % fin efficiency assumption. In the work investigated by Wang *et al*, most of the calculations were based on a fin-collar as a hydraulic diameter, which is considered inappropriate especially with corrugated and louvered fin coils. A more general definition should include the heat exchanger configuration (i.e. streamwise length, transfer surface area, minimum free flow area and fin pitch).
3. There are also inconsistencies in the effect of fin pitch on the thermofluid characteristics of the heat exchangers. Some researchers have reported that, the heat transfer coefficient was independent on the fin pitch such as Rich (1973). Whilst others reported that the heat transfer coefficient increased with a decrease of fin pitch, while for $N_R \geq 4$ the effect of fin pitch was reversed such as Wang *et al* (1999c). Wang and Chi (2000) reported that, the heat transfer performance increased with decrease of fin pitch for $N_R \leq 2$, and independent on fin pitch for $N_R \geq 4$.

4. Numerical solutions can offer a powerful insight into the performance characteristics of enhanced fin-surfaces on a scale and level of detail not always possible with experimental methods. However there are few studies based on CFD modelling of these fin-surfaces. Some of these studies dealt with an isothermal fin-and-tube and most assumed constant row-on-row temperatures besides zero thermal-resistance of the tube wall.
5. Some of the work reported assumes fully developed flow although most compact heat exchangers relevant to air conditioning applications results in core shapes that have large frontal areas and short channels for airflow.

Therefore, the present investigation has sought to address these omissions from previous studies, and it has been conducted in four phases:

I. The first deals with the two-dimensional CFD modelling of corrugated wall channels and tube bundle arrays. The effects of corrugation angle, aspect ratio, transverse tube pitch, longitudinal tube pitch and number of tube rows on the thermofluid characteristics of these heat exchangers are investigated in developing flow region. The purpose is to establish a scope of a more complex three-dimensional modelling of fin-and-tube cooling coils.

II. The second deals with the experimental analysis of fin and tube cooling coils having flat, corrugated and turbulated fins. The purpose is to provide a data of model validation and to investigate the influence of a set of design boundary conditions on the performance of these cooling coils applicable to a hot dry climate. The experimental results are validated with corresponding relevant results in literature.

III. The third deals with three-dimensional CFD modelling of the flat, corrugated and turbulated fin-and-tube cooling coils. The numerical approaches of isothermal fin-and-tubes, conjugate heat transfer, periodic boundaries and row on row temperature gradient with particular reference of developing flow region are investigated for these cooling coils types. Prediction of fin efficiency is then conducted based on validated model.

IV. Further parametric modelling studies of fin pitch, fin thickness, and fin material are also conducted for these cooling coils based on validated model.

CHAPTER –III-

Review of basic theory and numerical modelling

3.1 Introduction

In this chapter, the fluid flow and heat transfer governing equations and the concept of Computational Fluid Dynamics (CFD) are briefly described. The techniques for the numerical solution of these partial differential equations are indicated with particular reference to industry standard CFD codes. Both the Finite Volume code FLUENT-5.4.8 and the Finite Element code ANSYS-5.3 have been used in this work. Techniques to produce robust CFD results are presented. In addition, the concept of developing flow and the dimensionless parameters calculated in the post-processing of results are presented.

3.2 Computational fluid dynamics

Computational Fluid Dynamics, CFD, is the analysis of systems involving fluid flow and heat transfer by means of a computer-based simulation. CFD has emerged from the application of solution algorithms to fluid dynamics and transport phenomena. Improved accessibility to high performance computers has permitted CFD to become both an integral part of engineering design and a research tool in academe and industry. The fluid flow phenomena are described in mathematical form by a system of partial differential equations, PDEs. The aim of the numerical computation is to transform the set of PDEs into a discretised algebraic form and solve them in order to obtain a set of flow field values at discrete points in time and space. CFD can be utilised in conjunction with experimentation to highlight areas worthy of further investigation and to explain

system characteristics. Modelling enables the researcher to explore high temperature and pressure processes, which may otherwise be prohibitively expensive or dangerous, [Griffin, 1996]. CFD numerical analysis has become a tool for complementing laboratory experiments and prototyping. In the present work, CFD is used to understand the flow phenomena and performance characteristics in different heat exchanger fin patterns. Generally, the CFD numerical analysis of the fin-and-tube heat exchanger should consider the following:

- Definition of the modelling goals.
- Model and mesh generation.
- Choice of the computational model.
- Choice of physical models (laminar, or turbulent)
- Determination of the solution procedure
- Test results
- Grid refinement
- Result validation

3.3 Governing equations

The governing equations that describe the fluid motion are a set of non-linear partial differential equations, which ensure that

- The mass of a fluid is conserved.
- The rate of change of momentum equals the sum of the forces on a fluid particle (Newton's second law).
- The rate of change of energy is equal to the sum of the rate of heat addition to and the rate of work done on a fluid particle (First Law of Thermodynamics).

Full details on the development of the governing equations are provided in [Versteeg and Malalasesekera, 1995].

The study of fluid variables such as velocity, pressure and temperature may be considered for an element of the fluid which is considered within a control

volume, CV with sides *dx*, *dy* and *dz* as shown in Fig. (3.1). The analysis of changes in mass, momentum and energy within the control volume are as follows.

3.3.1 Continuity equation

The mass of fluid in the control volume (CV) is equal to the product of the density and the volume of the fluid element, so the rate of increase of mass with time and the net mass flow rates out of the CV through the faces normal to *x*, *y*, and *z* axes may be written as $\frac{\partial \rho}{\partial t} dxdydz$, $\frac{\partial (\rho u)}{\partial x} dxdydz$, $\frac{\partial (\rho \upsilon)}{\partial y} dxdydz$ and $\frac{\partial (\rho w)}{\partial z} dxdydz$ respectively. The continuity equation can be obtained by applying the conservation principle of mass through the CV:

$$\left\{\begin{matrix}\text{net rate mass} \\ \text{flux out of CV}\end{matrix}\right\} + \left\{\begin{matrix}\text{rate of accumulation of} \\ \text{mass within CV}\end{matrix}\right\} = 0$$

The continuity equation for unsteady-compressible flow in three-dimensions may be written as:

$$\frac{\partial \rho}{\partial t} + \frac{\partial \rho u}{\partial x} + \frac{\partial \rho \upsilon}{\partial y} + \frac{\partial \rho w}{\partial z} = 0 \qquad (3.1)$$

3.3.2 Momentum equation

The momentum equations of the three Cartesian axes (*x*, *y*, *z*) may be derived from Newton's second law, which states that:

$$\left\{\begin{matrix}\text{rate of increase of momentum} \\ \text{of a fluid particle}\end{matrix}\right\} = \left\{\begin{matrix}\text{sum of forces on} \\ \text{that fluid particle}\end{matrix}\right\}$$

The momentum is given as the product of velocity and mass. Considering initially the x-momentum, the rate of increase and the net outflow will be:

$$\left(\frac{\partial \rho u}{\partial t} + \frac{\partial(\rho u^2)}{\partial x} + \frac{\partial(\rho u \upsilon)}{\partial y} + \frac{\partial(\rho u w)}{\partial z}\right) dxdydz$$

Additionally the x-components of the forces need to be considered. There are two types of forces:

- **Body forces** (gravity, centrifugal, buoyancy and electromagnetic forces).
- **Surfaces forces** (pressure and viscous forces).

Generally, the body forces are small compared to the surface forces that act on the faces of the CV. The surface forces in the x-direction that are due to pressure P and stress components, (τ_{xx}, τ_{yx} τ_{zx}) are illustrated in Fig. (3.2a). The magnitude of a force resulting from a surface stress is the product of stress and area. Forces aligned with the direction of a co-ordinate axis get a positive sign and those in the opposite direction a negative sign. The net force in the x-direction is the sum of the force components acting in that direction. So, the net surface forces in the x-direction acting on the CV are given as:

$$\left(-\frac{\partial P}{\partial x} + \frac{\partial \tau_{xx}}{\partial x} + \frac{\partial \tau_{yx}}{\partial y} + \frac{\partial \tau_{zx}}{\partial z}\right) dxdydz$$

Hence, the momentum equation in the x-direction may be written as:

$$\frac{\partial(\rho u)}{\partial t} + \frac{\partial(\rho u^2)}{\partial x} + \frac{\partial(\rho u \upsilon)}{\partial y} + \frac{\partial(\rho u w)}{\partial z} = -\frac{\partial P}{\partial x} + \frac{\partial \tau_{xx}}{\partial x} + \frac{\partial \tau_{yx}}{\partial y} + \frac{\partial \tau_{zx}}{\partial z} + S_x \tag{3.3a}$$

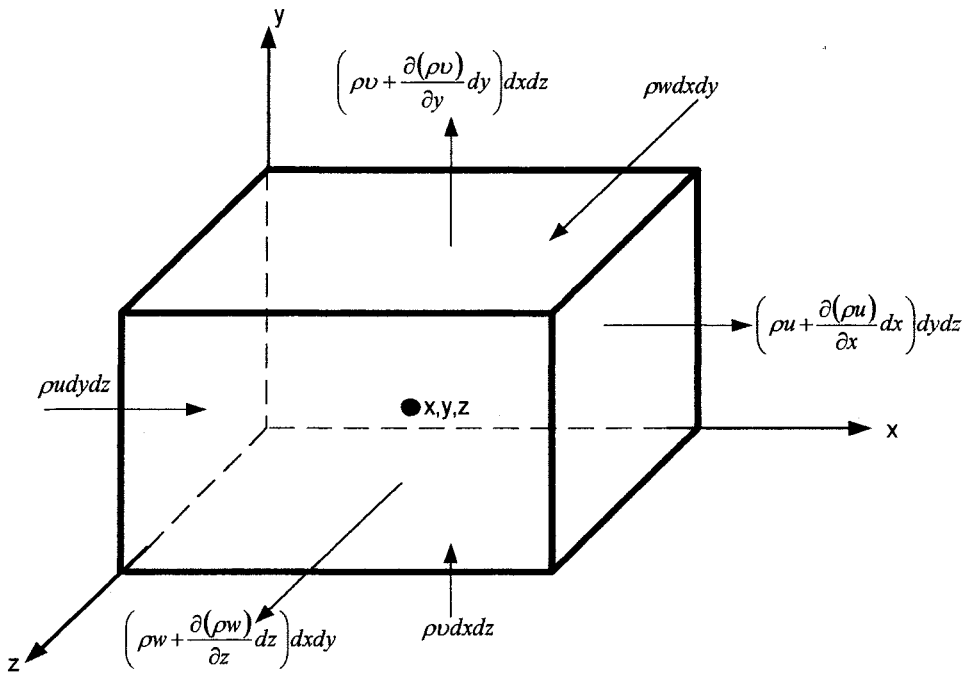

Fig. (3.1) Mass flow in and out of control volume (CV)

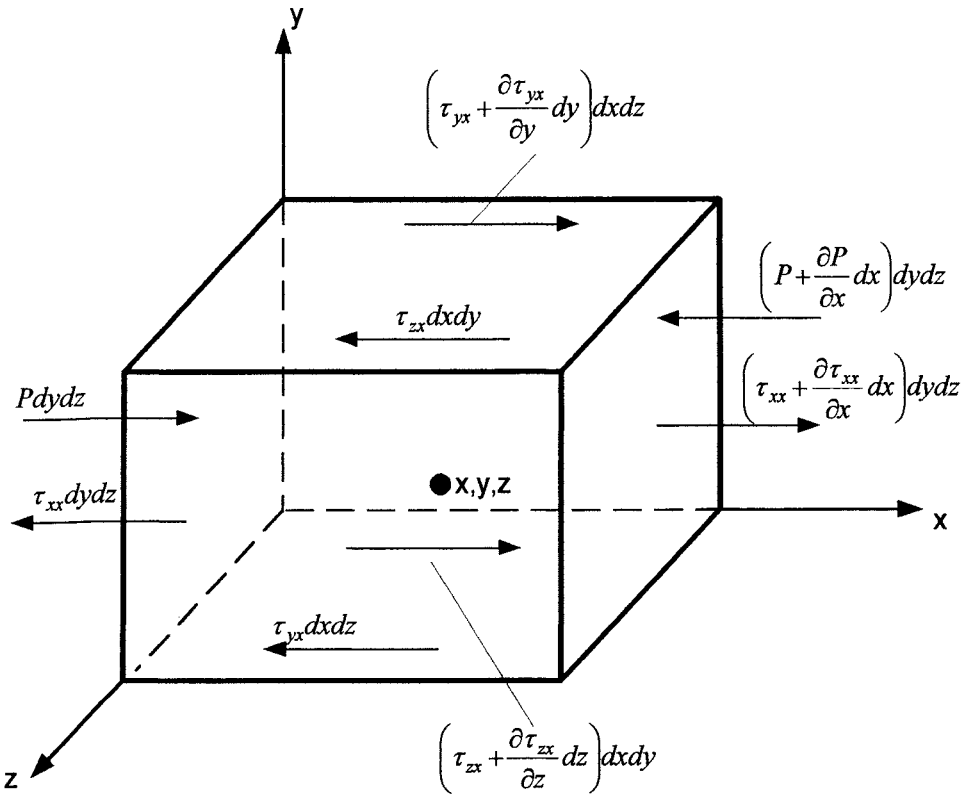

Fig. (3.2a) Stress components in the *x*-direction

By similarity, the y and z-components of the momentum equation are as follows:

$$\frac{\partial(\rho v)}{\partial t} + \frac{\partial(\rho u v)}{\partial x} + \frac{\partial(\rho v^2)}{\partial y} + \frac{\partial(\rho v w)}{\partial z} = -\frac{\partial P}{\partial y} + \frac{\partial \tau_{xy}}{\partial x} + \frac{\partial \tau_{yy}}{\partial y} + \frac{\partial \tau_{yx}}{\partial z} + S_y \tag{3.3b}$$

$$\frac{\partial(\rho w)}{\partial t} + \frac{\partial(\rho u w)}{\partial x} + \frac{\partial(\rho v w)}{\partial y} + \frac{\partial(\rho w^2)}{\partial z} = -\frac{\partial P}{\partial z} + \frac{\partial \tau_{xz}}{\partial x} + \frac{\partial \tau_{yz}}{\partial y} + \frac{\partial \tau_{zz}}{\partial z} + S_z \tag{3.3c}$$

The source terms S_x, S_y, and S_z include contributions due to body forces only. In a Newtonian fluid, the viscous stresses are proportional to the rates of deformation. Newton's law of viscosity includes two constants of proportionality: the dynamic viscosity, μ, which relates stresses to linear deformation, and the second viscosity, λ, which relates stresses to the volumetric deformation, usually taken as $-\frac{2}{3}\mu$. So, the viscous stress components are:

$$\tau_{xx} = 2\mu\frac{\partial u}{\partial x} + \lambda\left(\frac{\partial u}{\partial x} + \frac{\partial v}{\partial y} + \frac{\partial w}{\partial z}\right) \tag{3.4a}$$

$$\tau_{yy} = 2\mu\frac{\partial v}{\partial y} + \lambda\left(\frac{\partial u}{\partial x} + \frac{\partial v}{\partial y} + \frac{\partial w}{\partial z}\right) \tag{3.4b}$$

$$\tau_{zz} = 2\mu\frac{\partial w}{\partial z} + \lambda\left(\frac{\partial u}{\partial x} + \frac{\partial v}{\partial y} + \frac{\partial w}{\partial z}\right) \tag{3.4c}$$

$$\tau_{xy} = \tau_{yx} = \mu\left(\frac{\partial u}{\partial y} + \frac{\partial v}{\partial x}\right) \tag{3.4d}$$

$$\tau_{xz} = \tau_{zx} = \mu\left(\frac{\partial u}{\partial z} + \frac{\partial w}{\partial x}\right) \tag{3.4e}$$

$$\tau_{yz} = \tau_{zy} = \mu\left(\frac{\partial v}{\partial z} + \frac{\partial w}{\partial y}\right) \tag{3.4f}$$

The Navier-Stokes equations can be obtained by rearranging the terms of the viscous stresses and substituting in the momentum equations.

3.3.3 Energy equation

The first law of thermodynamics states that the increase in energy of a closed system is equal to the heat added to the system and the work done on the system. This principle may be applied to the CV as:

$$\left\{\begin{matrix}\text{rate of increase}\\ \text{of energy in CV}\end{matrix}\right\} = \left\{\begin{matrix}\text{net rate of heat}\\ \text{added to CV}\end{matrix}\right\} + \left\{\begin{matrix}\text{rate of work}\\ \text{done on CV}\end{matrix}\right\}$$

The rate of energy increase in the CV is $\frac{\partial(\rho E)}{\partial t} dxdydz$ and the net rate of transport energy out of CV by the flow per unit volume is:

$$\frac{\partial(\rho uE)}{\partial x} + \frac{\partial(\rho \upsilon E)}{\partial y} + \frac{\partial(\rho wE)}{\partial z} \tag{3.5}$$

The total rate of heat added to the fluid in CV due to heat flow across its boundaries per unit volume is:

$$-\left(\frac{\partial q_x}{\partial x} + \frac{\partial q_y}{\partial y} + \frac{\partial q_z}{\partial z}\right) = -div\, q \tag{3.6}$$

Fourier's law of heat conduction relates the heat flux to the local temperature gradient:

$$q_x = -k\frac{\partial T}{\partial x} \qquad q_y = -k\frac{\partial T}{\partial y} \qquad q_z = -k\frac{\partial T}{\partial z}$$

This can be written as:

$$q = -k\ grad\ T \tag{3.7}$$

Combining (3.6) and (3.7) yields the rate of heat addition to the fluid due to heat conduction across CV boundaries:

$$-div\ q = div\ (k\ grad\ T) \tag{3.8}$$

Where *div, grad* are the divergence of vector and gradient of scalar quantities respectively, ($div\ \mathbf{u} = \partial u/\partial x + \partial v/\partial y + \partial w/\partial z$), ($grad\ u = i\ \partial u/\partial x + j\ \partial u/\partial y + k\ \partial u/\partial z$).

The rate of work done by pressure on one side of the CV is the product of pressure, the area of the surface, and the normal velocity component as shown in Fig. (3.2b). So the net rate work done by pressure on the CV per unit volume is:

$$-\left(\frac{\partial(Pu)}{\partial x}+\frac{\partial(P\upsilon)}{\partial y}+\frac{\partial(Pw)}{\partial z}\right) = -div(P\mathbf{u}) \tag{3.9}$$

By similarity the net rate of the work done on the CV by normal stresses per unit volume is:

$$\frac{\partial(\tau_{xx}u)}{\partial x}+\frac{\partial(\tau_{yy}\upsilon)}{\partial y}+\frac{\partial(\tau_{zz}w)}{\partial z} \tag{3.10}$$

Also the rate of work done by shear stresses on the CV is:

$$\frac{\partial(\tau_{xy}u)}{\partial y}+\frac{\partial(\tau_{yx}\upsilon)}{\partial x}+\frac{\partial(\tau_{xz}u)}{\partial z}+\frac{\partial(\tau_{zx}w)}{\partial x}+\frac{\partial(\tau_{yz}\upsilon)}{\partial z}+\frac{\partial(\tau_{zy}w)}{\partial y} \tag{3.11}$$

Finally the energy equation for the unsteady compressible flow is:

$$\frac{\partial(\rho E)}{\partial t}+\frac{\partial(\rho uE)}{\partial x}+\frac{\partial(\rho \upsilon E)}{\partial y}+\frac{\partial(\rho wE)}{\partial z} = -\left(\frac{\partial(Pu)}{\partial x}+\frac{\partial(P\upsilon)}{\partial y}+\frac{\partial(Pw)}{\partial z}\right)+$$

$$+\frac{\partial(\tau_{xx}u)}{\partial x}+\frac{\partial(\tau_{xy}u)}{\partial y}+\frac{\partial(\tau_{xz}u)}{\partial z}+\frac{\partial(\tau_{yy}\upsilon)}{\partial y}+\frac{\partial(\tau_{yx}\upsilon)}{\partial x}+\frac{\partial(\tau_{yz}\upsilon)}{\partial z}+\frac{\partial(\tau_{zz}w)}{\partial z}+$$

$$+\frac{\partial(\tau_{zx}w)}{\partial x}+\frac{\partial(\tau_{zy}w)}{\partial y}-\left(\frac{\partial q_x}{\partial x}+\frac{\partial q_y}{\partial y}+\frac{\partial q_z}{\partial z}\right)+S_E \tag{3.12}$$

Where E represent the total energy which is the sum on internal and kinetic energy, $E = i + \frac{1}{2}\left(u^2 + \upsilon^2 + w^2\right)$

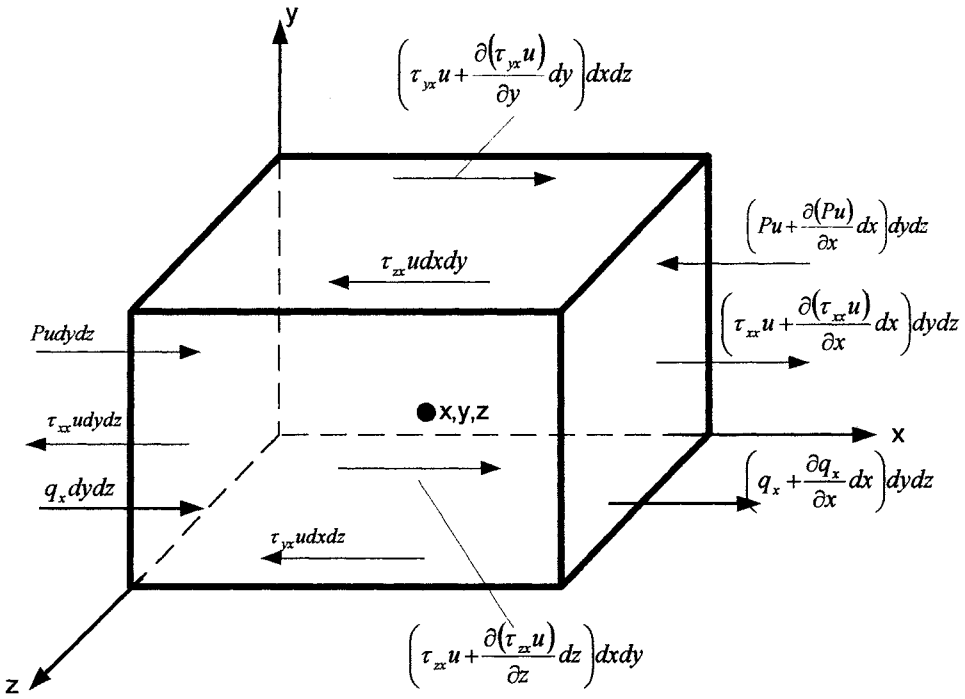

Fig. (3.2b) Energy flux components in the *x*-direction

3.3.4 Equation of state

A fundamental aim of CFD is to predict general types of fluid motion. This involves predicting pressure (P), density (ρ), temperature (T) and velocity components (u,v,w) at discrete points in space occupied by the fluid at discrete instants in time. In order to find values for these six unknown variables, six equations are needed. So far, five equations have been defined, mass conservation (3.1), x-, y- and z-momentum equations (3.3a-c) and energy equation (3.12). Since air can be assumed to be an ideal gas, the ideal gas law may be used for linking pressure with temperature:

$$P = \rho RT \tag{3.13}$$

3.3.5 Conservation form of the governing equations

The governing equations of the comprisable-Newtonian flow can be summarise in conservation form as:

Mass
$$\frac{\partial \rho}{\partial t} + div(\rho \mathbf{u}) = 0 \tag{3.14}$$

***x*-momentum**
$$\frac{\partial(\rho u)}{\partial t} + div(\rho u \mathbf{u}) = -\frac{\partial P}{\partial x} + div(\mu\, grad\, u) + S_x \tag{3.15a}$$

***y*-momentum**
$$\frac{\partial(\rho \upsilon)}{\partial t} + div(\rho \upsilon \mathbf{u}) = -\frac{\partial P}{\partial x} + div(\mu\, grad\, \upsilon) + S_y \tag{3.15b}$$

***z*-momentum**
$$\frac{\partial(\rho w)}{\partial t} + div(\rho w \mathbf{u}) = -\frac{\partial P}{\partial x} + div(\mu\, grad\, w) + S_w \tag{3.15c}$$

Internal energy
$$\frac{\partial(\rho i)}{\partial t} + div(\rho i \mathbf{u}) = -P\, div\, \mathbf{u} + div(k\, grad\, T) + \phi + S_E \tag{3.16}$$

Equation of state
$$P = \rho RT \quad \text{and} \quad i = C_v T \tag{3.17}$$

Where ϕ is the dissipation function which includes all the viscous stresses in the internal energy equation of a Newtonian fluid:

$$\phi = \mu\left\{2\left[\left(\frac{\partial u}{\partial x}\right)^2 + \left(\frac{\partial \upsilon}{\partial y}\right)^2 + \left(\frac{\partial w}{\partial z}\right)^2\right] + \left(\frac{\partial u}{\partial y} + \frac{\partial \upsilon}{\partial x}\right)^2 + \left(\frac{\partial u}{\partial z} + \frac{\partial w}{\partial x}\right)^2 + \left(\frac{\partial \upsilon}{\partial z} + \frac{\partial w}{\partial y}\right)^2\right\} + \lambda(div\, \mathbf{u})^2$$

For fluids of low viscosity at velocities less than sonic speed, ϕ is negligible compared to the other terms in the above, [Knudsen and Katz, 1958]. In the case of the incompressible steady-flow, the density and viscosity of the air can be treated as constant. Hence, the governing equation could be simplified by ignoring the derivative of density, viscosity and derivative with respect to time :

$$\frac{\partial *}{\partial t} = \frac{\partial \rho}{\partial *} = \frac{\partial \mu}{\partial *} = 0$$

3.3.6 General equation

The governing equations can be expressed in a general form of a general variable, φ as:

$$\frac{\partial(\rho\varphi)}{\partial t} + div(\rho\varphi\mathbf{u}) = div(\Gamma\, grad\,\varphi) + S_{\varphi} \qquad (3.18)$$

Where;

$\frac{\partial(\rho\varphi)}{\partial t}$	rate of change term of the general variable φ
$div(\rho\varphi\mathbf{u})$	convective term
$div(\Gamma\, grad\,\varphi)$	diffusive term
S_{φ}	source term

Equation (3.18) is a general governing equation, which can describe the continuity, momentum and energy of the fluid flow by setting the general variable φ equal to 1, (u, v, w) and T respectively. This equation is used as the starting point for the computational procedures.

3.4 Numerical methods

The three distinct approaches for the numerical solution of the governing equations are referred to as Finite Difference, Finite Element and Finite Volume methods. The Finite Element method originated from the field of structural analysis and the concept of "element" was referred to the techniques used in stress calculations. Ziekiewicz and Cheung-1965 reported that the finite element method could also be used to solve a fluid flow problem, [Hirsch, 1997]. The Finite Volume approach was introduced into the field of numerical fluid dynamics by McDonald-1971, [Hirsch, 1997]. This method is the most popular numerical discretization method used in CFD and it is similar in some ways to the Finite

Difference method. It was developed specifically to solve the equation of heat transfer and fluid flow, [Shaw, 1992].

The main differences between these methods are associated with the way in which the flow variables are approximated and with the discretization process. All numerical methods perform the following steps:

1- Approximation of the flow variable/unknown by means of simple functions
2- Discretization by substitution of the approximations into the governing flow equations.
3- Solution of the algebraic equations.

- **Finite Difference method-** describes the general variable, φ of the flow problem by means of point samples at the node points of grid lines (Fig. (3.3)). Truncated Taylor series expansions are often used to generate finite difference approximations of derivatives of φ at each grid point and its immediate neighbours. The mathematical expression of $\varphi_{i+1,j}$ is:

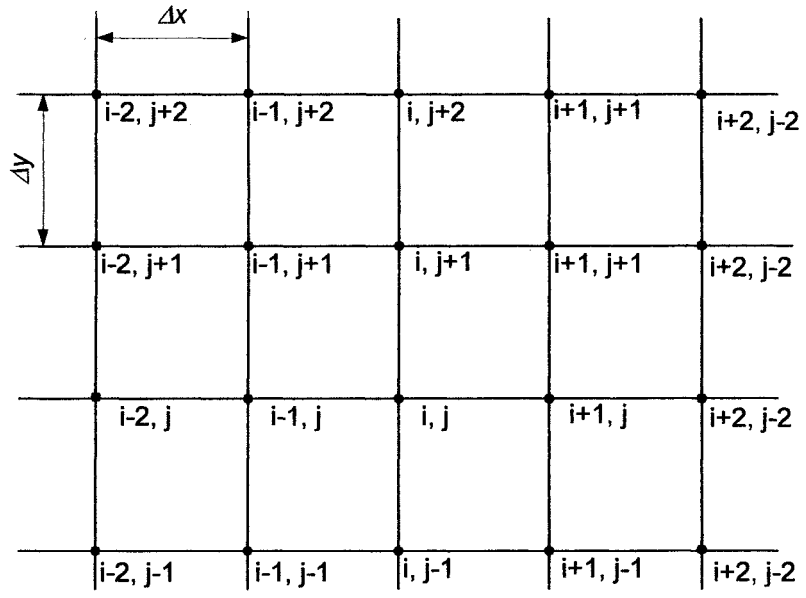

Fig. (3.3) Discrete grid points of finite difference method

$$\varphi_{i+1,j} = \varphi_{i,j} + \left(\frac{\partial \varphi}{\partial x}\right)_{i,j} \Delta x + \left(\frac{\partial^2 \varphi}{\partial x^2}\right)_{i,j} \frac{(\Delta x)^2}{2} + \left(\frac{\partial^3 \varphi}{\partial x^3}\right)_{i,j} \frac{(\Delta x)^3}{6} + \ldots\ldots \tag{3.19}$$

For numerical computations, it is impractical to carry an infinite number of terms. Therefore, equation (3.19) is truncated. In the case of second-order accuracy scheme, the terms of $(\Delta x)^3$ and higher are neglected while the terms of $(\Delta x)^2$ and higher are neglected for the first-order accuracy scheme. Thus, equation (3.19) may be rewritten as:

$$\varphi_{i+1,j} \approx \varphi_{i,j} + \left(\frac{\partial \varphi}{\partial x}\right)_{i,j} \Delta x + \left(\frac{\partial^2 \varphi}{\partial x^2}\right)_{i,j} \frac{(\Delta x)^2}{2} \tag{3.20a}$$

$$\varphi_{i+1,j} \approx \varphi_{i,j} + \left(\frac{\partial \varphi}{\partial x}\right)_{i,j} \Delta x \tag{3.20b}$$

From equation (3.19), the first-order forward difference of variable φ can be expressed as:

$$\left(\frac{\partial \varphi}{\partial x}\right)_{i,j} = \frac{\varphi_{i+1,j} - \varphi_{i,j}}{\Delta x} + O(\Delta x) \tag{3.20c}$$

Where $O(\Delta x)$ is the truncation error of higher order and it can be reduced by carrying more higher order accuracy and/or reducing the magnitude of Δx. After some mathematical manipulations, a first and second order-central difference for derivative of variable φ at grid point (i,j) can be expressed respectively as:

$$\left(\frac{\partial \varphi}{\partial x}\right)_{i,j} = \frac{\varphi_{i+1,j} - \varphi_{i-1,j}}{2\Delta x} + O(\Delta x)^2 \tag{3.21a}$$

$$\left(\frac{\partial \varphi}{\partial x}\right)^2_{i,j} = \frac{\varphi_{i+1,j} - 2\varphi_{i,j} + \varphi_{i-1,j}}{(\Delta x)^2} + O(\Delta x)^2 \tag{3.21b}$$

Equations (3.21a) and (3.21b) are then substituted into the governing equations to provide a series of finite-difference equations over the domain of interest. If this process is repeated at all the points in the solution domain, a set of equations for the variables at all points is formed and these are solved to give the numerical solution. The major limitation of the finite difference method is that the grid must be uniform, [Griffin, 1996].

- **Finite Element method-** uses simple piecewise function to describe the local variations of an unknown flow variable, φ. The domain over which the PDEs apply is split into a finite number of sub-domains, known as elements, which can be 2-D or 3-D (Fig. (3.4)). Over each element the flow variables are approximated using known functions and these may be linear or higher-order polynomials.

  In the present work, a two-dimensional CFD modelling of fully developed and developing flow through a long straight duct and corrugated wall-channel are investigated using the finite element CFD code (ANSYS V5.3).

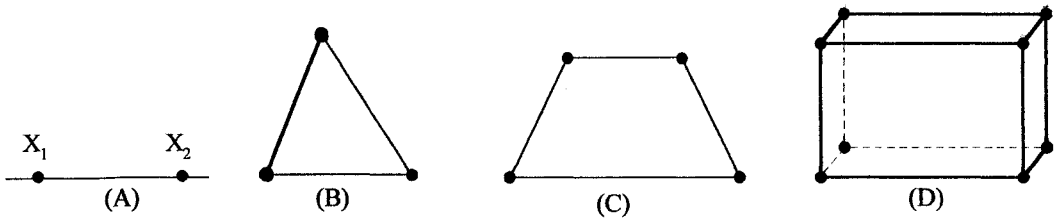

Fig. (3.4) Typical finite element configurations (A) 1-D line element (B) 2-D triangular element (C) 2-D quadrilateral element (D) 3-D hexahedron element

- **Finite Volume method-** uses the fluid flow governing equations in an integral form. The computational domain is divided into cells in which the conservation laws are applied to determine the flow field variables in some discrete points of the cells called "nodes". It considered a many degree of freedom in a grid types such as; triangular, quadrilateral, hybrid, and adaptive-grid.

Most of the numerical work presented in this thesis was undertaken using the finite volume method with the CFD code (FLUENT 5.4.8). A brief description on the finite volume method is presented here.

3.5 Finite Volume method

Discretization of the governing equations with the Finite Volume method can be illustrated most easily by considering integration on a control-volume of the general transport equation (3.18):

$$\int_{CV} \frac{\partial(\rho\varphi)}{\partial t} + \int_{CV} div(\rho\varphi \mathbf{u}) = \int_{CV} div(\Gamma\, grad\, \varphi) + \int_{CV} S_\varphi \qquad (3.22)$$

Considering Gauss' divergence theorem, the volume integration can be introduced as a surface integration on the entire bounding surface of the control-volume:

$$\int_{CV} div(\rho\varphi \mathbf{u}) = \int_{A} \mathbf{n}.(\rho\varphi \mathbf{u}) dA$$

Thus, a general steady-state transport equation can be expressed as:

$$\int_{A} n.(\rho\varphi \mathbf{u}) dA = \int_{A} n.(\Gamma\, grad\, \varphi) dA + \int_{CV} S_\varphi\, dv \qquad (3.23)$$

Where;

n	normal vector to surface element dA
u	Velocity vector

Γ_φ	Diffusion coefficient for φ
$grad\,\varphi$	Gradient of φ
S_φ	Source of φ per unit volume

Equation (3.23) is applied to each control volume or cell in computational domain. Discretization of equation (3.23) on a given cell (Fig (3.5)) yields

$$\sum_{f}^{N_{faces}} \mathbf{u}_f \varphi_f A_f = \sum_{f}^{N_{faces}} \Gamma_\varphi (div\varphi)_n A_f + S_\varphi V \qquad (3.24)$$

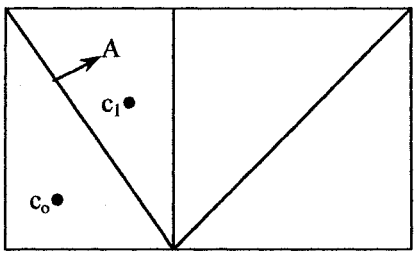

Fig. (3.5) Two-dimensional triangular cell of control volume

Where:

N_{faces}	number of faces enclosing cell
V	cell volume

The Finite Volume method solves the governing equations for the conservation of mass, momentum and energy and other scalars such as turbulence. A control-volume-based technique is used that consists of:

- Division of the domain into discrete control volumes using a computational grid.
- Integration of the governing equations on the individual control volumes to construct algebraic equations for the discrete dependent variables (unknowns) such as velocities, pressure, and temperature.
- Linearisation of the discretised equations and solution of the resultant linear equation system to yield updated values of the dependent variables.

3.5.1 Numerical Scheme

In the Finite Volume code, FLUENT, there are two solvers; a segregated solver and a coupled solver. In the case of incompressible flow, the segregated solver is appropriate while the coupled solver was originally designed for high-speed compressible flows. In the segregated solver, the governing equations are solved sequentially (i.e. segregated from one another) while in the coupled solver they are solved simultaneously (i.e., coupled together).

Because the governing equations are non-linear, several iterations of the solution loop must be performed before a converged solution is obtained. Each-iteration consists of the steps illustrated in Fig. (3.6). These steps are continued until the convergence criteria are met.

3.5.2 Linearization a set of governing equations

The discrete of a non-linear governing equations are linearised to produce a system of equations for the dependent variables in every computational cell. The resultant linear system is then solved to yield an updated flow-field solution. For a given variable, the unknown value in each cell is computed using a relation that includes both existing and unknown values from neighbouring cells. Therefore each unknown will appear in more than one equation in the system, and these equations must be solved simultaneously to give the unknown quantities. In the segregated solution method each discrete governing equation is linearised implicitly with respect to that equation's dependent variable. This will result in a system of linear equations with one equation for each cell in the domain. Because there is only one equation per cell, this is sometimes called a ``scalar'' system of equations. A point implicit (Gauss-Seidel) linear equation solver is used in conjunction with an algebraic method to solve the resultant scalar system of equations for the dependent variable in each cell. The segregated approach solves for a single variable field by considering all cells at the same time. It then solves for the next variable by again considering all cells at the same time, and so on.

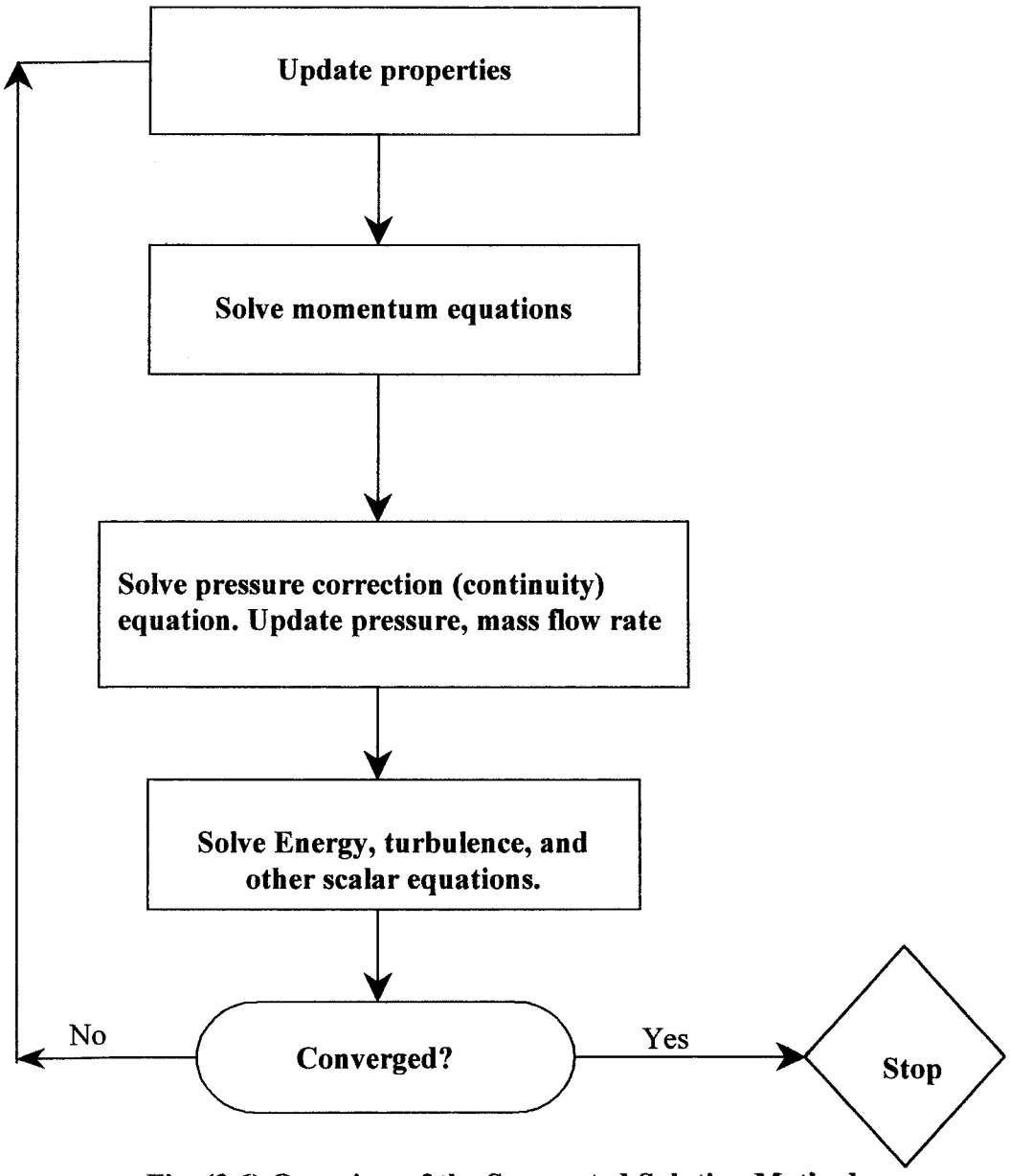

Fig. (3.6) Overview of the Segregated Solution Method

3.5.3 Discretization Schemes

Discretization schemes are used for the solution of convection terms of each governing equation. When the flow is aligned with the grid, (e.g., laminar flow with a quadrilateral or hexahedral grid) a first-order upwind discretization scheme may be acceptable. For triangular and tetrahedral grids,

since the flow is never aligned with the grid, more accurate-results will generally be obtained by using a second-order discretization. In most cases, a first-order discretization generally yields better convergence than a second-order scheme. (Upwinding means that the face value, φ_f, is derived from quantities in the cell upstream, relative to the direction of the normal velocity in equation (3.23))

In the present work, the first-order upwind scheme was considered. The quantities at cell faces are determined by assuming that the cell-centre values, φ, of any field variable represent a cell-average value and hold throughout the entire cell, the face quantities are identical to the cell quantities. Thus when first-order upwinding is selected, the face value, φ_f, is set equal to the cell-centre value, φ, in the upstream cell.

3.5.4 Pressure-Velocity Coupling

Pressure-velocity coupling is needed to derive an equation for pressure from the discrete continuity equation. FLUENT provides three methods for pressure-velocity coupling in the segregated solver: SIMPLE (semi-implicit method for pressure linked equations), SIMPLEC (SIMPLE-Consistent), and PISO. Steady-state calculations will generally use SIMPLE or SIMPLEC, while PISO (pressure implicit with splitting of operators) is recommended for transient calculations. In the present work, the SIMPLE algorithm is used for the pressure-velocity coupling.

The SIMPLE algorithm was originally explored by Patankar and Spalding, [1972] and it is essentially a guess-and-correct procedure for the calculation of pressure. It uses a relationship between velocity and pressure corrections to enforce mass conservation and thus obtain the pressure field. The method involves calculating pressure and velocities iteratively and when other scalars are coupled to the momentum equations, the calculation need to done sequentially. An overview of the SIMPLE algorithm is illustrated in Fig. (3.7)

3.5.5 Convergence and stability

The numerical solution φ_i approach to an exact solution φ (x, t) of governing equation at any point $x_i = i\ \Delta x$ and time $t_n = n\ \Delta t$ when Δx and Δt tend to zero, when the mesh is refined, x_i and t_n being fixed. This condition implies that i and n tend to infinity while Δx and Δt tend to zero. Convergence criterion is a normalized measure of the solution's rate of change from iteration to iteration. Convergence can be hindered by a number of factors. Large numbers of computational cells, overly conservative under-relaxation factors, and complex flow physics are often the main causes. Generally, there are no universal metrics for judging convergence. Residual definitions that are useful for one class of problem are sometimes misleading for other classes of problems. Therefore it is a good idea to judge convergence not only by examining residual levels, but also by monitoring relevant integrated quantities such as drag or heat transfer coefficient, [FLUENT manual, 1999].

Since the fluid flow governing equations are non-linear in nature, it is necessary to control the change in φ. This is typically achieved by under-relaxation in which the change of φ is reduced for each iteration. In a simple form, the new value of the variable φ within a cell depends upon the old value, φ_{old}, the computed change in φ, $\Delta\varphi$, and the under-relaxation factor, ζ, as follows:

$$\varphi = \varphi_{old} + \zeta\, \Delta\varphi \tag{3.25}$$

Lowering the under-relaxation factors in small increments can be advantageous in overcoming instabilities, [Drakulic, 1997].

3.5.6 Multigrid scheme

The multigrid scheme is used to accelerate the convergence of the solver by computing corrections on a series of coarse grid levels. The use of this multigrid scheme can greatly reduce the number of iterations and the CPU time

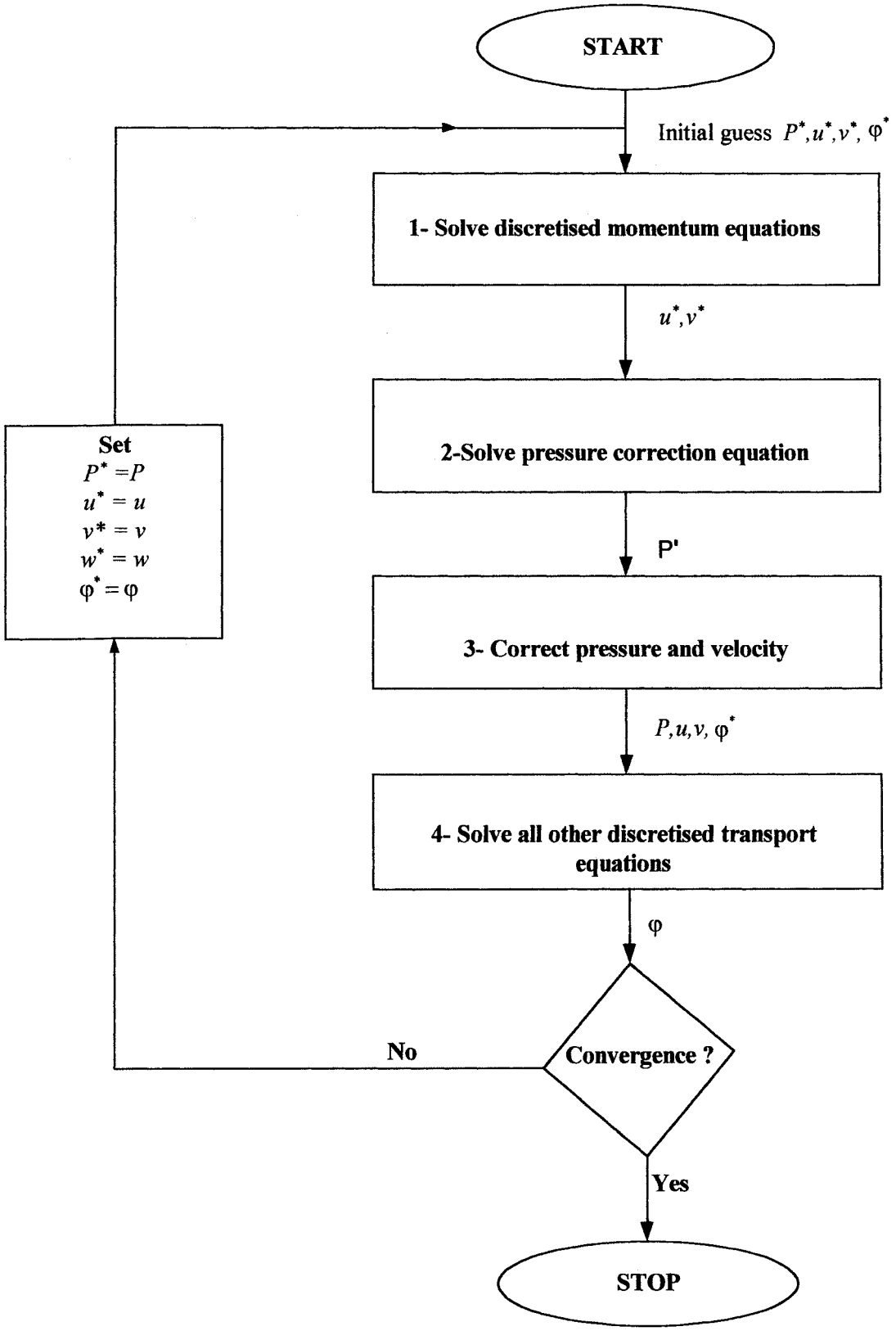

Fig. (3.7) Overview on The SIMPLE algorithm, [Versteeg, Malalaskera, 1995]

required to obtain a converged solution, particularly when the computational model contains a large number of control volumes.

Multigrid techniques used in FLUENT allow global error to be addressed by using a sequence of successively coarser meshes. This method is based upon the principle that global error existing on a fine mesh can be represented on a coarse mesh where it again becomes accessible as local error.

3.6 Numerical grid

As mentioned, the computational domain is discretised into a set of control volumes, which are arranged into a mesh. Mesh generation is a very important part in CFD simulation. The aim in this work was to generate a reasonable grid, which is used in modelling of the fin-and-tube heat exchangers with various fin geometries to satisfy a high accuracy requirement:

i. The grid lines should be as smooth as possible.
ii. Families of cross-lines should not intersect at highly oblique angles.
iii. In order to minimise numerical diffusion, one set of grid lines should be aligned with the main flow direction.
iv. Concentration of grid-lines in the regions of interest should be made.

To verify these requirements a pre-processor program (GAMBIT1.3) was used for modelling and mesh generation and for specification of the boundary condition types.

3.6.1 Grid Adaptation

Adaptive meshing is a useful aspect in CFD modelling where accurate results and economical computations are needed. Although the solution accuracy increases with increased number of grids, the CPU and memory requirements to compute the solution and post-processing of results also increase. Solution with adaptive-grid refinement can be used to increase grid density based on the

evolving flow field, and thus provides the potential for more economical use of grid points. The adaptive-grid is the mesh refinement technique which allows refining the grid locally at the region of interest to get a more precise calculation in that region, thus enabling the features of the flow field to be better resolved. In the FLUENT, two different types of adaption are available: "conformal" and "hanging node" adaptation. The conformal adaptation method is only valid for triangular and tetrahedral grids, while the hanging node adaptation can be applied to all supported cell shapes. Grids produced by the hanging node procedure are characterised by nodes on edges and faces that are not vertices of all the cells sharing those edges or faces. It provides the ability to operate on grids with a variety of cell shapes, including hybrid grids. However, although the hanging node scheme provides significant grid flexibility, it does require additional memory to maintain the grid hierarchy, which is used by the rendering and grid adaptation operations.

3.6.2 Grid smoothing

Smoothing and face swapping are tools that complement grid adaptation, usually increasing the quality of the final numerical mesh. Smoothing repositions the nodes and face swapping modifies the cell connectivity to achieve these improvements in quality. Two smoothing methods are available in FLUENT: Laplace smoothing and skewness-based smoothing. The first can be applied to all types of grids, but the second is available only for triangular/tetrahedral meshes.

3.7 Source of numerical errors

The exact analytical solution of the PDEs, which are described a fluid flow motion is very difficult and hence the use of a numerical approaches is essential. Some sources of errors are associated with the numerical procedures such as:

- Discretization error; is simply the truncation error of discretised governing-equations in addition to any errors introduced by the numerical treatment of the boundary conditions.
- Round-off error; the numerical error represented after a repetitive number of calculations in which the computer is constantly rounding the numbers to some significant figure, [John, 1996].

The numerical errors can be reduced by some procedures such as; mesh refinements, high order schemes, curvilinear mesh coordinates, and good convergence criteria.

3.9 Developing flow

The subject of developing flow is pertinent in the present work because often highly compact heat exchangers used for air conditioning applications (as fin-and-tube heat exchangers) result in core shapes that have large frontal areas and short channels for the airflow. The characteristics of the forced convection phenomena in the entrance region represent an important class of solutions for compact heat exchangers. The laminar flow development from a uniform flow profile at the inlet to the parabolic profile at a fully developed region is illustrated in Fig. (3.8). The hydrodynamic boundary layer is characterised by the presence of a velocity gradient and shear stress, while the thermal boundary layer is characterised by the temperature gradient and heat transfer. The hydrodynamic boundary layer thickness, δ increases with the distance from the leading edge and the flow is fully developed when the velocity profile no longer changes with increasing x. The boundary layer thickness is defined as the value of y for which $\frac{u}{u_i} \geq 0.99$, [Incropera and DeWitt, 1996]

The thermal boundary layer is developing when there is a temperature gradient between the wall-surface and the flowing air where the flow is thermally fully developed for which $\frac{(T_w - T)}{(T_w - T_i)} \geq 0.99$.

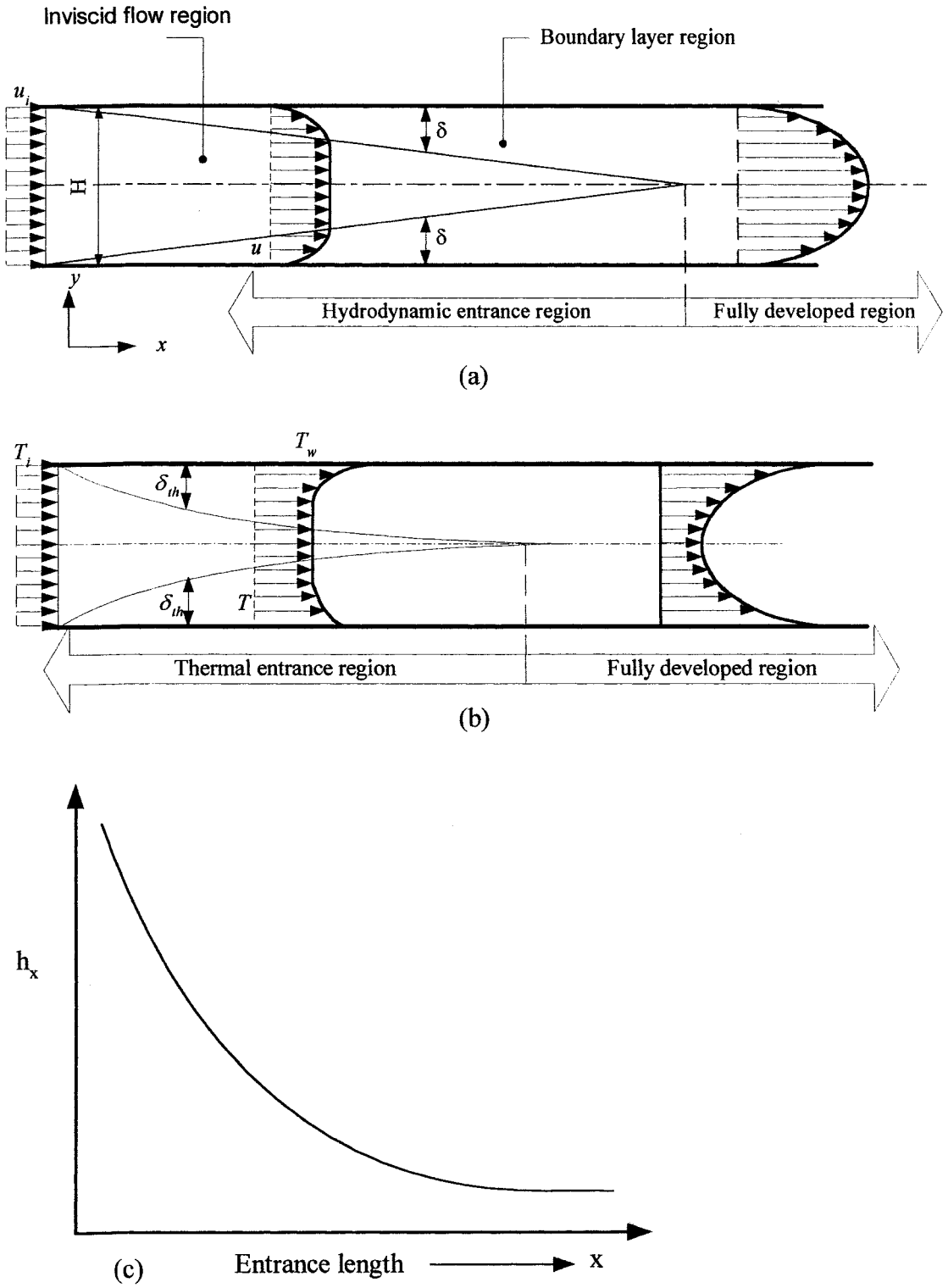

Fig. (3.8) Laminar boundary layer development (after Incropera, 1996)

(a)-Hydrodynamic, (b)-Thermal, (c)-Boundary layer-heat transfer coefficient.

At the wall surface, the air velocity is equal to zero and heat transfer occurs only by conduction. So, the heat flux may be obtained from:

$$q_w = -k_a \frac{\partial T}{\partial y}\Big|_{y=0} \tag{3.26}$$

According to Newton's law of cooling, these heat flux is transferred to the fluid by convection and then the heat transfer coefficient in the entrance region, h_x, may be expressed as:

$$h_x = \frac{-k_a \frac{\partial T}{\partial y}\Big|_{y=0}}{(T_w - T_i)} \tag{3.27}$$

Since $(T_w - T_i)$ is independent of x, the heat transfer coefficient in the entrance region is dependent on the temperature gradient on the wall, $\frac{\partial T}{\partial y}\Big|_{y=0}$.

Clearly, as x increases the temperature gradient decreases and thus there is a decrease in the heat transfer coefficient, as illustrated in Fig. (3.8). Therefore, one of the aims of the present work is to restrict the growth of the laminar boundary layer leading to an improvement in heat transfer in low velocity applications.

3.8 Dimensionless groups

The physical quantities often merge to represent a dimensionless parameters or groups which are characteristics of a given fluid flow and heat transfer process. The importance of the dimensionless groups lies in the interpretation of the fluid flow and heat transfer characteristics of the fin-and-tube heat exchangers. In this work, relevant groups are introduced and briefly explained.

- **Reynolds number, Re.** The Reynolds number represents the ratio of flow momentum rate, i.e. the inertial force, to the viscous force. This flow index is used to determine whether flow is laminar, transitional, or turbulent:

$$\mathrm{Re} = \frac{\rho u D_h}{\mu} \tag{3.28}$$

Where;

$$D_h = \frac{4(\text{cross section area})}{\text{wetted perimeter}} \tag{3.29}$$

The basic definition of the hydraulic diameter (equ. 3.29) is used in the two-dimensional calculations involved the long straight duct, corrugated wall channel and tube bundle. In the three-dimensional work, Kays and London [Kays and London, 1984] extended the above definition multiplying the numerator and denominator by the streamwise length to become applicable to fin-and-tube heat exchangers. This definition (equ. 3.30) is more relevant to fin-and-tube heat exchangers with modified fin surfaces (corrugated, turbulated and louver), since the heat exchanger details of streamwise length, fin pitch, tube diameter, tube arrangements, and heat exchanger dimensions are considered. In the experimental and three-dimensional modelling of the fin-and-tube cooling coils, equation (3.30) is applied to all calculations.

$$D_h = \frac{4 \text{ minimum flow area x streamwise length}}{\text{transfer surface area}} \tag{3.30}$$

- **Prandtl number Pr.** The Prandtl number defines as the ratio of momentum diffusivity to thermal diffusivity:

$$\mathrm{Pr} = \frac{\mu cp}{k} \tag{3.31}$$

- **Nusselt number, Nu.** The Nusselt number is equal to the dimensionless temperature gradient at the face and it provides a measure of the convection heat transfer occurring at the surface:

$$\mathrm{Nu} = \frac{h\,D_h}{k} = \left.\frac{\partial T^*}{\partial y^*}\right|_{y^*=0} \tag{3.32}$$

- **Friction factor, *f*.** The friction factor is defined as the ratio of the equivalent shear stress in the flow direction to the flow kinetic energy.

$$f = -\frac{dP}{dx}\frac{D_h}{\frac{1}{2}\rho u^2} \tag{3.33}$$

- **Fin efficiency, η_f.** The fin efficiency is defined as the actual heat transfer from the finned-tube divided by the heat transfer when the fin (single fin) is uniformly at the same temperature as the tube:

$$\eta_f = \frac{Q_{conjugate}}{Q_{isothermal}} \tag{3.34}$$

CHAPTER –IV-

Two-dimensional numerical analysis of heat exchange components

4.1 Introduction

Since the three-dimensional CFD analysis of fin-and-tube heat exchangers is not trivial due the complex nature of the geometry and the thermo-fluid characteristics through the fin-and-tube domain, it has been necessary to undertake two-dimensional flow analyses to investigate more effectively a range of geometric parameter relationships on the heat exchanger design, which is reported in this chapter.

Two sections through a corrugated fin-and-tube heat exchanger have been adopted. A horizontal section to consider corrugated wall geometry and the other is a vertical cross section to consider a staggered bundle of tubes. This chapter is presented in three parts. The first deals with the preliminary simulation of the fully developed flow through a long straight duct, as illustrated in Fig. (4.1). The objective was to verify the finite element CFD code by comparing the numerical results with the analytic solution and to investigate the grid dependence on the accuracy of the CFD solutions.

The second deals with the analysis of the heat transfer and friction characteristics of the corrugated wall channel, as shown in Fig. (4.2), in order to investigate the effect of corrugation angle, β and aspect ratio, A_r on the heat transfer and friction. Heat transfer per unit pumping power is quantified to establish the best design of the corrugated wall channel.

The third deals with the analysis of the staggered tube bundle array as illustrated in Fig. (4.3), in order to study the effect of transverse tube pitch, S_t, longitudinal tube pitch, S_L and number of tube rows crossed, N_R on the characteristics of heat transfer and pressure drop.

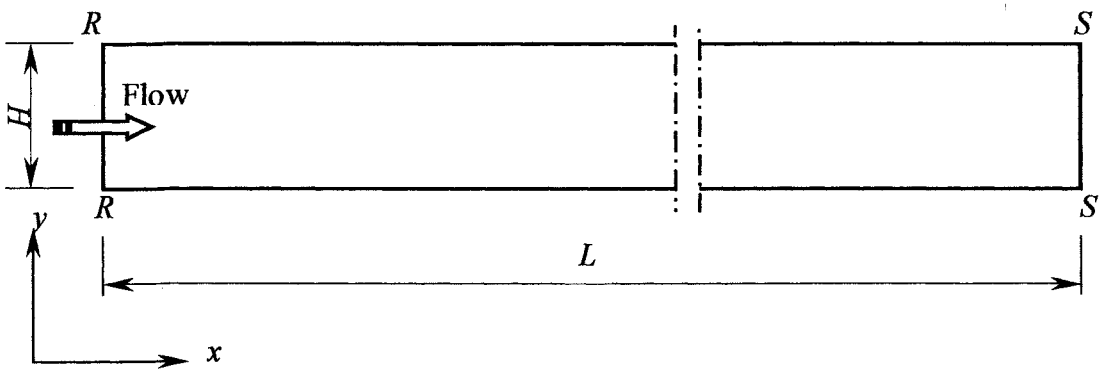

Fig. (4.1) Schematic diagram of long straight duct

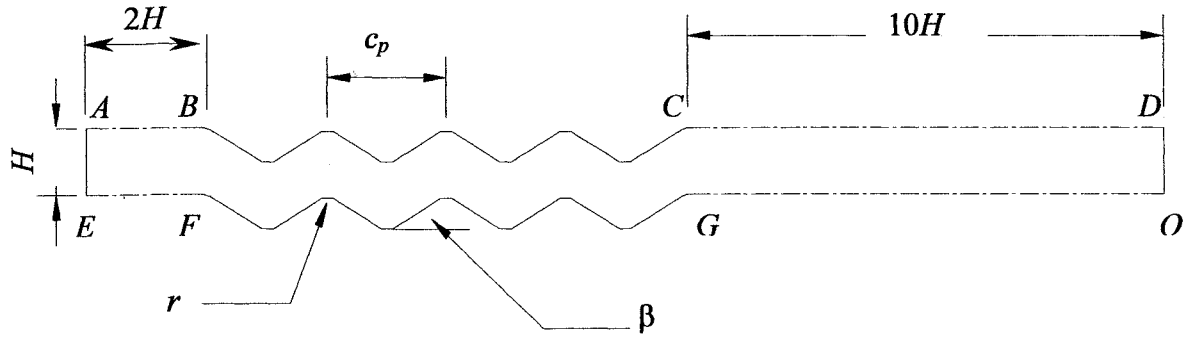

Fig. (4.2) Schematic diagram of the corrugated wall channel

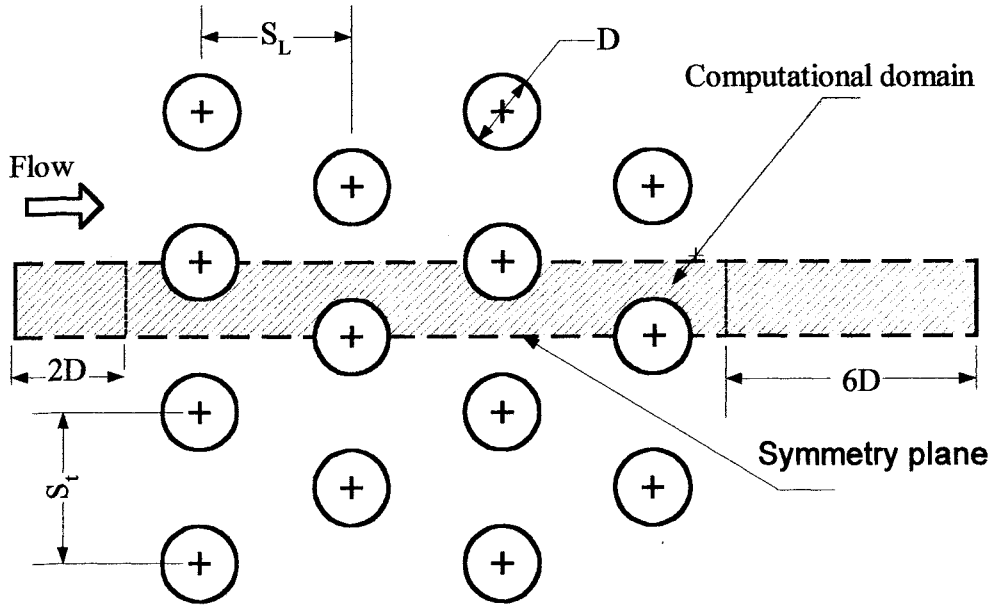

Fig. (4.3) Schematic diagram of the staggered tube bundle array

Both Finite Element and Finite Volume methods are considered in the analysis of the heat exchange components. An attempt is made to verify the results of both methods. Comparisons are also made with results in literature.

4.2 Statement of the problem

The airflow is considered to be two-dimensional, laminar and the buoyancy effect is neglected [Jang *et al*, 1996]. The description of the solution domain of the long straight duct, corrugated-wall channel and staggered tube bundle array are given:

- **Long straight duct**

A typical solution domain is represented in Fig. (4.1). The duct aspect ratio L/H = 200. The purpose of using such a large aspect ratio of the duct was to ensure that the flow became fully developed to provide a result, which is verified with theory (the hydrodynamic entrance length $\approx$ 0.05 D_h Re [Incropera and DeWitt, 1996]). The laminar fluid flow through the straight duct was tested for one value of Reynolds number, Re = 945 corresponding to an inlet air velocity, u_i = 0.015 m/s. In order to investigate the effect of grid density on the accuracy of the CFD modelling results, thirty-eight permutations of grid densities have been tested as part of this work.

- **Corrugated wall channel**

A typical solution domain is represented in Fig. (4.2) and consists of a series of repeated corrugation cycles. The geometry of the corrugated wall channel is specified using the corrugation pitch (c_p), wall spacing (H), and corrugation angle (β). The Reynolds number ranged from 100 to 1000 corresponding to an inlet air velocity ranging from 0.188 to 1.88 m/s. The reason for not using Reynolds number greater than 1000 was to avoid the low convergence criterion (which is discussed later in section 4.7). The results were compared with straight duct results ($\beta = 0^o$).

In order to minimize the pressure drop and also get a better converged solution, the sharp-edged corners of the corrugated–wall channel were approximated by rounded corners with curves with a radius of curvature, r. The radius of curvature is assumed as a small number equal to one tenth of the cycle length [Gomaa *et al*, 1999]. At a fixed mass flow rate, the friction factor decreased even more than the Nusselt number for the rounded-edge corner compared with that of a sharp-edge corner [Sparrow and Hossfeld, 1984]. Calculations were carried out for four values of the corrugation angle, $\beta = 10^{o}$, 15^{o}, 20^{o}, and 30^{o} and for four values of the dimensionless aspect ratio, $A_r = 2$, 4, 6 and 8 (corresponding to $c_p = 8$, 16, 24 and 32 mm respectively).

- **Staggered tube bundle array**

The solution domain of the tube bundle array is represented in Fig. (4.3). The geometry of the tube bundle is specified as a typical geometry of the air conditioning coil manufactured by Thermal Transfer Technology (3T) LTD. Numerical analysis was carried out for three values of the dimensionless transverse tube pitch X_t = 1.57, 2.36 and 3.15 (corresponding to S_t = 20, 30, 40 mm), three values of the dimensionless longitudinal tube pitch X_L = 1.25, 1.5 and 2 (corresponding to S_L = 15.875, 19.05 and 26 mm) and three values of number of tube rows crossed, N_R = 2, 3, and 4. The Reynolds number used ranged from 100 to 2000 corresponding to air velocities of 0.12 m/s $\leq ui \leq$ 2.4 m/s.

4.3 Boundary conditions

The boundary conditions are sufficiently important to warrant a detailed description of the computational domains. The boundary conditions applied to the two-dimension flow of the long duct, corrugated wall channel and to the staggered tube bundle array were quite similar. At the inlet boundary, uniform flow with velocity u_i and temperature T_i are specified. At the outlet boundary, the pressure, P_o is set to zero. At the symmetry planes, normal components and its gradients are set to zero. At the solid surface, no-slip conditions and constant wall temperature

T_w were specified. Further details of the boundary conditions applied in each case are given:

- **Long straight duct** - Referring to the domain in Fig (4.1), the boundary conditions of the long duct were as follows:

  Inlet boundary, *RR*: $u = u_i$

  Wall boundary, *RS*: $u = v = 0$

  Outlet boundary, *SS*: $P_o = 0$

- **Corrugated wall channel** - Referring to the domain in Fig. (4.2), the boundary conditions for the corrugated wall channel were as follows:

  Inlet boundary, *AE*: $\begin{cases} u = u_i \\ T = T_i \end{cases}$

  Wall boundaries, *BC* and *FG*: $\begin{cases} u = v = 0 \\ T = T_w \end{cases}$

  Symmetry boundaries, *AB, EF, CD* and *GO* $v = \frac{\partial u}{\partial y} = \frac{\partial v}{\partial y} = \frac{\partial T}{\partial y} = 0$

  Outlet boundary, *DO* $P_o = 0$

  The symmetry boundaries, *CD* and *GO* are attached to the end of the corrugated wall channel in order to approach uniform temperature and velocity conditions at the outlet boundary.

- **Staggered tube bundle array**

The dashed lines in Fig. (4.3) indicate the computational domain using symmetry conditions are defined on the mid-plane between two columns of tubes. At the upstream boundary, (located two times the tube diameter from the first upstream tube-row, which helped to meet a converged solution), uniform flow with velocity u_i and temperature T_i were specified [Gomaa *et al*, 2001]. At the

downstream end of the computational domain, (located six-times the tube diameter from the last downstream row [Versteeg and Malalasekera, 1995]), the pressure was set to zero.

4.4 Computational details

A finite element discretization method using non-orthogonal body-fitted coordinates was used for the solution of the long straight duct and corrugated wall channel. The numerical solution was performed using computation fluid dynamics program ANSYS-5.3/FLOTRAN. A TDMA solver (Tri-Diagonal Matrix Algorithm) was used for solving velocities and temperature equations while the PCGM (Preconditioned Conjugate Gradient Method) for the pressure equation, which is preferred for incompressible flow. The TDMA solver is special case of the standard Gauss-Seidel iterative method for a solution of algebraic equations.

- **Long straight duct**

The computations were performed with differing number of grids in both x and y directions (N_x and N_y) respectively. The grid distributed with fine spacing towards the duct walls and to the flow inlet as shown in Fig. (4.4) with a geometric space ratios, $b/a = 2.5$ and $c/d = 3$.

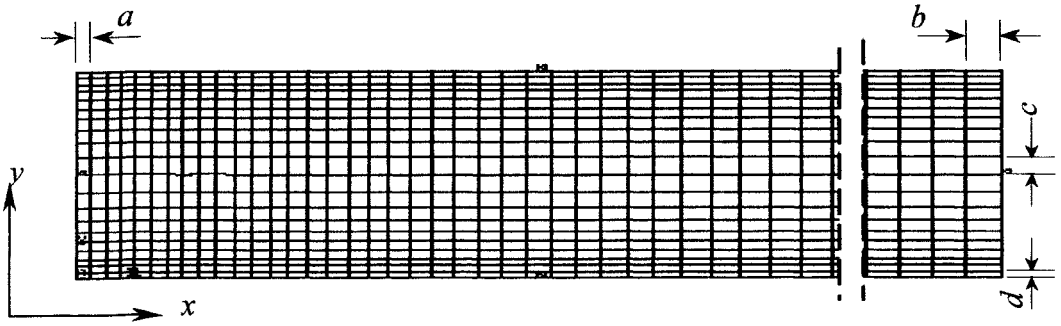

Fig. (4.4) Grid distribution of the long straight duct

The grid was set denser in the wall zone and towards to the inlet of the duct to get a more precise calculation in the developing region. Various grid strategies are listed in Table (4.1). The solution procedure was iterative and the computations were terminated when the residuals in both velocity and pressure are less than 5×10^{-5} for all runs.

Table (4.1) Grid strategies for long straight duct

Case	N_x	N_y
One	100	30, 40, 50, 60, 70, 75 & 80
Two	100, 150, 200, 250 & 300	30
Three	100, 150, 200, 250 & 300	40
Four	100, 150, 200, 250 & 300	50
Five	100, 150, 200, 250 & 300	60

- **Corrugated wall channel**

Most of the computations were performed with the 40 x 30 grid-points per corrugation cycle with space ratios of 2 and 3 in the x and y directions respectively as shown in Fig. (4.5). The grid was refine towards the wall zone and to the peak and valley of the corrugated channel in order to get a more precise calculation in that region.

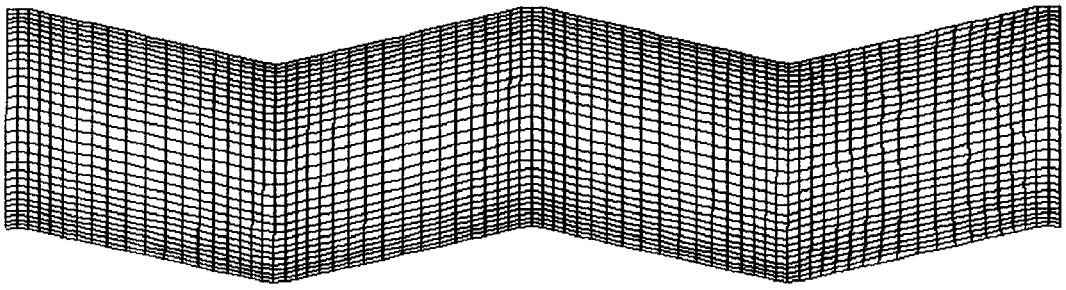

Fig. (4.5) Typical grid distribution of corrugated-wall channel

The values of the convergence criterion attainable were found to depend on the corrugation angle, Reynolds number, and to a limited extent on the aspect ratio. The temperature converged to the specified criteria of less than 10^{-5} for all runs. The values of the convergence criterion achieved for the velocity and pressure are listed in table (4.2). The number of iterations ranged from 300 to 1000. It was difficult to obtain convergence criteria below 5×10^{-3} for high corrugation angle and/or Reynolds number where the default value was 10^{-6}. In addition, a higher computational time was observed. This has motivated the use of an alternative different CFD program in next analysis (further details are given in section 4.6).

Table (4.2) Values of the convergence criterion

β	**Velocity convergence**			**Pressure convergence**		
10° , 15°	5×10^{-5}	to	5×10^{-4}	5×10^{-5}	to	5×10^{-4}
20° , 30°	5×10^{-5}	to	5×10^{-3}	5×10^{-4}	to	5×10^{-3}

- **Staggered tube bundle**

A finite volume discretization method using non-orthogonal body-fitted coordinates and a SIMPLE-based solution algorithm (semi-implicit method for pressure linked equations) of the velocity-pressure coupling was used with a segregated solver. The momentum and energy equations were solved by the first order upwind scheme. The numerical solution was performed using CFD pre-processor, GAMBIT 1.3 and post-processor, FLUENT 5.4.8.

Since the computation domain of the two-dimensional staggered tube bundle array was quite similar to the computational domain of the flat fin-and-tube heat exchanger regardless of the third projection, many types of meshing strategies were examined for the staggered tube bundle as illustrated in Fig. (4.6). The techniques of mapped mesh, hybrid mapped-triangular mesh, hybrid mapped mesh and adaptive multi-block mapped mesh were adapted.

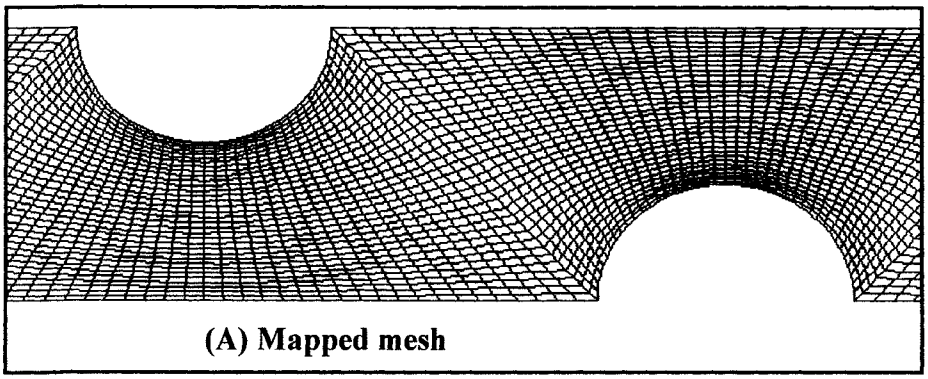

(A) Mapped mesh

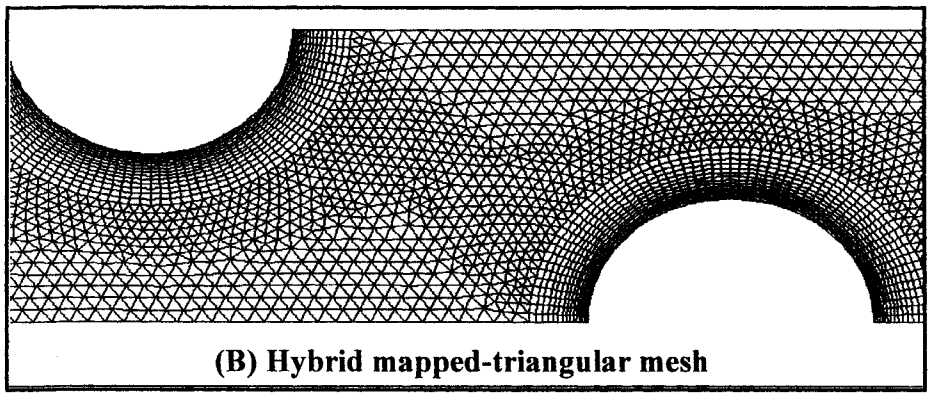

(B) Hybrid mapped-triangular mesh

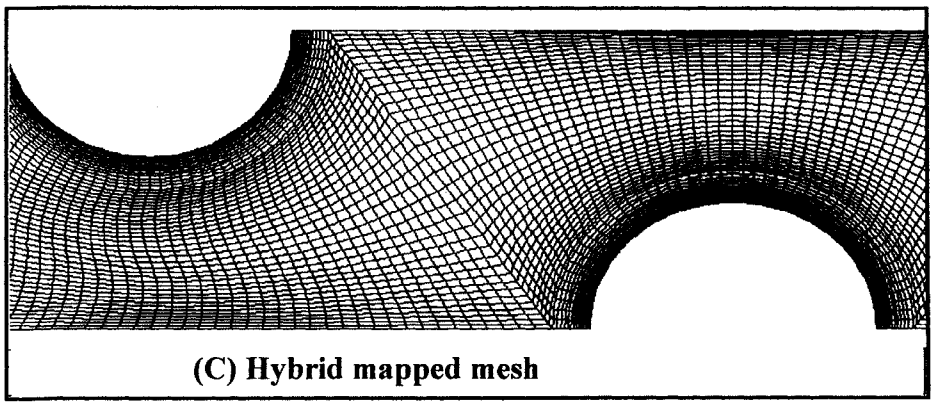

(C) Hybrid mapped mesh

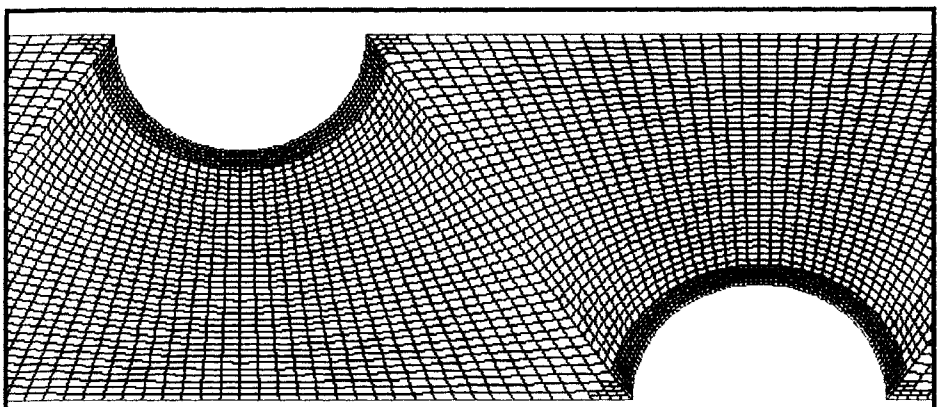

(D) Adaptive multi-Block mapped mesh

Fig. (4.6) Mesh-types tested with the tube bundle array

Comparison of the Nusselt number and friction factor was made between all mesh types.

After some initial mesh refinements, an adaptive multi-block mesh technique was chosen. Solution with adaptive-grid refinement was used to increase the grid density based on the evolving flow field, and thus provides the potential for more economical use of grid points. The quadrilateral cells provide better resolution of the viscous gradients near the tube walls [FLUENT manual, 1999].

Most of the computations were performed with a nominal grid of 400 x 35 grid-points (16000 nodes) and with the boundary grid adaption based on the number of cells set at 3 at the wall zone by the use of a "hanging" nodes technique as shown in Fig. (4.7).

The refinement of the grids near boundary zones was necessary because important fluid interactions often occur in these regions, such as the velocity and temperature gradients in the boundary layer near a tube wall.

The values of the convergence criteria were found to strongly depend on the transverse tube pitch, longitudinal tube pitch, Reynolds number, and weakly on the number of tube rows. An under-relaxation factor of 0.2 for momentum was chosen to produce more stability of the solution. The temperature converged to the specified criteria of less than 10^{-5} for all runs whereas the values of the convergence criterion for the velocity and continuity were in the range of $5x10^{-6}$ to $5x10^{-4}$. The number of iterations ranged from 700 to 1500.

4.5 Methods of calculation

The log-mean temperature difference "*LMTD*" method of calculation was used in the calculation [Yang *et al*, 1995]. The average heat transfer coefficient is given by:

$$h = \frac{\dot{m} Cp (T_{ao} - T_{ai})}{A_s \theta} \tag{4.1}$$

Where;

$$\dot{m} = \rho A_c u_i,$$

$$\theta = \frac{(T_w - T_{ai}) - (T_w - T_{ao})}{\ln \frac{(T_w - T_{ai})}{(T_w - T_{ao})}}$$

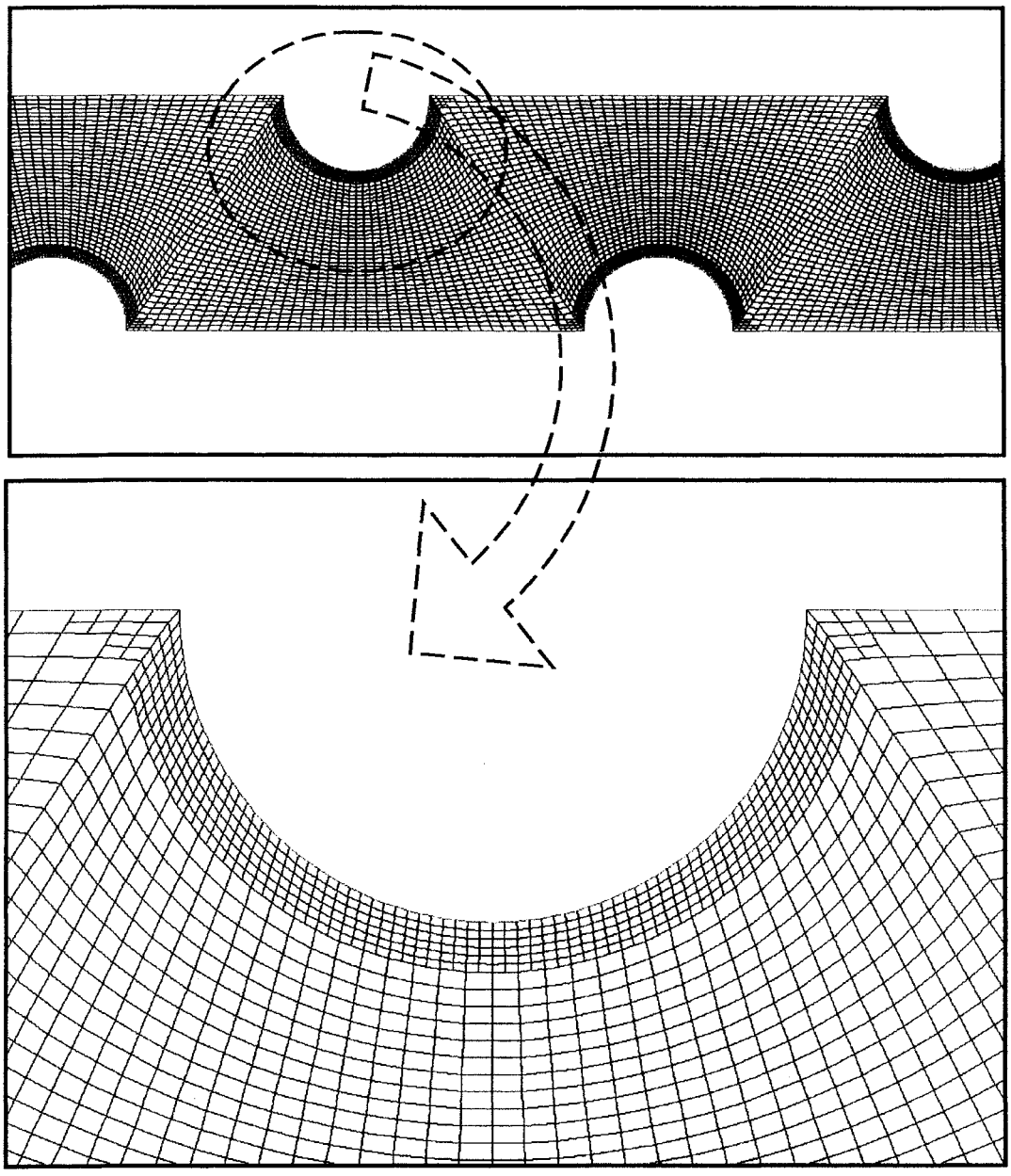

Fig. (4.7) Grid distribution of the staggered tube bundle arrays

The outlet temperature T_o of the flow field is computed by dividing the integral of the product of local temperature and the dot product of the facet area and momentum vectors by the integral of the dot product of the facet area and momentum vectors. The boundary temperature diagram of heat exchanger is illustrated in Fig. (4.8).

$$T_o = \frac{\int T \rho \vec{u} \cdot d\vec{A}}{\int \rho \vec{u} \cdot d\vec{A}} \tag{4.2}$$

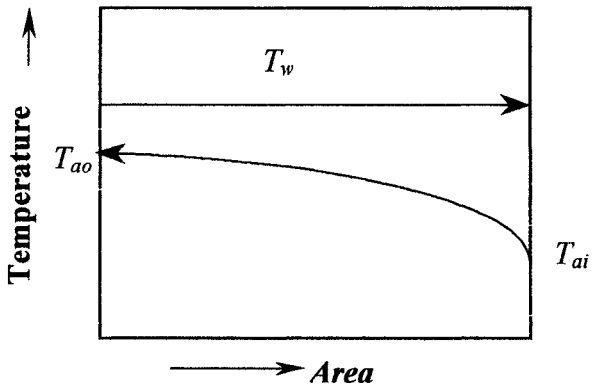

Fig. (4.8) Heat exchanger boundary temperature

The average Nusselt number is defined as:

$$\mathrm{Nu} = \frac{h D_h}{k} \tag{4.3}$$

The Reynolds number depends upon the air velocity at the minimum flow area and hydraulic diameter:

$$\mathrm{Re} = \frac{\rho u D_h}{\mu} \tag{4.4}$$

The hydraulic diameter, D_h was defined as;

$$D_h = \frac{4(\text{cross section area})}{\text{wetted perimeter}} \tag{4.5}$$

- For the long straight duct and corrugated wall channel

$$D_h = \frac{4\,(H\ L_z)}{2(L_z + H)} \quad or \quad D_h = \frac{2H}{1+H/L_z}$$

where:

L_z is the duct-width in the third projection

In the case of two-dimensional flow in x-y plane

$$D_h = \lim_{L_z \to \infty} \left[\frac{2H}{1+H/L_z}\right]$$

$$D_h = 2H \tag{4.6}$$

- For the tube bundle array

$$D_h = D \tag{4.7}$$

- The flow velocity for the long straight duct and corrugated wall channel is given as;

$$u = u_i$$

- For the staggered tube bundle arrays;

$$u = u_{max}$$

In the staggered tube bundle the maximum flow velocity (u_{max}) may occur at either the transverse plane or the diagonal plane depending on the values of S_t, S_L and D. In all cases of the present study, the maximum flow velocity occurs at the transverse plane, and it is given as;

$$u_{\max} = u_i \frac{S_t}{S_t - D} \tag{4.8}$$

4.5.1 Theoretical performance criteria

- **Long straight duct**

In an attempt to verify the predictive accuracy of the numerical solution, predictions of the flow velocity and friction factor in a long straight duct were compared with a known analytically exact solution. The theoretical maximum flow velocity in fully developed laminar flow through a straight duct, is given by Burmeister (1983):

$$u_{max} = 1.5\, u$$

Thus the theoretical dimensionless maximum velocity $(R_{max})_{theory}$ can be given as:

$$(R_{\max})_{theory} = \frac{u_{\max}}{u} = 1.5 \tag{4.9}$$

The value of the dimensionless maximum velocity $(R_{max})_{theory}$ is compared with the a value predicted by a numerical solution. The results are presented as the percentage error, which can be expressed as;

$$E_R = \left[\frac{(R_{\max})_{theory} - (R_{\max})_{ansys}}{(R_{\max})_{theory}} \right] \text{x } 100 \tag{4.10}$$

The theoretical friction factor of the long straight duct can be expressed using Poisseuille's equation [Knudsen and Katz, 1958]:

$$f_1 = \frac{24}{\mathrm{Re}} \tag{4.11}$$

Whereas the CFD predicted friction factor may be expressed as [Incropera, and DeWitt, 1996]:

$$f_2 = \frac{2\tau_w}{\rho u_i^2} \tag{4.12}$$

The value of the theoretical friction factor, f_1, is compared with the value of the predicted friction factor, f_2. The results are presented in the form of percentage error, which can be expressed as;

$$E_f = \left[\frac{f_1 - f_2}{f_2}\right] \text{x } 100 \tag{4.13}$$

- **Corrugated wall channel**

The friction factor of the corrugated wall channel is define as [Asako and Faghri, 1987]:

$$f = -\frac{dp}{dx}\frac{D_h}{\frac{1}{2}\rho u_i^2} \tag{4.14}$$

The heat transfer per unit pumping power, Q/P_p per unit temperature difference is given by:

$$Q/P_p = \frac{\rho\, Cp}{\Delta P} \tag{4.15}$$

- **Staggered tube bundle array**

The average friction factor is define as [Launder and Massey, 1978]:

$$f = \frac{\Delta P}{\frac{1}{2}\rho u_{max}^2 \, N_R} \tag{4.16}$$

The inlet pressure is calculated in a similar manner to that of the outlet air temperature (equation (4.2)):

$$P_i = \frac{\int P \, \rho \, \vec{u} \, . \, d\vec{A}}{\int \rho \, \vec{u} \, . \, d\vec{A}} \tag{4.17}$$

4.6 Results

The results for the three test cases are presented as follows:

- **Long straight duct**

The results of the long straight duct are presented in the form of percentage error for both maximum velocity and friction factor. Fig. (4.9) shows the variation of the percentage error in maximum velocity E_R with number of iterations N_t for N_x = 100 and N_y = 30, 40, 50, 60, 70, 75 and 80. Under converged conditions, the value of percentage error decreases as the number of grids in y-direction increase. For the value of N_y = 30, convergence is obtained within 75 iterations with a percentage error of 1.5 whereas for the value of N_y = 80, convergence is obtained within 150 iterations with percentage error of 0.17. The effect of the number of grids in x-direction on the percentage error of maximum velocity is illustrated in Figs. (4.10) and (4.11) for the values of N_y = 30, 60 respectively. The values of E_R tend to 1.5 % and 0.5 % respectively for all values of N_x. Thus different values of N_x have a negligible effect on the accuracy of the solution.

The percentage error in friction factor versus number of grids in y-direction for values of N_x = 100, 150, 200 and 250 is illustrated in Fig. (4.12). The percentage errors in friction factor decrease with the number of grids in the y-direction. Further investigations are given in Table (4.3)

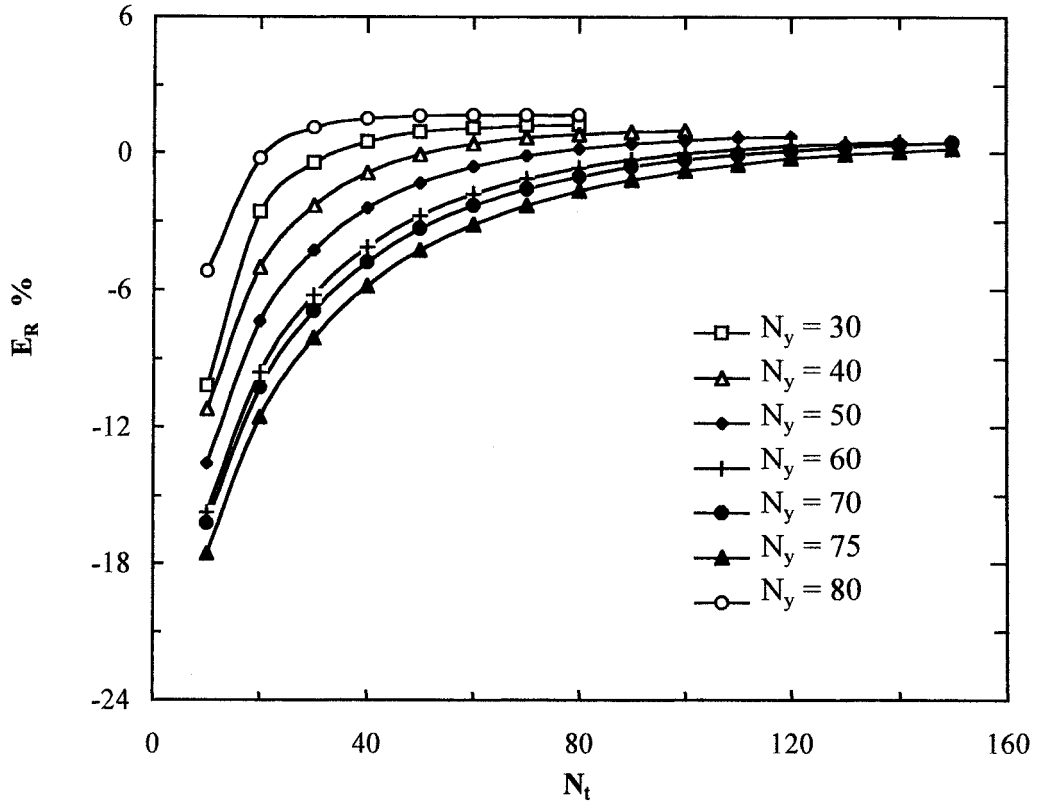

Fig (4.9) Percentage error of maximum velocity for $N_x = 100$

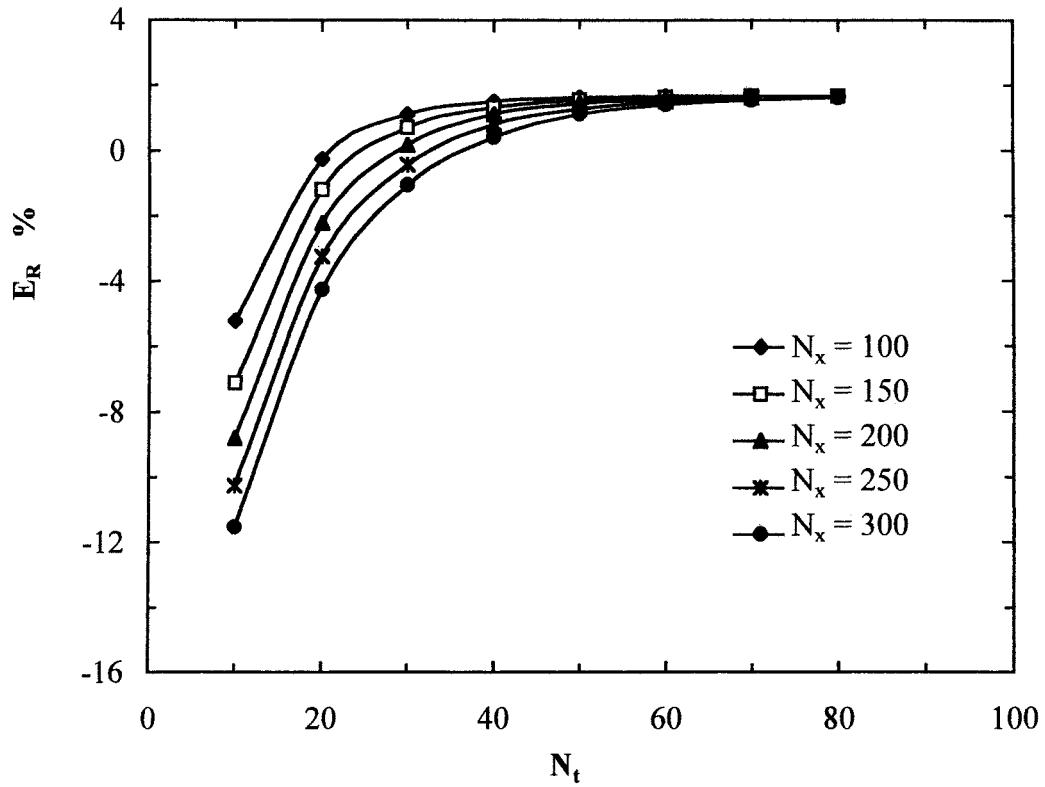

Fig. (4.10) Percentage error in maximum velocity for $N_y = 30$

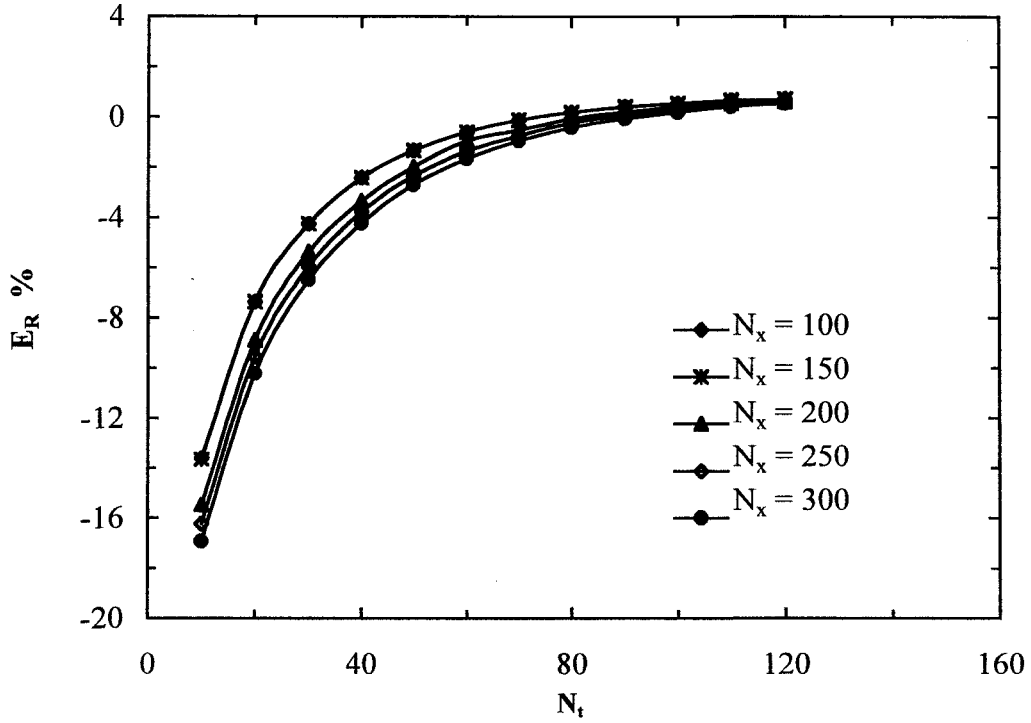

Fig. (4.11) Percentage error in maximum velocity for $N_y = 60$

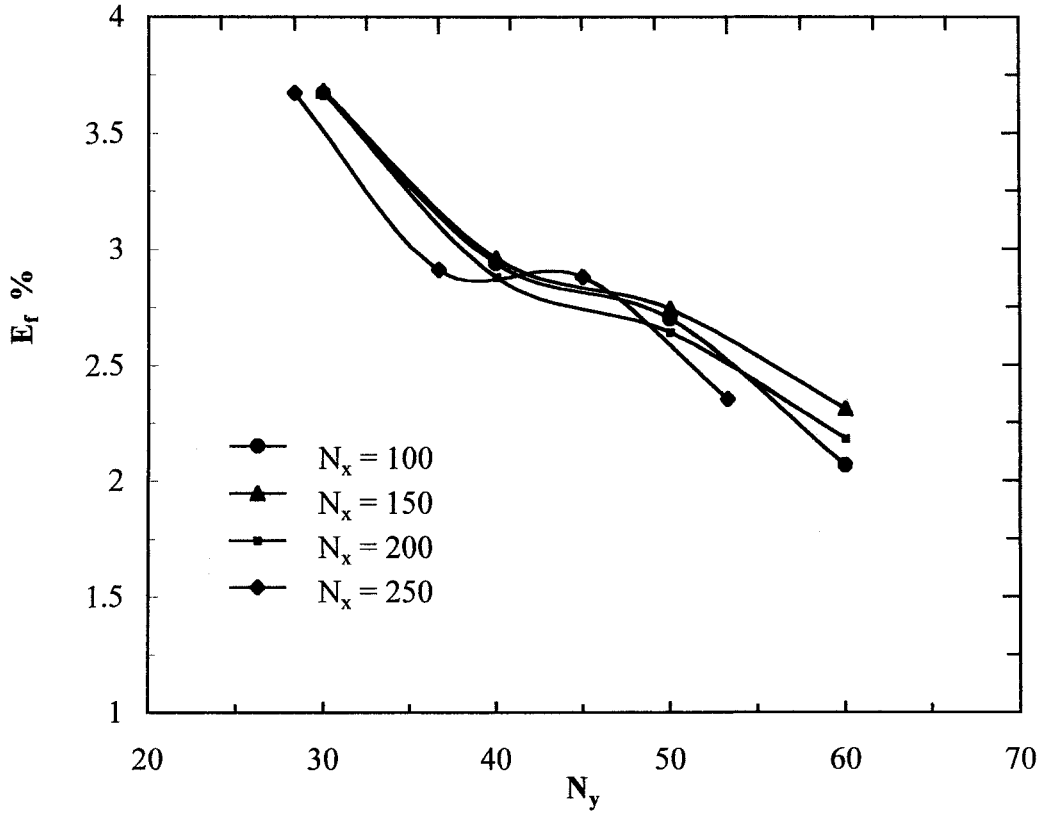

Fig (4.12) Percentage error in friction factor

Table (4.3) Effect of number of elements and space ratio on E_R and E_f

Mesh	Space ratio	Re	E_R %	E_f %
200 x 20	1 x 1	994.5	5.33	8.33
200 x 20	2.5 x 1	994.5	5.33	8.33
300 x 30	1 x 3	994.5	1.80	2.92
300 x 20	1 x 2	994.5	3.33	8.33
320 x 35	2.5 x 3	994.5	1.60	2.50
300 x 40	2.5 x 3	994.5	1.13	2.50
300 x 40	2.5 x 3	994.5	1.07	2.08
320 x 40	2.5 x 3	994.5	1.20	2.08
320 x 45	2.5 x 3	994.5	1.20	2.08
320 x 50	2.5 x 3	994.5	1.20	2.08
300 x 30	2.5 x 2	1127	2.00	4.76

- **Corrugated wall channel**

A grid dependence check was performed for the case $\beta = 15^{\circ}$, $A_r = 4$ and Re = 500 for nominal grid (40 x 30 grid-points per corrugation cycle) against a coarser grid (32 x 25) and a finer grid (48 x 35). The maximum differences in the Nusselt number and friction factor between the coarser and the nominal grids were 2.4 % and 2.43 % respectively. Between nominal and finer grids, the differences were 1.93 % and 2.11 % respectively. Thus, the medium grid was chosen to maintain relatively high accuracy and relatively moderate CPU time.

The flow field through the corrugated wall channel is illustrated in Fig. (4.13) for $\beta = 15^{\circ}$ and aspect ratio $A_r = 4$. The flow separates from the rear-facing facet and reattaches to the front facing facet thus creating a recirculating flow at the corrugation peak. The reason for the separation was that the fluid was unable to turn sufficiently sharply to follow the geometry of the corrugation.

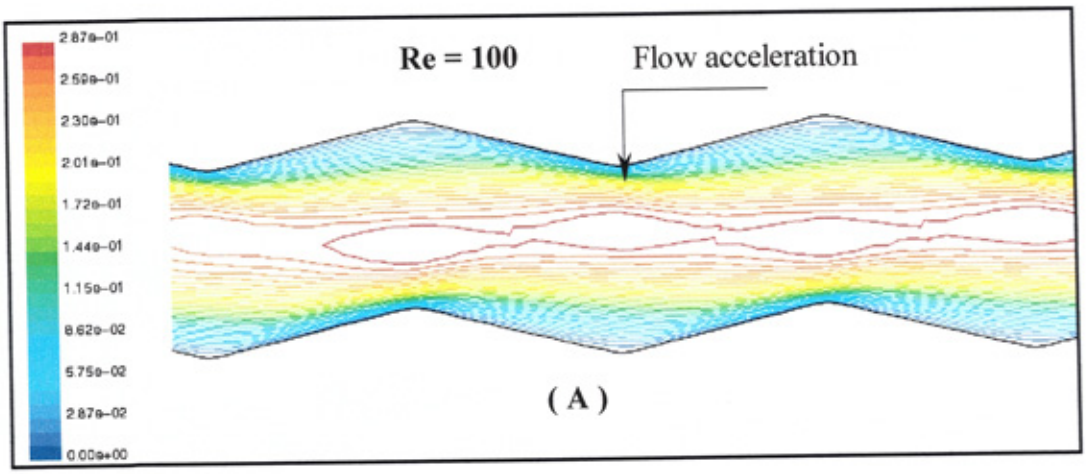

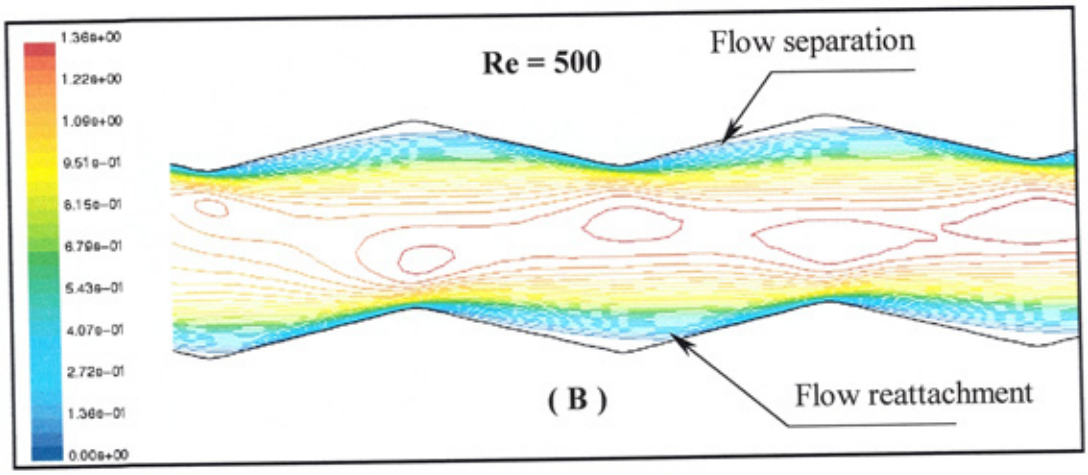

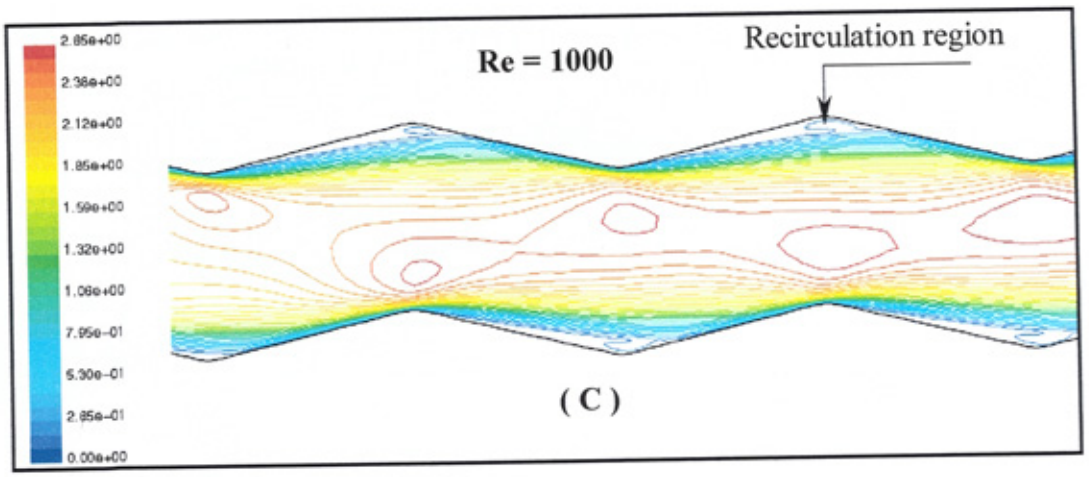

Fig. (4.13) Velocity contour for $\beta = 15^{o}$, $A_r = 4$

The average Nusselt number for $\beta = 15^{\circ}$ and 30° is illustrated in Figs. (4.14) and (4.15) respectively. The results are presented for the sake of clarity as a semi-log graphs. For a given Reynolds number the Nusselt number was greater than that of a straight duct. For the same aspect ratio, the Nusselt number increases as the corrugation angle increases. However, for the same corrugation angle, the Nusselt number decreases with increase of aspect ratio. This results are evident for $\beta = 10^{\circ}$ and 20°. The results are compared with the published works of [Yang *et al*, 1995] and [Asako and Faghri, 1987].

The variation of the friction factor as function of the Reynolds number for for $\beta = 15^{\circ}$ and 30° is illustrated in Figs. (4.16) and (4.17) respectively. These results are compared with the straight duct data and with the previous published works of [Yang *et al*, 1995] and [Asako and Faghri, 1987] for a corrugated angle $\beta = 30^{\circ}$. The friction factor of the straight duct geometry was lower than that of the corrugated duct and decreases monotonically with increasing Reynolds number. The friction factor increases as the corrugation angle increases however it decreases with increases of A_r. This results are also evident for $\beta = 10^{\circ}$ and 20°.

In general there is fair agreement between the present work and the previously published work [Yang *et al*, 1995] and [Asako and Faghri, 1987] and the differences are attributed to the differences in aspect ratio, the nature of flow, and the radius of curvature as given in the table (4.4).

The distribution of the average Nusselt number with the axial distance (x/c_p) from leading edge of developing flow regime for Re = 500 is illustrated in Fig. (4.18). This figure shows that the Nusselt number decreases with the axial distance and the maximum value is obtained at $x = c_p$. This is due to the boundary layer thickness increase with the flow axial-distance and is zero when the axial distance tends to zero.

It was evident that, as corrugation angle increases both Nusselt number and friction factor increase. As aspect ratio increases both the Nusselt number and friction factor decrease. Hence, a compromise between the enhancement of heat transfer and increase in friction factor is needed.

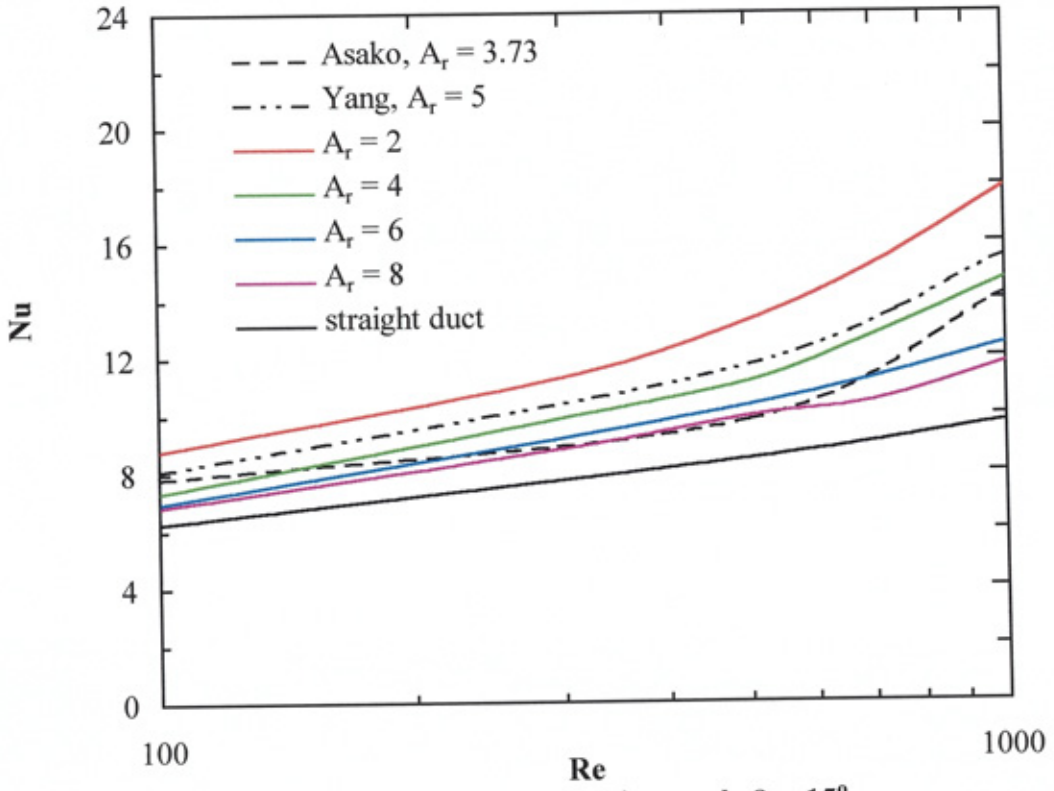

Fig (4.14) Nusselt number for corrugation angle $\beta = 15^o$

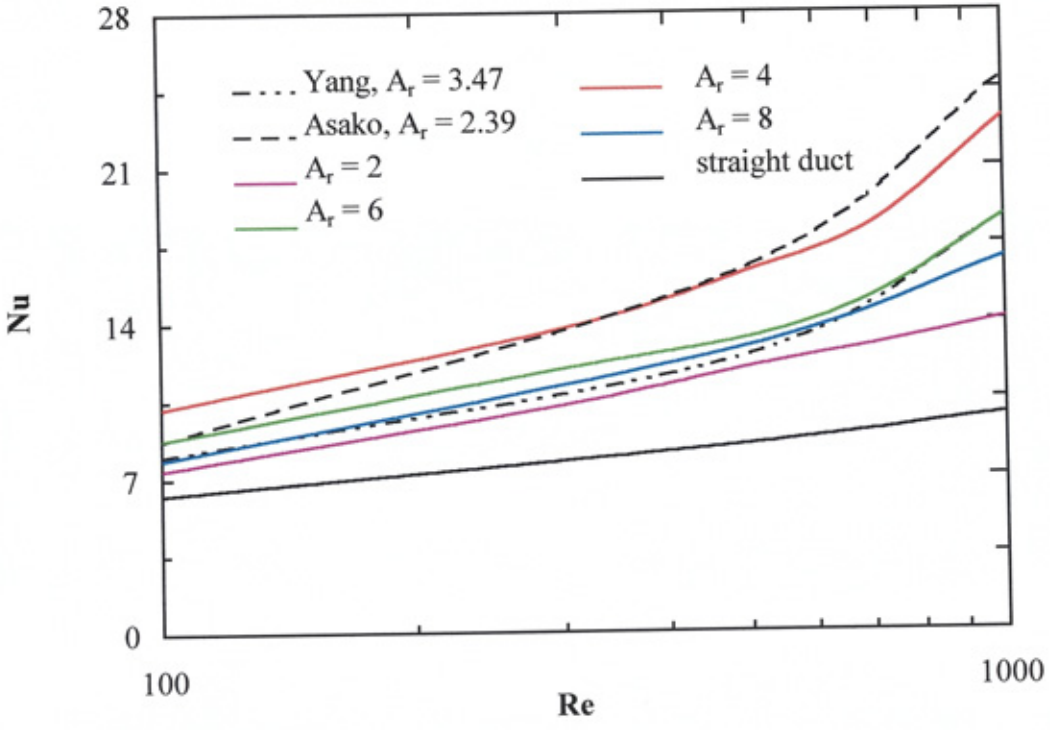

Fig (4.15) Nusselt number for corrugation angle $\beta = 30^o$

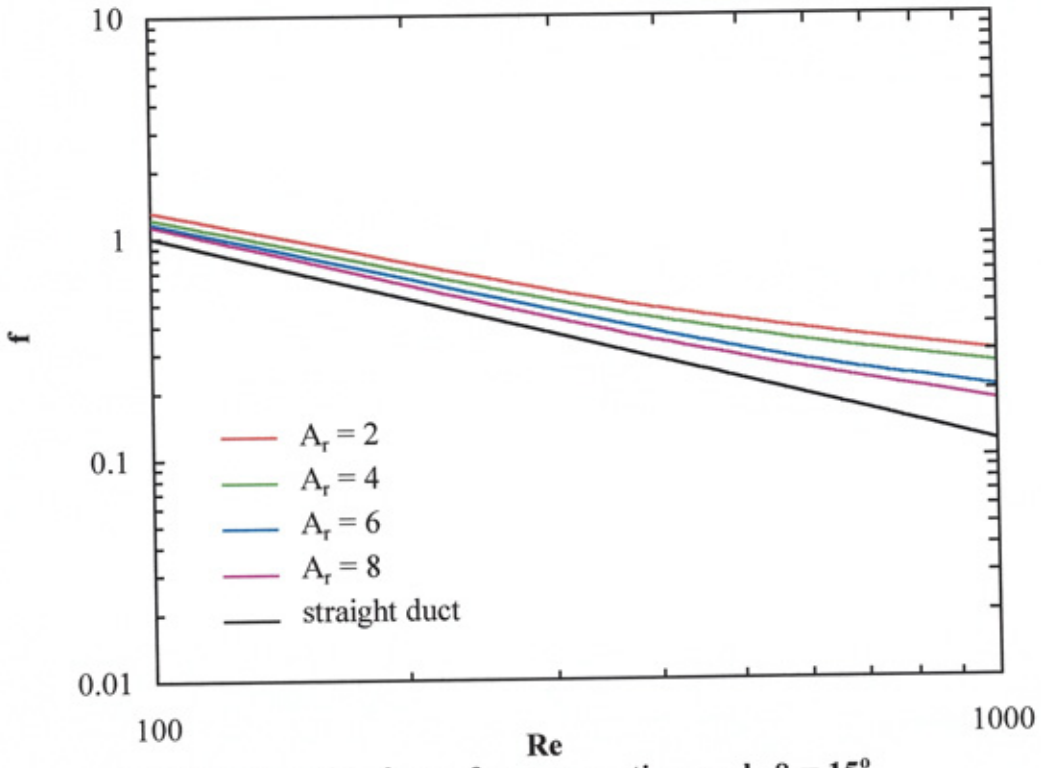

Fig (4.16) Friction factor for corrugation angle β = 15°

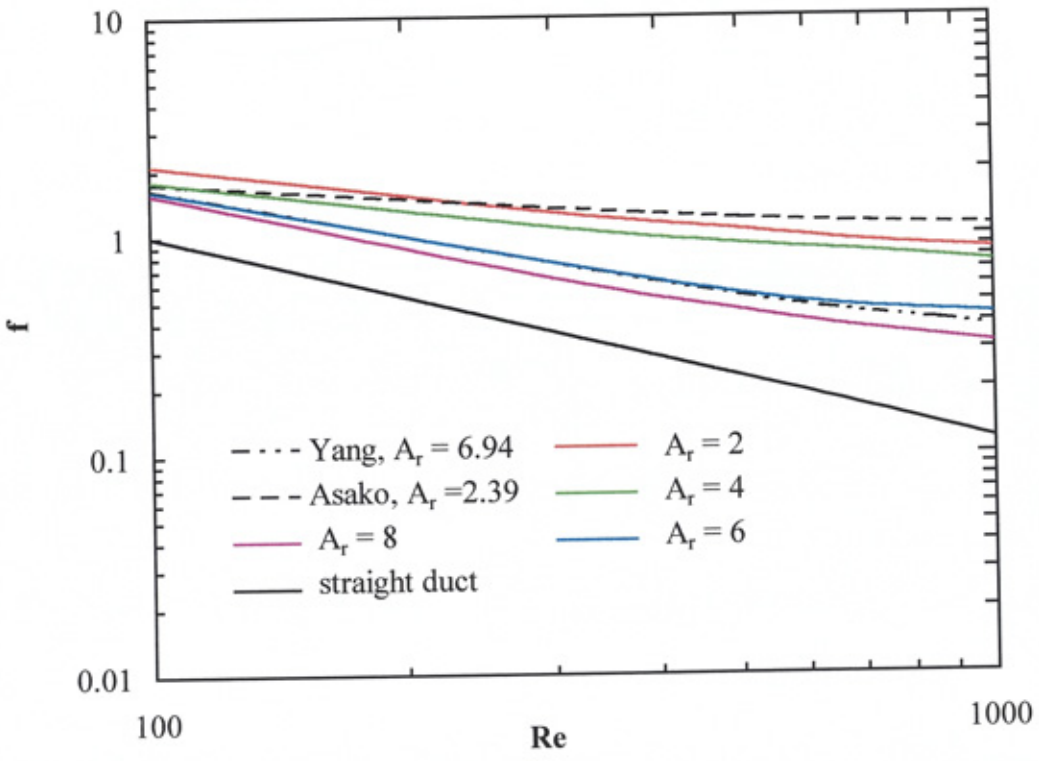

Fig (4.17) Friction factor for corrugation angle β = 30°

The heat transfer per unit pumping power per unit temperature deference was quantified to establish the best design of the corrugated wall channel. The heat transfer rate per unit pumping power per unit temperature difference versus Reynolds number is illustrated in Fig. (4.19). The results show that the corrugation angle of 10^{o} and aspect ratio of 2 gives the highest value of the heat transfer per unit pumping power. This corrugation angle will be considered in the next stage of investigation of the corrugated fin-and-tube cooling coil.

Table (4.4) Present and published work comparison

Items	Present work	Yang et al, 1995	Asako, 1987
Flow nature	Developing	Periodic fully developed	Periodic fully developed
Numerical scheme	Finite element	Finite difference	Finite volume
Aspect ratio	2, 4, 6, 8	3.47, 5, 6.94	2.39, 3.47
Round corner	$r = c_p/10$	Cord length = $c_p/5$	r = Small value

- **Staggered tube bundle arrays**

The mesh strategies are very important issue in the accuracy of the CFD results as well as the computational time and convergence criteria. Therefore, a comparison between the results of the four different mesh types (mapped (A), hybrid mapped-triangular (B), hybrid mapped (C) and adaptive-multi block mapped (D)) are illustrated in Figs. (4.20) and (4.21) respectively. There was a fair agreement between the different systems of meshing strategies whereas a higher computation time was noted with hybrid mapped-triangular mesh type under the same converged conditions.

A grid dependence check was performed for the case of adaptive-multi block mapped mesh with $X_t = 2.36$, $X_L = 2$ and Re = 500. For compared a nominal grid (400 x 35) with boundary grid adaption of 3 (16000 nodes) against a coarser grid (350 x 30) with boundary grid adaption of 2 (11746 nodes), and a finer grid (432 x 38) with boundary grid adaption of 5 (20048 nodes).

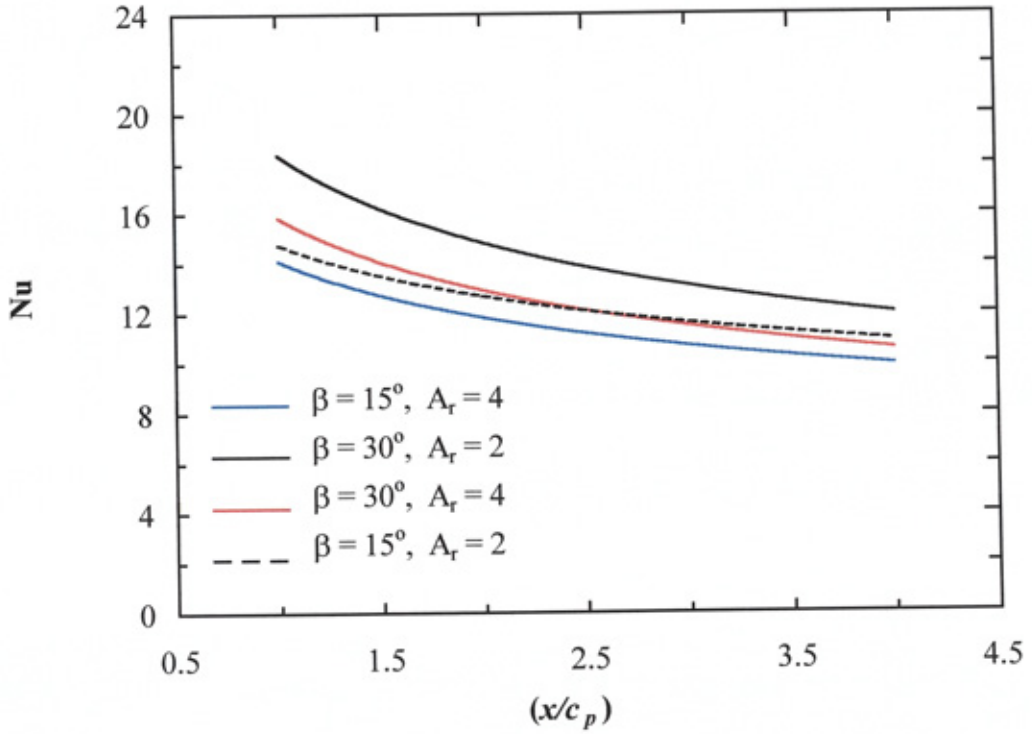

Fig. (4.18) Average Nusselt number vs axial distance for Re = 500

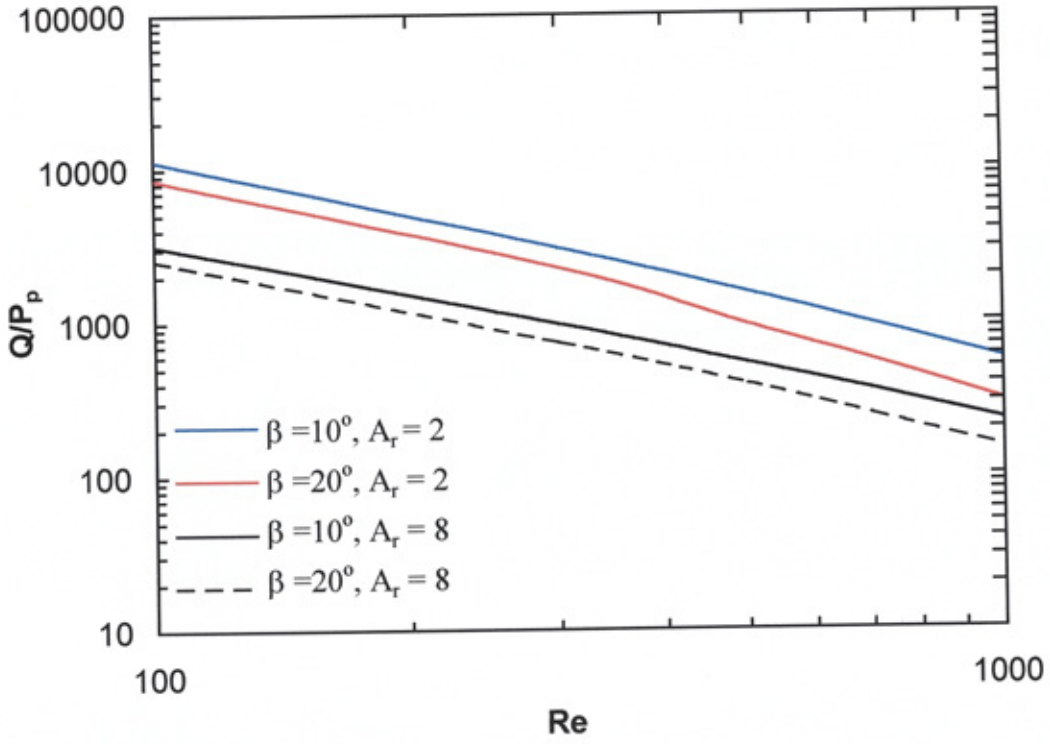

Fig. (4.19) Heat transfer rate per unit pumping power per unit of ΔT

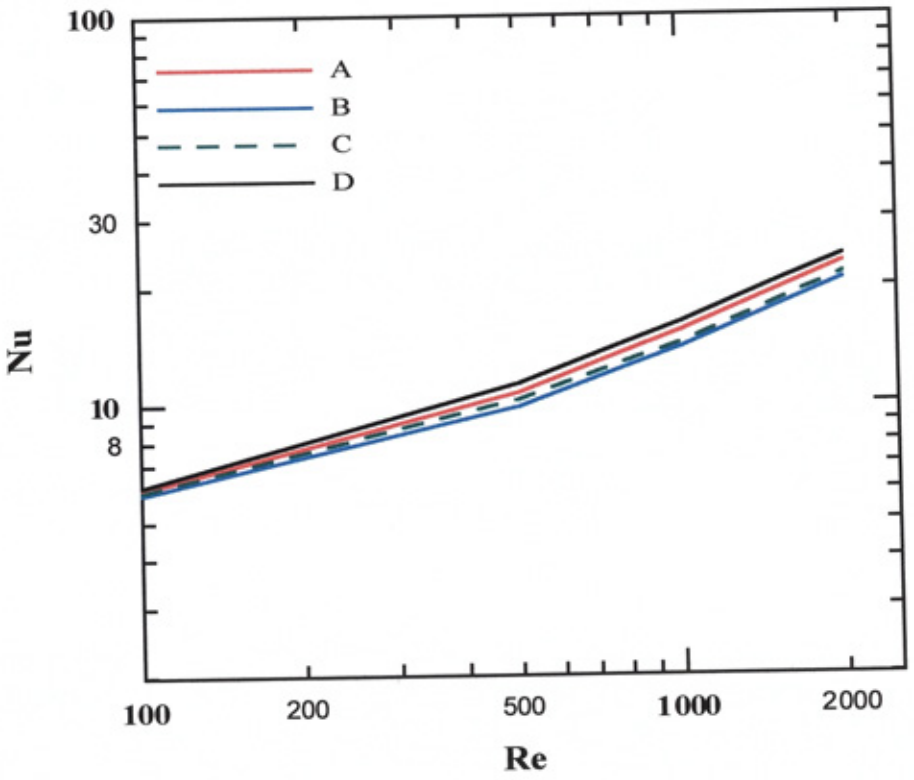

Fig. (4.20) Nusselt number for the mesh types of A, B, C, and D

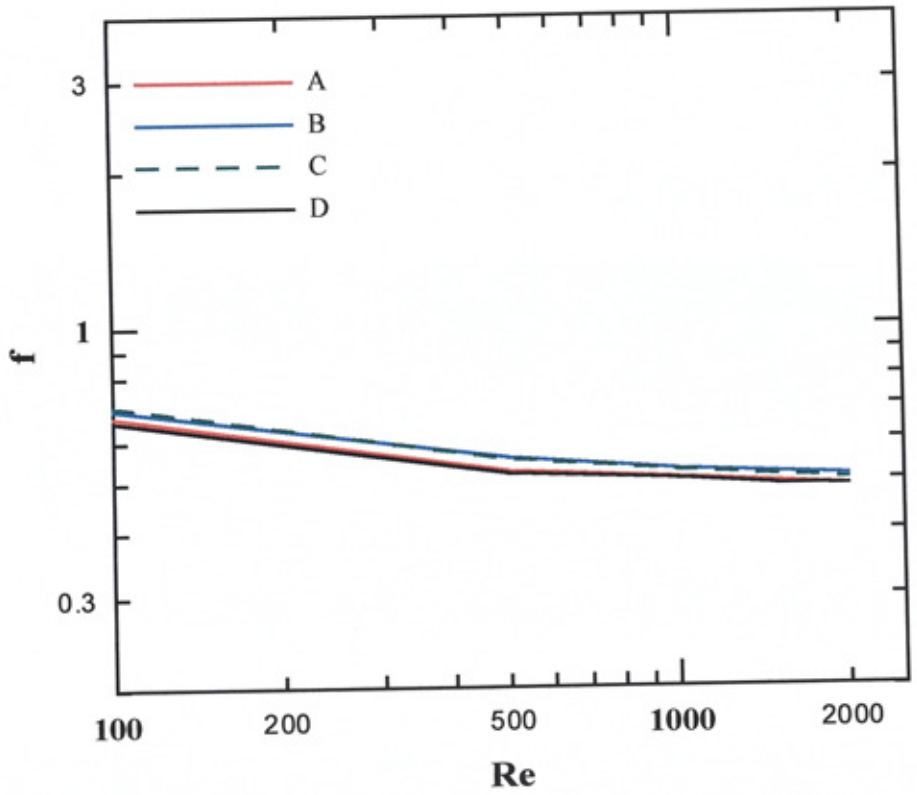

Fig. (4.21) Friction factor for the mesh types of A, B, C, and D

The maximum differences in the Nusselt number and friction factor between the coarser grid and the nominal grid were within - 4 % and 4.5 % respectively and between the nominal grid and the finer grid, within -1.7 % and 6 % respectively. Thus the nominal grid is chosen to maintain relatively high accuracy and relatively moderate computational time.

The flow pattern distribution for X_t = 2.36 and X_L = 2 was illustrated in Fig. (4.22). The standing vortex ring that is formed at the rear of each cylinder becomes larger with increasing Reynolds number. The velocity, pressure and temperature contours of the computational domain are presented in Figs. (4.23), (4.24), and (4.25) respectively. The flow appears to be in a curved channel of periodically converging and diverging cross section whereas the flow pattern around a tube row was influenced by the surrounding tubes. In the direction of flow, the flow accelerated from row-on-row and the size of the weak zone behind each tube-row increased. Zones of maximum velocity highly gradient were observed at circumferential flow angle of about ± 80° while maximum pressure corresponding to circumferential flow angle of zero.

The average Nusselt for X_t = 1.57, 2.36 and 3.15 was compared with experimental fully developed flow data of Zukauskas (1987) as illustrated in Fig. (4.26). For the same value of Reynolds number, the Nusselt number decreases as X_t increases. At a low value of Reynolds number the difference between Nusselt number of X_t = 1.57 and X_t = 3.15 was relatively large compared with higher values of Reynolds number, this is may be explained due the size of vortices induced at high Reynolds number which lead to better flow mixing for both values. The Nusselt number of the present study is higher than that of Zukauskas (1987) especially at low Reynolds number. This could be attributed to differences in tube-bundle configuration and also for the heat transfer in the developing flow region being higher than that of fully developed flow. The effect of longitudinal tube pitch, X_L on the Nusselt number for X_t = 2.36 compared with the fully developed flow data of Chen and Wung (1989) is illustrated in Fig. (4.27). The longitudinal tube pitch had relatively small effect on the Nusselt number. The deviation between the present data and the data of Chen and Wung is again attributed to differences in the tube-bundle geometry and the type of flow.

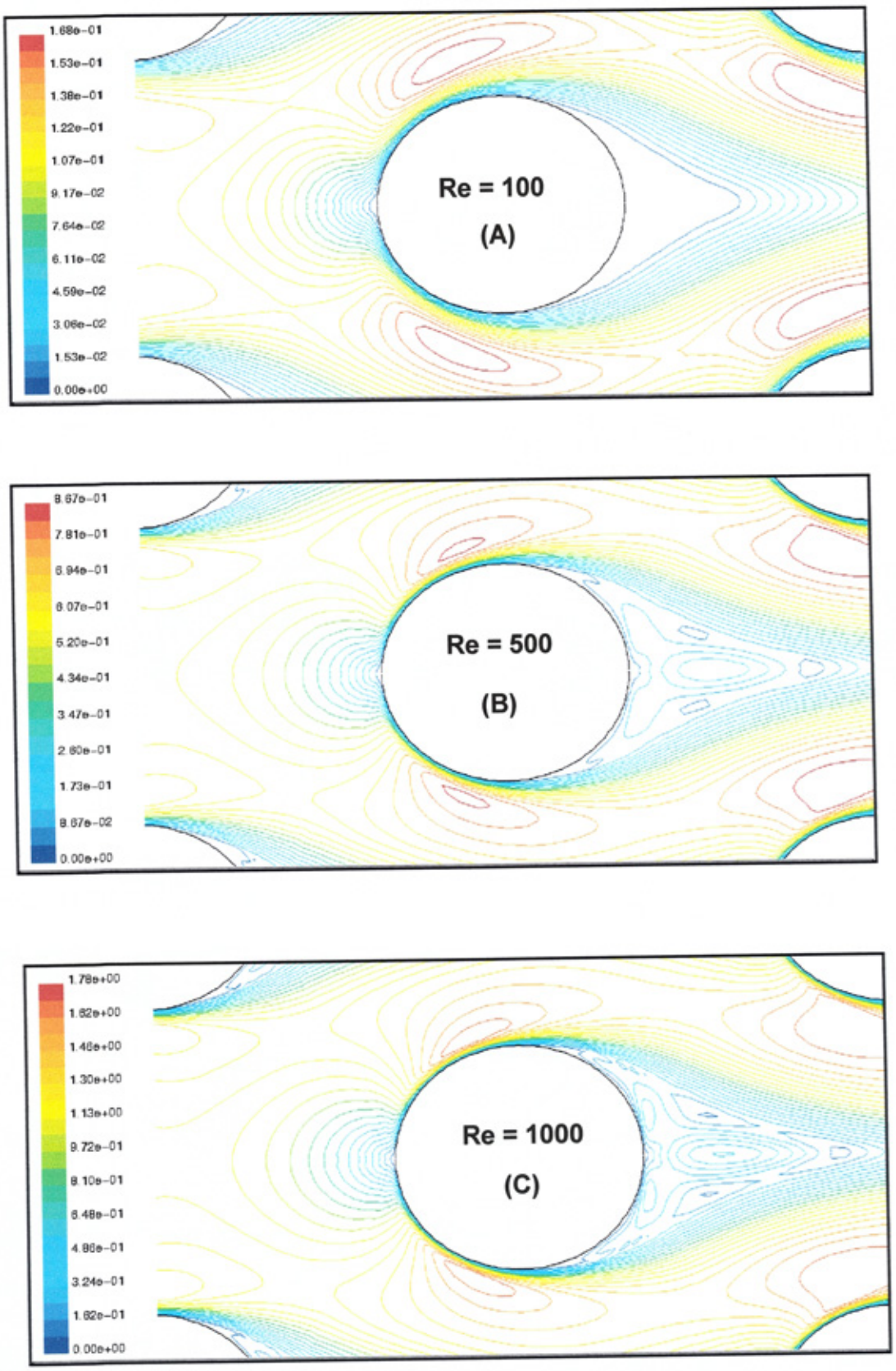

Fig. (4.22) Velocity contour around the second-row of the tube array

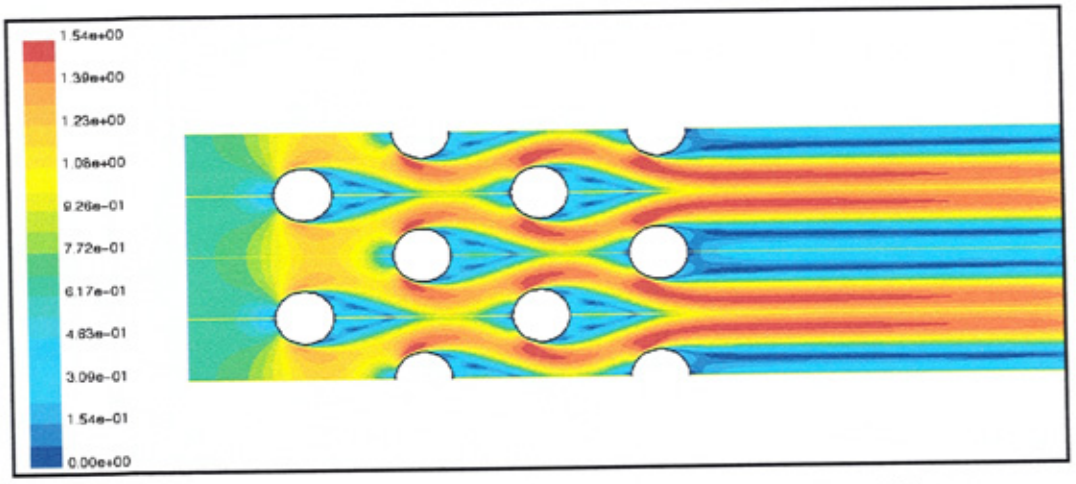

Fig. (4.23) Velocity contour of the tube bundle array at Re = 500

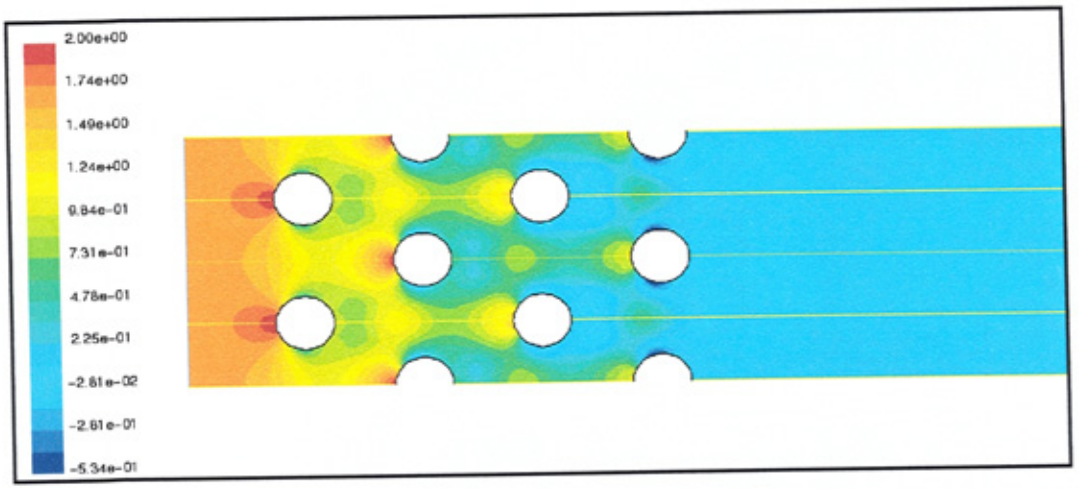

Fig. (4.24) Pressure contour of tube bundle array at Re = 500

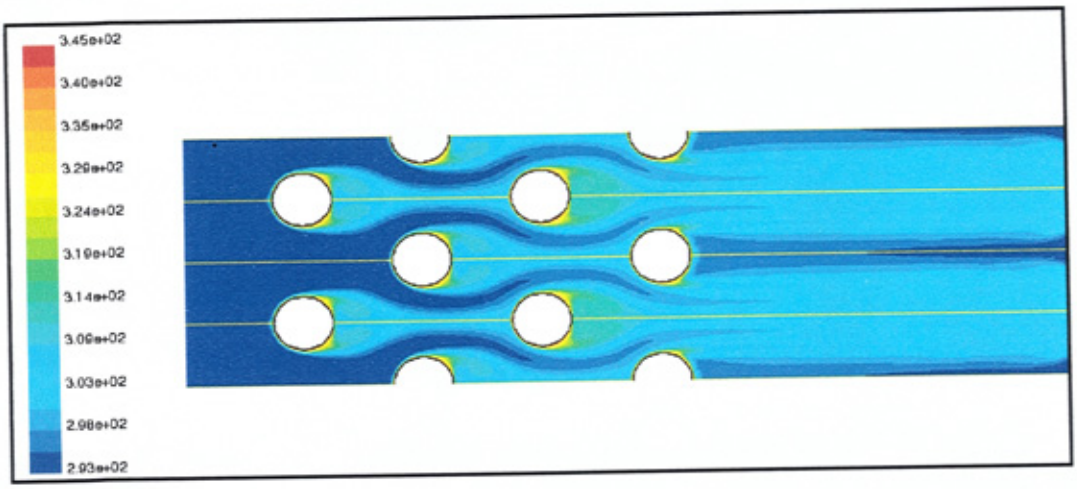

Fig. (4.25) Temperature contour of the tube bundle array at Re = 500

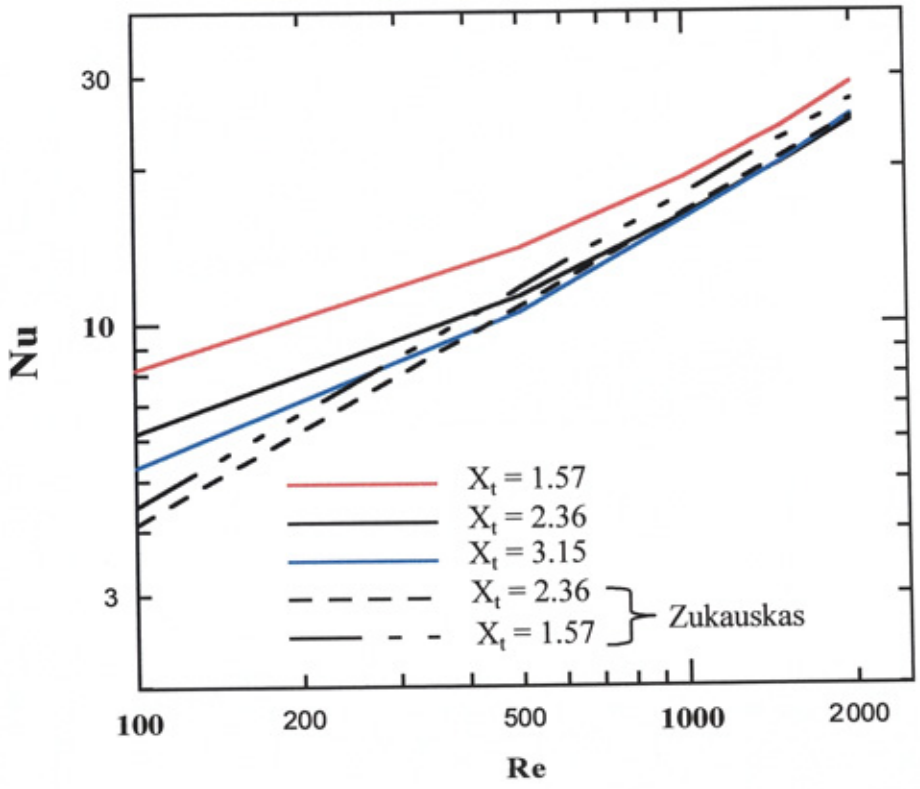

Fig. (4.26) Nusselt number for $X_L = 2$, $N_R = 4$

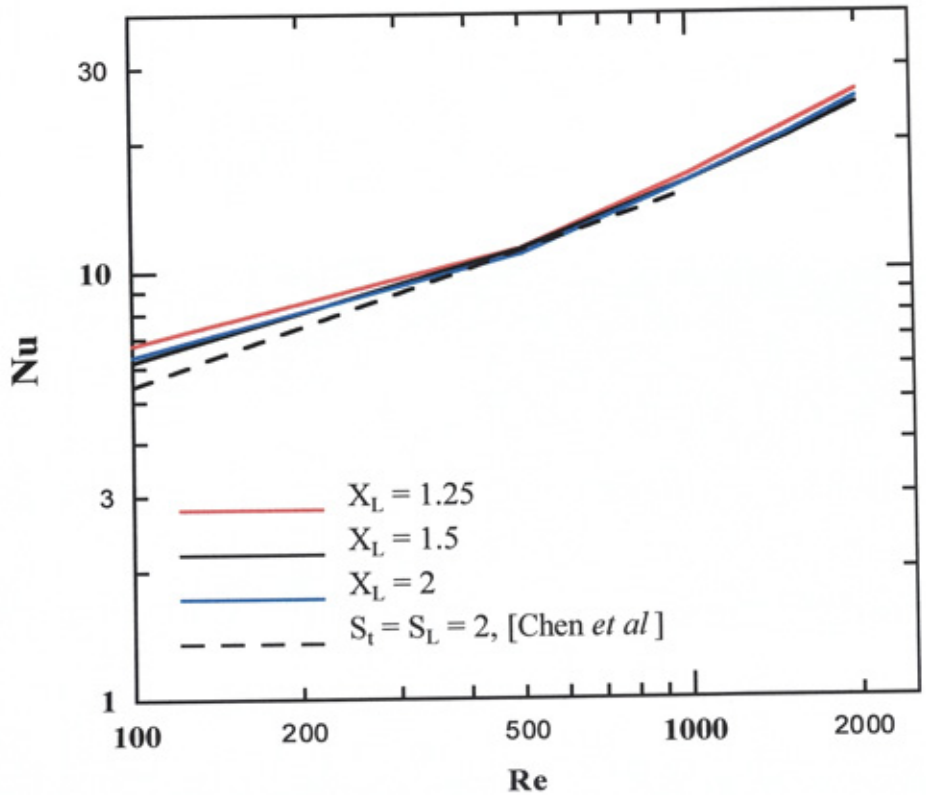

Fig. (4.27) Nusselt number for $X_t = 2.36$, $N_R = 4$

The effect of the number of tube rows on the Nusselt number is illustrated in Fig. (4.28). It is observed that the Nusselt number decreases as the number of tube rows increases.

The average friction factor for X_t = 1.57, 2.36 and 3.15 compared with the experimental fully developed flow data of Zukauskas (1987) is illustrated in Fig. (4.29). The friction factor decreases as Reynolds number increases however the friction factor decreases as the value of X_t increases.

There is fair agreement between the friction factor of the present work and the experimental data of Zukauskas. The friction factor for X_L =1.25, 1.5 and 2 is illustrated in Fig. (4.30). It is noted that the friction factor decreases with increases in longitudinal tube pitch. The effect of the number of tube rows on the friction factor is illustrated in Fig. (4.31) revealing that, at Reynolds number, Re > 300, the friction factor increases marginally as the number of tube rows decrease.

4.6.1 Verification of the CFD codes

Tests were conducted to verify the data generated by the ANSYS/FLOTRAN CFD code and also to test the accuracy when a different method, and solver are applied for the same meshing and number of nodes. This comparison was carried out between the ANSYS/FLOTRAN finite element code and the FLUENT finite volume code in the case of corrugated wall channel and also for the staggered tube bundle array. The Nusselt number and friction factor of the corrugated wall channel for $\beta = 15^{\circ}$ and $A_r = 4$ are illustrated in Figs. (4.32) and (4.33) respectively. The same comparison was carried out for the staggered tube bundle with X_t = 2.36, X_L = 2 and N_R = 4 as illustrated in Figs. (4.34) and (4.35) respectively. Within certain limits of accuracy, there is a good agreement between the finite element code and the finite volume code.

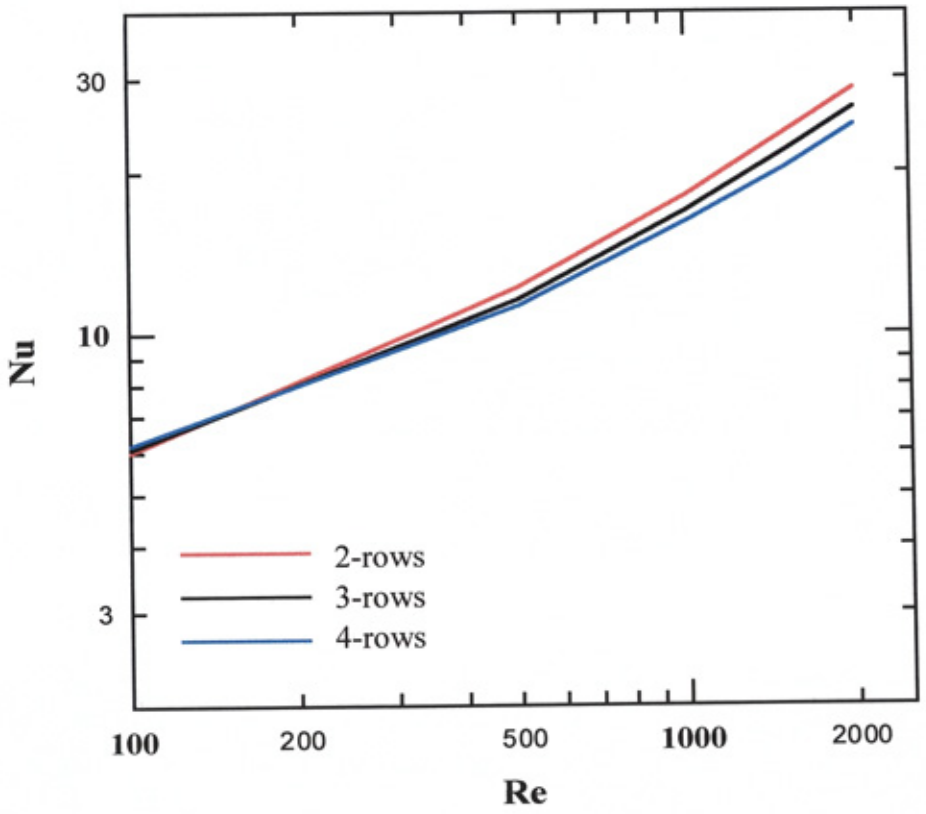

Fig. (4.28) Nusselt number for $X_t = 2.36$ and $X_L = 2$

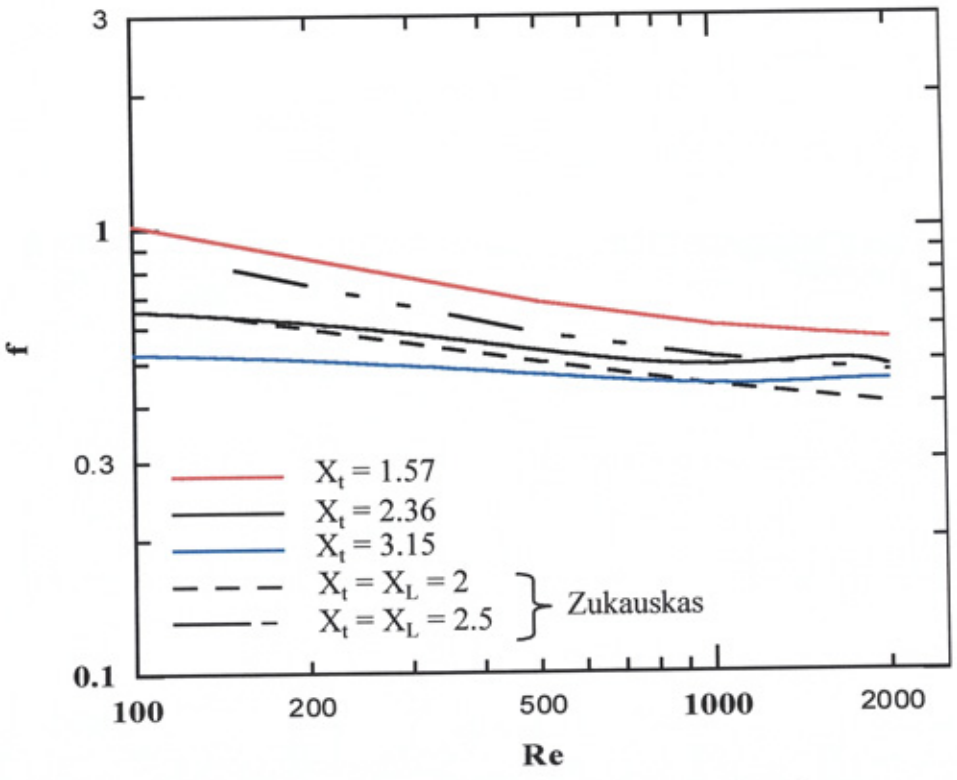

Fig. (4.29) Friction factor for $X_L = 2$, $N_R = 4$

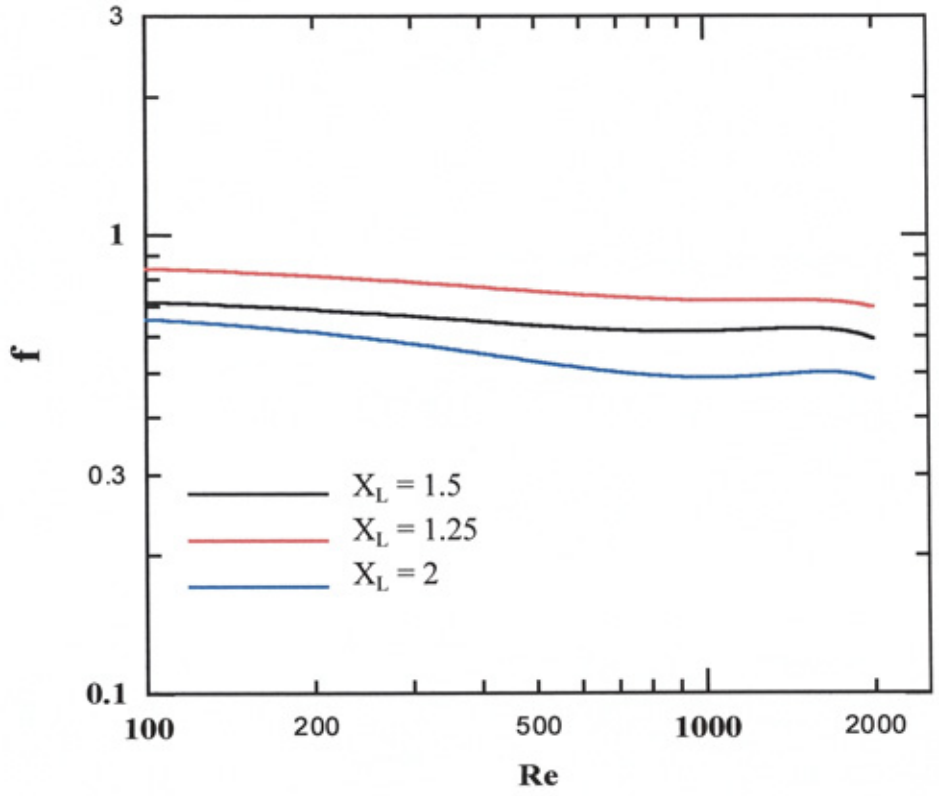

Fig. (4.30) Friction factor for $X_t = 2.36$, $N_R = 4$

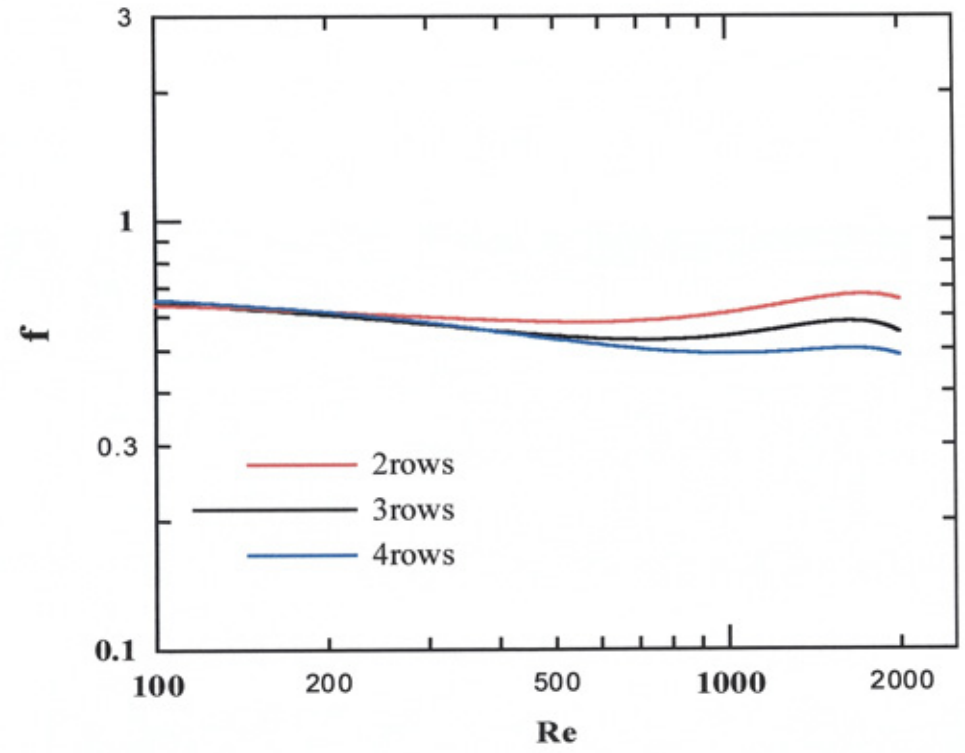

Fig. (4.31) Friction factor for $X_t = 2.36$ and $X_L = 2$

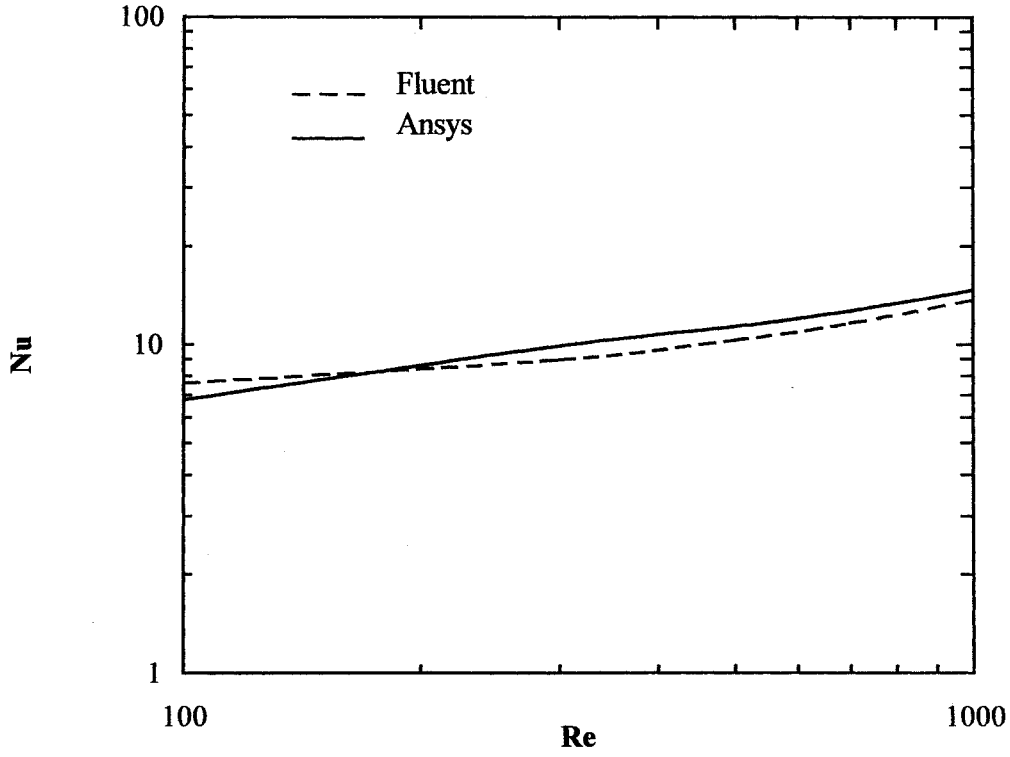

Fig. (4.32) Nusselt number for $\beta = 15^0$ and $A_r = 4$

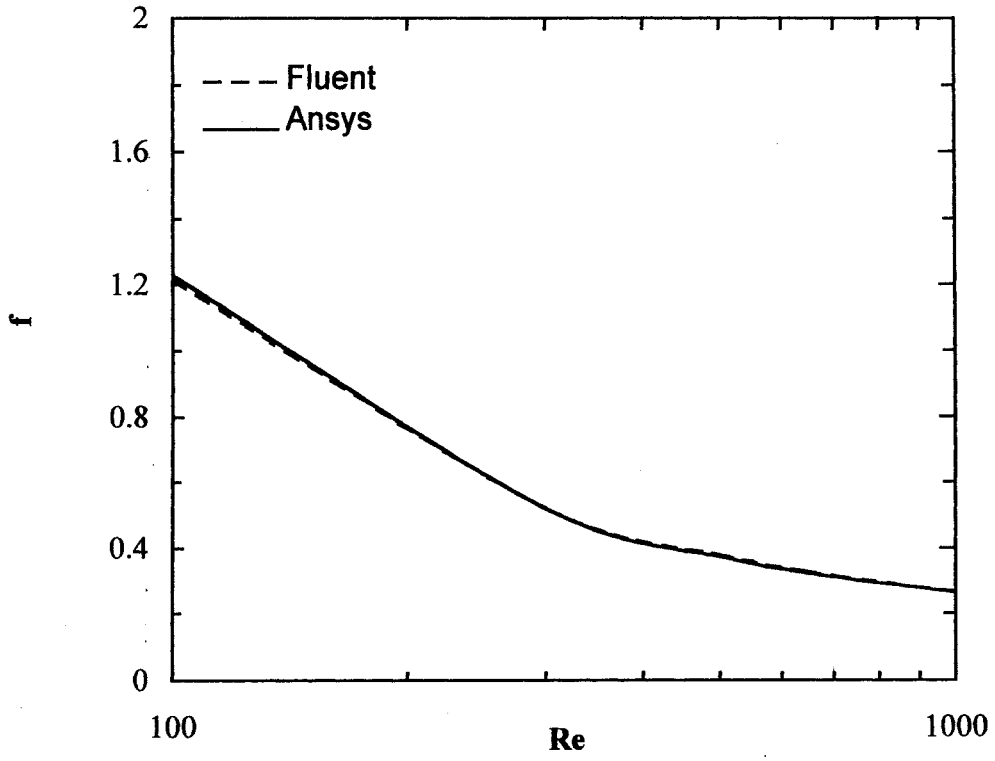

Fig. (4.33) Friction factor for $\beta = 15^0$ and $A_r = 4$

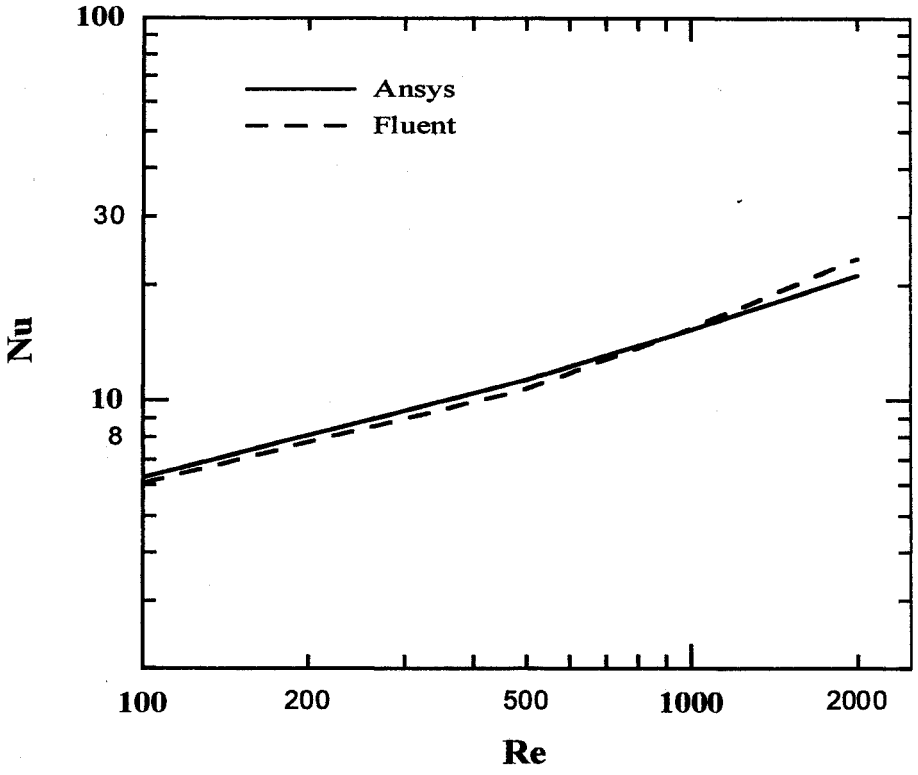

Fig. (4.34) Nusselt number for $X_t = 2.36$, $X_L = 2$ and $N_R = 4$

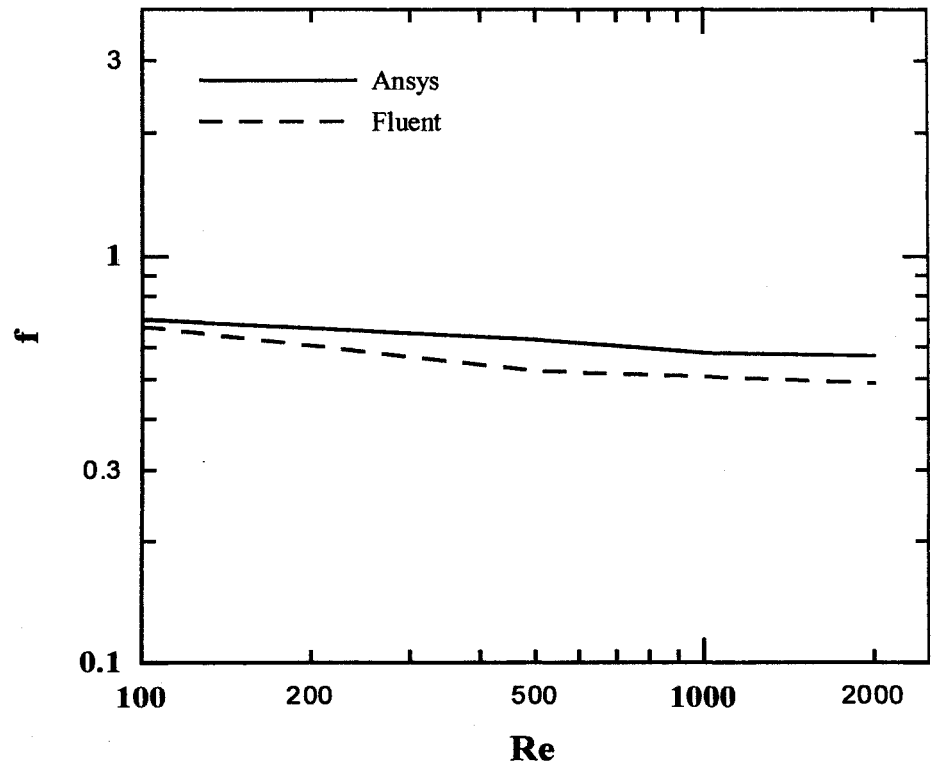

Fig. (4.35) Friction factor for $X_t = 2.36$, $X_L = 2$ and $N_R = 4$

4.7 Discussion

In this section the results of long straight duct, corrugated wall-channel and staggered tube bundle are discussed.

- **Long straight duct**

The verification of the finite element CFD code against exact analytical results for the solution of the fully developed laminar flow through a long straight duct indicated that the number of grid nodes and their distribution critically influence the accuracy of the numerical solution. The minimum percentage error in maximum velocity, E_R = 0.17 % was obtained with a large number of nodes in y-direction (80) based on 150 iterations and a minimum percentage error in the friction factor, E_f = 2.1 % was obtained with a number of nodes 150 x 60 based on 120 iterations.

The main factor affecting the accuracy of the numerical solution through the long straight duct is the number of grid points in the y-direction compared with the number of grid points in x-direction, as well as their spacing ratio. A satisfactory accuracy of the numerical solution requires an excessive number of nodes, large number of iterations, and higher computational time. A compromise between satisfactory accuracy and the higher computational time has to be sought.

- **Corrugated wall channel**

As Reynolds number increases, the size of the recirculating (in peaks) region as well as separation-reattachment zones increase. These types of flow created vortices, which led to a good flow mixing and hence augmentation of heat transfer is achieved. This may be explained by the increase of the Nusselt number with the increase of the corrugation angle however the flow resistance increases. The recirculation zone decreased with a higher value of aspect ratio (as the aspect ratio increased the corrugated channel became more close to the straight duct) resulting in less flow mixing which led to lower values of Nusselt number. Compared with results of the straight wall channel, a significant increase in heat

transfer characteristics can be achieved using corrugated wall channels at the expense of the pumping power needed.

The highest values of the heat transfer rate per unit pumping power per unit temperature difference are achieved at a corrugation angle $\beta = 10^{o}$ and an aspect ratio $A_r = 2$ while the maximum heat transfer per unit volume is achieved at high values of corrugation angle and low aspect ratios. However the pumping power required was higher under these circumstances.

The design of the corrugated wall channel ($\beta = 10^{o}$ and $A_r = 2$) which characterised by a maximum heat transfer per unit pumping power is considered in the construction of corrugated fin-and-tube cooling coil (which is investigated ongoing chapters).

The convergence criterion is very important issue in the CFD simulation of the physical problems. Convergence can be affected by a number of factors. Large numbers of computational cells, conservative under-relaxation factors, complex flow physics, mesh types and element size gradient. The convergence criterion is a normalized measure of the solution's rate of change from iteration to iteration denoting by the general field variable, (φ). The convergence monitor (equation 4.18) represents the sum of changes of the variable calculated from the results between the current k^{th} iteration and the previous (k-1)th iteration, divided by the sum of the current values. The summation is performed over all N nodes, using the absolute values of the differences.

$$\text{Convergence monitor} = \sum_{i=1}^{N} \frac{\left|\varphi_i^k - \varphi_i^{k-1}\right|}{\left|\varphi_i^k\right|} \qquad (4.18)$$

Although Longtenberg and Dixon stated that there is no single exact answer of the convergence criterion, especially in complex geometries [Longtenberg and Dixon, 1998], it is considered that ANSYS/FLOTRAN code was weaker in attaining a good convergence criteria when a higher Reynolds number is applied at a complex flow-geometries.

After many trials, the finite volume code (FLUENT) was chosen instead of the finite element code (ANSYS/FLOTRAN) for the three-dimensional numerical analysis of the fin-and-tube cooling coils for the following reasons;

1. There was difficulty in attaining a good convergence criterion using the ANSYS/FLOTRAN finite element code.
2. The ANSYS/FLOTRAN finite element code was found to be inflexible in generating a three-dimensional grid of fin-and-tube heat exchangers.
3. The computational time with ANSYS/FLOTRAN was about twice the computational time with FLUENT for the same number of nodes.

A comparison between the finite element code and the finite volume code is summarised in Table (4.5).

Table (4.5) Comparison between ANSYS/FLOTRAN and FLUENT

Items	ANSYS-5.3/FLOTRAN	FLUENT-5.4
Method	Finite element	Finite volume
Scheme	TDMA (velocity and temperature equations)	First upwind (momentum and energy equations)
Solver	PCGM (pressure equation)	Segregated (velocity-pressure coupling)
Algorithm	TDMA	SIMPLE
Convergence	$5 \times 10^{-3} - 5 \times 10^{-5}$	$5 \times 10^{-4} - 5 \times 10^{-6}$
CPU time	≅ Double time	Time
Flexibility	weak	Good
3-D work	Difficult	----------
CFD Conjugate modelling	Not supported	Supported
Model generation	--------	Difficult
Results Viewer	Very Good	Good

- **Staggered tube bundle array**

In the developing region, the flow and temperature fields varied from the leading edge with simultaneous hydrodynamic and thermal entrance length. In the direction of flow, the flow accelerated from row-on-row and the size of the weak zone behind each tube-row increased. The Nusselt number was strongly dependent on the flow pattern around the tube row, which was influenced by the surrounding tubes. The Nusselt number of the staggered tube bundle is determined by geometrical parameters of the tube arrangement (S_L, S_t, D, N_R). As the transverse tube pitch increased the Nusselt number decreased as well as the friction factor.

As the longitudinal tube pitch decreased there was a small increase in Nusselt number, however a significant increase in friction factor was noted. The pressure drop across staggered tube banks was proportional to the number of tube rows however a small decrease in both Nusselt number and friction factor was noted.

The number of nodes, mesh style and size of elements play a significant role in the accuracy of the CFD results as well as the stability and convergence rate. In general, the larger the number of grids, the better the solution accuracy.

4.8 Conclusion

In this chapter the problem of developing and fully developed laminar fluid flow and heat transfer characteristics of the key components of the fin-and-tube heat exchanger were solved numerically using finite element and finite volume CFD techniques. The investigation of key heat exchanger design parameters including corrugation angle, aspect ratios, longitudinal tube pitch, transverse tube pitch and number of tube rows was considered. Grid generation, type of mesh strategy, accuracy of results and computational time were also points of interest. Results from the two contrasting CFD programmes were compared as a basis for choosing a candidate program for a subsequent three-dimensional analysis. The results give key insights into the required modelling strategies

needed for the more complex three-dimensional problem of the composite fin-and-tube heat exchanger which is given in chapter -VI -.

The main conclusions are as follows:

- The more accurate results require an excessive number of nodes, large number of iterations, and hence higher computational time.
- In a corrugated flow, as Reynolds number increases the size of recirculating (in peaks) region as well as separation-reattachment zones increase. These types of flow created vortices which lead to good flow mixing and hence augmentation of heat transfer is achieved.
- For a given Reynolds number, the highest values of the Nusselt number is achieved at a low value of the aspect ratio and a high value of the corrugation angle. However, the friction factor also increases.
- The highest values of the heat transfer rate per unit pumping power per unit temperature difference are achieved at a corrugation angle $\beta = 10^{o}$ and an aspect ratio $A_r = 2$, while maximum heat transfer per unit volume is achieved at a corrugation angle $\beta = 30^{o}$ and an aspect ratio $A_r = 2$.
- In the case of a tube bundle, the Nusselt number and the friction factor are strongly dependent on the geometric parameters of the tube arrangement. Both factors decrease with increase in transverse tube pitch.
- An increase in the number of tube rows results in a small decrease in the Nusselt number and friction factor.
- For the same type of meshing and number of nodes, there was a fair agreement between the results of both finite element code and the finite volume code.

CHAPTER -V-

Experimental analysis of fin-and-tube cooling coils

5.1 Introduction

In this chapter, the performance characteristics of three chilled-water cooling coils were investigated in a pilot scale air conditioning plant as illustrated in Fig. (5.1). Three types of cooling coils are considered here involving flat, corrugated and turbulated-fin geometries under a range of boundary conditions. The purpose of the experimental work was the following:

1- To evaluate the performance characteristics of heat transfer and friction of the cooling coils having various fin passage geometries.

2- To investigate the effects of various design conditions (entering air temperature, entering chilled-water temperature and air velocity) on the cooling coils performance.

3- To generate data appropriate for the validation of CFD modelling results of these cooling coils

The investigation is applicable to the hot arid climate of Egypt (in particular Cairo) for which external design conditions at 37.8 °C (db), 20.5 °C (wb) are applicable [ASHRAE fundamental, 1997]. Using the Psychrometric chart, the dew point temperature of air at this condition is 10.2 °C which is below a minimum air supply condition of 13 °C (Typically the chilled water supply of 7 °C + 6 K-temperature rise, [ASHRAE HVAC systems, 2000]). Even when mixing with indoor air, the air dew point temperature is below the air supply temperature as illustrated in Fig. (5.2). Hence this work is bounded by sensible cooling phenomena.

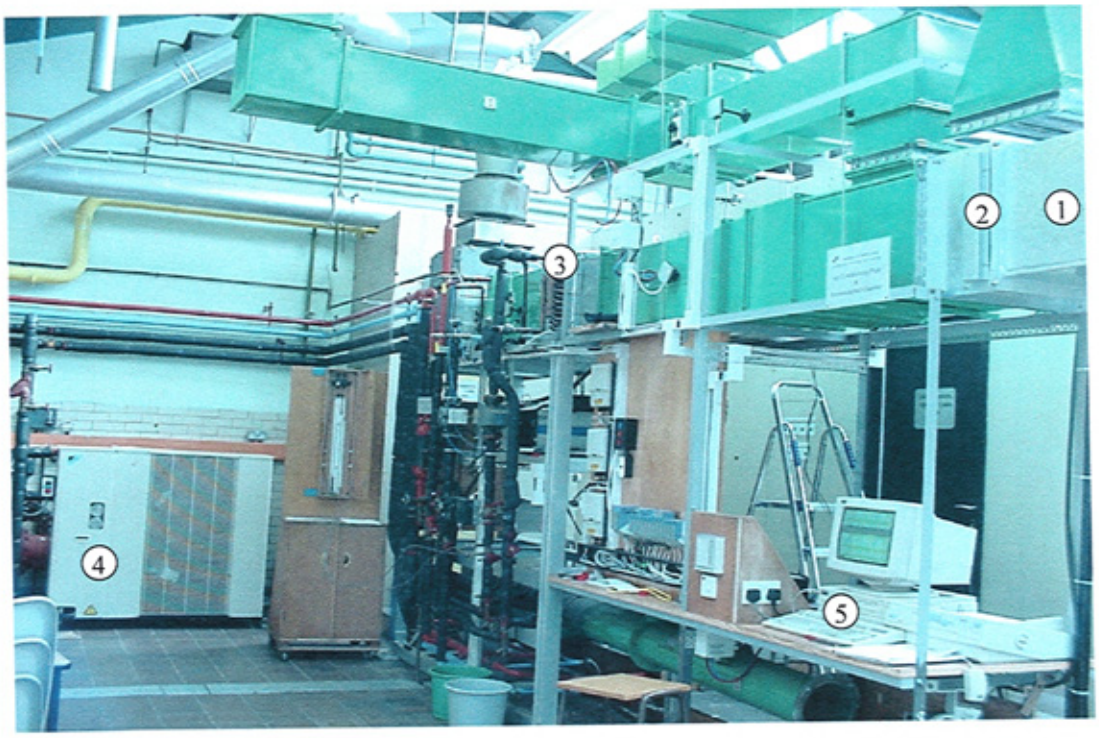

Fig. (5.1) Photograph of the test rig

1- Preheat section
2- Heating coil
3- Cooling coil
4- Water chiller
5- Data acquisition

5.2 Test rig

Experiments were conducted using a pilot air-conditioning test rig adapted to give a set of boundary conditions which cover most of the air-conditioning applications relevant to the hot arid climate of Egypt (see Table (5.1)). It consists of a pilot long duct (6000 mm long and 400 mm x 530 mm is cross-section) constructed from 1mm galvanised steel. The rig has a centrifugal fan capable of generating induct velocities of up to 3.8 m/s, 13 kW electric two-rows fin-and-tube heating coil and a chilled water refrigeration plant. A schematic of the experimental test rig is illustrated in Fig. (5.3). The refrigerating medium supplied to the test coil was ethylene glycol with a 30 % glycol solution concentration.

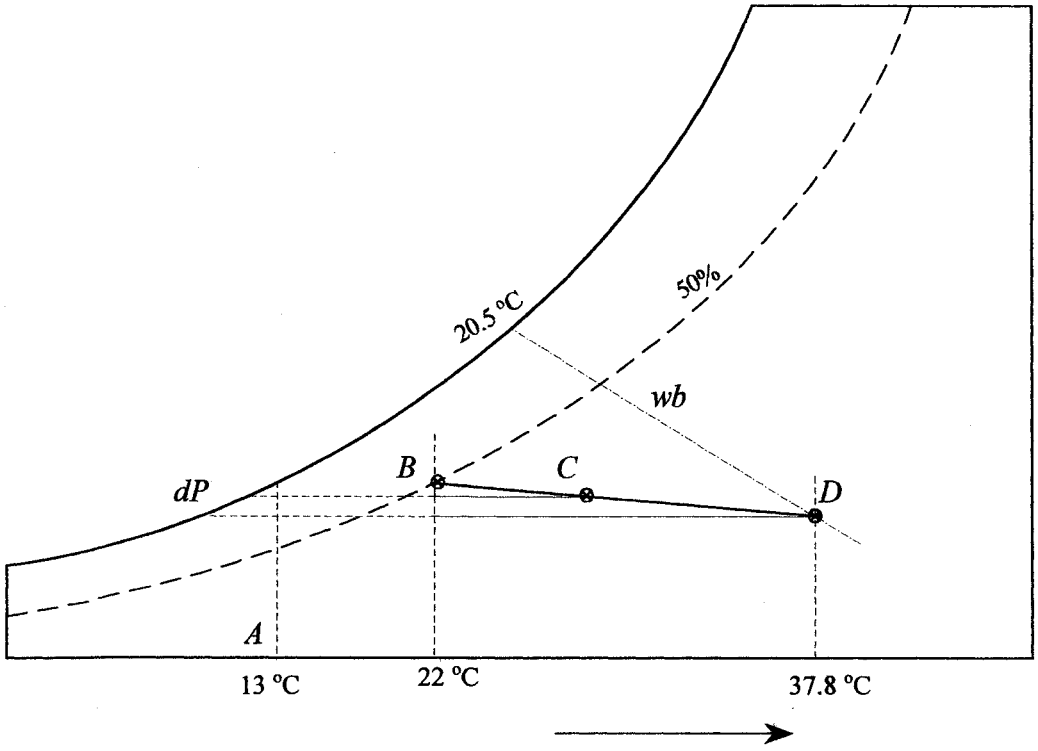

A	air supply	*C*	Mixing point (40 %)
B	Return air	*D*	Outside design condition

Fig. (5.2) Psychrometric diagram of the design-condition of Cairo

Table (5.1) List of boundary conditions

Item	Range
Average inlet air velocity	0.65 m/s $\leq u_{ai} \leq$ 3.8 m/s
Average inlet air temperature	23 °C $\leq T_{ai} \leq$ 42 °C
Average chilled water temperature	5 °C $\leq T_{wi} \leq$ 15 °C

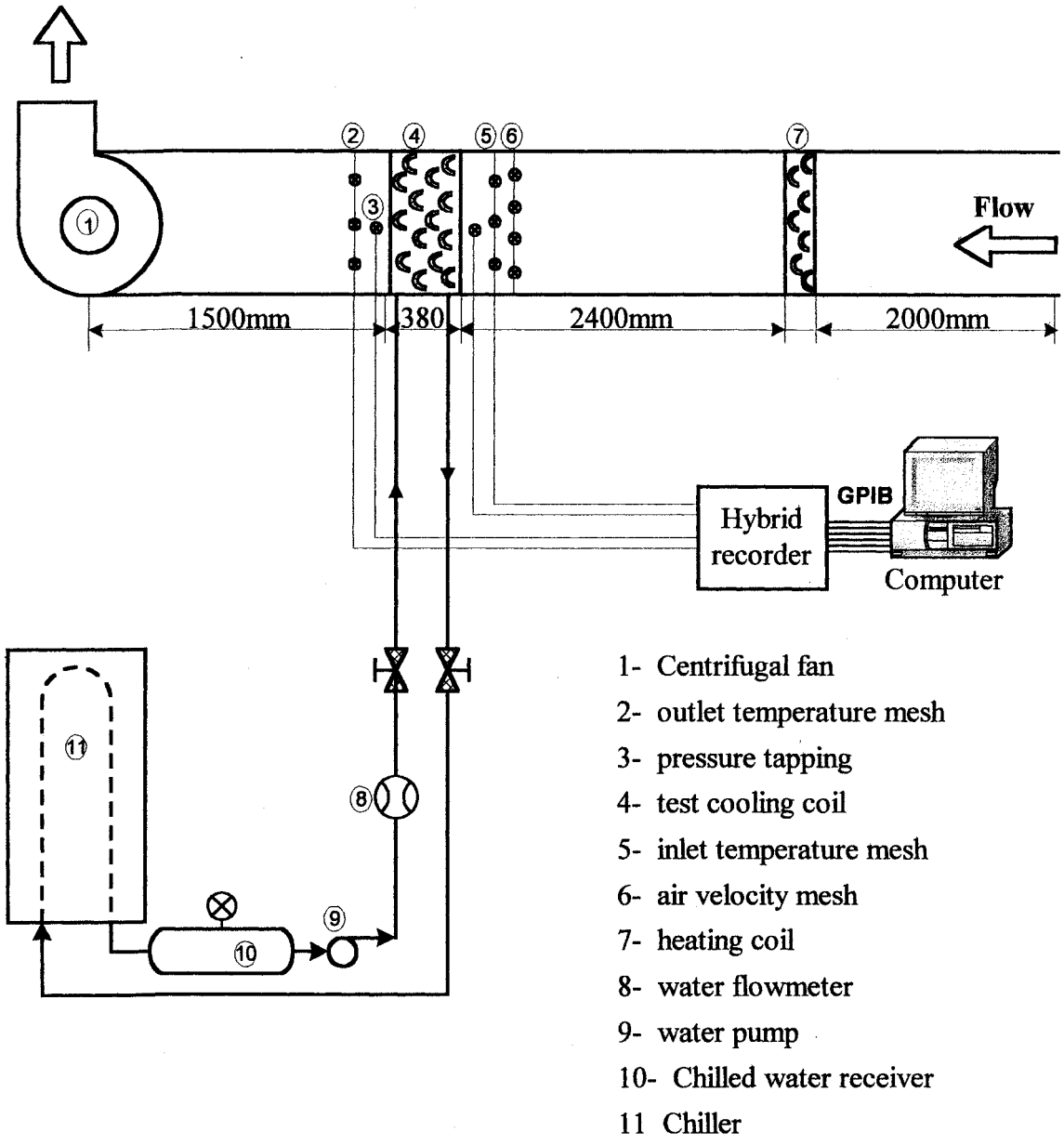

Fig. (5.3) Schematic of the experimental rig

5.3 Test coils

All the cooling coils were of four-row staggered tube construction with identical design parameters except for fin geometry. Photographs of the various fin sheets are illustrated in Figs (5.4a-c). The geometry of the flat, corrugated and turbulated fin configurations are illustrated in Figs. (5.5), (5.6) and (5.7) respectively.

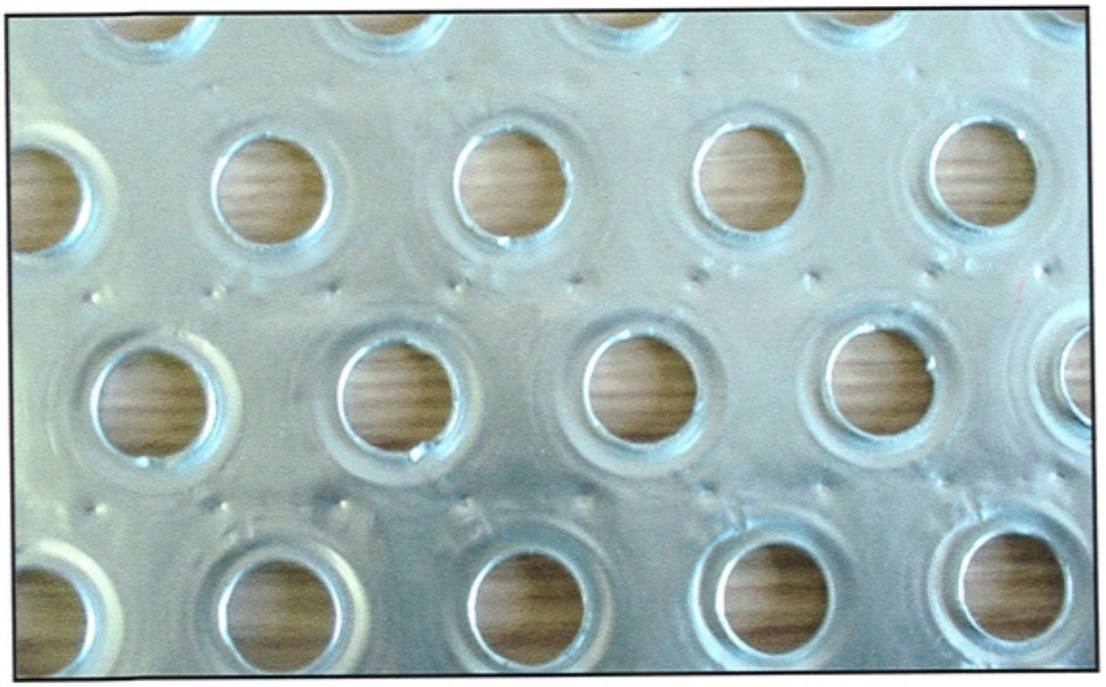

Fig. (5.4a) photograph of the flat fin geometry

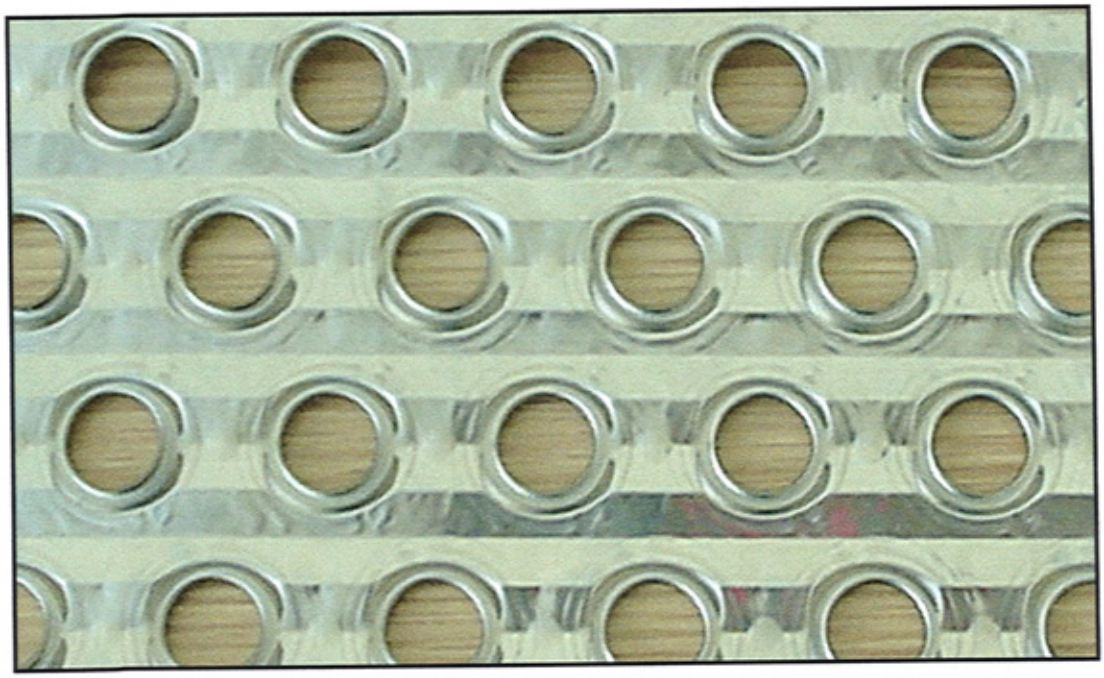

Fig. (5.4b) photograph of the corrugated fin geometry

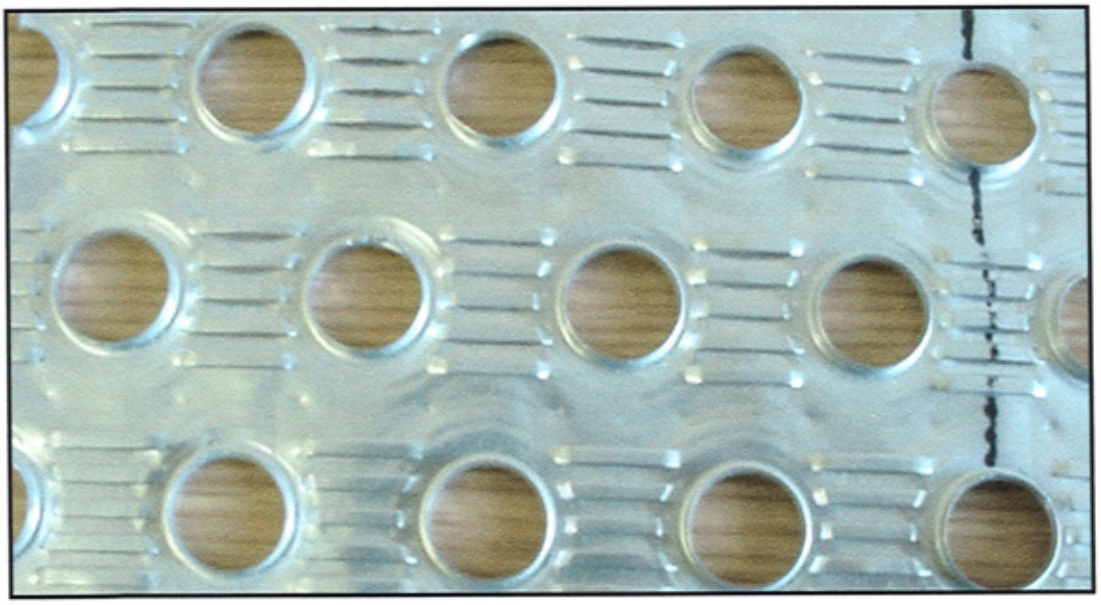

Fig. (5.4) Photograph turbulated fin geometry

The cooling coils specifications are listed in table (5.2). The tubes were arranged in a four-circuit configuration cross-counter flow conditions as illustrated in Fig. (5.8).

5.4 Measuring instruments and tolerances

The measuring instruments used in the experimental work to measure the velocity, temperature and pressure in both the air and chilled water streams were:

- **Air side**

1. A hotwire anemometer (TESTO 435) and digital indicator to measure the air velocity just before the cooling coil at 12 grid points with an uncertainty of ± 0.05 m/s + 5 % of measured value.
2. A digital micromanometer with a range of 0-2000 Pa with uncertainty of ± 0.5 % and data logger (PICO-ADC-11) with an uncertainty of ± 1 % were used to measure the differential pressure of the air across the coil.
3. Platinum resistance temperature detectors *PRTD* with a range of -70 °C to 600 °C with an uncertainty of ± 0.15 °C (Class A) and data logger system

with truncation uncertainty of 2.4×10^{-4} and maximum resolution of 0.009 used to measure the air temperature through eighteen positions just before and after the cooling coil.

4. A sling psychrometer was used to record the wet and dry bulb temperatures of the ambient air.

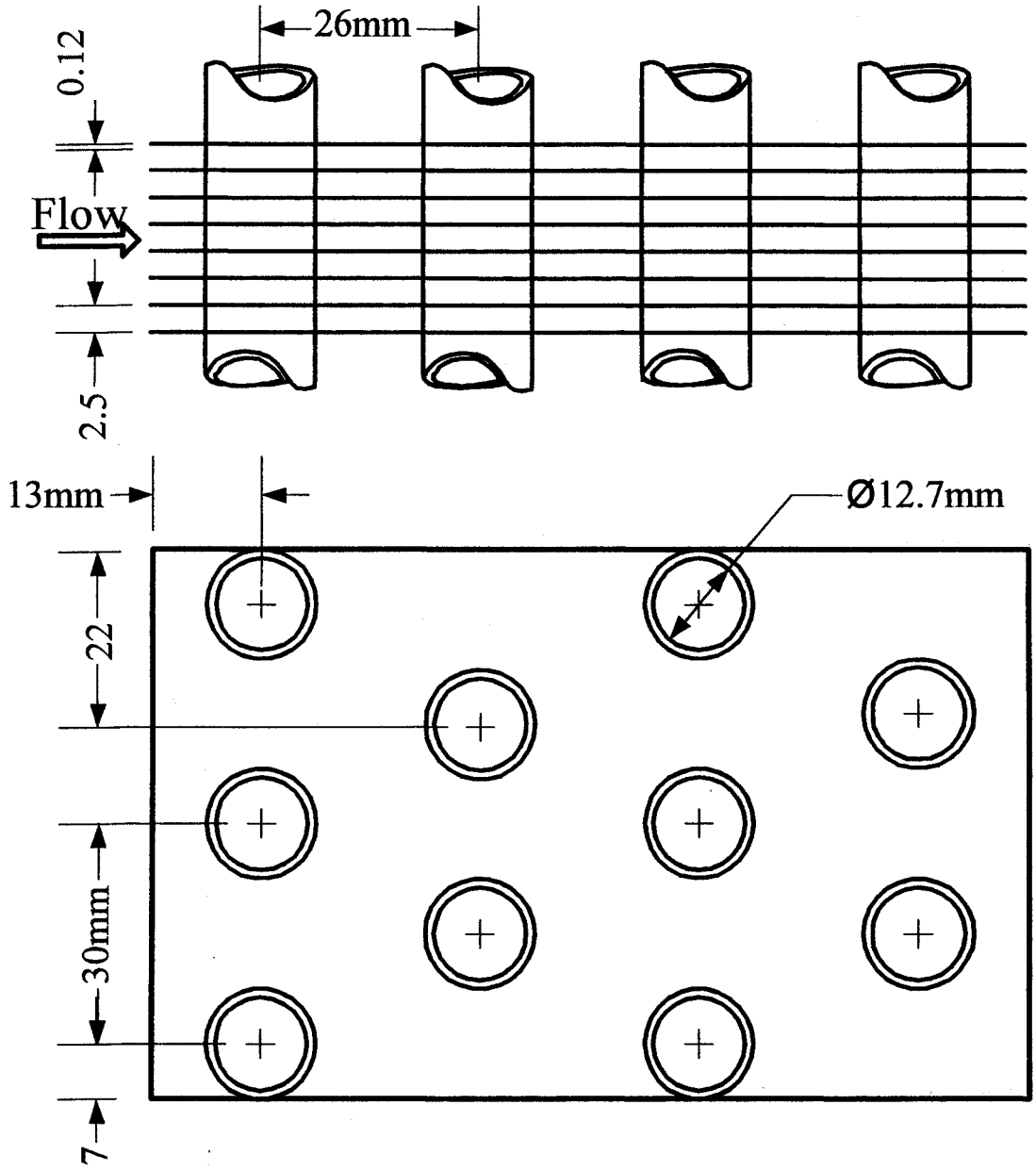

Fig. (5.5) Geometry of the flat fin coil

5. A Crane flow measuring and regulating valve (0.00001 m^3/s to 0.0015 m^3/s) with an uncertainty of ± 5 % and a Poddymeter (up to 450 mmHg) with an uncertainty of ± 1 % were used to measure the water flow rate.

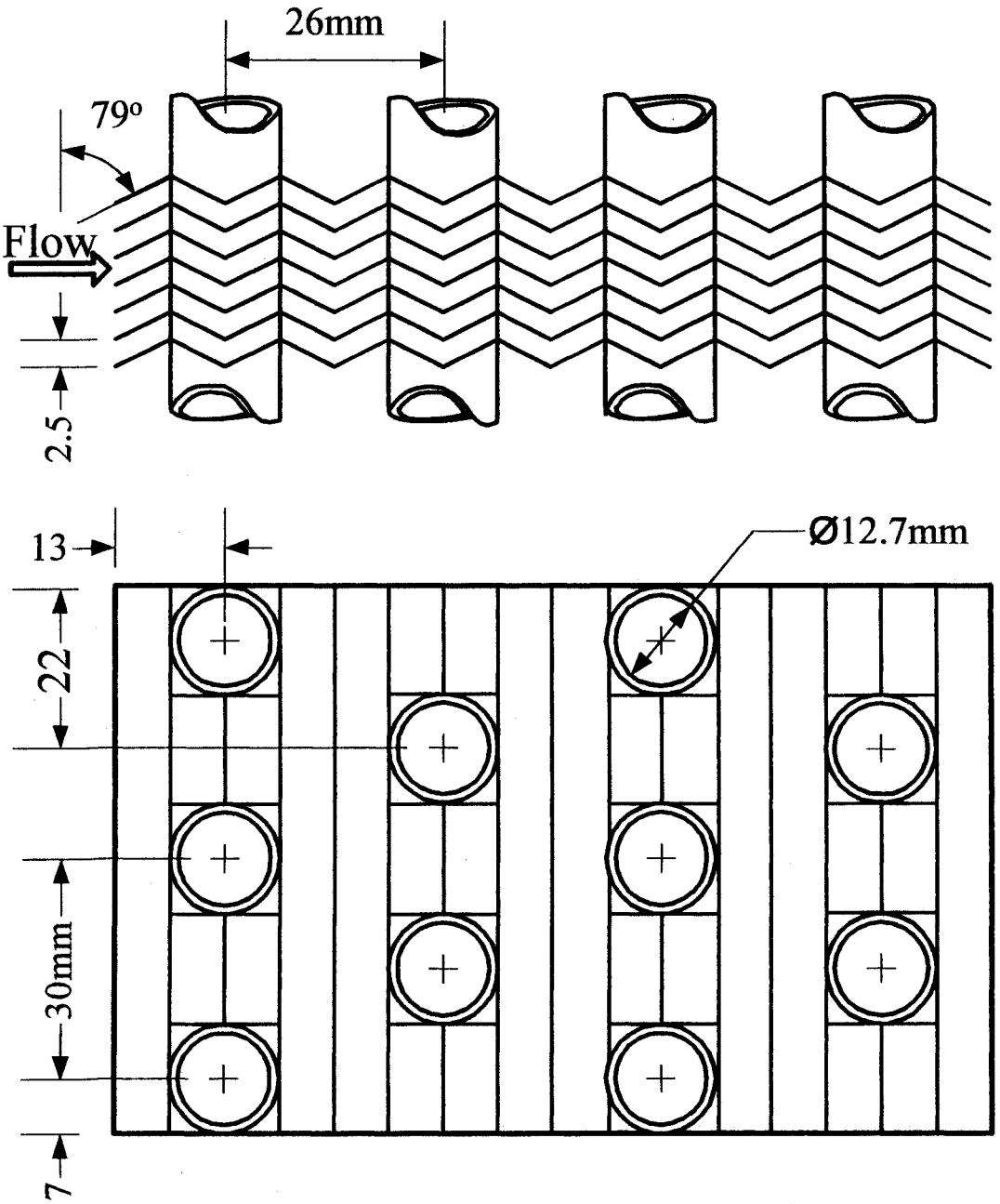

Fig. (5.6) Geometry of the corrugated fin coil

6. Platinum resistance temperature detectors *PRTD* with a range of -70 °C to 600 °C with uncertainty of ± 0.3 °C (class B) and a data logger system with truncation uncertainty of 2.4×10^{-4} and maximum resolution of 0.009 were used to measure the inlet and outlet temperature of waterside.

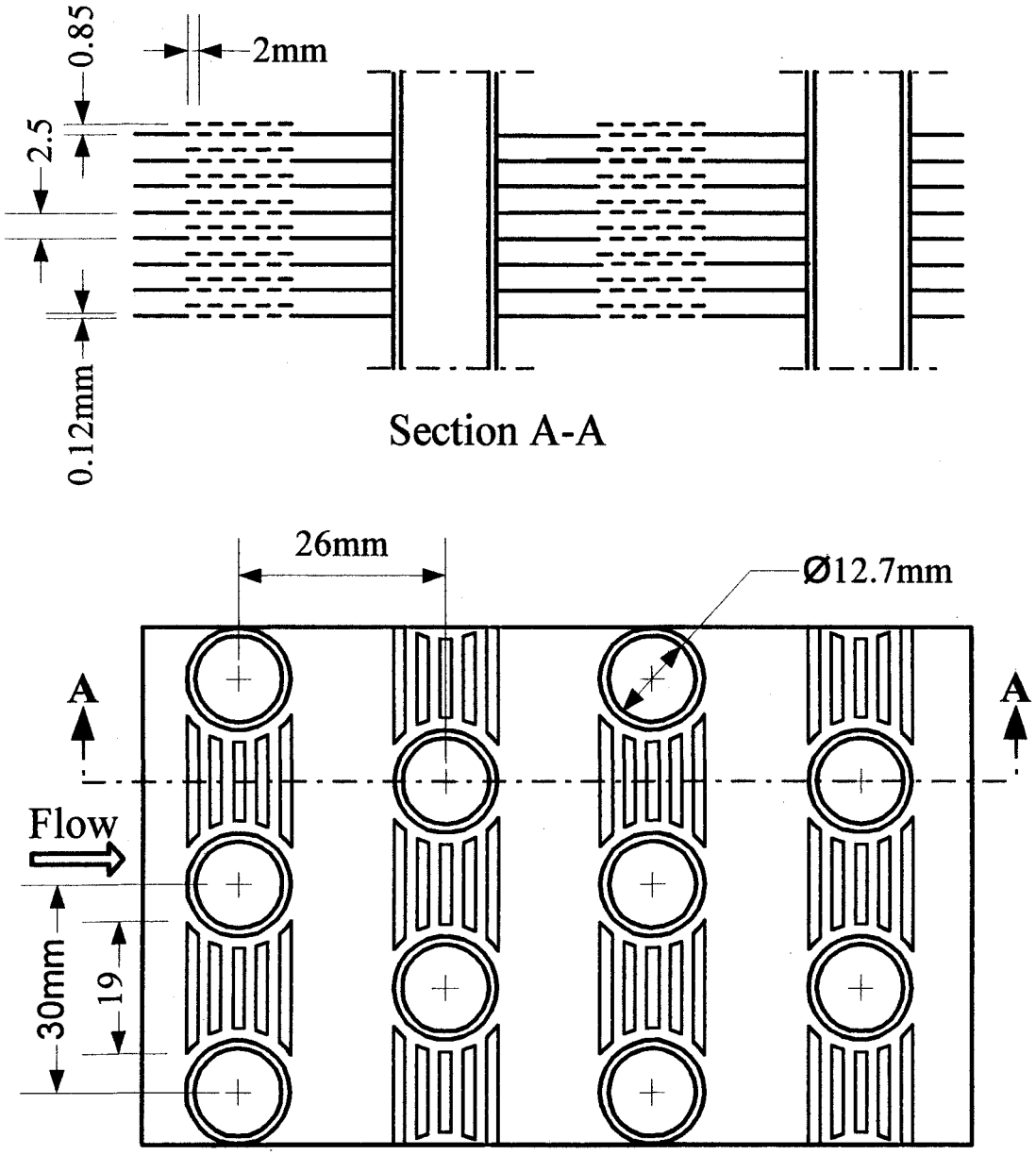

Fig. (5.7) Geometry of the turbulated fin coil

Table (5.2) Cooling coils specifications

Specification	Flat fins	Corrugated fins	Turbulated fins
Coil dimensions	530 x 420 x 104	530 x 420 x 104	530 x 420 x 104
Tube rows	4	4	4
Tube material	Cu	Cu	Cu
Tube D_o/D_i	12.7/11.88 mm	12.7/11.88 mm	12.7/11.88 mm
Longitudinal tube pitch	26 mm	26 mm	26 mm
Transverse tube pitch	30 mm	30 mm	30 mm
Tube length	530 mm	530 mm	530 mm
Fin material	Al	Al	Al
Fin thickness	0.12 mm	0.12 mm	0.12 mm
Fin pitch	2.5 mm	2.5 mm	2.5 mm
Corrugation angle, β	--------	11°	--------
Corrugation height, C_h	--------	1.27 mm	--------
Slit width, S_w	--------	--------	2 mm
Slit height, S_h	--------	--------	0.85 mm

5.5 Experimental procedures

The ambient airflow was induced across the test coil by means of a centrifugal fan with a voltage regulator. The air was pre-heated by a direct resistance electric two-row heating coil. The heating coil outlet temperature was varied between 23 °C to 45 °C, generating conditions appropriate for a hot arid climate. The air velocity was measured by hotwire anemometer at twelve positions across the cross section of the duct, which provided an averaging mechanism for the air velocity variation (the locations of the hotwire sensor is illustrated in Fig. (5.9)). The average velocity was in the range 0.65 to 3.8 m/s. Two meshes of platinum-resistance temperature (*PRT*) sensors were set in the air path to measure the inlet and outlet temperatures across the test coil. Both the inlet and outlet meshes consisted of nine *PRT* sensors. The sensor locations inside the plant were

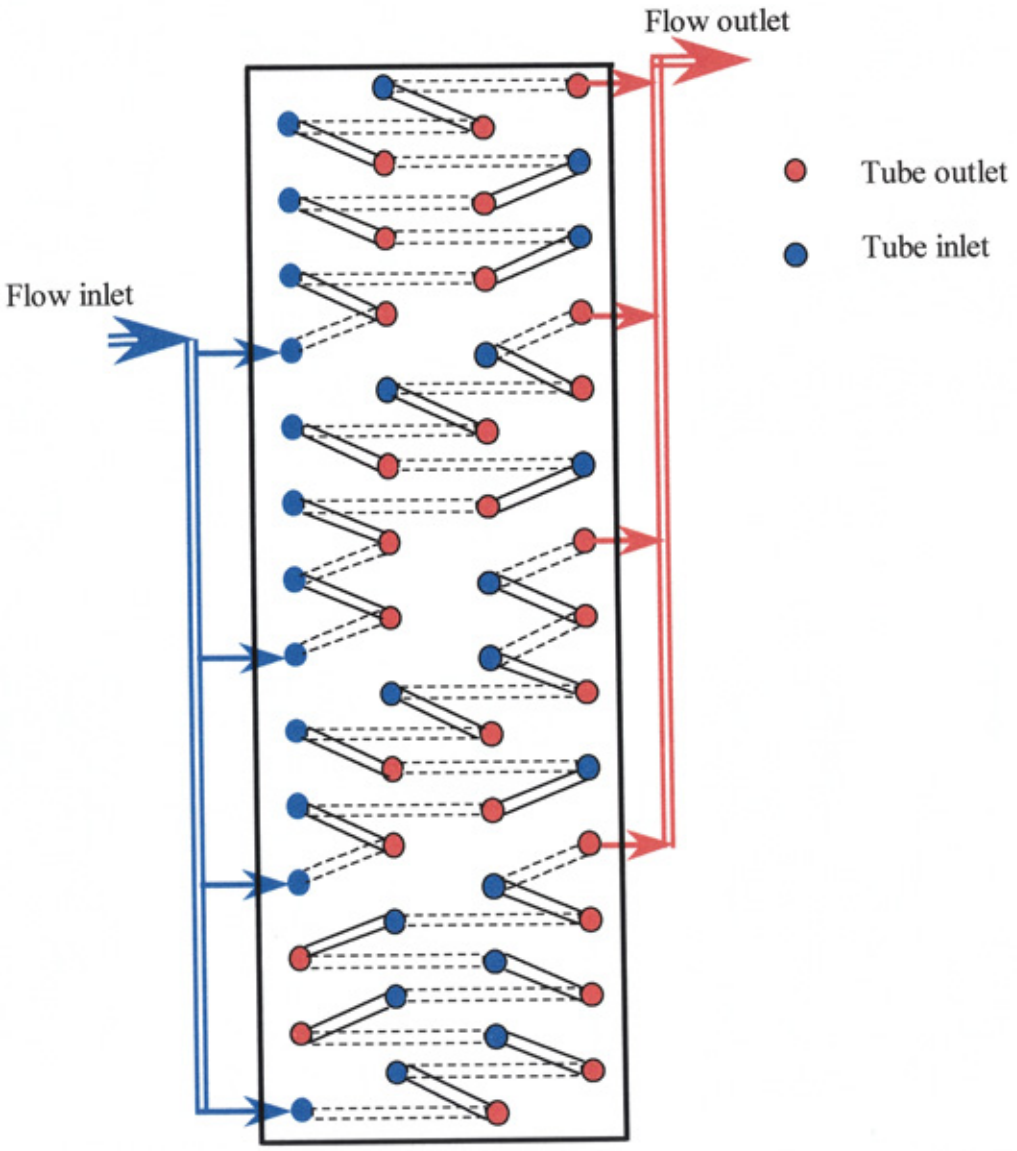

Fig. (5.8) Chilled-water flow circuits of the cooling coil-tubes

established according to ASHRAE recommendations [ASHRAE fundamental, 1997]. The airside pressure drop across the cooling coil was measured from upstream and downstream pressure tappings, which were connected to a digital micromanometer pressure transducer. The reading of the micromanometer was noted to fluctuate randomly. For this reason a data acquisition system and interface card were connected to the micromanometer for the purpose of time-averaging the pressure drop results, (samples of fluctuating pressure drop are illustrated in Fig. (5.10)).

The working fluid inside the cooling coil was a chilled glycol solution whose temperature was varied in the range of $5\,^{\circ}C \leq T_{wi} \leq 15\,^{\circ}C$. The fluid was supplied from a Daikin vapour compression chiller with a nominal cooling capacity of 18.3 kW. The water flow rate was circulated by a water-pump and it was increased to a maximum rate to achieve fully turbulent flow (Re ≅ 19000) in order to minimise the temperature gradient through the heat exchanger tubes. The main flow rate was divided into four circuits inside the coil, with a Reynolds number for each circuit branch of Re ≅ 7650. Both the inlet and outlet chilled water temperatures were measured using a *PRT* sensor. A Perflow "Poddymeter" was used to measure the water flow rate via a Crane commissioning set. The dry-bulb and wet-bulb temperatures of the ambient air were recorded. All temperature results were logged using a Schlumberger Orion data logger. All the temperature and pressure signals were collected and converted using a data acquisition system (a hybrid recorder). The data acquisition system transmitted the converted signals to the host computer through an interface card for further processing. The rig was allowed to run without refrigeration until the circulating glycol solution temperature reached about 30 °C before the next run started. All the measured parameters are presented in Appendix (A).

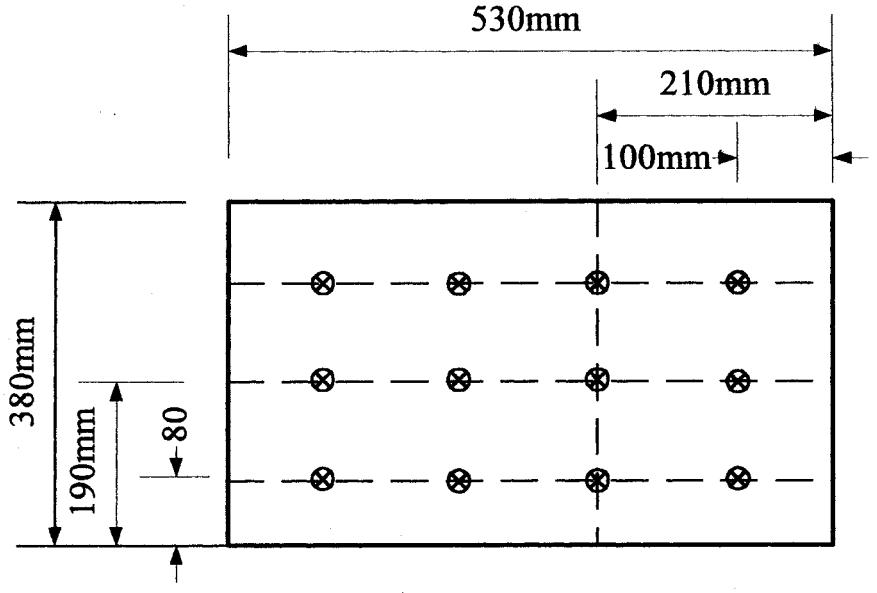

Fig. (5.9) Hotwire probe locations through the duct cross-section

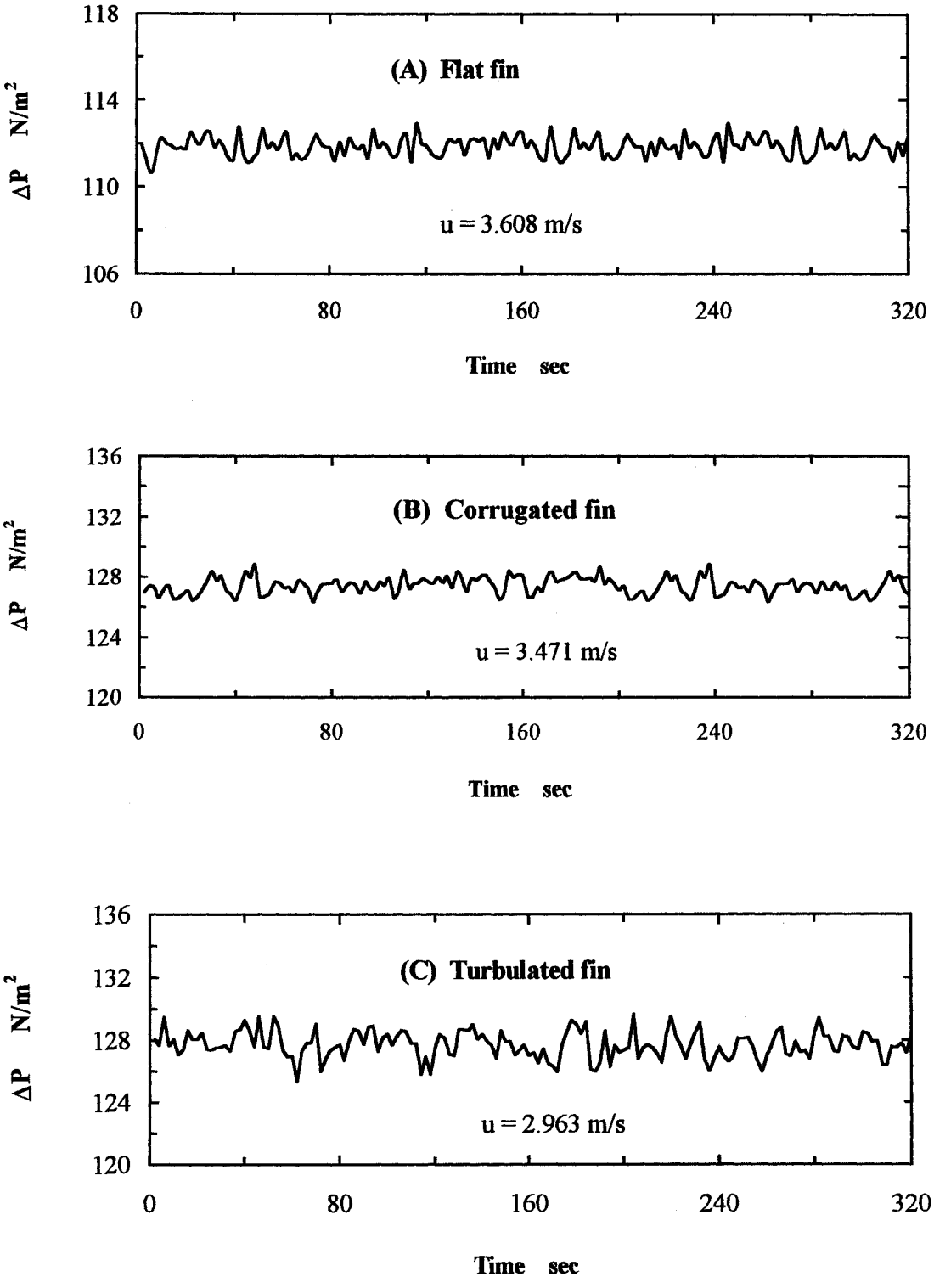

Fig. (5.10) Fluctuation of the pressure drop across the cooling coils

5.6 Method of calculation

The log-mean temperature difference "*LMTD*" method of calculation was applied since the hot and cold fluid temperatures are known. The air and the chilled water properties were evaluated at the fluid bulk temperature.

- **Heat transfer (Airside)**

  The rate of heat transfer on the airside is defined as:

$$Q_a = m_a \, Cp_a \, \Delta T_a \tag{5.1}$$

- **Heat transfer (Waterside)**

  The rate of heat transfer on the waterside is defined as:

$$Q_w = m_w \, Cp_w \, \Delta T_w \tag{5.2}$$

- **Average rate of heat transfer**

Due to the uncertainty in measurements and heat losses from the test rig, the rate of heat transfer in the airside is not equal to the rate of heat transfer in the waterside. For this purpose, the total heat transfer rate used in the calculation is the mathematical average of the airside and waterside heat transfer rate, [Wang *et al*, 1998], and it is defined as:

$$Q_{av} = \frac{Q_w + Q_a}{2} \tag{5.3}$$

- **Heat transfer balance**

$$Q_{av} = A_o \, U_o \, \theta_m \tag{5.4}$$

Where:

A_o Total transfer surface area, = $A_f + A_t$

θ_m Log-mean temperature difference, the heat exchanger boundary temperature is illustrated in Fig. (5.11).

$$\theta_m = \frac{(T_{ao} - T_{wi}) - (T_{ai} - T_{wo})}{\ln \frac{(T_{ao} - T_{wi})}{(T_{ai} - T_{wo})}} \tag{5.5}$$

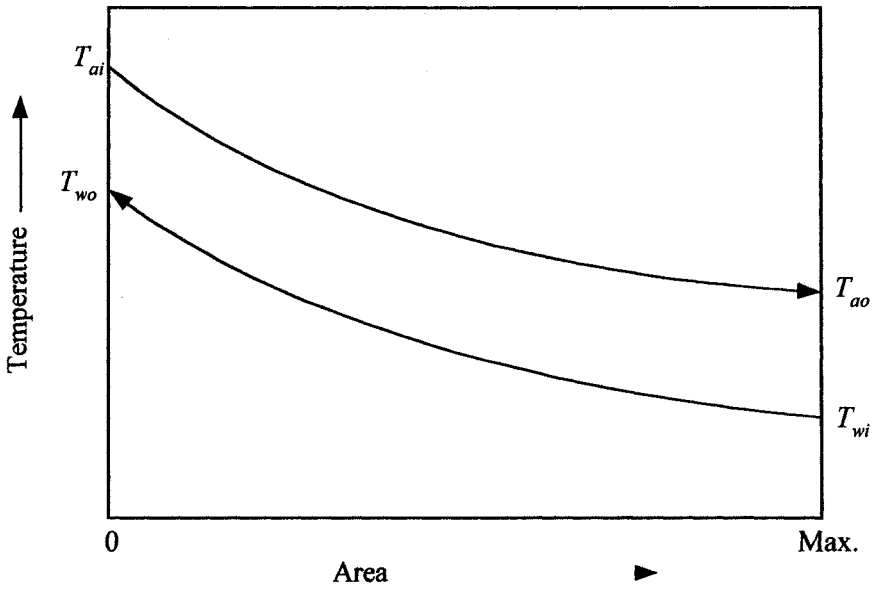

Fig. (5.11) Heat exchanger boundary temperature

- **Overall heat transfer coefficient**

The overall heat transfer thermal resistance is defined as;

$$\frac{1}{A_o U_o} = \frac{1}{\eta_o A_o h_o} + \frac{ln(D_o / D_i)}{2\pi l k} + \frac{1}{A_i h_i} \tag{5.6}$$

- **Waterside heat transfer coefficient**

The heat transfer coefficient on the waterside, h_i is calculated from the Gnielinski semi-empirical correlation [Gnielinski, 1976]:

$$h_i = \left(\frac{k}{D_i}\right) \frac{(\mathrm{Re}_{Di} - 1000)\,\mathrm{Pr}\,(f_i/8)}{1 + 12.7\sqrt{f_i/8}\,(\mathrm{Pr}^{2/3} - 1)},$$

$$3000 \leq \mathrm{Re}_{Di} \leq 5 \times 10^6 \tag{5.7}$$

$$f_i = (0.79\ln(\mathrm{Re}_{Di}) - 1.64)^{-2} \tag{5.8}$$

- **Overall surface efficiency**

The overall surface efficiency, η_o is related to the fin surface area, total surface area, and fin efficiency:

$$\eta_o = 1 - \frac{A_f}{A_o}(1 - \eta_f) \tag{5.9}$$

In the case of fin-sheet attached with staggered tube bundle, the fin length, L_f (Fig. (5.12)) is exactly unspecified. So the fin efficiency for the staggered tube arrays with continuous-plate fins may be calculated using the method proposed by Schmidt [McQusiton and Parker, 1994] based on hexangular fin arrays. A validation between the Schmidt fin efficiency and the fin efficiency predicted from the CFD modelling of the fin-and-tube cooling coils is investigated in chapter-VI-.

$$\eta_f = \frac{Tanh\,(m r_i\,\phi)}{(m r_i\,\phi)} \tag{5.10}$$

Where:

$$m = \sqrt{\frac{2h_o}{k_f t}}, \qquad \phi = (R_s - 1)[1 + 0.35\ln(R_s)]$$

$$R_s = 1.27\frac{M}{r_i}\left(\frac{L_R}{M} - 0.3\right)^{\frac{1}{2}}$$

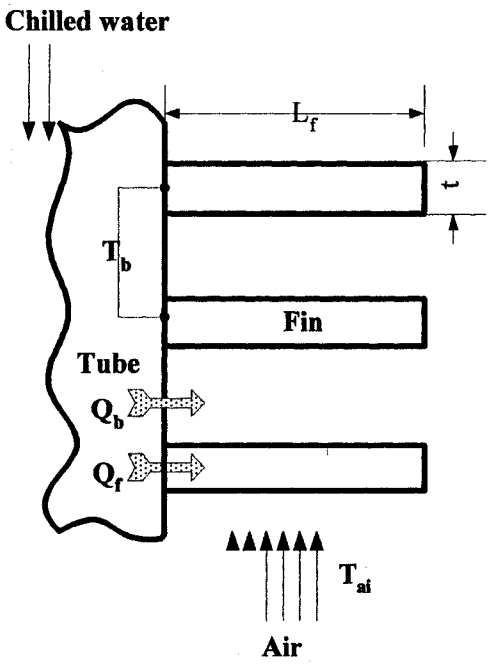

Fig. (5.12) Single tube with multi-fins

The heat transfer coefficient and the fin efficiency are inter-dependent variables and therefore need to be calculated iteratively.

- **Reynolds number**

The Reynolds number on the airside is defined as:

$$\mathrm{Re} = \frac{u_{max} D_h}{\nu} \tag{5.11}$$

D_h = the hydraulic diameter of the heat exchanger and it is defined as:

$$D_h = \frac{4 \text{ minimum free flow area x streamwise length}}{\text{transfer surface area}}$$

$$D_h = \frac{4 A_{ff} L_s}{A_o} \tag{5.12}$$

- **Nusselt number**

The Nusselt number is defined as:

$$Nu = \frac{h_o D_h}{k} \tag{5.13}$$

- **Friction factor**

The friction factor is defined according to [Kays and London, 1984] as:

$$f = \frac{A_{ff} \rho_m}{A_o \rho_i}\left[\frac{2\Delta P \rho_i}{G^2} - \left(1 + \sigma^2\left(\frac{\rho_i}{\rho_o} - 1\right)\right)\right] \tag{5.14}$$

Where:

$$u_{max} = \frac{u}{\sigma}, \qquad \rho_m = \frac{\rho_i + \rho_o}{2}, \qquad \sigma = A_{ff} / A_{fr},$$

$$G = \frac{\rho u}{\sigma}$$

5.7 Error analysis

Errors in the experimental data will apply to those values that are known to contain uncertainty. Uncertainty varies a great deal depending upon the circumstances of the experiment, hence, the magnitude of the experimental error is always in itself uncertain.

The different types of experimental error are as follows;

1. Errors in the apparatus construction and in the measurement.
2. Permanent error, which will cause repeated readings to be in error by approximately the same amount (sometimes called systematic errors)
3. Random errors, which may be caused by observation, round up and interpolation.

Given W_1, W_2, W_3, ..., W_n uncertainties in the independent variables (X_1, X_2, X_3, ...X_n) and W_R is the uncertainty in the result at the same odds, then the uncertainty in the result can be given as; [Holman, 1994]

$$W_R = \left[\left(\frac{\partial R}{\partial X_1} W_1 \right)^2 + \left(\frac{\partial R}{\partial X_2} W_2 \right)^2 + \left(\frac{\partial R}{\partial X_3} W_3 \right)^2 + ...+ \left(\frac{\partial R}{\partial X_n} W_n \right)^2 \right]^{\frac{1}{2}} \tag{5-15}$$

Since the values of the partial derivatives and the uncertainties in the measured parameters may be positive or negative, then the absolute values are considered to yield the maximum absolute uncertainty in the result W_R, [Ghanim *et al*, 1996]. Details of the error analysis procedures and tabulated values of uncertainties of all parameters of average heat transfer, *LMTD*, overall heat transfer coefficient, Nusselt number and friction factor are given in appendix (C).

5.8 Results

The experimental results are presented according to dimensionless groups (Nu, *f*, Re) as function of the fin types, nominal inlet air temperature and nominal inlet chilled-water temperature.

The percentage uncertainty in the Nusselt number and friction factor for all coil types is illustrated in Figs. (5.13) and (5.14) respectively. It noted that the uncertainty in Nusselt number is more sensitive to the air temperature than in the case with friction factor and the higher value of uncertainty in Nusselt number was yielded at lower values of inlet air temperature. In both Nusselt number and friction factor, the highest uncertainties were associated with lowest values of Reynolds number. The average value of uncertainty in Nusselt number and friction factor was within ± 13 % and ± 10 % respectively. While, the average energy balance between the airside and tube-side was within 15 % including the convection-radiation losses from the coil casing to the surrounding.

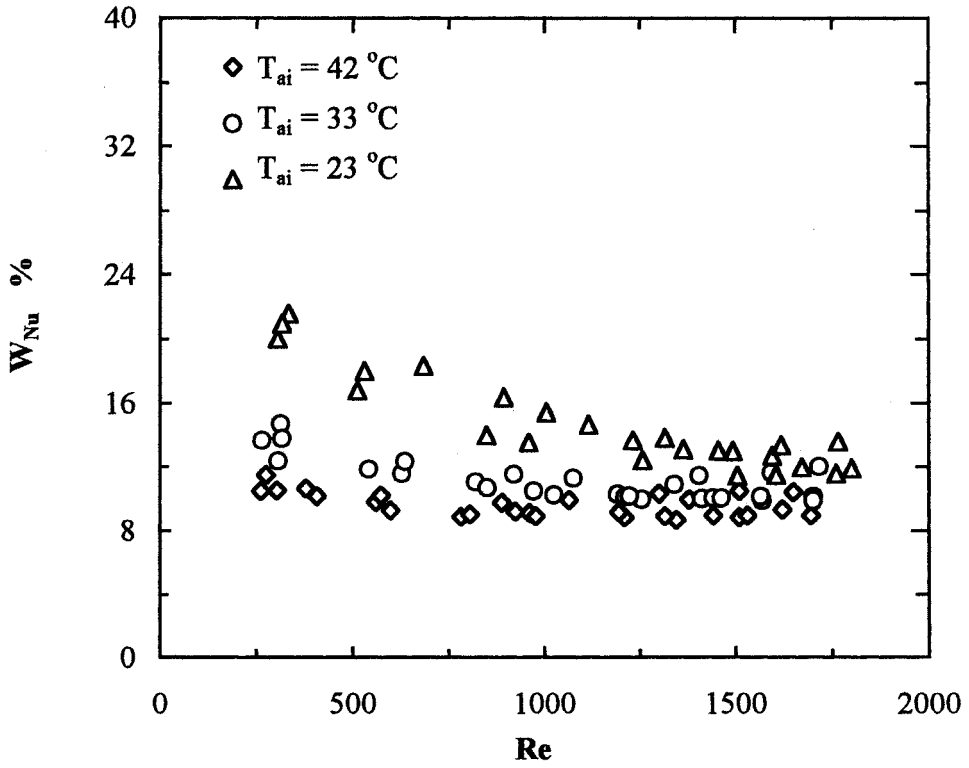

Fig. (5.13) Error plot of Nusselt number for T_{wi} = 10 °C

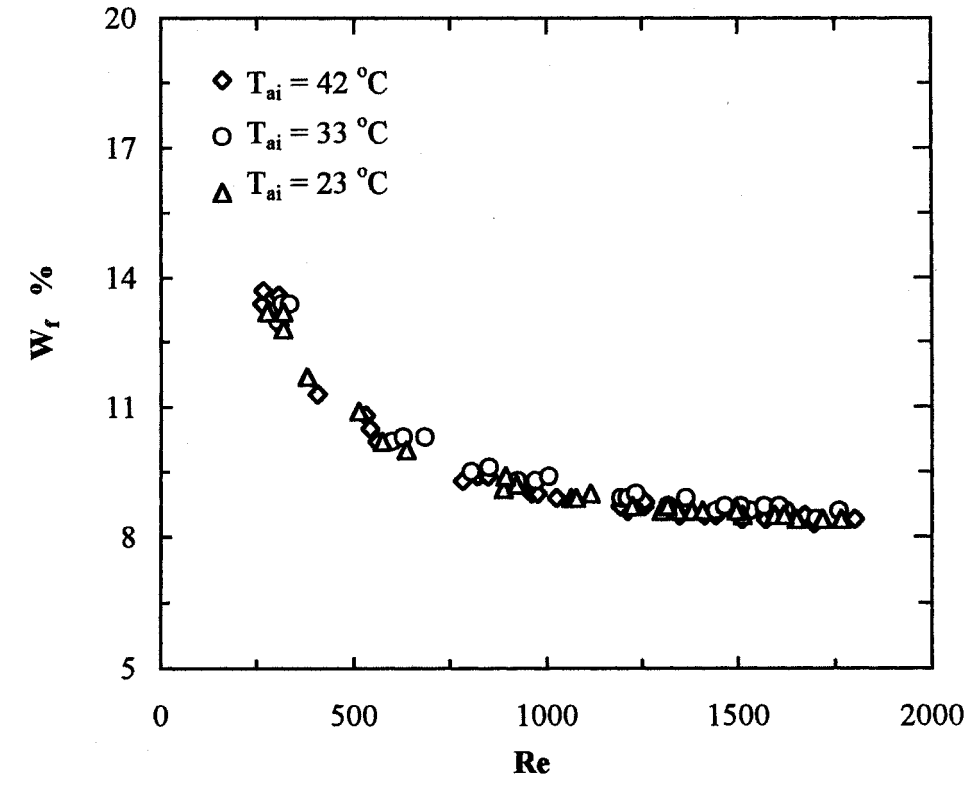

Fig. (5.14) Error plot of friction factor for T_{wi} = 10 °C

5.8.1 Flat fin results

The Nusselt number for the flat fin cooling coil at the nominal chilled water temperature = 5 °C and 10 °C is illustrated in Figs. (5.15) and (5.16) respectively. It observed that the effect of the air temperature on the Nusselt number of the flat-fin cooling coil is very small. The Nusselt number for the nominal inlet air temperature = 33 °C and 42 °C is illustrated in Figs. (5.17) and (5.18) respectively. It is observed that the chilled water temperature have a negligible effect on the Nusselt number.

The pressure drop and the friction factor of the flat-fin cooling coil for the nominal inlet-air temperatures T_{ai} = 23 °C, 33 °C, and 42 °C are illustrated in Figs. (5.19) and (5.20) respectively. It noted that the inlet-air temperature has negligible effect on the friction. Both results confirm that the Nusselt number and friction factor are almost independent on the temperature difference of both fluid streams.

Since the performance of the fin-and-tube heat exchangers depends on a variety of the design parameters and conditions (Do, S_L, S_t, N_R, t, f_p, C_h, β, S_w, S_h, S_n, Re_{air}, and Re_{water}), it is difficult to compare directly the results with the published data in the literature. In addition, a significant difference of airside performance may occur owing to the differences of reduction method, [Wang, *et al*, 1999b & 2000a]. However, a comparison between some of the more relevant published data of fin-and-tube heat exchangers with the present data of fin-and-tube cooling coils seems to be a necessity to give indication of the validity of results.

The flat fin results of Nusselt number and friction factor are compared with the corresponding experimental results of Abu Madi *et al* [Abu Madi *et al*, 1998] as illustrated in Figs. (5.15) and (5.20). Good agreement between the present and the published data of Abu Madi *et al* especially in the case of Nusselt number. The deviation between the present and the data of Abu Madi *et al* is attributed to the difference in the tested coil configuration as summarised in the Table (5.3).

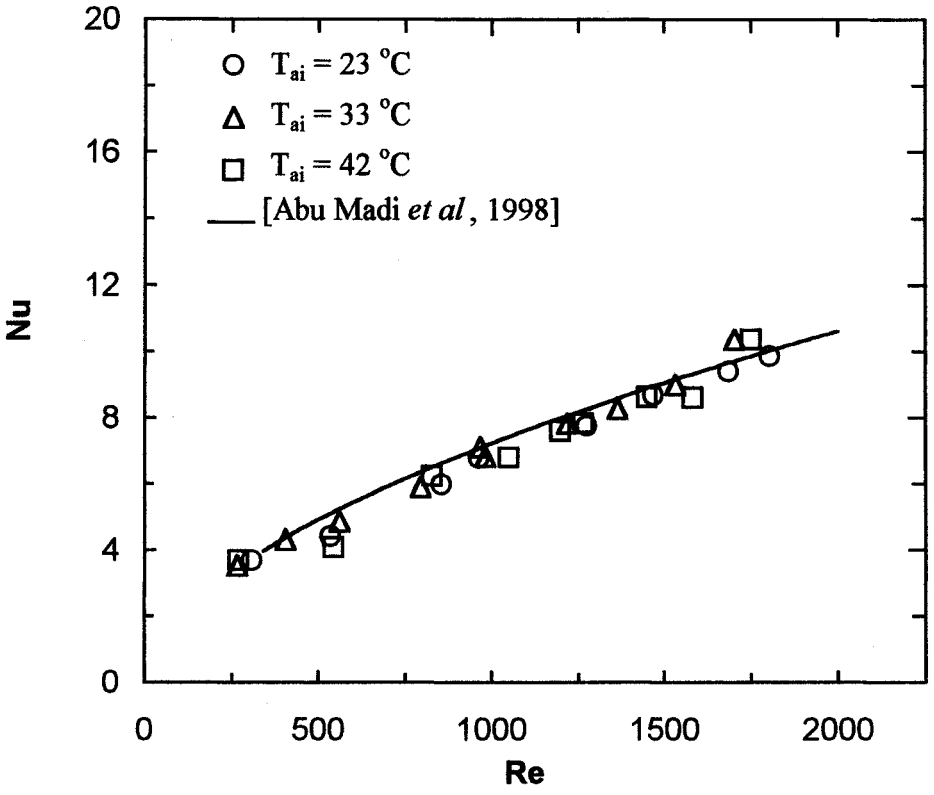

Fig. (5.15) Nusselt number of the flat fin cooling coil for T_{wi} = 5 °C

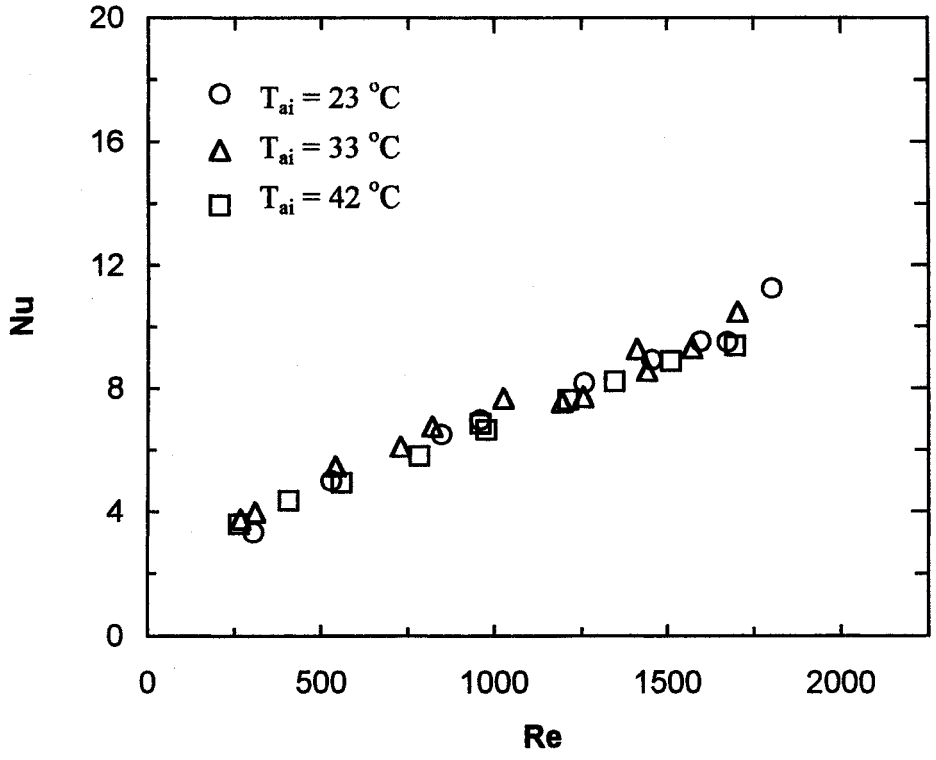

Fig. (5.16) Nusselt number of the flat fin cooling coil for T_{wi} = 10 °C

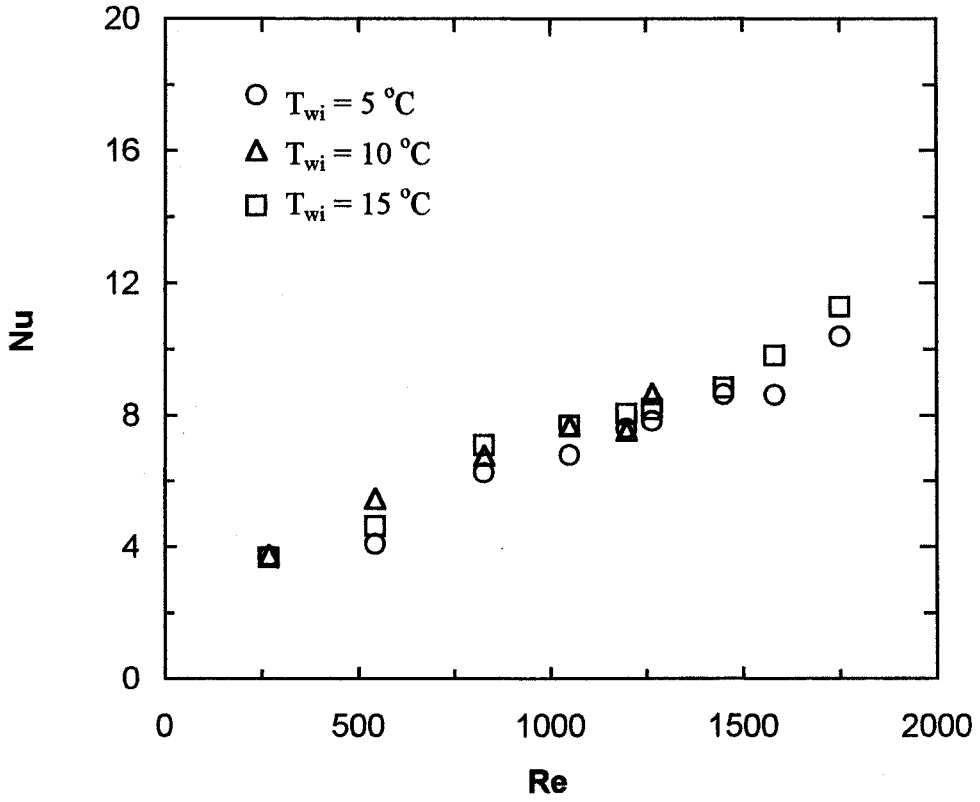

Fig. (5.17) Nusselt number of the flat fin cooling coil for T_{ai} = 33 °C

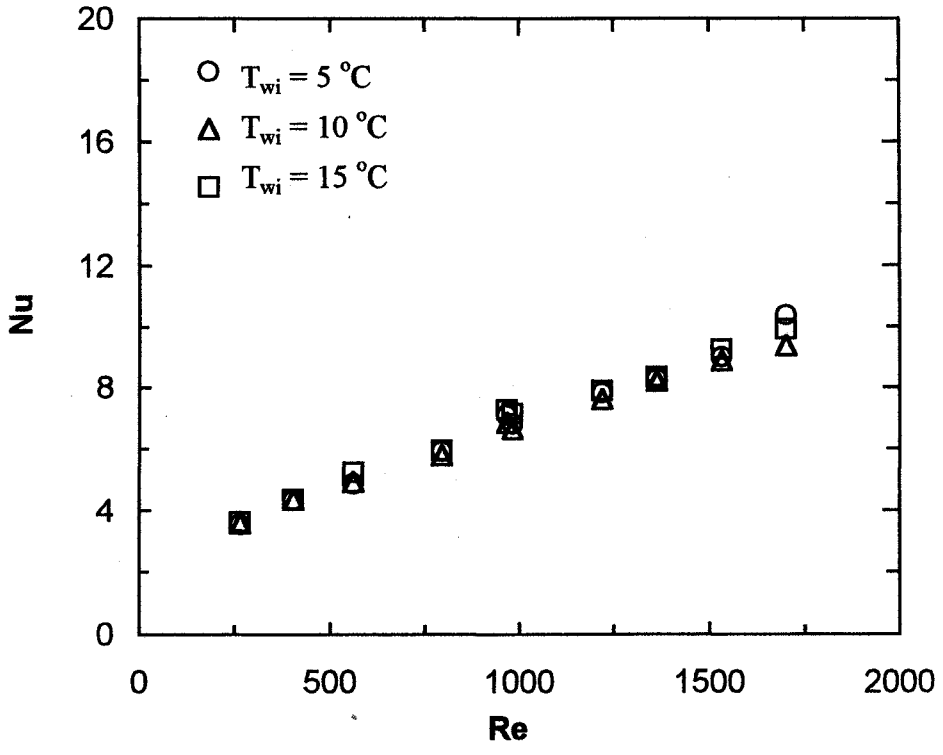

Fig. (5.18) Nusselt number of the flat fin coil for T_{ai} = 42 °C

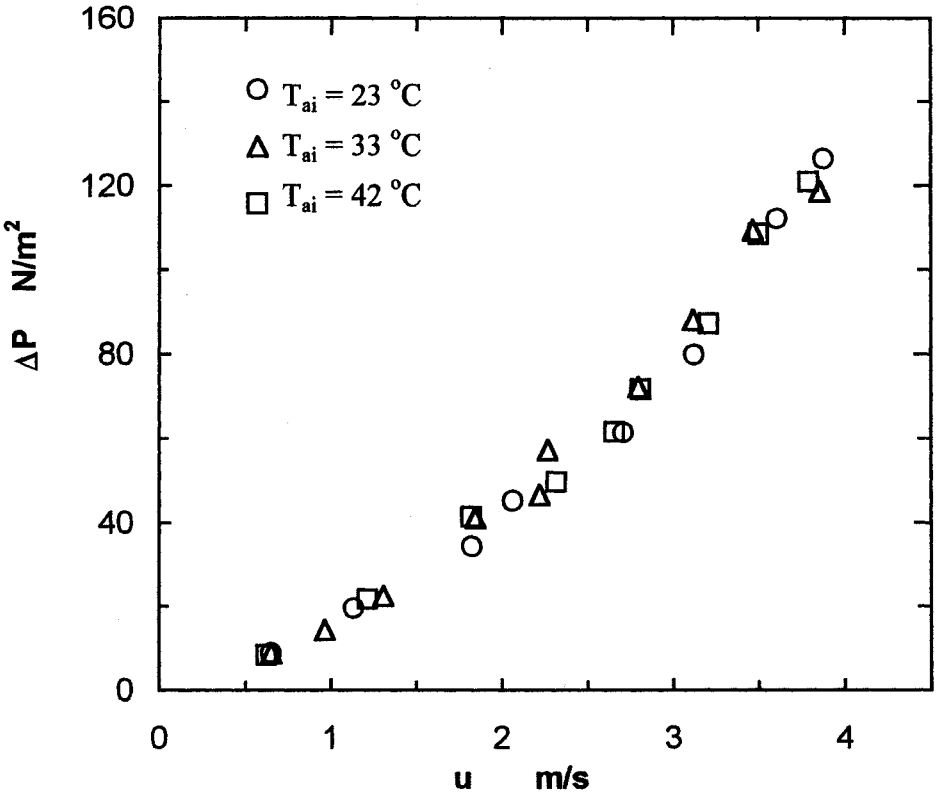

Fig. (5.19) Pressure drop of the flat fin cooling coil

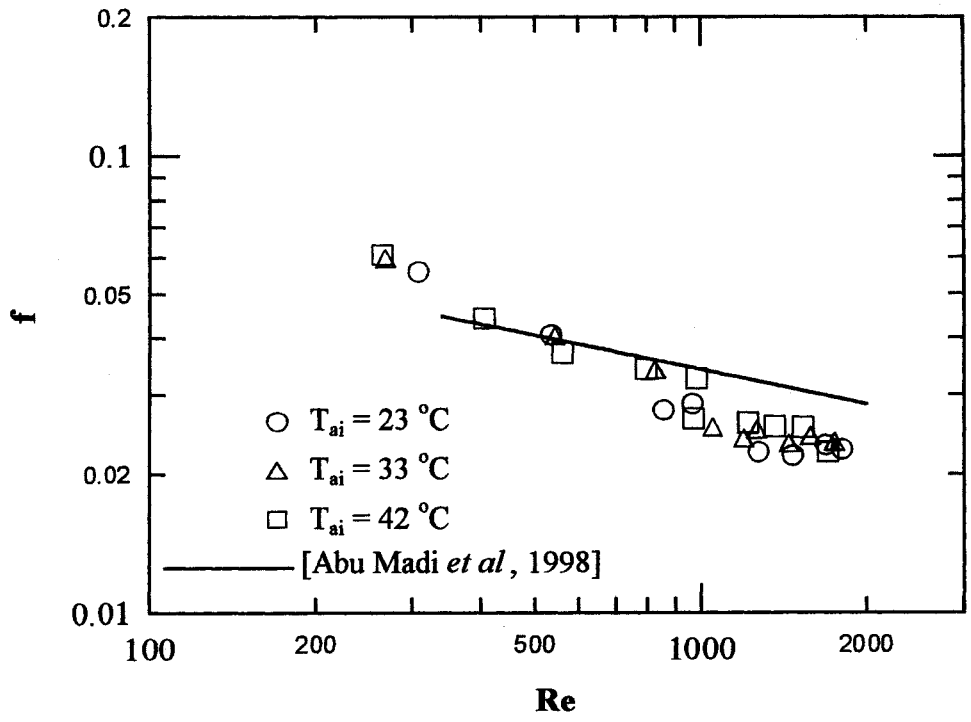

Fig. (5.20) Friction factor of the flat fin cooling coil

5.8.2 Corrugated fin

The Nusselt number for the corrugated fin coil at the nominal chilled water temperature T_w = 10 °C and for the inlet air temperature T_{ai} = 42 °C is illustrated in Figs. (5.21) and (5.22) respectively. The rest of results for T_w = 5 °C and 15 °C and also for T_{ai} = 23 °C and 33 °C are given in appendix (B). The pressure drop and the friction factor of the corrugated-fin cooling coil are illustrated in Figs. (5.23) and (5.24) respectively. The independence of both Nusselt number and friction factor to the air and chilled water temperature are evident. The corrugated fin results of Nusselt number and friction factor are compared with the corresponding experimental results of Abu Madi *et al* (Figs. 5.22 & 5.24) [Abu Madi *et al*, 1998]. Good agreement between the present and the published data of Abu Madi *et al* especially in the case of Nusselt number. The deviation between the present and the data of Abu Madi *et al* is attributed to the difference in the tested coil configuration as summarised in the Table (5.3).

Table (5.3): Present and published work comparison

Items	Present work	Abu Madi *et al*, 1998-Flat-fin	Abu Madi *et al*, 1998-Corrugated	Wang *et al*, 1999c-Slit-fin
D_o	12.7 mm	9.956 mm	9.956 mm	10.1 mm
N_R	4	4	4	4
S_L	26 mm	16.5 mm	22 mm	22 mm
S_t	30 mm	19 mm	25.4 mm	25.4 mm
t	0.12 mm	0.13 mm	0.13 mm	0.12 mm
f_p	2.5 mm	2.545 mm	2.567 mm	2.47 mm
β	11°	----------	Not specified	----------
C_h	1.27 mm	----------	Not specified	----------
S_w	2 mm	----------	----------	2.2 mm
S_h	0.85 mm	----------	----------	0.99 mm
S_n	5	----------	----------	4

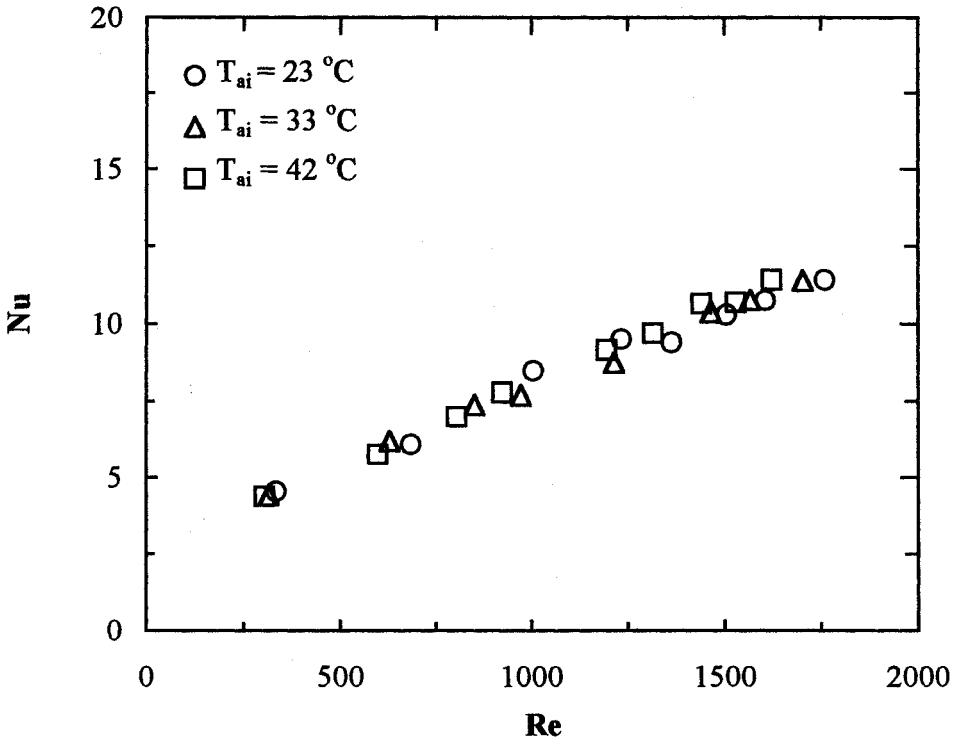

Fig. (5.21) Nusselt number of the corrugated fin coil for T_{wi} = 10 °C

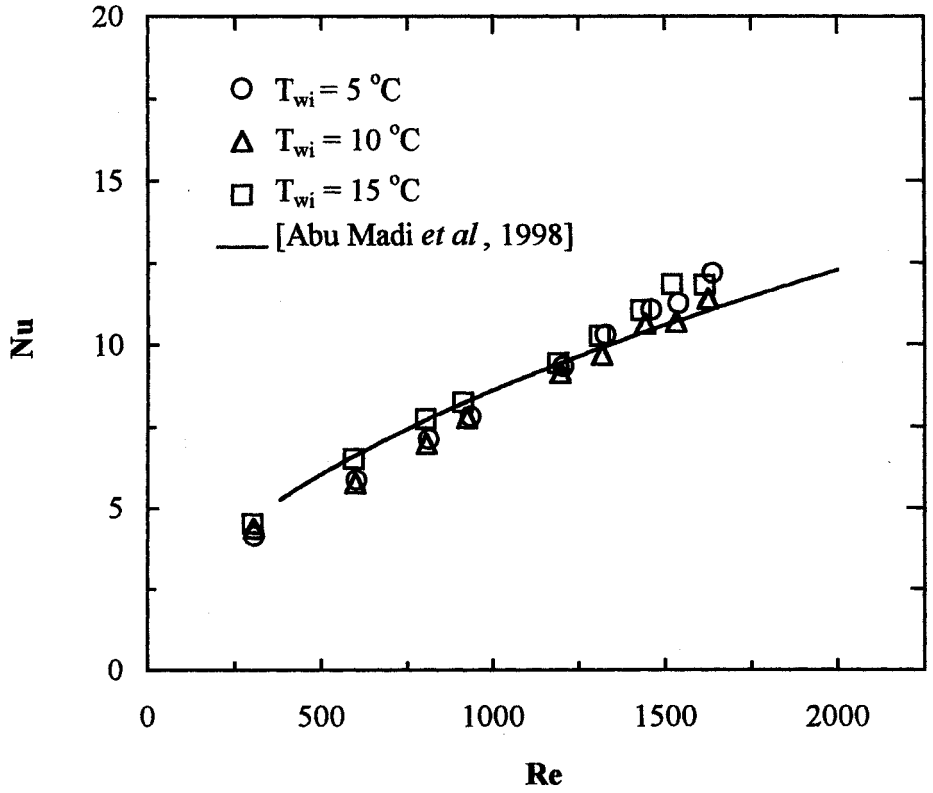

Fig. (5.22) Nusselt number of the corrugated fin coil for T_{ai} = 42 °C

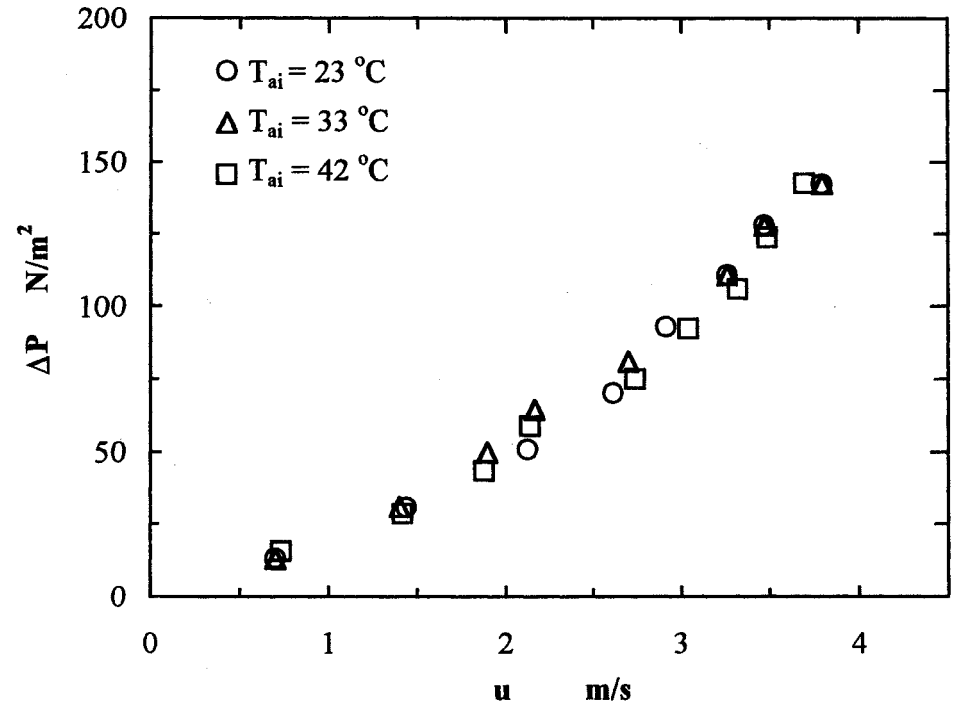

Fig. (5.23) Pressure drop of the corrugated fin cooling coil

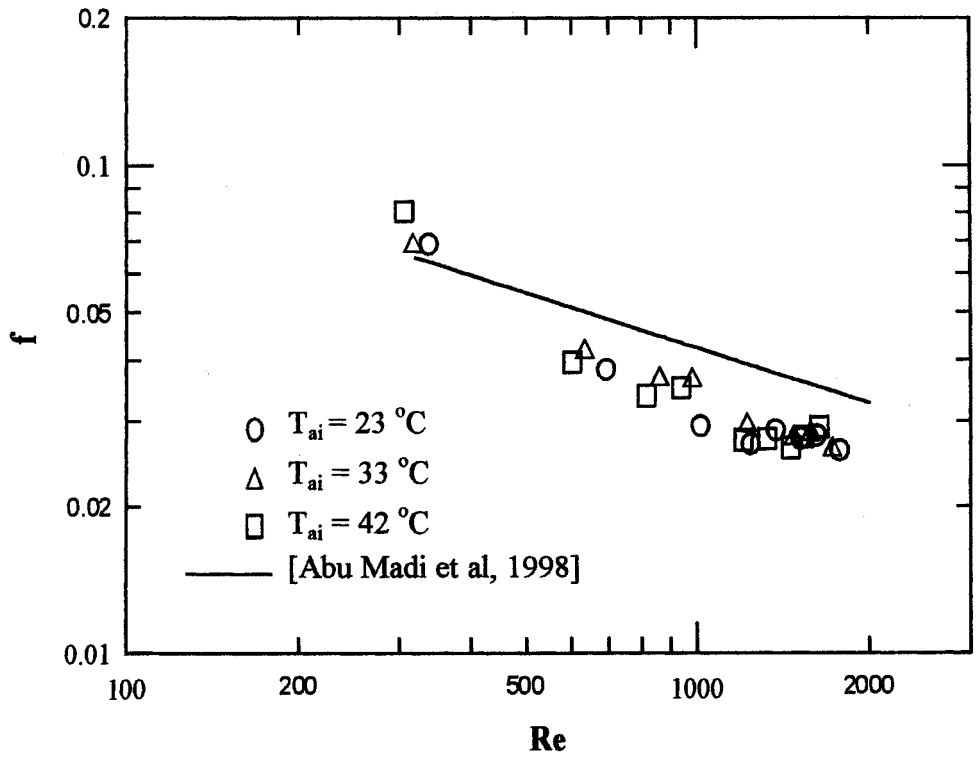

Fig. (5.24) Friction factor of the corrugated fin cooling coil

5.8.3 Turbulated fin

The Nusselt number and the friction factor of the turbulated fin cooling coil for the chilled water temperature T_{wi} = 10 °C are illustrated in Figs. (5.25) and (5.26) respectively. The rest of the turbulated fin results of T_{ai} = 23 °C, 33 °C, 42 °C and for T_{wi} = 5 °C, 15 °C are also given in appendix (B). The results of the turbulated fin case at the various boundary temperatures once again confirm boundary temperature independence by both Nusselt number and friction factor. The turbulated fin results of Nusselt number and friction factor are compared with the corresponding experimental results of Wang *et al* of slit-fin-and-tube heat exchanger, [Wang *et al*, 1999c]. Good agreement between the present and the published data of Wang *et al*. Details of the slit fin-and-tube heat exchanger tested by Wang *et al* (1999c) are given in Table (5.3).

5.8.4 Comparison between all fin types

In order to provide a reasonable guide for designing a more efficient heat exchanger, it is important to evaluate the performance of the corrugated and turbulated-fin cooling coil compared with the traditional flat-fin cooling coil. The heat transfer coefficient and the pressure drop of the flat, corrugated and turbulated fin cooling coils are illustrated in Figs. (5.27) and (5.28) respectively. The turbulated fin coil has the highest value of both heat transfer coefficient and pressure drop while the flat fin coil has the lowest values. The Nusselt number and friction factor versus Reynolds number are illustrated in Figs. (5.29) and (5.30) respectively. It also evident that the turbulated-fin coil has the highest values of both Nusselt number and friction factor and the corrugated-fin coil come next whereas the flat-fin coil has the lowest values.

In order to compare the relative performance of the two enhanced fin strategies against the basic flat fin case, it is helpful to resort to a metric that expresses heat transfer performance against friction loss performance whilst incorporating an economic indicator.

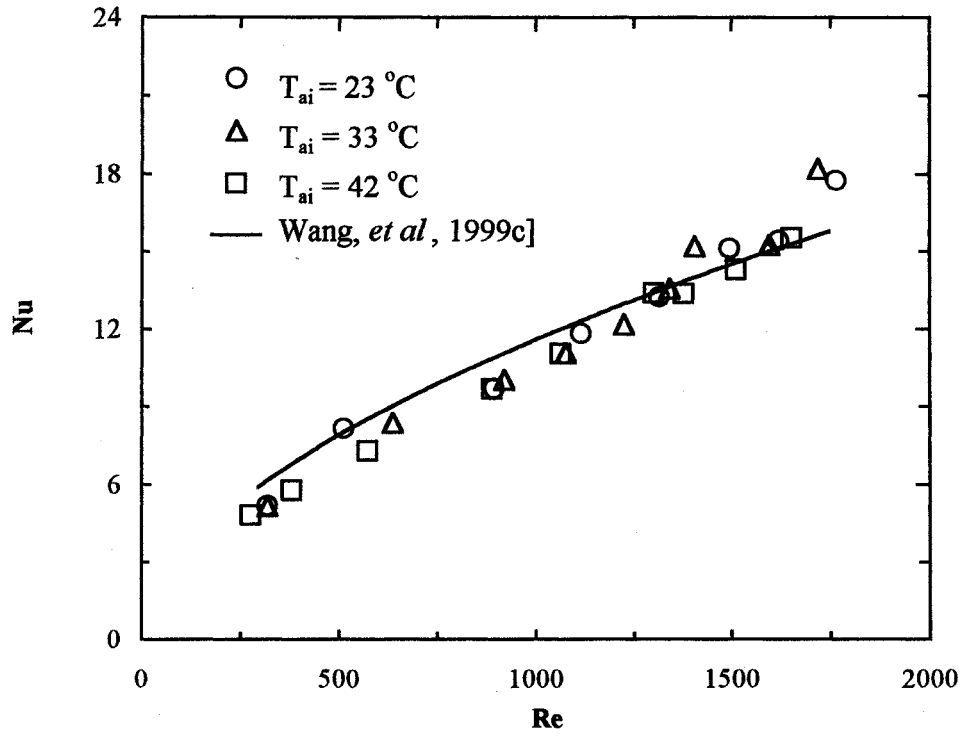

Fig. (5.25) Nusselt number of the turbulated fin coil for T_{wi} = 10 °C

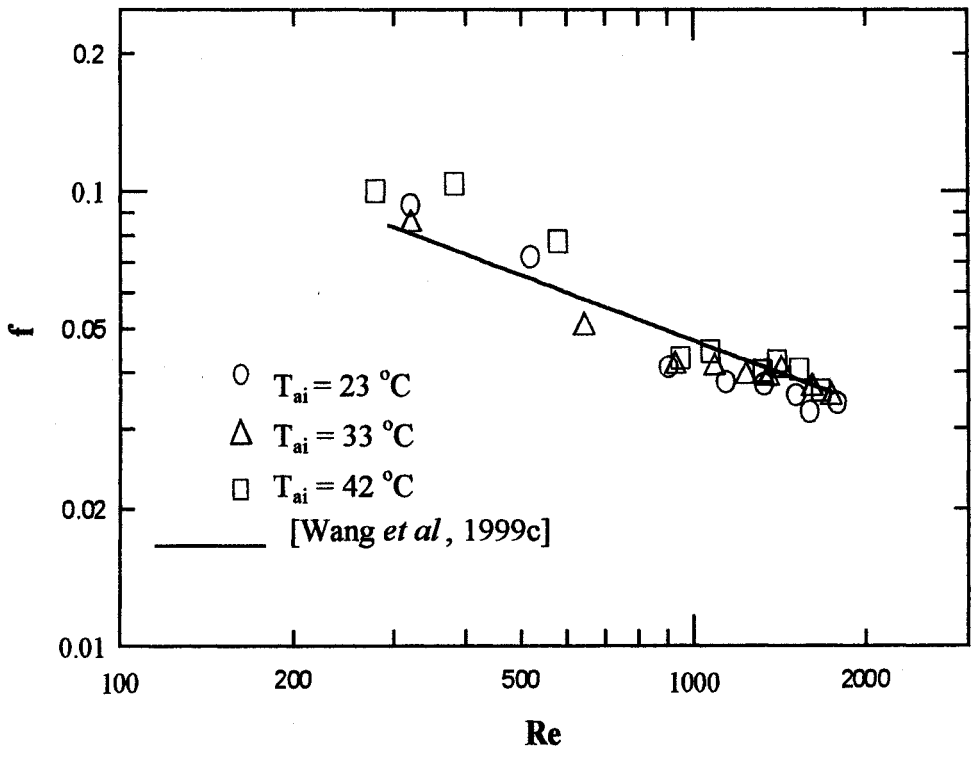

Fig. (5.26) Friction factor of the turbulated fin cooling coil

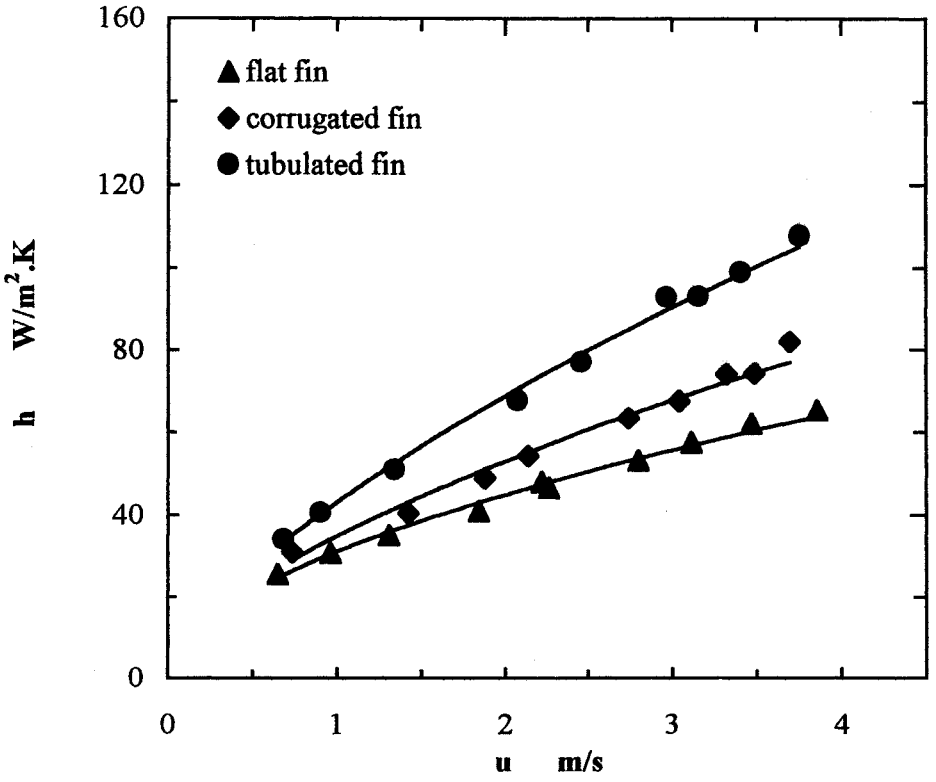

Fig. (5.27) Heat transfer coefficient for T_{ai} = 42, T_{ai} = 10 °C

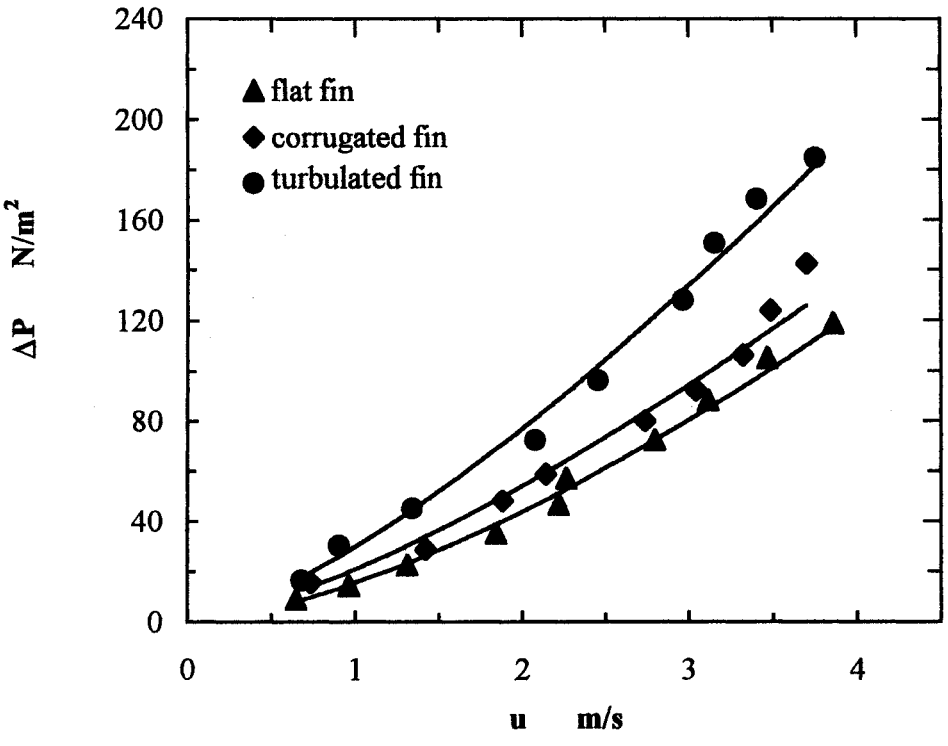

Fig. (5.28) Pressure drop for T_{ai} = 42, T_{wi} = 10 °C

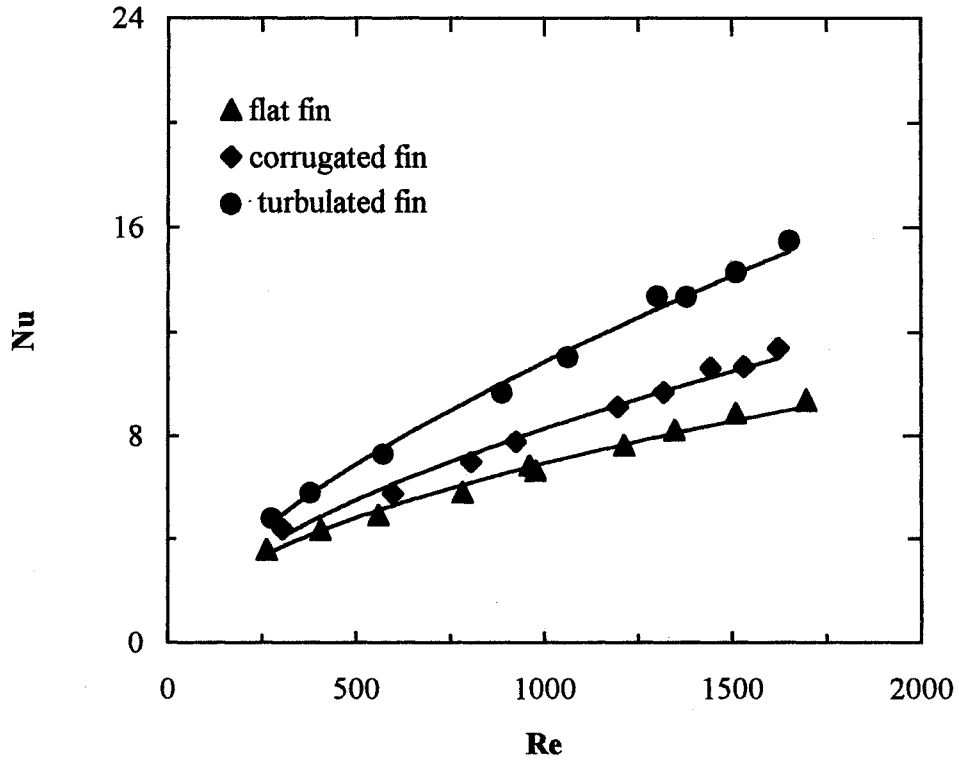

Fig. (5.29) Nusselt number for T_{ai} = 42, T_{wi} = 10 °C

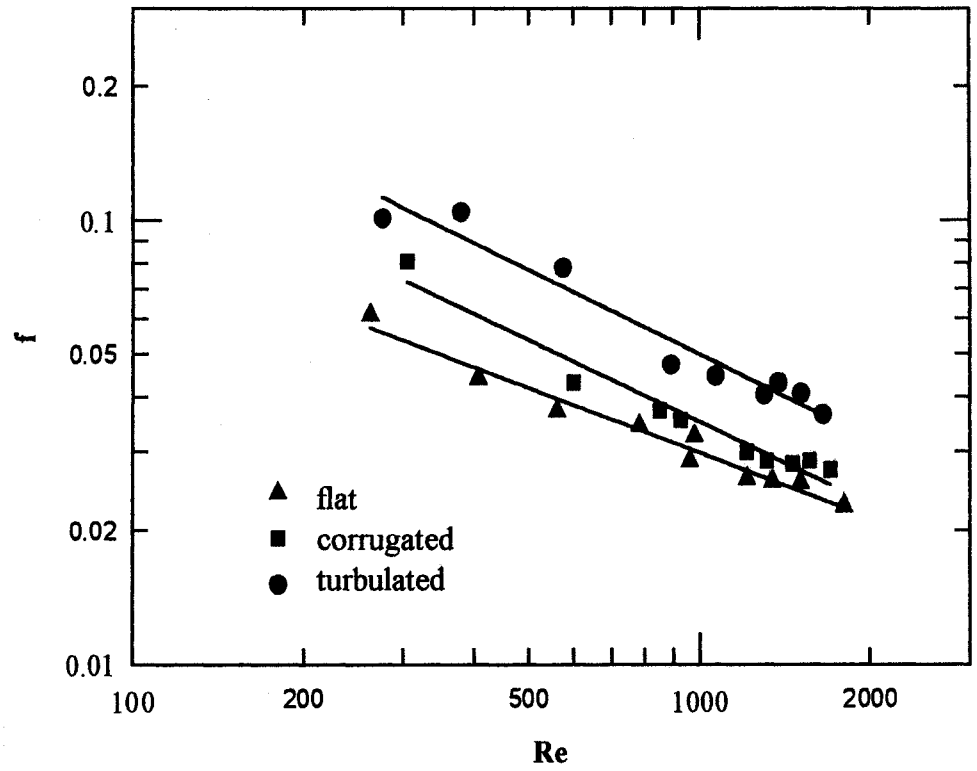

Fig. (5.30) Friction factor for T_{ai} = 42, T_{wi} = 10 °C

For this purpose, three methods are presented to quantify the effectiveness of these flow mechanisms throughout the corrugated and turbulated fin passages.

The first was a direct comparison of the heat transfer coefficient with pressure drop at the same inlet conditions. Fig. (5.31) shows the variation of the heat transfer coefficient versus pressure drop of the cooling coils. It is evident that, both the turbulated and the corrugated fin coils have the higher values of heat transfer coefficient compared with the flat fin coil at the same pressure drop. For a given value of pressure drop ΔP = 53 N/m^2 (corresponding to 2.3 ms^{-1}) the heat transfer coefficient of the turbulated fin was higher than that of flat fin by 21.5 % while the corrugated fin heat transfer coefficient was higher by 10.5 %.

The second method was the "volume goodness factor", which was suggested by Kays and London [Kays and London, 1984], and it given as ($h\alpha$) versus ($E_p\alpha$.) Where ($h\alpha$) represent the heat transfer rate per unit temperature difference per unite core volume, and the ($E_p\alpha$) represent the friction power expenditure per unit core volume. A higher value of $h\alpha$ characterises that surface was best from the viewpoint of heat exchanger volume required. Fig. (5.32) shows the variation of "$h\alpha$" versus "$E_p\alpha$" for the three types of the fin geometry. The turbulated fin geometry have the highest "$h\alpha$" values among the corrugated and flat fin geometries and the corrugated fin geometry come in second while the flat fin geometry have the lowest values. This indicates that the turbulated and the corrugated fin coils required core volumes less than that of flat fin coil for a given performance (heat transfer and friction).

The third method was the using the "VG-1" criteria of Webb [Webb, 1994], which measure the possible reduction of the surface area of the heat exchanger. This methodology compares the required total airside surface area for fixed values of the pumping power, heat duty, flow rate and temperature difference. Fig. (5.33) shows the variation of the airside surface area of the corrugated and turbulated fin relative to flat fin, (1-A_o/A_{oflat}), where the ratio A_o/A_{oflat} is defined as, [Webb, 1994]:

$$\frac{A_o}{A_{o,flat}} = \left(\frac{f}{f_{flat}}\right)^{1/2} \left(\frac{j_{flat}}{j}\right)^{3/2} \qquad (5.16)$$

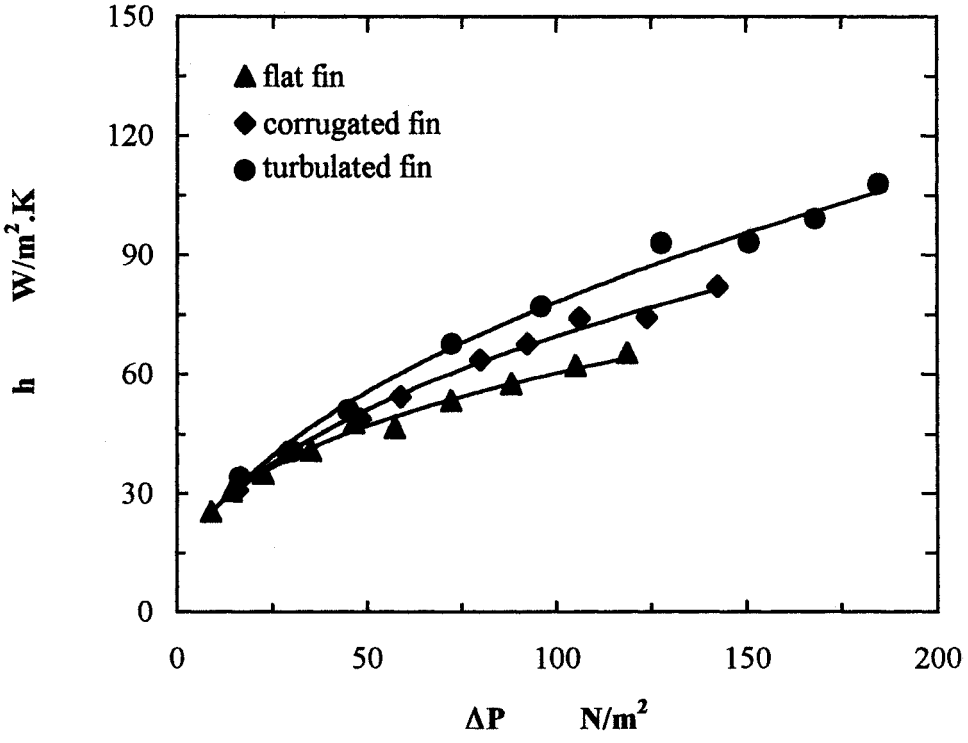

Fig. (5.31) Heat transfer coefficient vs pressure drop

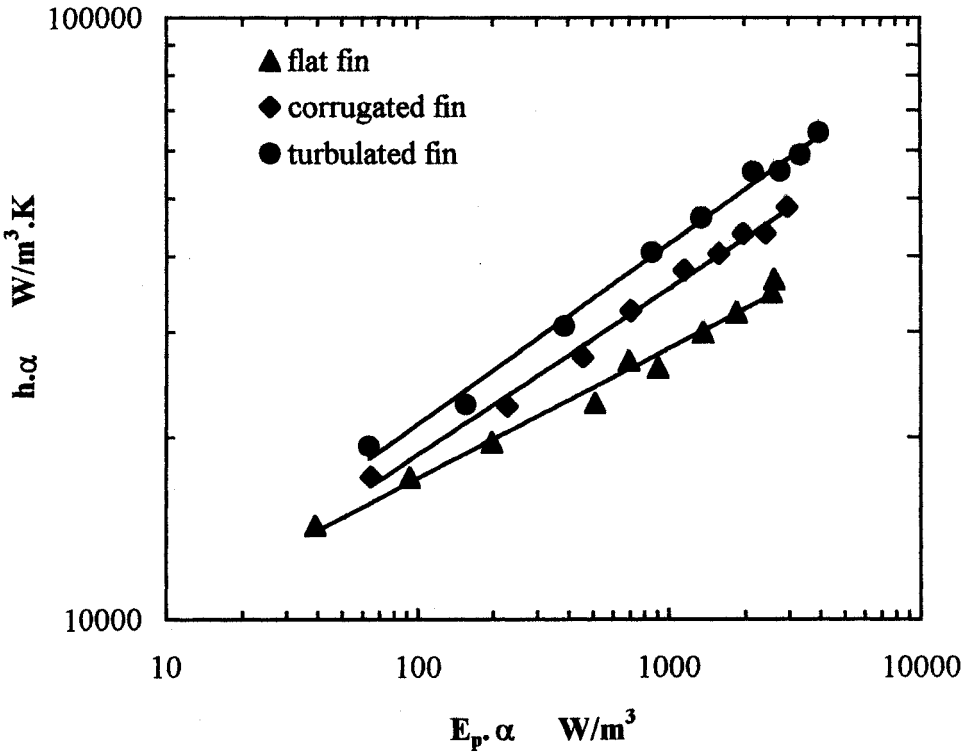

Fig. (5.32) Volume goodness factor comparison

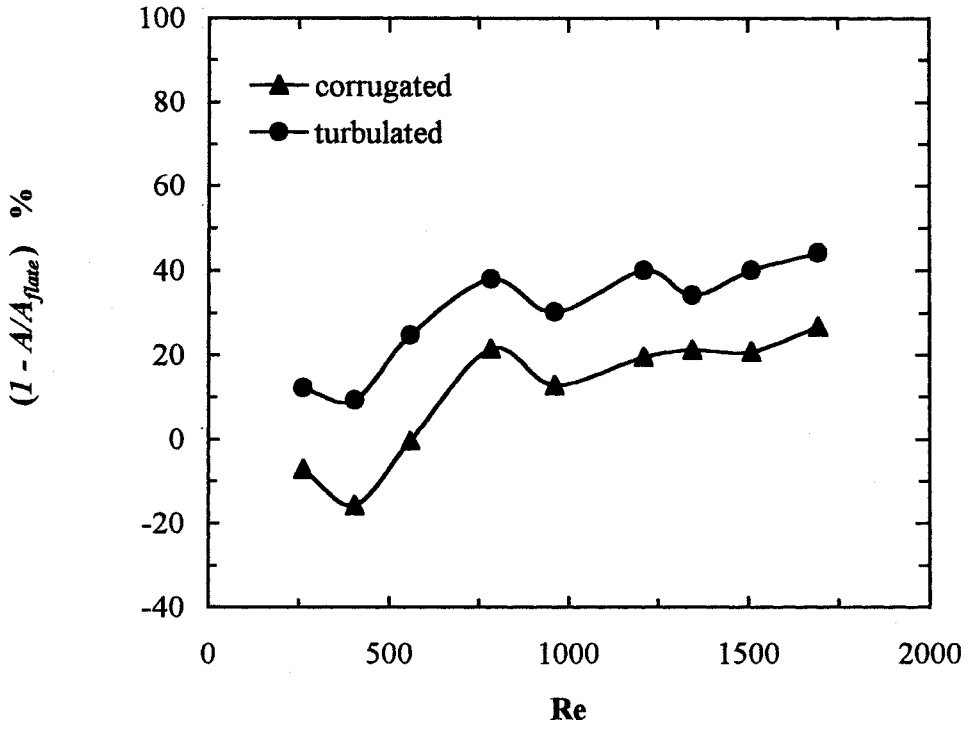

Fig. (4.33) Ratio of the surface area reduction relative to flat fin

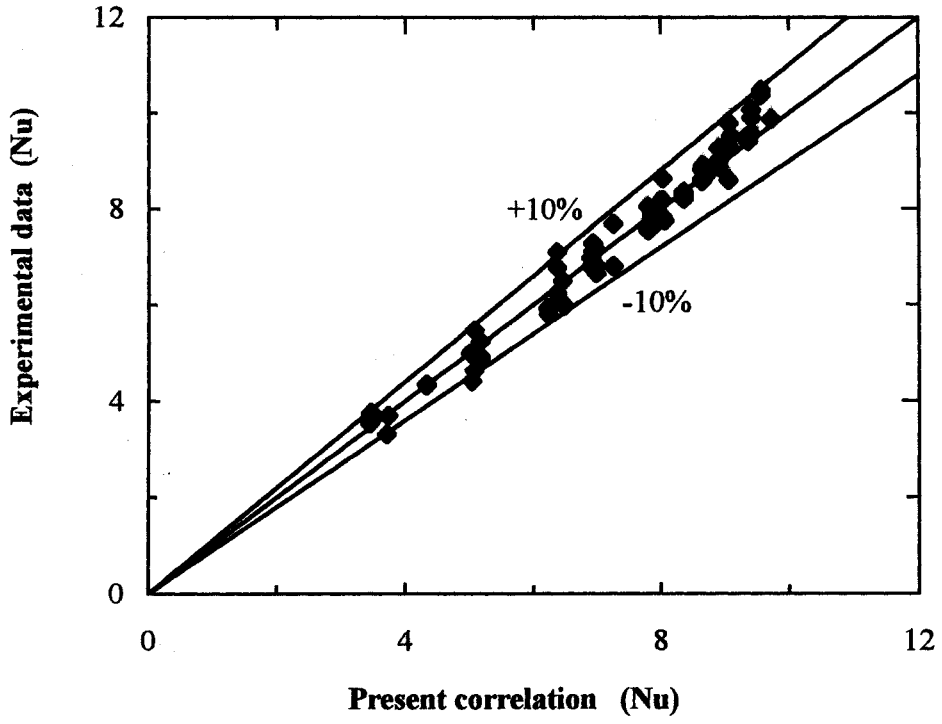

Fig. (5.34) Comparison between the present correlation and the experimental data of the flat fin

Based on Webb's criterion, at the nominal operating conditions for air-cooled heat exchanger (approximately $900 \leq \mathrm{Re} \leq 1200$; corresponding to $2 \text{ m/s} \leq u_{ai} \leq 2.5 \text{ m/s}$), the reductions in surface area were 16 % and 35 % for corrugated and turbulated-fin respectively.

The heat transfer and friction loss performance of all coil types may be correlated for $270 \leq \mathrm{Re} \leq 1850$, $23\ ^{\circ}\mathrm{C} \leq T_{ai} \leq 42\ ^{\circ}\mathrm{C}$, and $5\ ^{\circ}\mathrm{C} \leq T_{wi} \leq 15\ ^{\circ}\mathrm{C}$ with the indicated maximum deviations between the experimental and the correlated data as shown in Table (5.4), based on the following general expressions:

$$\mathrm{Nu} = A\mathrm{Re}^{a}\ \mathrm{Pr}^{b} \tag{5.17}$$

$$f = B\mathrm{Re}^{c}\ \mathrm{Pr}^{b} \tag{5.18}$$

Table (5.4): Summary of correlated heat transfer and friction loss results

Fin type	*A*	*B*	*a*	*b*	*c*	Deviation (%)
Flat	0.189	1.194	0.541	0.333	-0.520	±10 See Fig. (5.34)
Corrugated	0.178	2.090	0.571	0.333	-0.580	±12
Turbulated	0.100	3.330	0.707	0.333	-0.601	±14

5.9 Discussion

Experiments were conducted on the three types of finned-tube cooling coils having the same configuration except fin geometry. Twenty-seven tests were run on the cooling coils including various fin geometries, various inlet air temperatures and various inlet chilled water temperatures. Generally, the rate of the heat exchange throughout the cooling coil depends mainly on the temperature

difference between the chilled water and the air, the design of flow-path of both fluid streams, and the Reynolds number of both air and water streams.

The change in the air properties due to the change in the bulk air temperature from 25 °C to 42 °C is relatively small, which may be explained the independence of Nusselt number and the friction to the inlet air temperature. In the case of chilled water, the change in the water properties due to the change in the bulk temperature of the fluid from 8 °C to 18 °C is more significant than in air. However, as the fluid temperature increases, the properties of density, viscosity and Prandtl number decrease while the thermal conductivity and specific heat increase which led to close equilibrium in the heat transfer coefficient.

The turbulated-fin coil has the highest values of both Nusselt number and friction factor and the corrugated-fin coil come next whereas the flat-fin coil has the lowest values. At a nominal air velocity of 2 m/s (Re = 930), the Nusselt number and the friction factor of the turbulated fin coil was higher than that of the flat fin coil by 57 % and 60 % respectively. While the corrugated fin coil was higher by 19 % and 16.4 % respectively. It is evident that the use of corrugated and turbulated fins enhance the heat transfer coefficient that led to enhancement of cooling capacity of the air conditioning unit at the expense of increased of pressure drop and hence fan power.

The pressure drop of the corrugated fin coil is higher than that of the flat fin coil due to the increase of flow resistance produced by the fluid flows along an undulating path of peaks and valleys of the corrugated fin. The turbulated fin coil has the highest values of the pressure drop among the flat and the corrugated fin coils due to increase of the flow resistance increase produced by interrupted fin surfaces and the increase of the drag caused by the leading and trailing edges of the slits.

To compare the relative performance of the two enhanced fin strategies against the basic flat fin case, it is helpful to resort to a metric that expresses heat transfer performance against friction loss performance whilst incorporating an economic indicator. For the same inlet velocity and pressure drop the turbulated fin has the higher values of the heat transfer coefficient and the flat fin coil has the lower values.

Based on Webb's criterion, the corrugated-fin coil results in a net reduction in heat exchange surface area at Re > 500 whereas the turbulated-fin case might always be expected to lead to a reduction in heat exchange surface area compared to the flat-fin case. Both turbulated-fin and corrugated-fin coils offer peak reductions in surface area over the flat-fin case at approximately Re = 750. At the nominal operating conditions ($900 \leq Re \leq 1200$ corresponding to 2 m/s $\leq u_{ai} \leq$ 2.5 m/s) the reductions in surface area are 16 % and 35 % for corrugated and turbulated-fin respectively. The air conditioning fin-and-tube coils employing these high performance fins (corrugated and turbulated) contribute a significant to the volume reduction and energy conservation of the air conditioning plant.

The percentage uncertainty in the measuring instruments increases with lower readings of velocity and temperature. These may be explained the highest uncertainties in the Nusselt number and friction factor were associated with low values of Reynolds number and inlet air temperature (see appendix (C)).

5.10 Conclusions

In this chapter the experimental analysis of the dry fin-and-tube cooling coils with particular reference of a hot arid climate of Cairo is investigated. The effect of various fin geometries, inlet-air condition and inlet-chilled water temperature on the heat transfer and friction characteristics is explored. The error analyses of measurements and the evaluation criteria of comparison of the various cooling coils are presented. Correlations of the Nusselt number and friction factor of various fin geometries and for the rang of 0.6 m/s $\leq u_{ai} \leq$ 3.8 m/s, 23 °C $\leq T_{ai} \leq$ 42 °C, and 5 °C $\leq T_{wi} \leq$ 15 °C are also addressed. The main conclusions were:

- The Nusselt number and the friction factor were found to be practically independent of both inlet air and chilled-water temperatures.

- Corrugated and turbulated fin coils were found to enhance the heat transfer coefficient, leading to an improvement in cooling capacity at the expense of an increase of pressure drop and hence fan power.
- At a nominal face velocity of 2 m/s the Nusselt number and the friction factor of the turbulated fin coil was higher than that of the flat fin coil by 57 % and 60 % respectively. While the corrugated fin coil was higher by 19 % and 16.4 % respectively
- For the same values of both inlet velocity and pressure drop the turbulated fin coil has the highest value of heat transfer coefficient and the corrugated fin come next while the flat fin coil has the lowest value.
- At a typical operating conditions (2 m/s $\leq u_{ai} \leq$ 2.5 m/s) and for the same fan power and heat transfer, the corrugated and turbulated-fin coils required fin surface area of 16 % and 35 % less than that of flat fin respectively.
- The mean uncertainties in the Nusselt number and friction factor were ascertained to be ± 13 % and ± 10 % respectively while the higher uncertainties were associated with lower values of Reynolds number and inlet air temperature.
- The cooling coils employing the corrugated and turbulated fin geometry contribute a significant to the volume reduction and energy conservation of the air conditioning plant.
- Further investigations are needed to expand the performance data to cover variations in specific coil geometry including fin spacing; fin sheet thickness; and fin material. Evidence from experimental work also suggests that manufacturing flaws consisting of edge burrs of the turbulated-fin case should be considered. Ongoing chapters using computational fluid dynamics modelling is currently addressing these issues.

CHAPTER -VI-

Three-dimensional CFD modelling of fin-and-tube cooling coils

6.1 Introduction

In this chapter, the three-dimensional CFD modelling of fin-and-tube air-conditioning cooling coils is investigated based on a set of practical coils manufactured by Thermal Transfer Technology (3T) LTD. CFD is used to develop and solve a mathematical model of the three dimensional fluid flow and heat transfer characteristics through the complex geometries of the fin-and-tube cooling coils having flat, corrugated and turbulated fin geometries (see Figs (5.5)-(5.7)). The computational domain is illustrated in Fig. (6.1). The calculations were carried out for sensible heat transfer phenomena at an inlet air temperature T_{ai} = 310 K (as an outdoor design temperature of Cairo). The Reynolds number was varied in the range 285 to 1880 corresponding to air inlet velocity of 0.6 m/s to 4 m/s, which covers the range of most air conditioning applications.

6.2 Mesh strategy

The mesh structure, size and the shape of the individual mesh cells have a considerable influence on the accuracy of the solution and stability of the solution algorithm. The smaller the cell size the smaller the discretization error, but this will be at a cost of higher computational effort [Drakulic, 1997]. The grid density and its distribution can have significant effects on the resulting solution accuracy. It is useful to perform grid-dependence studies and comparisons with experimental data to determine appropriate grid generation metrics and to

establish a level of confidence in the solution. The strategy for three-dimensional numerical meshing for the fin-and-tube cooling coils should satisfy the following;

1. Good distribution of the mesh structure along the computational domain to give maximum numerical accuracy.
2. Minim the CPU time where possible.

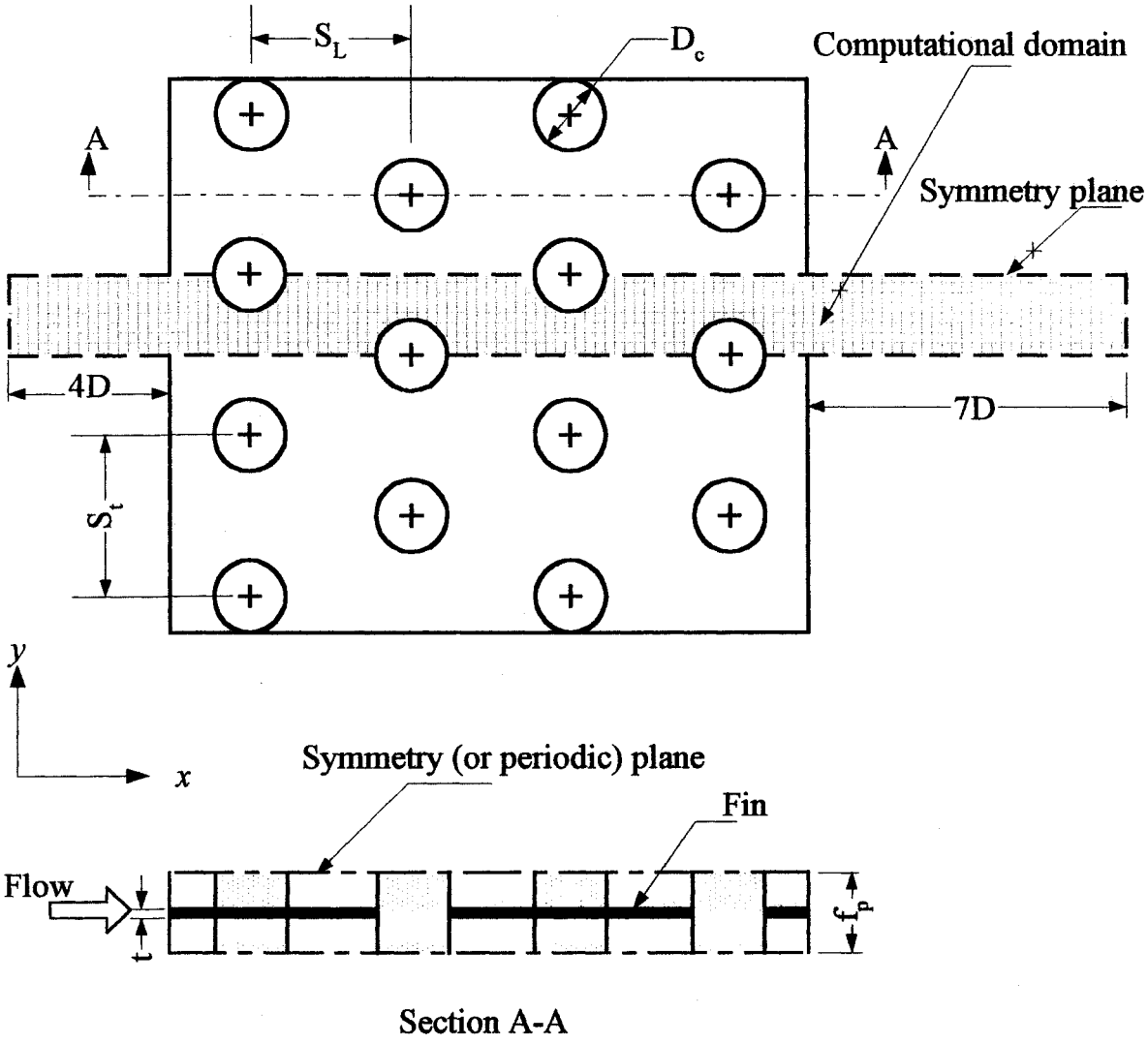

Fig. (6.1) Schematic diagram of the computational domain

To verify these objectives, a pre-processor and mesh generation code GAMBIT 1.3 was used for the following;

- Creation of computational domains for the three coil types
- Mesh generation
- Specification of the boundary condition types.

A three-dimensional multi-block structured grid technique was used in all computational domains. The purpose for using structured grids was to minimize numerical diffusion and to get accurate results, [Fluent user's guide, 1999]. The computational domains were divided into smaller identical modules (blocks) of a logical cube in order to meet a structured grid criterion. The modules were merged together to form two united volumes; fluid (air) volume and solid (fin) volume. A Laplacian smoothing operator was applied to the unstructured grid to reposition nodes. The new node position is the average of the positions of its nodal neighbours. After some initial refinements to the mesh strategies starting from the grid system proposed by Jang *et al* [Jang *et al*, 1996 and 1997], the following were adopted:

- **Flat fin** – The computational domain of the flat fin case was divided into logical cubes, an example of which block is shown in Fig. (6.2). The number of elements of the logical cube edges were, $a_1 = 5$, $a_2 = 1$, $a_3 = 35$, and $a_4 = 40$ with a space ratio equal to one. The element aspect ratio was 1.5 and the total grid system was 520 x 35 x 11 (246020 nodes), which was approximately double the grid system of Jang *et al*. The full computational domain of the flat fin geometry is illustrated in Fig. (6.3)

  Corrugated fin - The three-dimensional multi-block structured grid of the corrugated fin model was more difficult to establish than that of the flat fin model due to the waviness in the flow path. The computational domain was divided into logical cube, for example as shown in Fig. (6.4). The number of elements of the logical cubes edges were, $a_1 = 5$, $a_2 = 1$, $a_3 = 33$, and $a_4 = 19$ with space ratio equal to one. The element aspect ratio was 1.2 and the total grid system was 564 x 33 x 11 (250040 nodes). The full computational domain is illustrated in Fig. (6.5).

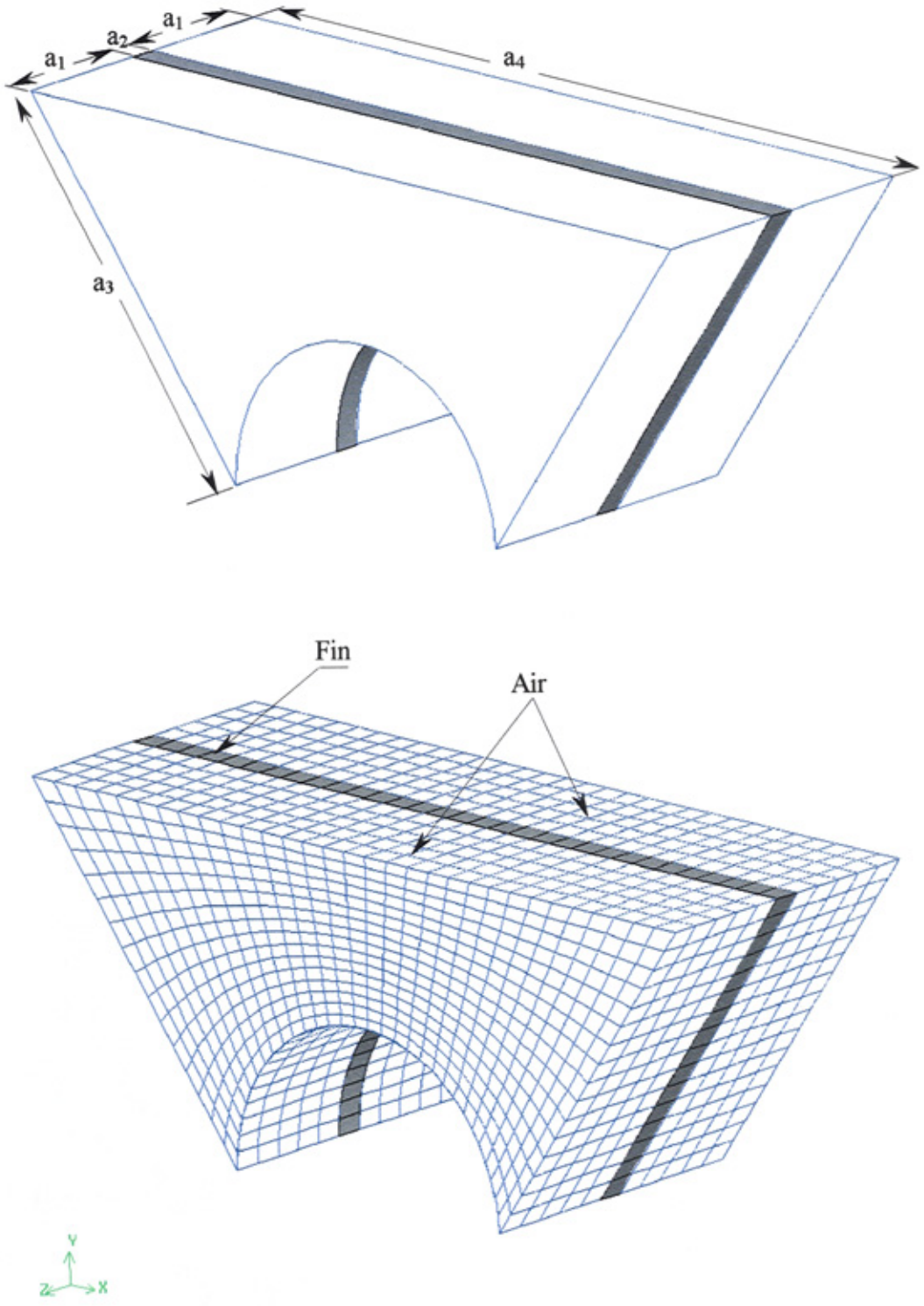

Fig. (6.2) Example of brick-mesh distribution (flat fin)

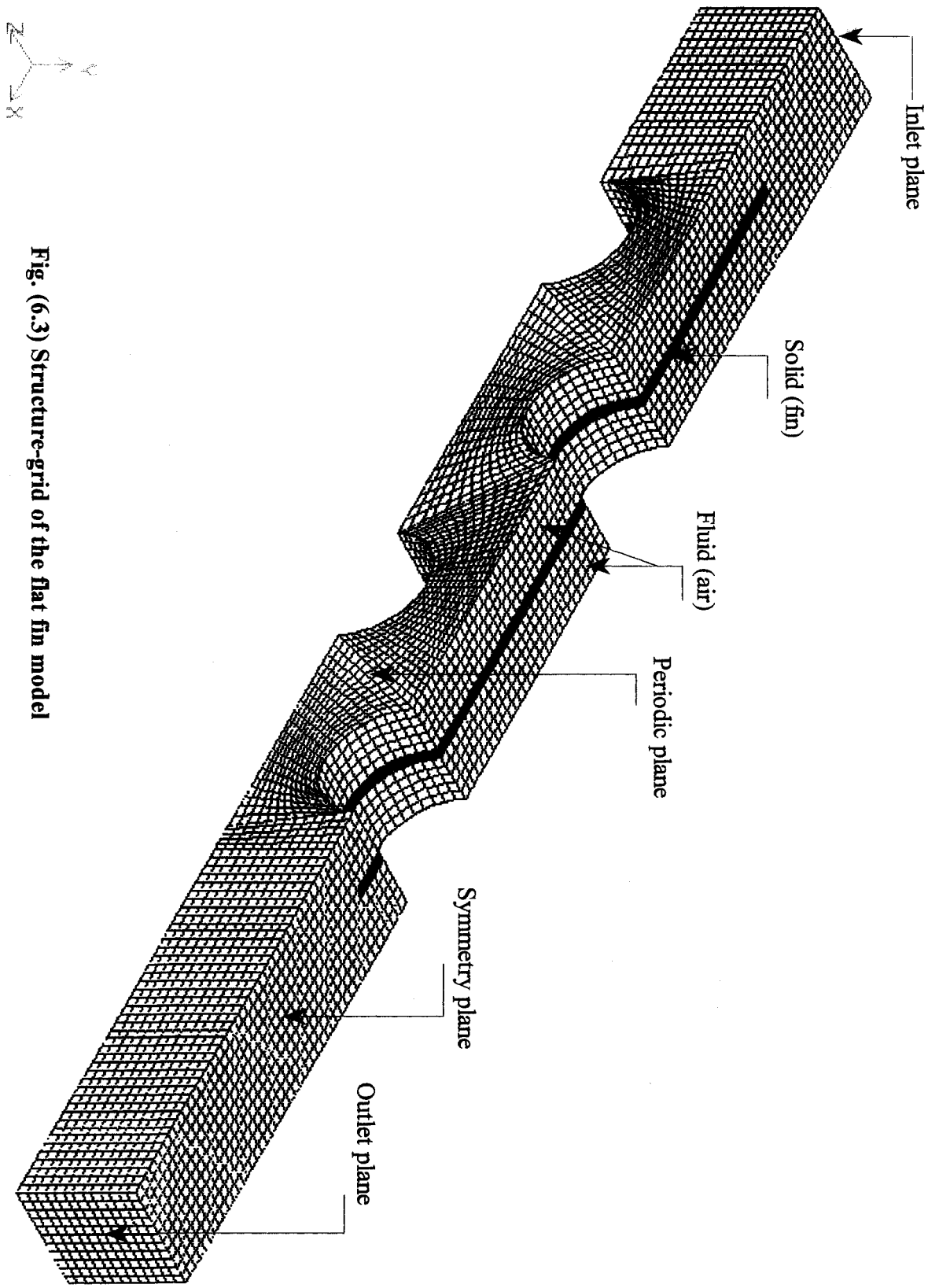

Fig. (6.3) Structure-grid of the flat fin model

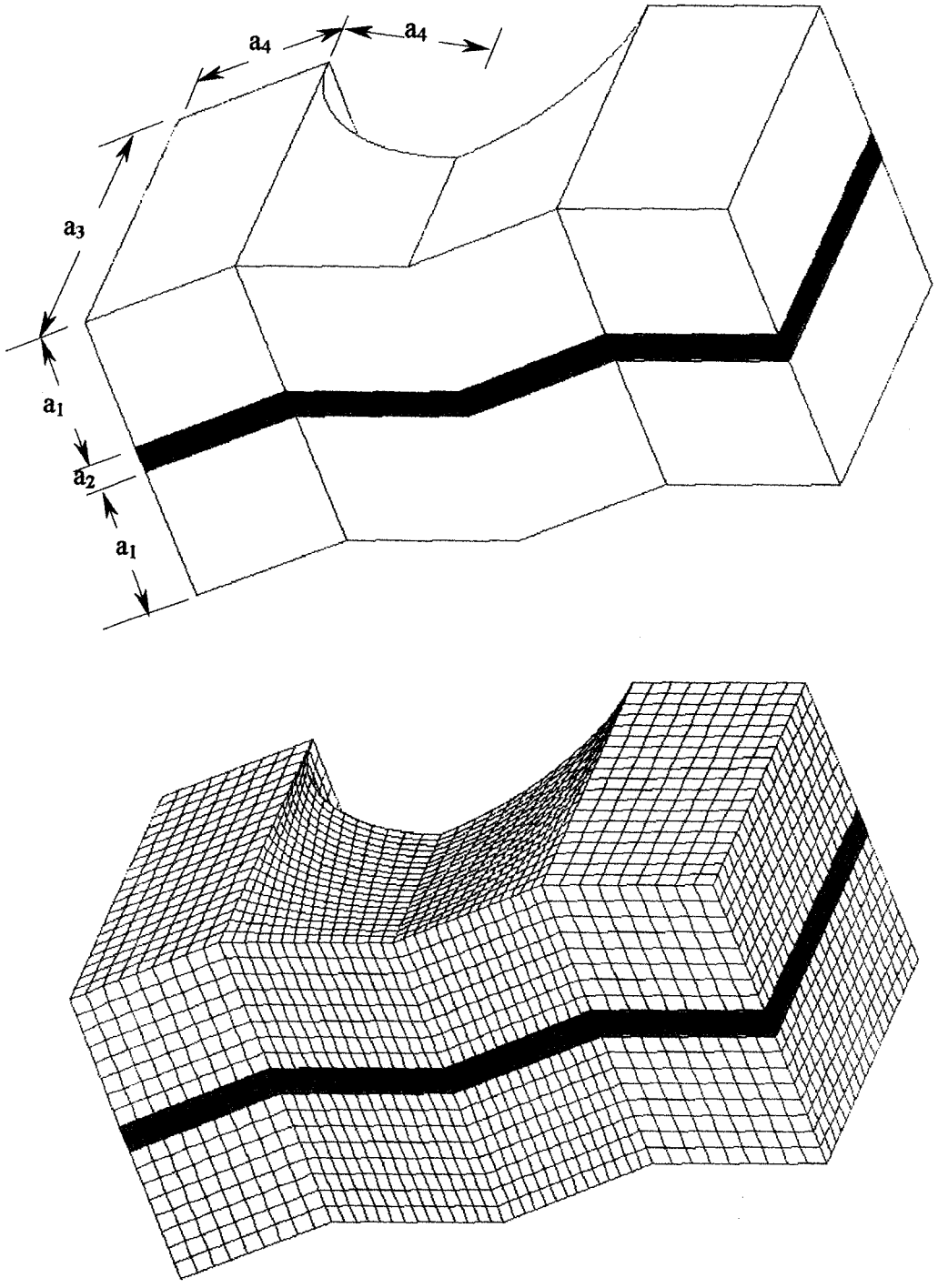

Fig. (6.4) Example of brick-mesh distribution (corrugated fin)

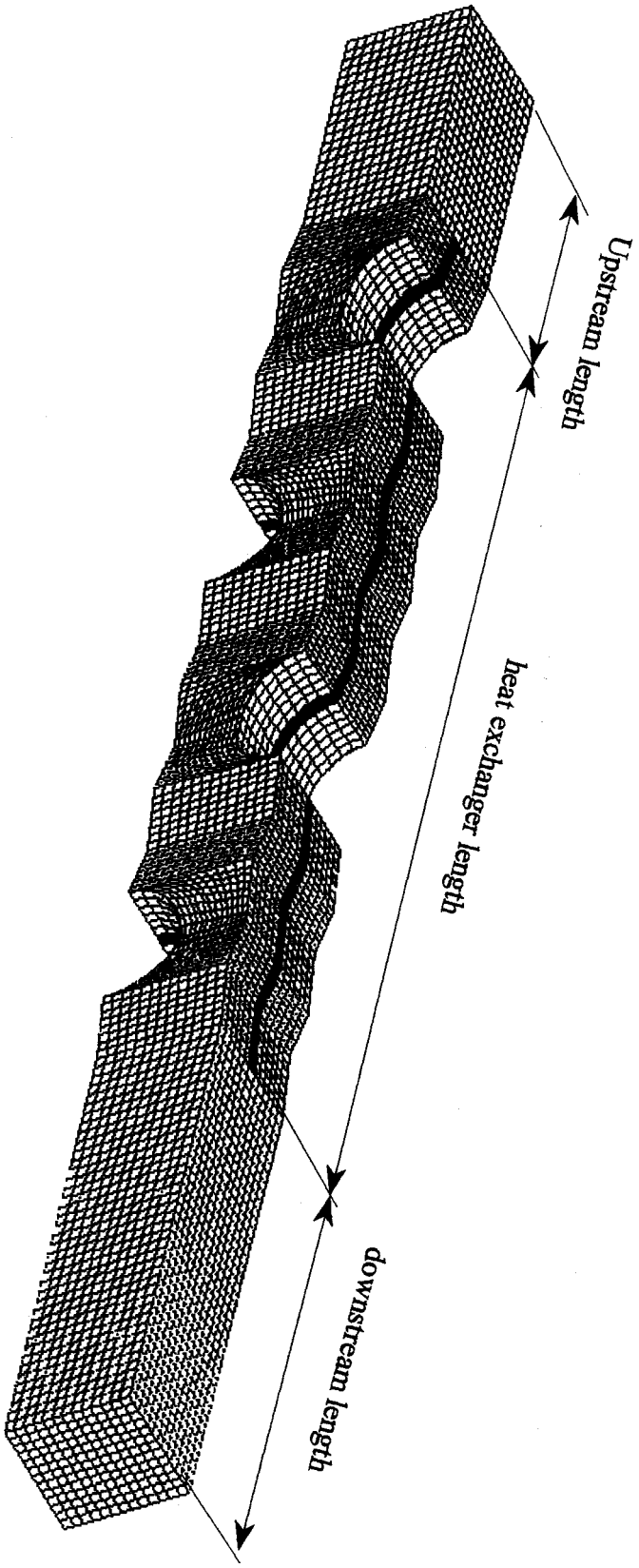

Fig. (6.5) Structure-grid of the corrugated fin model

- **Turbulated fin** - The multi-block structured grid of this case was more difficult than the previous two models due to interrupted-fin surfaces, where the fin face lies on the *x-y-z* planes as illustrated in Fig. (6.6). The computational domain was divided into logical cubes, an example of which is shown in Fig. (6.7) for the fin sheet and Fig. (6.8) for the overall block structure using computational blocks. The number of elements of the logical cubes edges were, $a_1 = 11$, $a_2 = 5$, $a_3 = 30$, $a_4 = 10$, $a_5 = 4$, $a_6 = 3$, $a_7 = 1$, and $a_8 = 7$ with space ratio equal one. The element aspect ratio was 1.5 and the total grid system was 548 x 30 x 11 (258000 nodes). The full computational domain of the turbulated fin case is illustrated in Fig. (6.9).

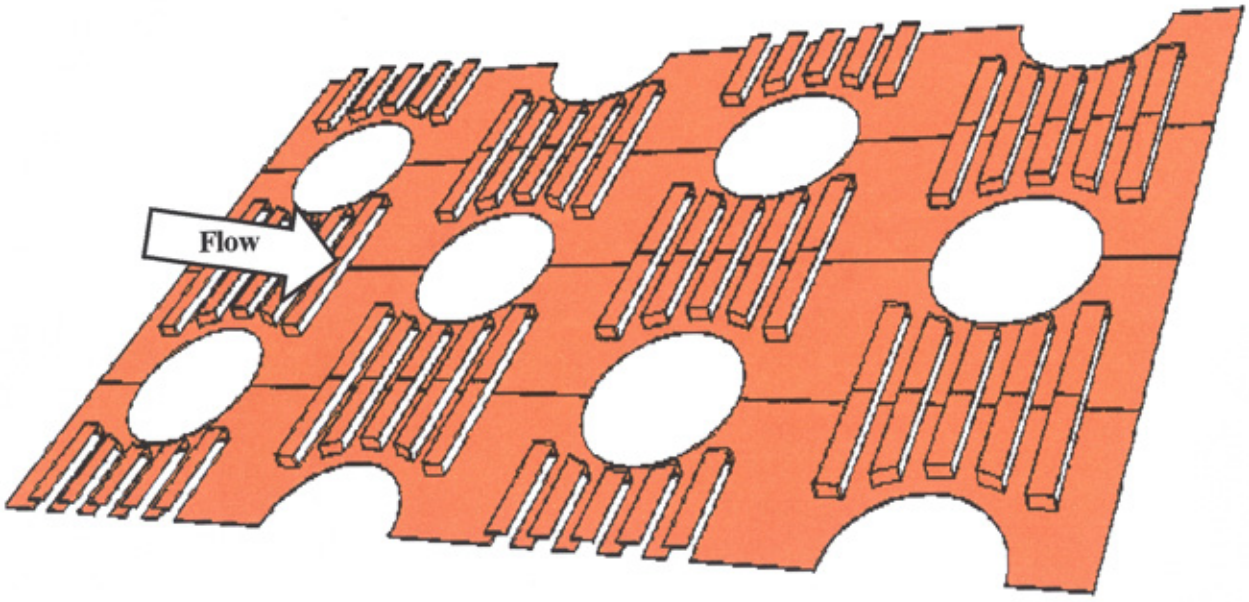

Fig. (6.6) Turbulated fin sheet geometry

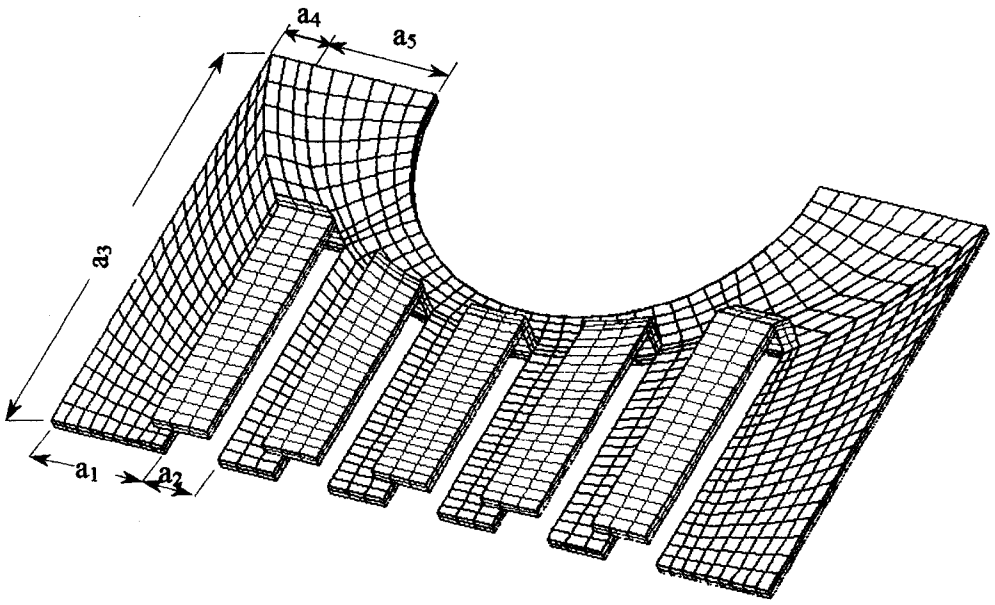

Fig. (6.7) Example of brick-mesh of turbulated fin sheet

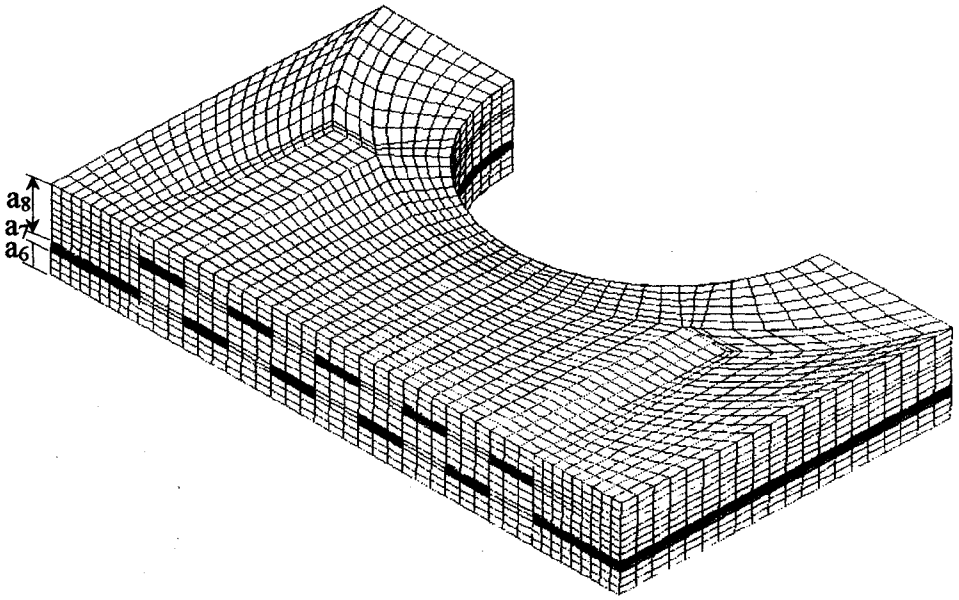

Fig. (6.8) Example of brick-mesh distribution (turbulated fin)

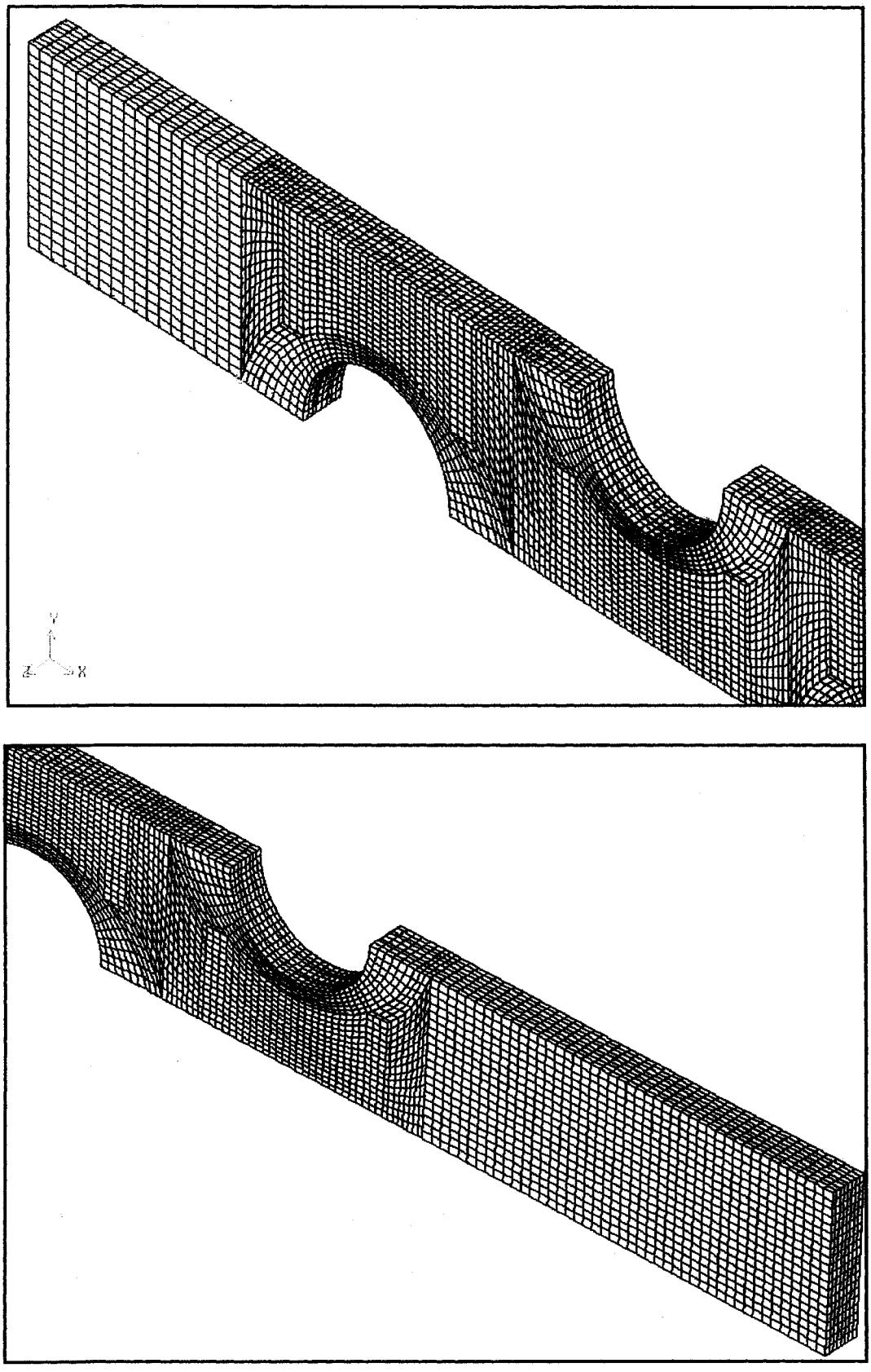

Fig. (6.9) Overall computational domain of the turbulated fin geometry

6.3 Boundary conditions

Since the governing equations are elliptic in spatial coordinates, boundary conditions are required for all boundaries of the computation domain. The computational domain extends further than the heat exchanger length in both upstream and downstream directions in order to reduce numerical oscillations [Mendez, 2000]. The dashed lines in Fig. (6.1) designate the computational domain used. Symmetrical planes are taken to lie along the centres of two consecutive sets of tubes and at the mid-point between two adjacent fin spaces. More details of the boundary conditions applied to the computational domains of the three coil types are as follows;

- **Inlet** - At the inlet boundary, located at four times the tube diameter from the fin tip, uniform flow velocity and temperature were specified assuming v_{ai} = w_{ai} = zero, (in the experimental work, the section of measuring velocity was far from the cooling coil by approximately forty times the tube diameter, for economical grid system this distance was reduced by ratio of tenth).

- **Outlet** - At the downstream end of the computational domain, located seven-times tube diameter from the fin trailing edge, pressure is set to zero. For a good accuracy the downstream length should be greater than ten-times of tube radius, [Versteeg and Malalasesekera, 1995]

- **Symmetrical planes** – A symmetrical plane boundary condition is used to reduce the size of the computational domain by placing a boundary along a plane of geometrical and flow symmetry. The normal velocity components and the normal gradients of all variables are set to zero.

- **Walls** - At the wall boundaries (fin and tube walls), no-slip conditions were specified ($u = v = w = 0$) and temperatures was initially assumed to be constant.

6.4 Computational details

A finite volume discretization method using body-fitted coordinates and a SIMPLE-based solution algorithm of the velocity-pressure coupling were used with a segregated solver [Sheu and Tdai, 1998]. The SIMPLE algorithm was found to give the shortest computer running time [Atkinson, *et al* 1998]. The momentum and energy equations were solved by the first order upwind scheme. The numerical solution was performed using the pre-processor GAMBIT 1.3 and the CFD code FLUENT 5.4. The computations were carried out using Windows NT computers of Pentium-II- 350 MHz processors. The values of the convergence criteria were less than 10^{-4} for continuity and velocity residuals and less than 10^{-6} for temperature. An example of the convergence criterion approach is illustrated in Fig. (6.10). The accuracy and validity of the numerical results were checked in by two ways. The first was to compare the CFD predicted results against experimental results (which come later). The second was a grid dependence test. Three grid systems were tested for each type of cooling coils (at Re = 710 corresponding to u_{ai} = 1.55 m/s) with a coarse grid, a medium grid and a fine grid. The details of the grid dependence test of the flat, corrugated and turbulated fin models are summarised in Tables (6.1), (6.2) and (6.3) respectively. For all fin types, the medium grids were chosen to maintain relatively high accuracy at relatively moderate CPU time.

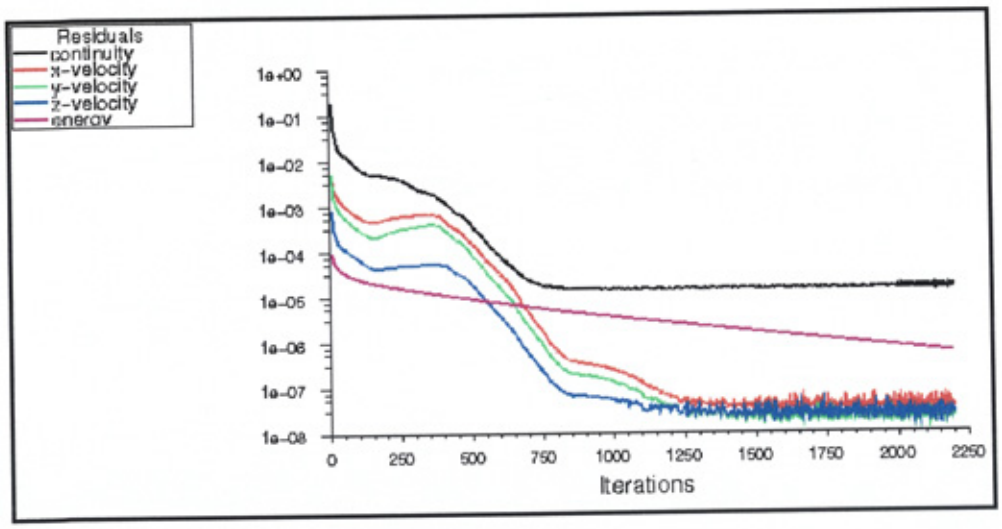

Fig. (6.10) Convergence criteria approach (u_{ai} = 3 m/s-turbulated fin)

Table (6.1) Flat fin grid dependent check

Items	Coarse grid	Medium grid	Fine grid
Grid system	420 x 30 x 9 (147216 nods)	520 x 35 x 11 (246020 nodes)	490 x 40 x 13 (313116 nods)
Nu/Nu_{medium}	5.6 %	-	-2.9 %
f/f_{medium}	5.9 %	-	-3.2 %
CPU time	-	24 hours	-
CPU time/medium grid	50 %	-	140 %
Number of iterations	1800	1800	1800

Table (6.2) Corrugated fin grid dependent check

Items	Coarse grid	Medium grid	Fine grid
Grid system	506 x 28 x 11 (190314 nods)	564 x 33 x 11 (250040 nodes)	622 x 38 x 11 (317686 nods)
Nu/Nu_{medium}	9 %	-	- 4 %
f/f_{medium}	0.5 %	-	-1 %
CPU time	-	26 hours	-
CPU time/medium grid	70 %	-	170 %
Number of iterations	2000	2000	2000

Table (6.3) Turbulated fin grid dependent check

Items	Coarse grid	Medium grid	Fine grid
Grid system	482 x 25 x 11 (209736 nods)	548 x 30 x 11 (258000 nodes)	594 x 35 x 11 (306260 nods)
Nu/Nu_{medium}	7.5 %	-	-5 %
f/f_{medium}	1 %	-	-3.5 %
CPU time	-	30 hours	-
CPU time/medium grid	82 %	-	220 %
Number of iterations	2200	2200	2200

6.5 CFD models and refinements

In the first phase of the work, the three fin cases were expressed initially as isothermal model (the fin and tube are considered at the same temperature) with symmetrical boundaries [Jang *et al*, 1996 & 1997]. Subsequently, four approaches of CFD refinements were then developed as follows:

1. Conjugate heat transfer.
2. Periodic boundaries.
3. Tube-rows temperature gradients.
4. Modelling the turbulated fin-edge burrs.

Further details on model refinements are given:

6.5.1 Conjugate heat transfer model

Conjugate heat transfer problems have been received increasing attention in the modelling of the fin-and-tube heat exchangers involving conduction-convection coupling since in the majority of cases, the assumption of isothermal conditions through the fins is unrealistic. In this part of the work, the assumption of constant fin-and-tube wall temperature was relaxed and conduction through the fin-and-tube was coupled with convection in the adjacent fluid region. The three-dimensional conjugate heat transfer model was developed for the flat, corrugated and turbulated fin cooling coils with particular reference to the developing region. The temperature was specified on the tube-wall only and the conduction heat transfer problem between the fin and tube is solved numerically by solving the three-dimensional conduction equation (3.8). The thermal resistance of the fin material leads to variable temperature profiles in the interior. The conjugate heat transfer solutions accounts for parallel heat flow paths of conduction-convection coupling between the air and the finned tube (Fig. (6.11)). The fin materials were aluminium with $\rho = 2719$ kg/m^3, $Cp = 871$ J/kg.K, and $k = 202.4$ W/m.K.

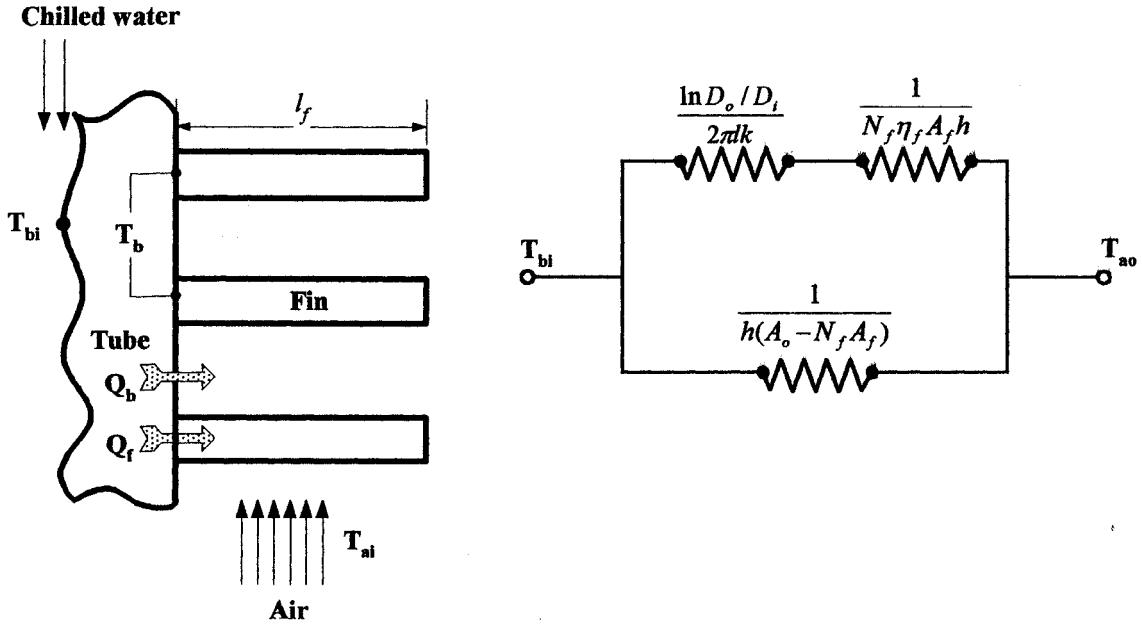

Fig. (6.11) Fin array and thermal circuit

6.5.2 Periodic boundaries model

In general, periodic flow occurs when the physical geometry of interest and the expected pattern of the flow solution have a periodically repeating nature. In the case of fin-and-tube heat exchangers, two types of periodic flow occur. The first is when the axial length of the cooling coil is long enough (i.e. containing a number of the tube rows greater than seven [Launder and Massey, 1978]) such that flow-pattern is repeatable in a periodic manner. The second case is where the geometry of the fin surface varies in a repeating manner (fin array) perpendicular to the flow direction as illustrated in Fig. (6.12) which is considered here. Periodic boundaries are used when the flows across two opposite planes in the computational domain are identical while the symmetrical boundaries are used when the physical geometry of interest, and the expected pattern of the flow solution, has mirror symmetry. The assumption of symmetrical boundaries mean that all the normal components and gradients are zero, which is unlikely in the case of corrugated and turbulated flow-passages. A comparison was therefore

made between periodic conditions with those symmetrical conditions. In order to apply periodic boundaries, a mesh hard link between the identical pair of faces to which the boundary condition is created, in addition it should assign a periodic boundaries type to both faces, [Gambit modelling guide 1999].

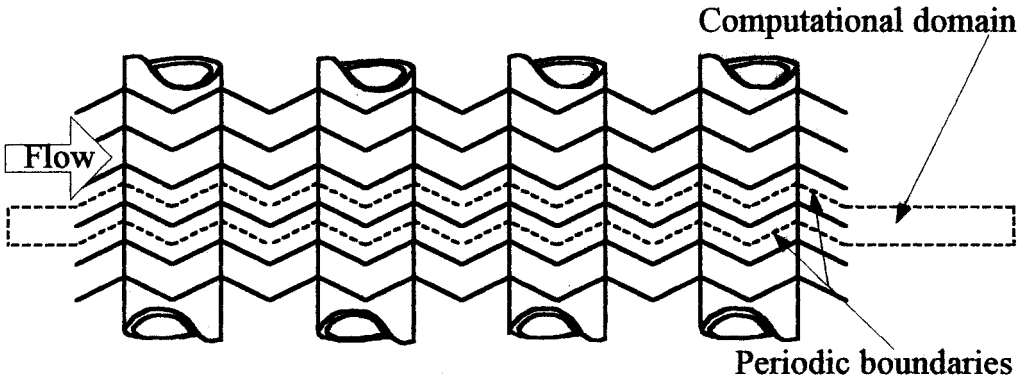

Fig. (6.12) Periodic boundaries illustration

6.5.3 Tube-row temperature gradient (TRTG) model

In practice, the temperature not only varies along the fin surface (conjugate model) but also varies through the tube wall-thickness, tube length and also gradually from row to row (indirect expansion refrigeration plant cases). Since the computational domain tube-length to the real coil tube-length was less than 0.5 %, the temperature variation through the computational domain tube-length was very small and it was satisfactory to assume a constant wall-temperature. However different temperatures on the tube-rows were specified to interpret the row-on-row variation. From experimental results, the temperature difference of the chilled waterside, ΔT_w was varied between (2.77 °C to 5.18 °C) at T_{ai} = 33 °C and (4.2 °C to 5.35 °C) at T_{ai} = 42 °C corresponding to a range of air velocity of (0.65 m/s to 3.8 m/s). An average value of ΔT_w = 4.5 °C was chosen. The temperature gradient through the tube wall-thickness was estimated to be

0.5 K due to the thermal-resistance of the tube thickness. Hence, $\Delta T_{wall} = 5$ °C was specified as the temperature gradient between the first row and the fourth row. A comparison between the isothermal fin-and-tube model, conjugate model, and tube-row temperature gradient model were carried out for each cooling coil type. The model of tube-row temperature gradient having periodic boundaries was considered as CFD model that it is validated with the experimental results

6.5.4 Modelling the turbulated fin-edge burrs

A burr is defined as "plastically" deformed material left attached on the work piece after pressing [Lin, 2000]. The forming of burrs on the workpiece was undesirable but mostly unavoidable. In the case of the manufacturing of the turbulated fin sheet, burrs are formed on every side of the slits during the pressing process of the fin sheet. The thickness, height and shape of burrs are dependent upon the cutting tool, tool quality, tool speed and ductility of the fin sheet material. In order to reveal a microscopic observation of the slits-burr, a selected area (30 mm x 10 mm) from the turbulated fin sheet was chosen. The sample was mounted using conductive carbon filled powder in the Pneumet II Mounting Machine. The mounted sample was polished up to 0.001 mm and then ultrasonically cleaned. The microscopic examination clearly showed the upper edge and lower edge burrs of the fin-slits as illustrated in Figs (6.13a) and (6.13b). A two-dimensional CFD model of the turbulated fin passage with burrs was adopted and compared with the same model without burrs. Since the burr shape was asymmetrical, two types of burr models were investigated. The first was based on the maximum dimension of the burr and the other was based on half of the maximum dimension (considered to be the average dimension of the burr). A typical two-dimensional adaptive-mapped mesh of the turbulated fin passage with and without burrs is illustrated in Figs. (6.14) and (6.15) respectively.

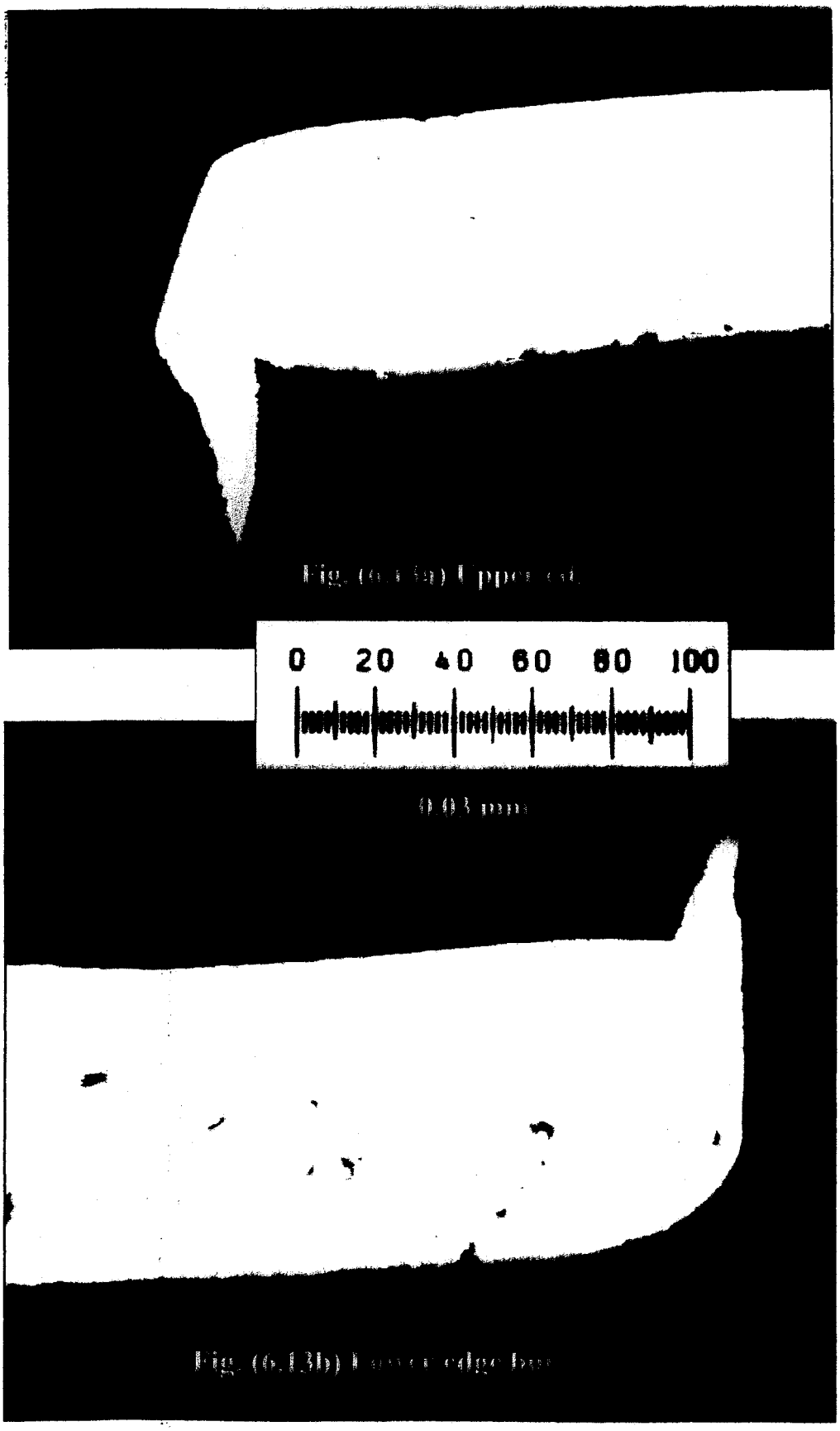
0 20 40 60 80 100

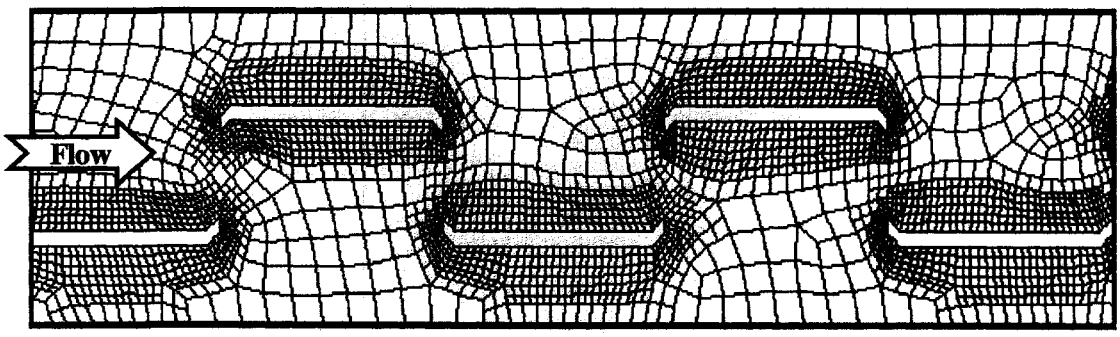

Fig. (6.14) Adaptive-mapped mesh for slits with burrs

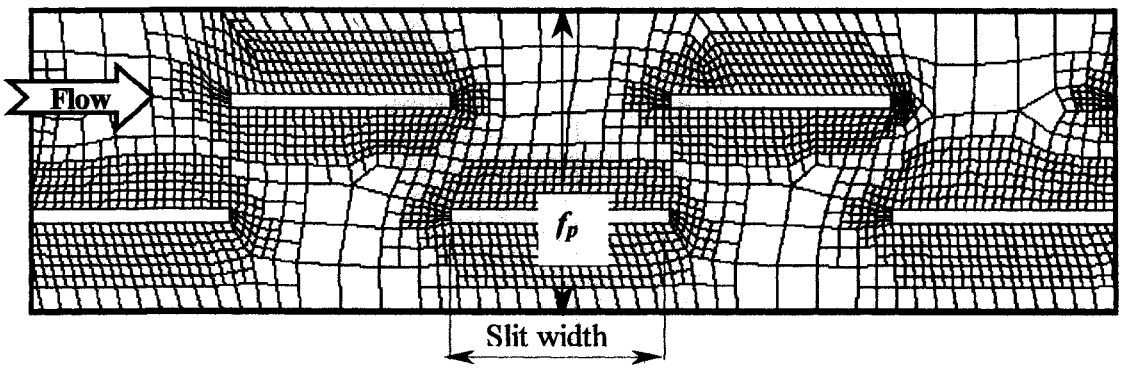

Fig. (6.15) Adaptive-mapped mesh for slits without burrs

6.6 Method of calculation

The log-mean temperature difference method of calculation was also used in the CFD analysis of the cooling coils so that these results could be compared directly with the experimental data. Fluid properties were evaluated at the fluid bulk temperature.

The heat balance equation across the computational domain can be expressed as;

$$\dot{m}_a \, Cp_a \left(T_{ai} - T_{ao}\right) = \eta_o \, A_o \, h \, \theta_m \quad \text{or;}$$

$$h = \frac{\dot{m}_a \, Cp_a \, (T_{ai} - T_{ao})}{\eta_o \, A_o \, \theta_m} \tag{6.1}$$

Where;

η_o is the overall surface efficiency

Since the fin efficiency, η_f, characterises the performance of a single fin, the overall surface efficiency, η_o, characterises an array of fins and tubes, and is defined as the total heat transfer from fins and tubes divided by the maximum possible heat transfer from fins and tubes (which clearly occurs when the fins are at the same temperature as the tubes). This term may be written as;

$$\eta_o = \frac{Q_{total}}{Q_{max}} \tag{6.2}$$

- In this case of an isothermal fin-and-tube;

$$\eta_o = 1$$

- In this case of conjugate heat transfer;

$$\eta_o = \frac{Q_{conjugate}}{Q_{isothermal}}$$

- In the case of the tube-row temperature gradient (TRTG) model;

$$\eta_o = \frac{Q_{TRTG}}{Q_{isothermal}}$$

The outlet temperature T_{ao} of the flow field is computed by dividing the integral of the product of the temperature and the dot product of the facet area and

momentum vectors by the integral of the dot product of the facet area and momentum vectors.

$$T_{ao} = \frac{\int T\ \rho\ \vec{u}\ .\ d\vec{A}}{\int \rho\ \vec{u}\ .\ d\vec{A}} \tag{6.3}$$

The Nusselt number and friction factor are computed in the same manner as in the experimental analysis, where ΔP ($P_i - P_o$) is the pressure drop across the computational domain. The inlet pressure P_i is computed as in the same manner as T_{ao}:

$$P_i = \frac{\int P\ \rho\ \vec{u}\ .\ d\vec{A}}{\int \rho\ \vec{u}\ .\ d\vec{A}} \tag{6.4}$$

6.7 Results

Most of results are presented in dimensionless form however, the heat transfer coefficient and pressure drop are also given. These results are presented as:

- Isothermal fin-and-tube
- Conjugate heat transfer
- Tube-rows temperature gradient
- Periodic boundaries
- Burrs effect

6.7.1 Isothermal fin-and-tube

The flow velocity distribution on the mid-plane between two neighbouring-fins is illustrated in Fig. (6.16) at Re = 1406 (u_{ai} = 3 m/s) for the flat, corrugated and turbulated-fin models. The velocity field was varied significantly from row-on-row due to development flow field in the entrance region. It can be seen that the figures reveal a complex flow pattern. The flat fin case has the largest wake zone at the rear of each of the tube row and the turbulated fin case has the smallest zone. The larger wake zone, the poorer heat exchange.

The pressure field distribution on the mid-plane between two neighbouring-fins for Re = 1406 is illustrated in Fig. (6.17) for all fin types. The pressure drop is due to the tube form-drag and the shear force of the flow through the narrow fin spacing. For each of the tube rows, a higher pressure-zone occurs at the stagnation point (circumferential angle of zero) of each tube and a lower pressure-zone occurs at the zone of higher velocity gradient (circumferential angle of 90°).

The variation of the heat transfer coefficient for the isothermal fin model is illustrated in Fig. (6.18). The turbulated fin coil gives the highest value of heat transfer coefficient, while the flat fin coil gives the lowest value. In the case of the turbulated fin, the slits interrupted the growth in the laminar boundary layer over the fin surface, which produces a good flow mixing and hence, higher heat exchange is achieved. The corrugated fins lengthen the flow path as well as the recirculation regions produced by the effect of the flow waviness. It is clear that the turbulated and corrugated fin geometries enhance the heat transfer compared to the flat fin. However, the pressure drop penalty high as illustrated in Fig. (6.19). This is due to the increase in flow resistance resulting from the complicated nature of the flow pattern throughout the corrugated and turbulated fin arrays. A trade-off needs to be assessed between the enhancement of heat transfer coefficient which led to an improvement in the cooling capacity of the air conditioning plant and the increase in pressure drop which led to increase in the fan friction power needed.

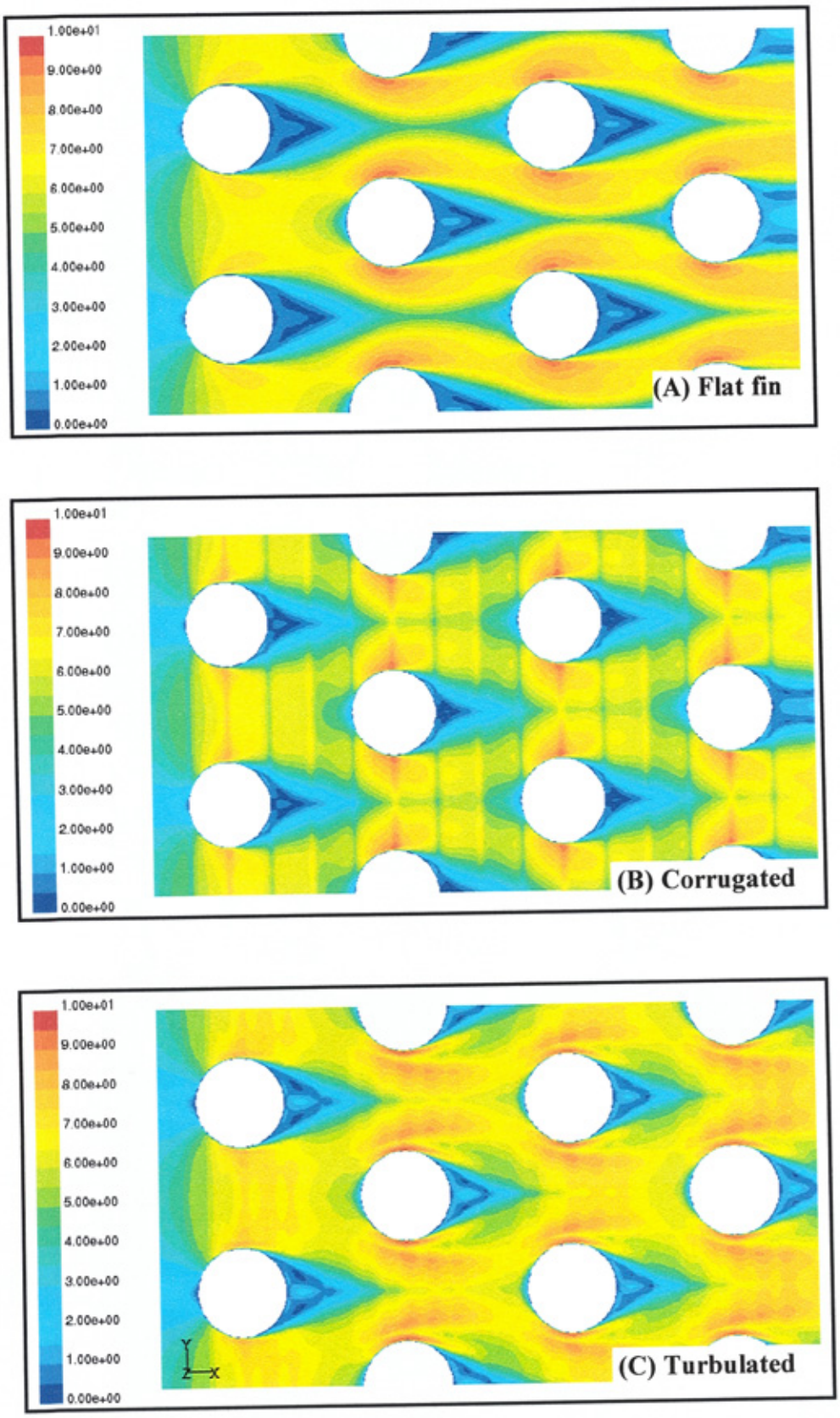

Fig. (6.16) Velocity field of mid-plane between two neighbouring-fins

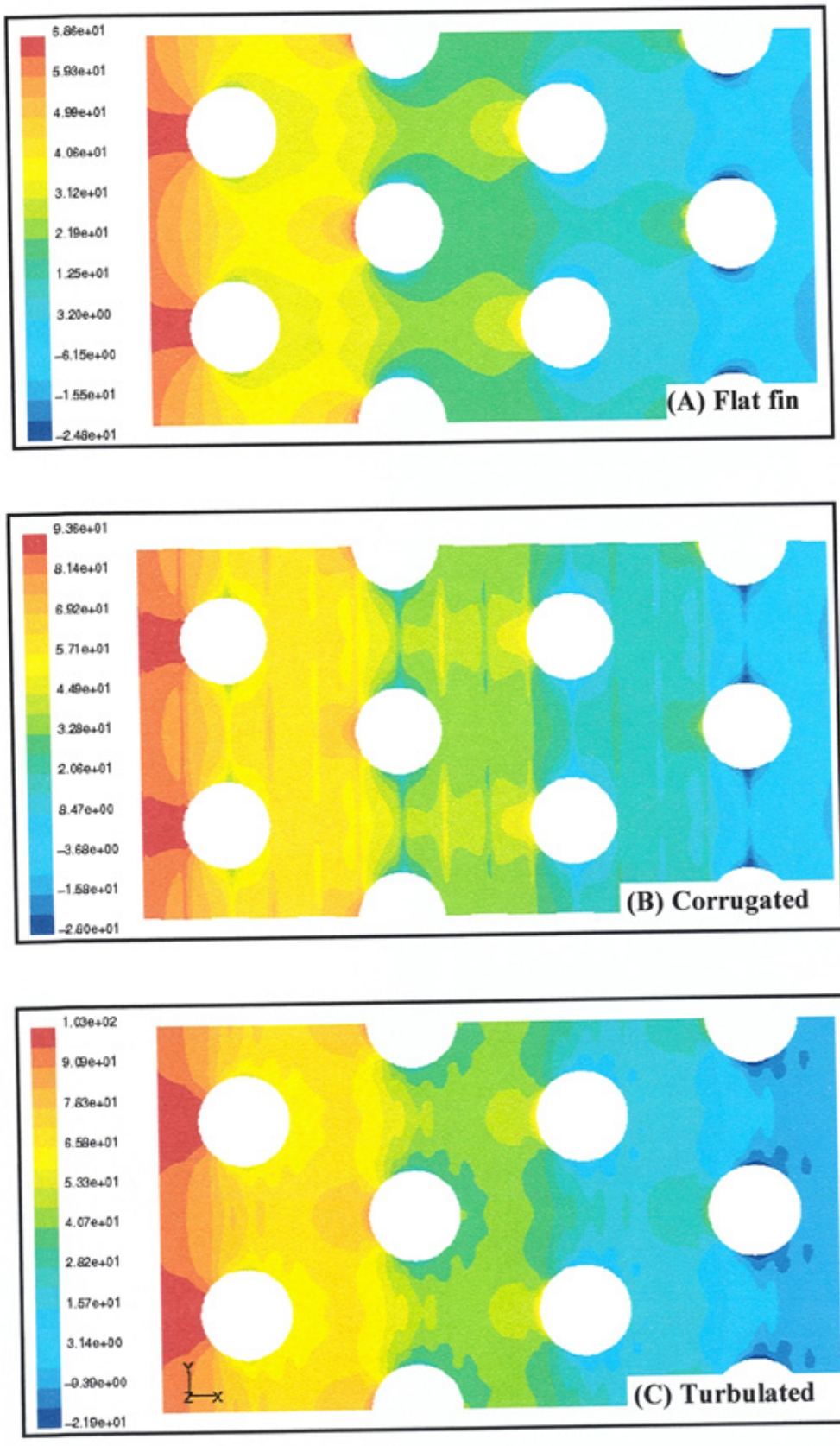

Fig. (6.17) Pressure field of mid-plane between two neighbouring-fins

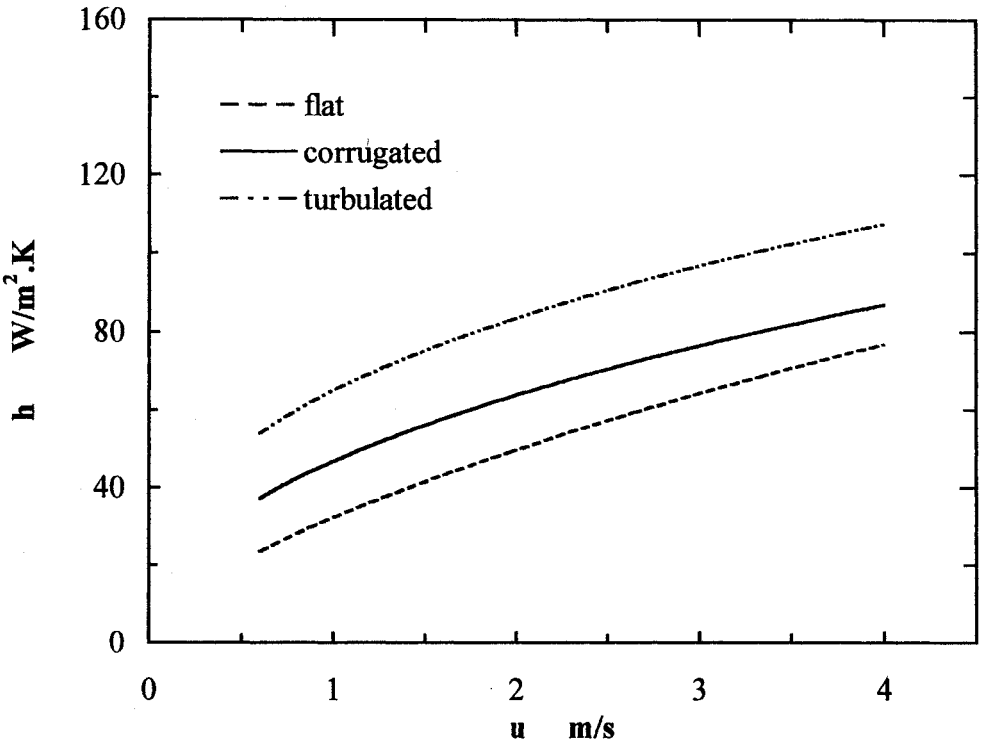

Fig. (6.18) Heat transfer coefficient of the isothermal fin-and-tube

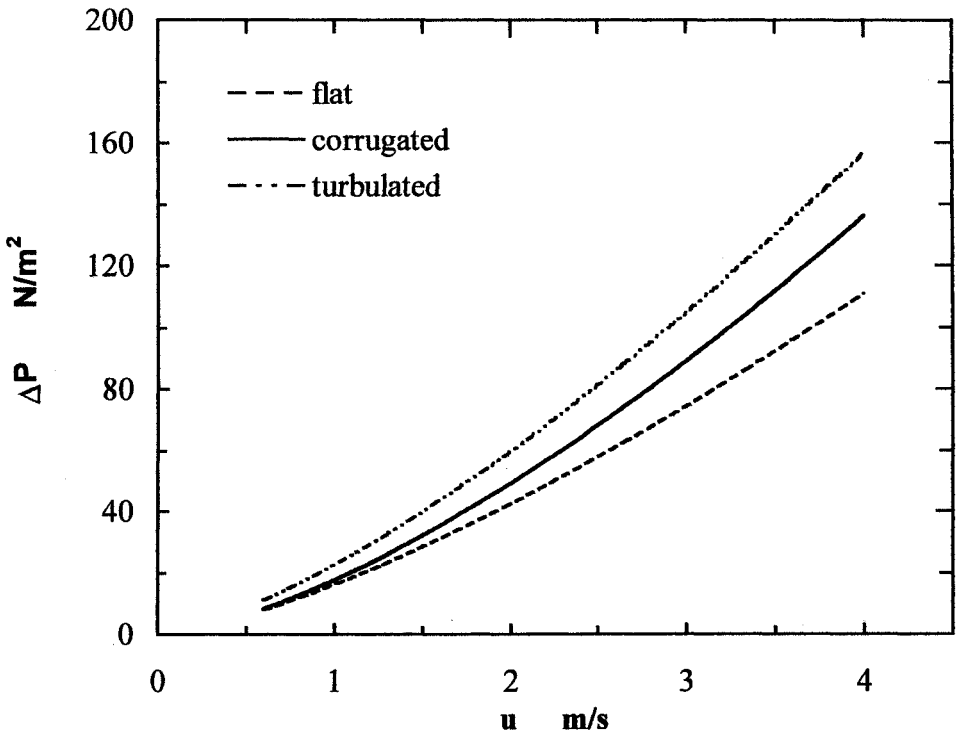

Fig. (6.19) Pressure drop of the isothermal fin-and-tube

The Nusselt number and friction factor for all coil types are illustrated in Figs. (6.20) and (6.21) respectively. The higher values of both Nusselt number and friction factor for the turbulated and corrugated fin are evident. The friction factor of the turbulated fin was higher that that of the flat and corrugated fin cases by 32 % and 19 % respectively while the friction factor of the corrugated fin coil was higher than that of the flat fin by 11.5 %. This clearly has implications for fan friction power which will be returned to later in section 6.9.

6.7.2 Conjugate heat transfer

The temperature field distribution on the mid-plane between two neighbouring-fins of all fin types is illustrated in Fig. (6.22) for Re = 1406. It can be seen that a large cooling fluid area was produced with the turbulated and corrugated fin cases while a small cooling area associated with the flat fin case. This is due to the high flow mixing induced by the turbulated-fin geometry followed by corrugated geometry. The distribution of the surface temperature gradient of the fins is illustrated in Fig. (6.23). The surface temperature gradient increases with the increase the radial distance from the fin root which is due to the gradual increase of the fin thermal resistance with the distance from the fin root (fin length). An increase of the fin surface temperature is evident at the inlet region due to the heating effect of the inlet air.

Fig. (6.24) shows the variation of the Nusselt number with the Reynolds number for the three coil types. In the flat fin case, the gradual growth of the flow stream results a growth of boundary layer and hence a decrease in Nusselt number is achieved. Whereas in the turbulated and corrugated cases, a better flow mixing is produced which constrains the growth of the boundary layer thickness leading to an increase in Nusselt number. The Nusselt number of the turbulated fin is enhanced by 52 % and 22 % compared with the flat and corrugated fin respectively while the Nusselt number of the corrugated fin geometry is enhanced by 24.5 % compared to the flat fin.

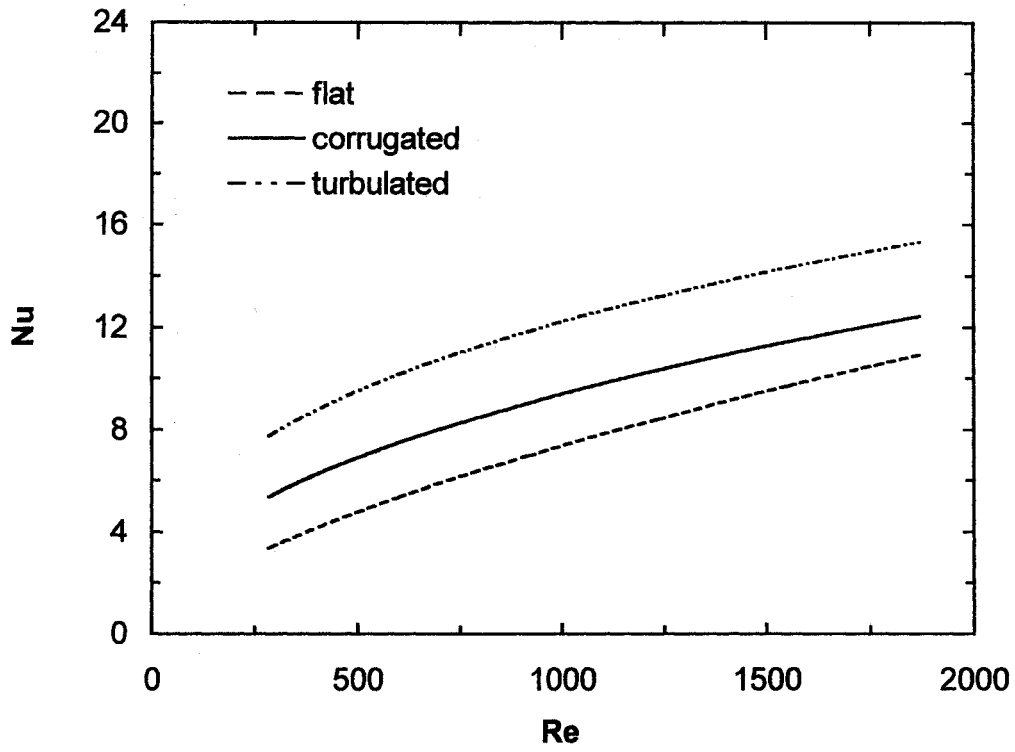

Fig. (6.20) Nusselt number of the isothermal fin-and-tube

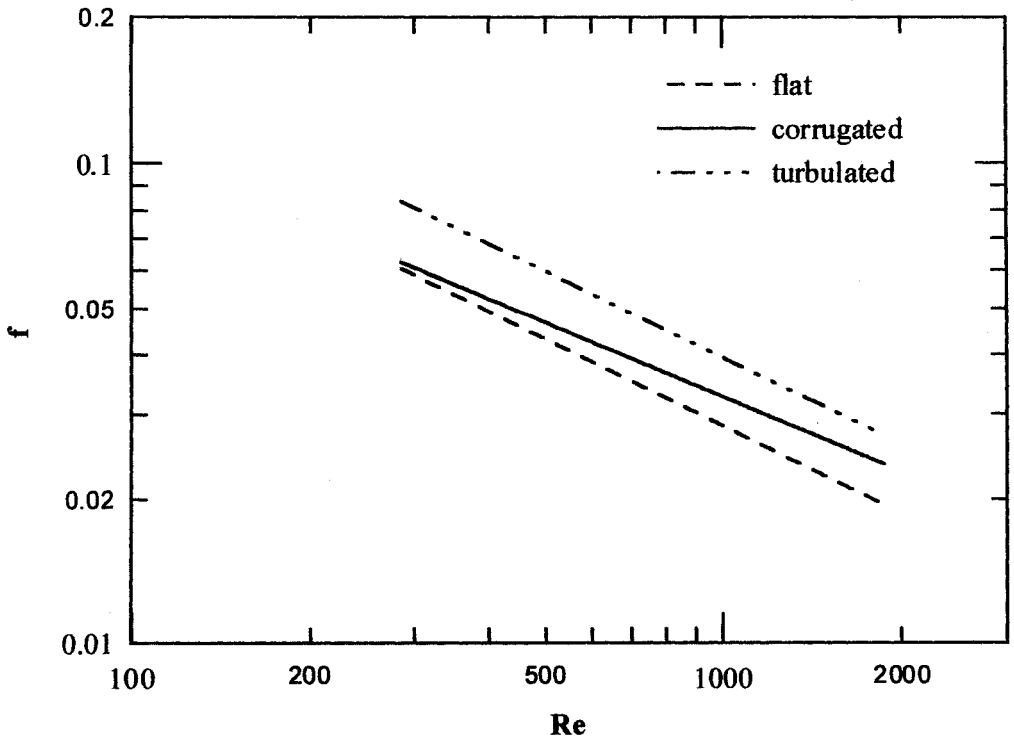

Fig. (6.21) Friction factor of the isothermal fin-and-tube

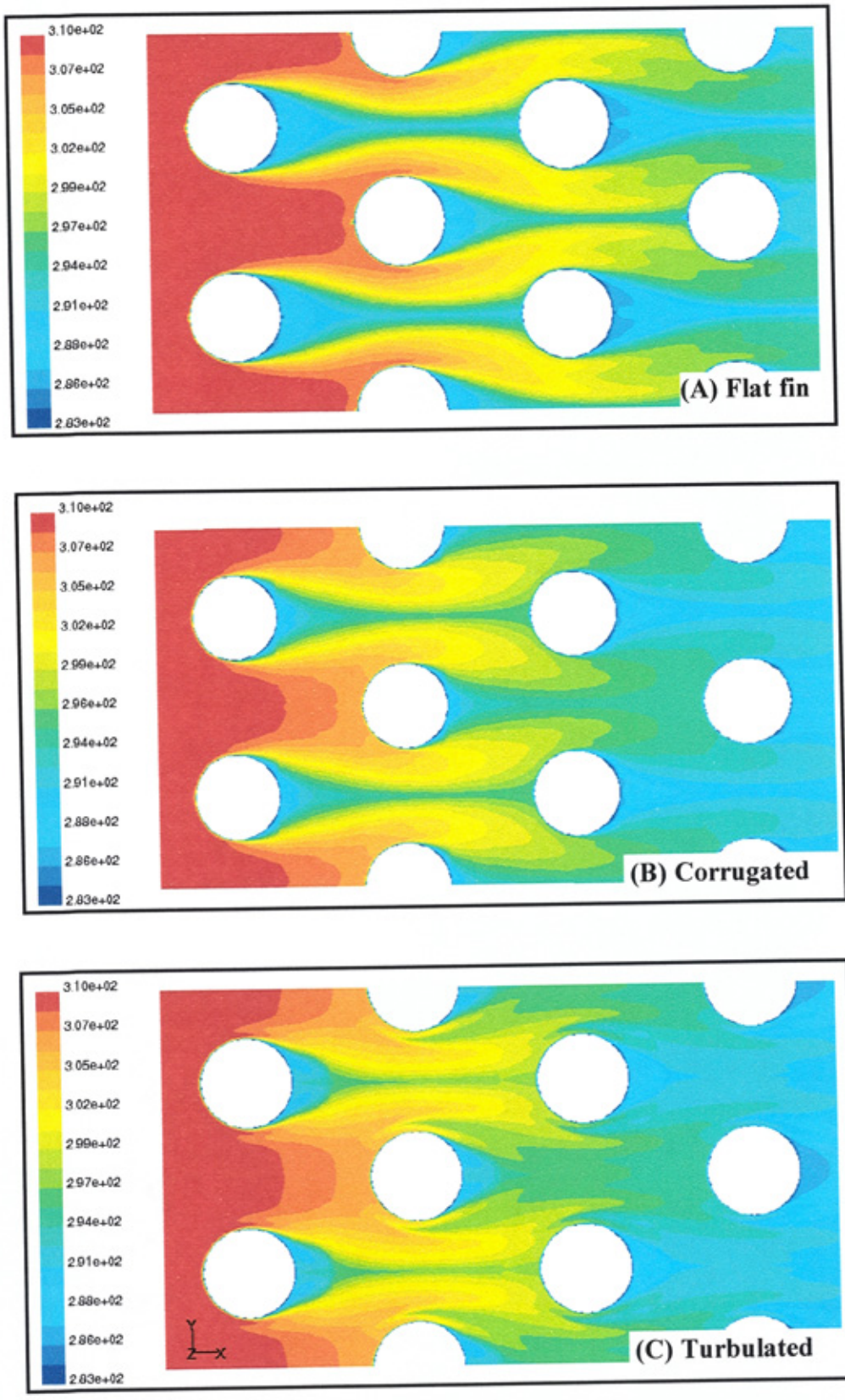

Fig. (6.22) Temperature field of mid-plane between two neighbouring-

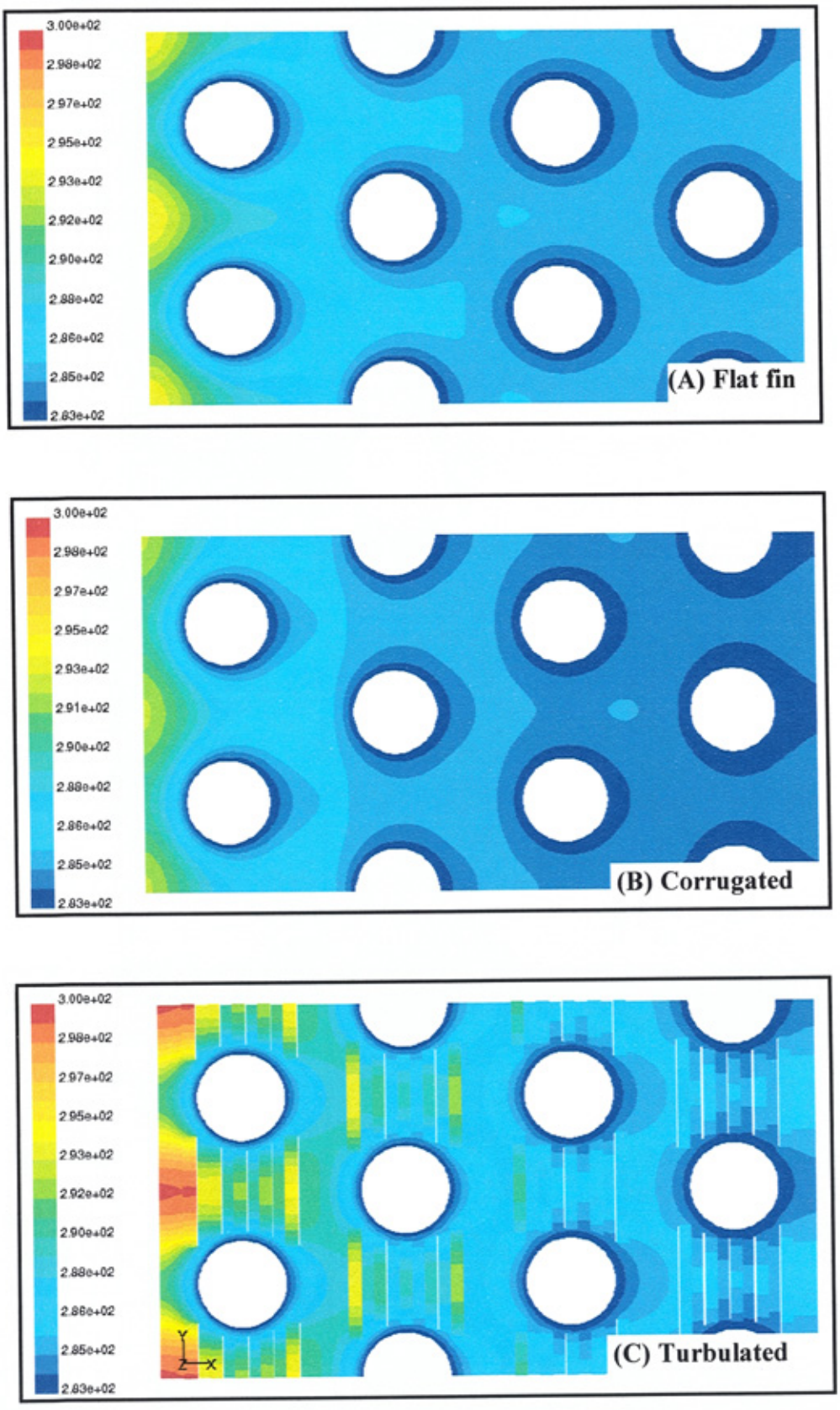

Fig. (6.23) Temperature distribution on the fin surface

6.7.3 Effect of periodic boundaries

The Nusselt number and the friction factor of the three coil types with both symmetrical and periodic boundaries are illustrated in Figs. (6.25) and (6.26) respectively. It was noted that the computational time for the periodic boundaries model was higher than that of the symmetrical one by approximately 15 %. The results of the flat fin case was unaffected by choice between the symmetrical and periodic boundaries and the assumption of the symmetrical boundaries was considered satisfactory. It is evident that there were significant differences between the two boundaries types in the case of the corrugated and turbulated fins. For the symmetrical boundaries the y-velocity component is assumed to be zero in which most of the flow is in the x-direction, this may be valid for flat fin case. Unlike the cases of corrugated and turbulated fin where the y-velocity components and its gradient are not equal to zero. Hence, symmetrical boundaries are considered inappropriate for last two cases.

6.7.4 Tube-row temperature gradient

The Nusselt number characteristic for the isothermal model, conjugate heat transfer model and tube-row temperature gradient model "TRTG" applicable to the flat, corrugated and turbulated fin cooling coils are illustrated in Figs. (6.27), (6.28) and (6.29) respectively. It was found that the isothermal fin-and-tube approximation overpredicted the Nusselt number by a range of 8.5 % to 43 % compared to the conjugate heat transfer results. At the same time, the Nusselt number of the conjugate heat transfer was higher than that of the TRTG model by a range of 6 % to 9 %. However the TRTG model is considered as most practical model in which the temperature gradients of tube thickness, row-on-row, fin length and periodic boundaries are addressed.

The friction factor of the TRTG model is illustrated in Fig. (6.30). The friction factor of the turbulated fin is higher than that of flat and corrugated fin coils by 33 % and 18.2 % respectively while the friction factor of the corrugated fin was higher than that of the flat fin by 12.5 %.

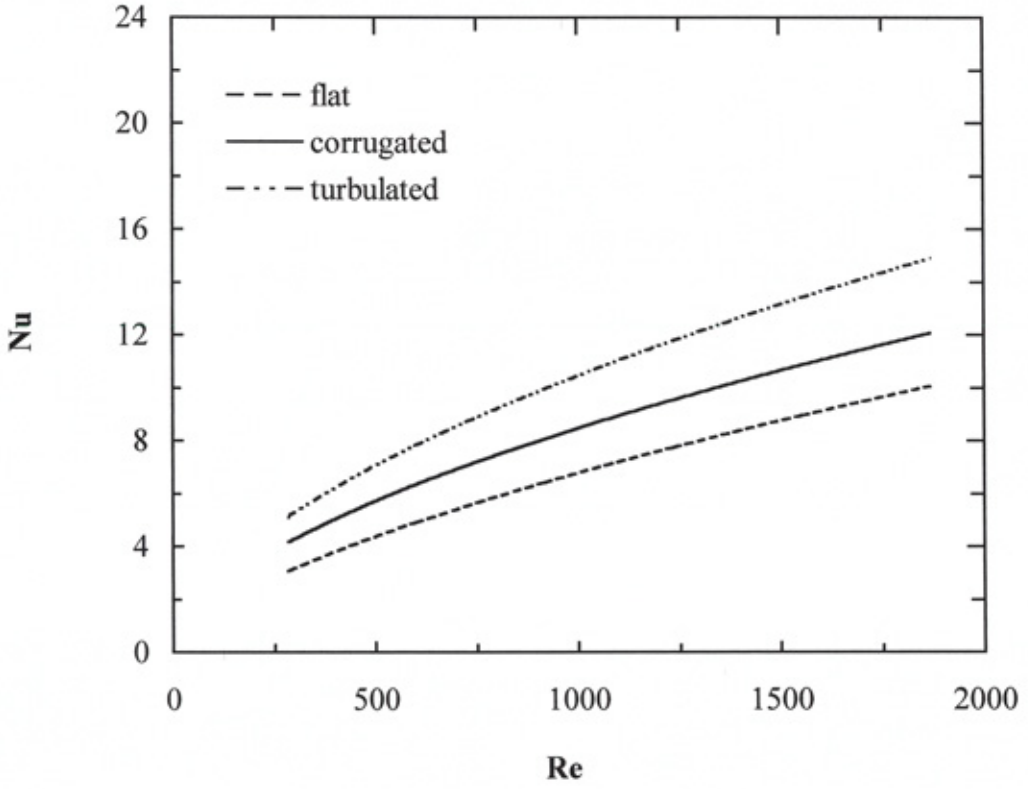

Fig. (6.24) Nusselt number of the conjugate heat transfer model

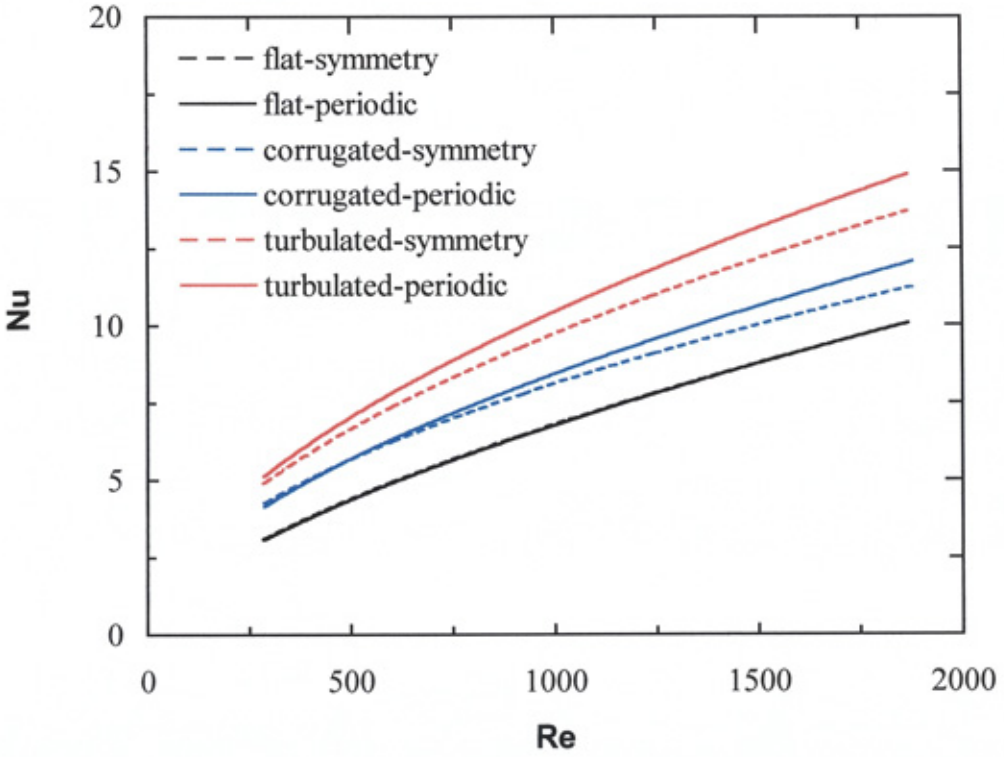

Fig. (6.25) Nusselt number for symmetrical and periodic boundaries

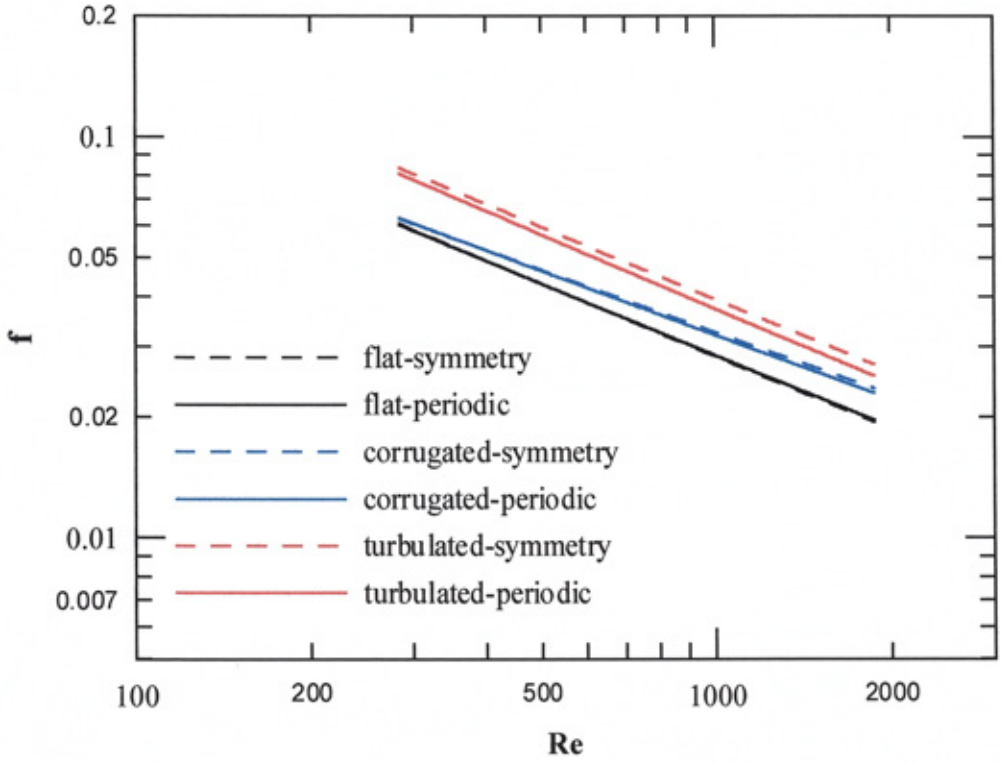

Fig. (6.26) Friction factor for symmetrical and periodic boundaries

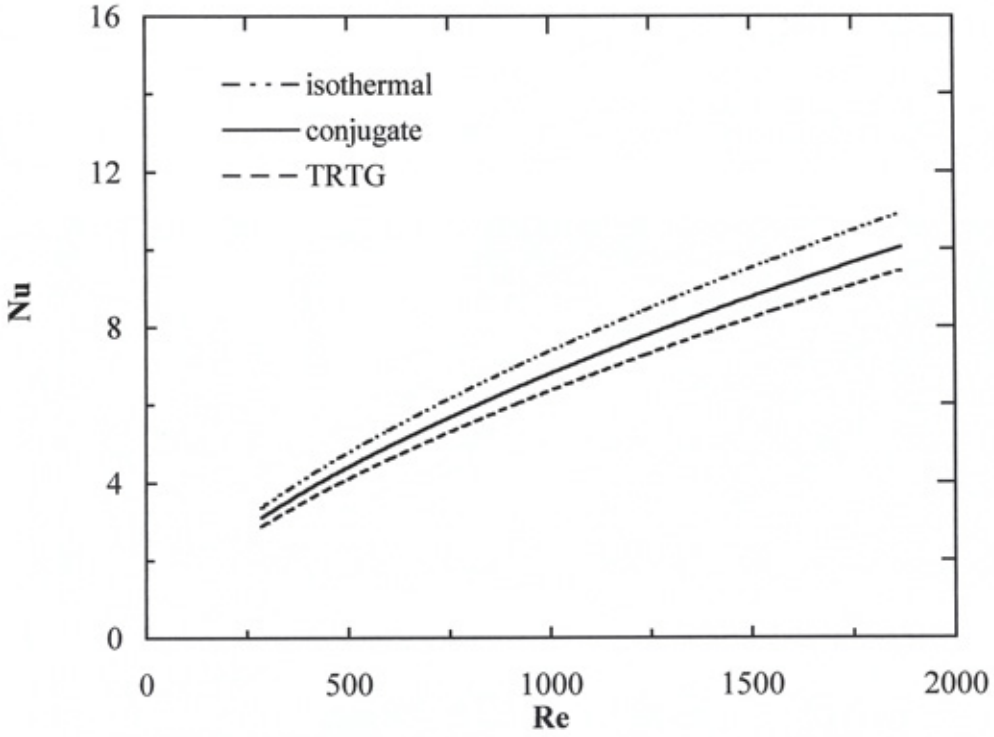

Fig. (6.27) Nusselt number of the flat fin coil

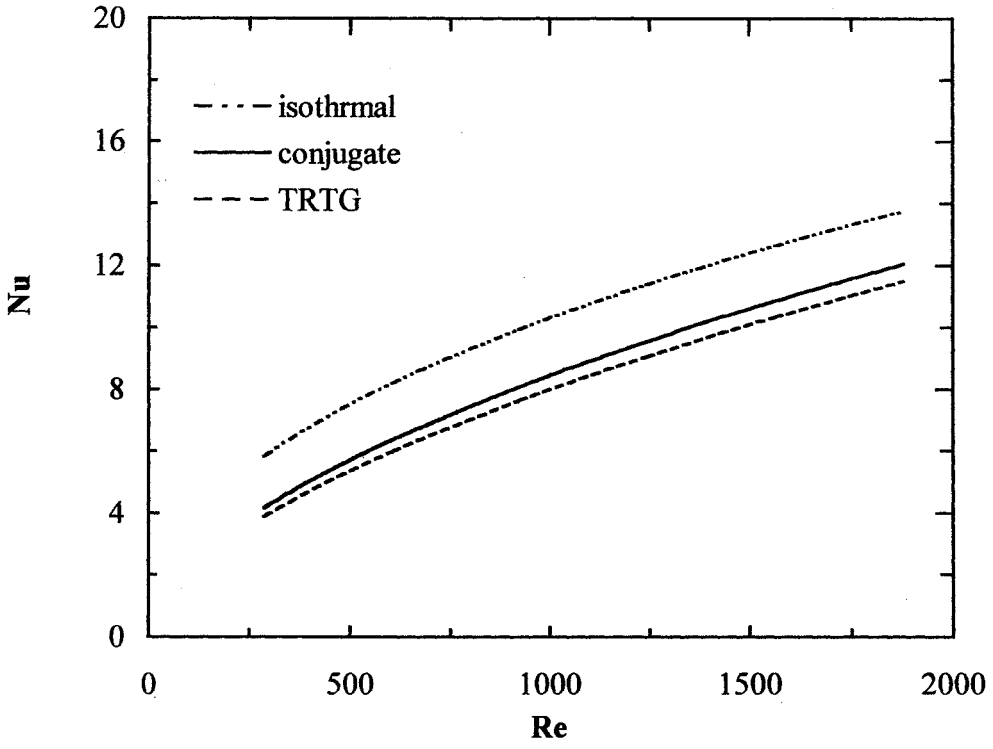

Fig. (6.28) Nusselt number of the corrugated fin coil

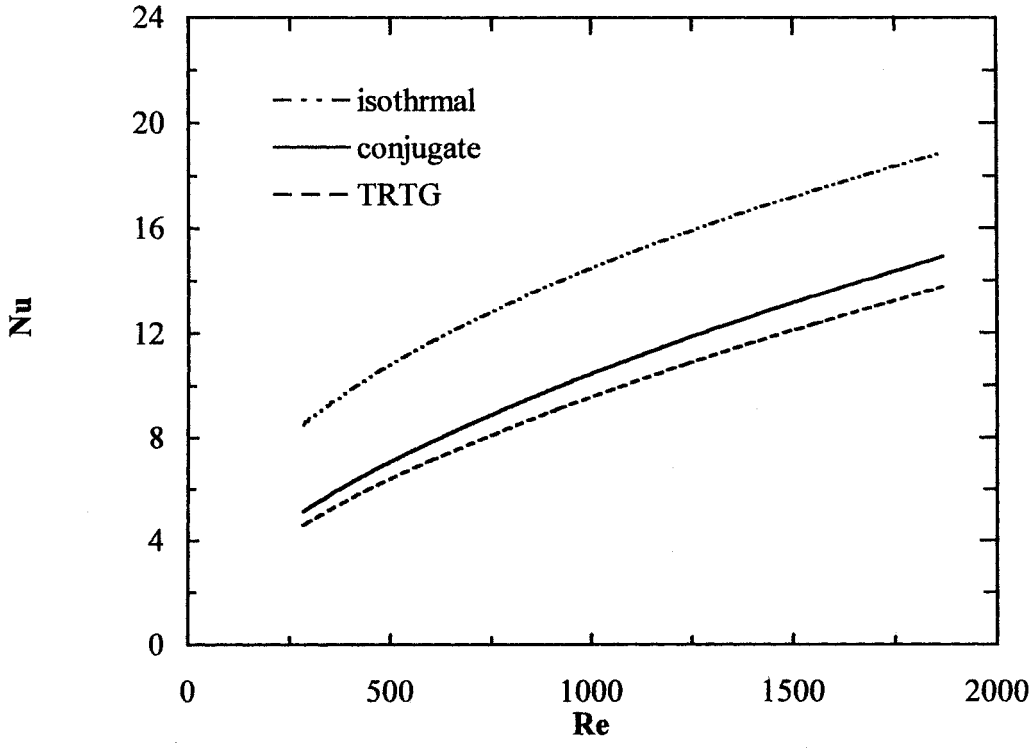

Fig. (6.29) Nusselt number of the turbulated fin coil

6.7.5 Influence of the turbulated-fin edge burrs

The flow vector plot of the 2-D burr model is illustrated in Fig. (6.31). The Nusselt number-ratio (Nu_{burr} / $Nu_{no\text{-}burr}$) of the turbulated fin passage with and without burrs is illustrated in Fig. (6.32). For the burr model, the Nusselt number is higher that that of without burr by 8 %. The friction factor ratio with and without burrs is illustrated in Fig. (6.33). The friction factor of the mid-burr model (the average burr length) is higher than that of without burrs by 27 %. It is observed that the friction factor is more sensitive to the existence of slit burrs than is the Nusselt number.

6.8 Results validation

For the purpose of gaining confidence in the CFD modelling-results, the CFD results of the tube-row temperature gradient model are validated against the experimental results for the three cooling coil types. The numerical and experimental results (including the uncertainty error bars) of the heat transfer coefficient and the pressure drop for the flat-fin cooling coil are illustrated in Figs. (6.34) and (6.35) respectively. It is clear that, there is a good agreement between the CFD results of TRTG model and the experimental results (including mean uncertainties of 10 % and 6 % in heat transfer coefficient and pressure drop respectively). The same agreement is evident for both Nusselt number and friction factor. The validation of the CFD modelling-results for the corrugated fin against the experimental results is illustrated in Figs. (6.36) and (6.37). The CFD corrugated model results are in a good agreement with the experimental data. However, in the case of the turbulated fin coil a fair agreement between the numerical and the experimental results is evident as illustrated in Figs. (6.38) and (6.39). The deviation in the experimental results of heat transfer coefficient and pressure drop with the higher value of the air velocity, $u_i \geq 2.2$ m/s is attributed to the burr effect where the three-dimensional CFD model of the turbulated fin coil was generated as burrsless model.

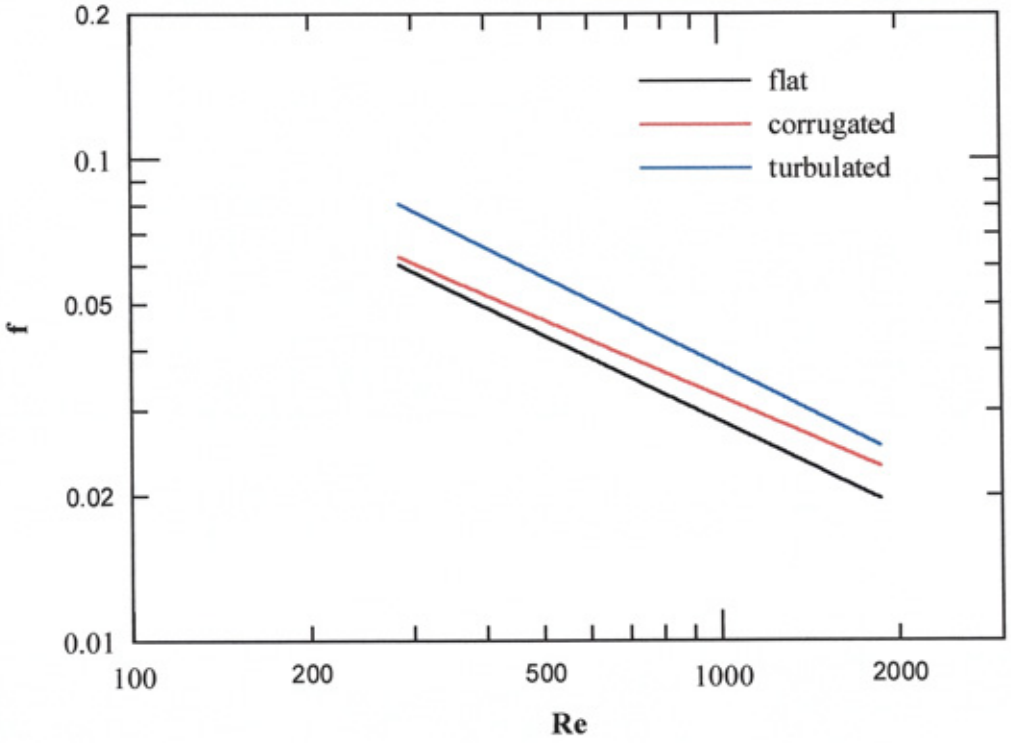

Fig. (6.30) Friction factor of the TRTG model

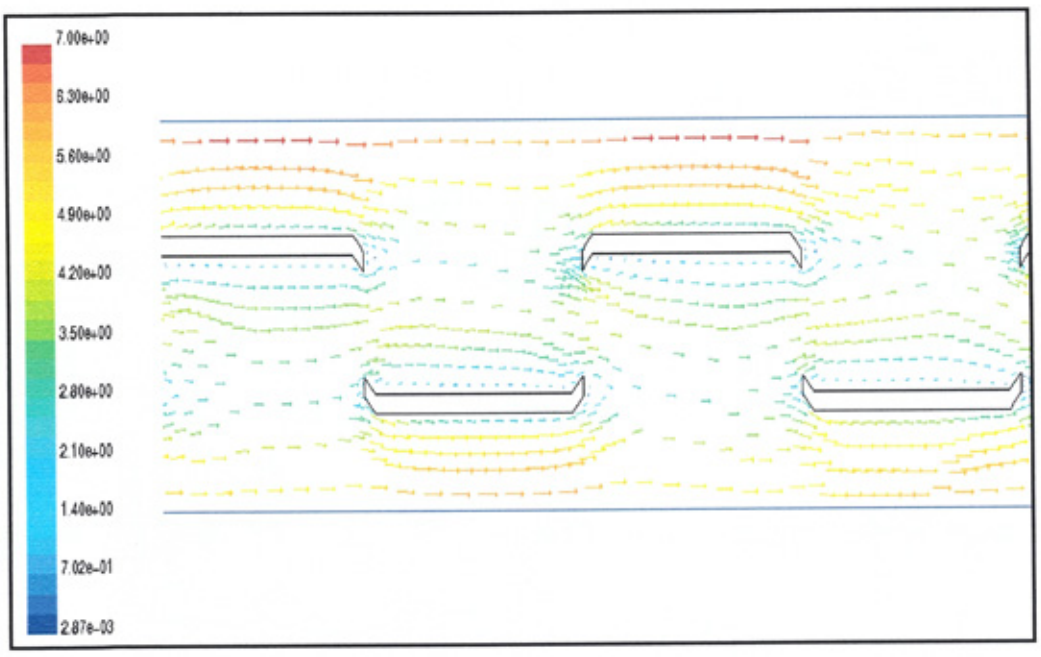

Fig. (6.31) Vector plot through the turbulated-fin passage with burrs

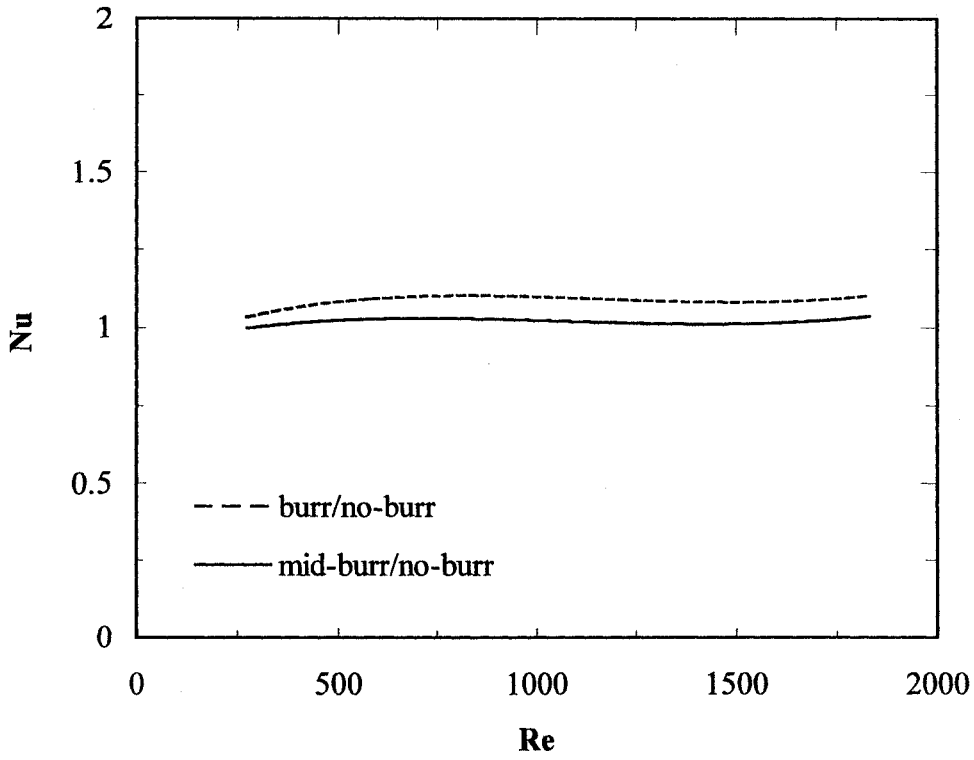

Fig. (6.32) Nusselt number of the 2-D burrs-model

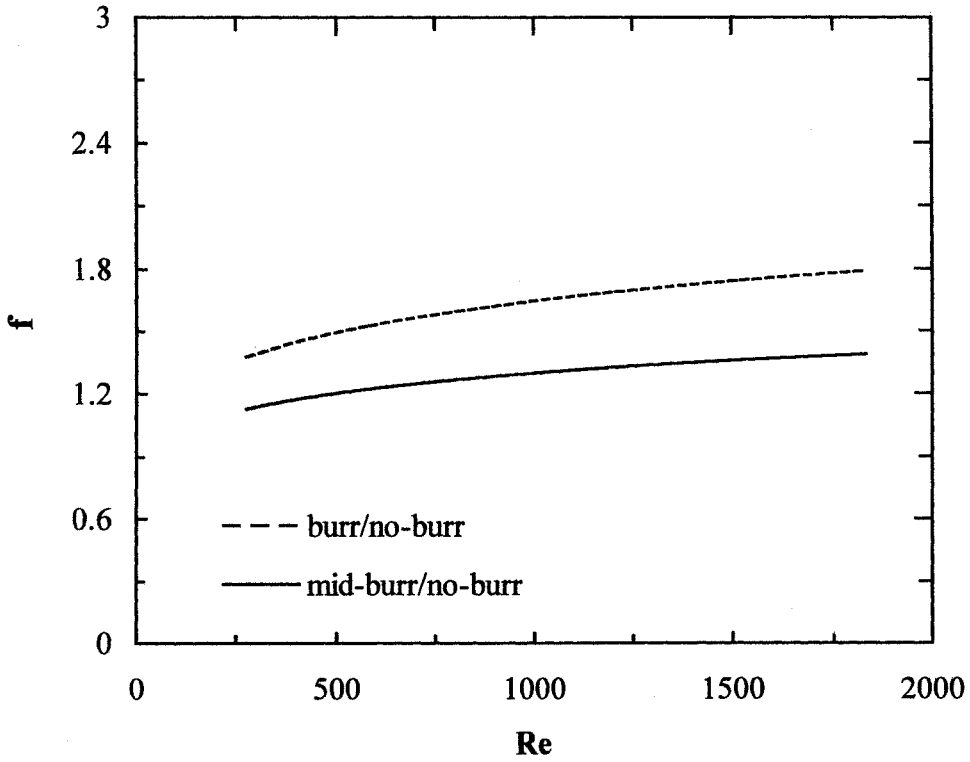

Fig. (6.33) Friction factor of the 2-D burrs-model

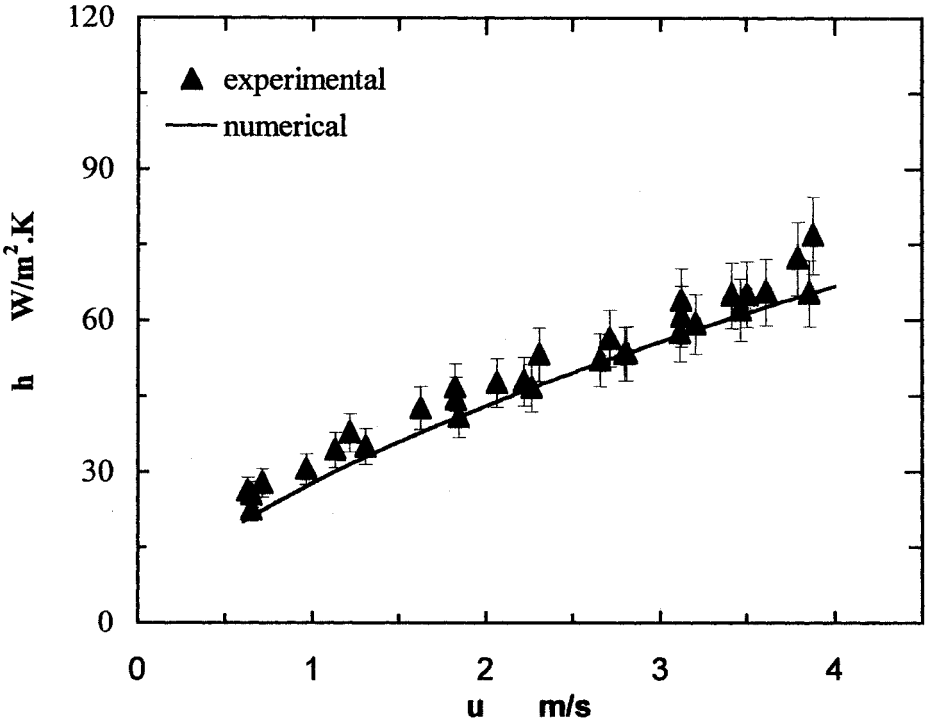

Fig. (6.34) Heat transfer coefficient of the flat fin cooling coil

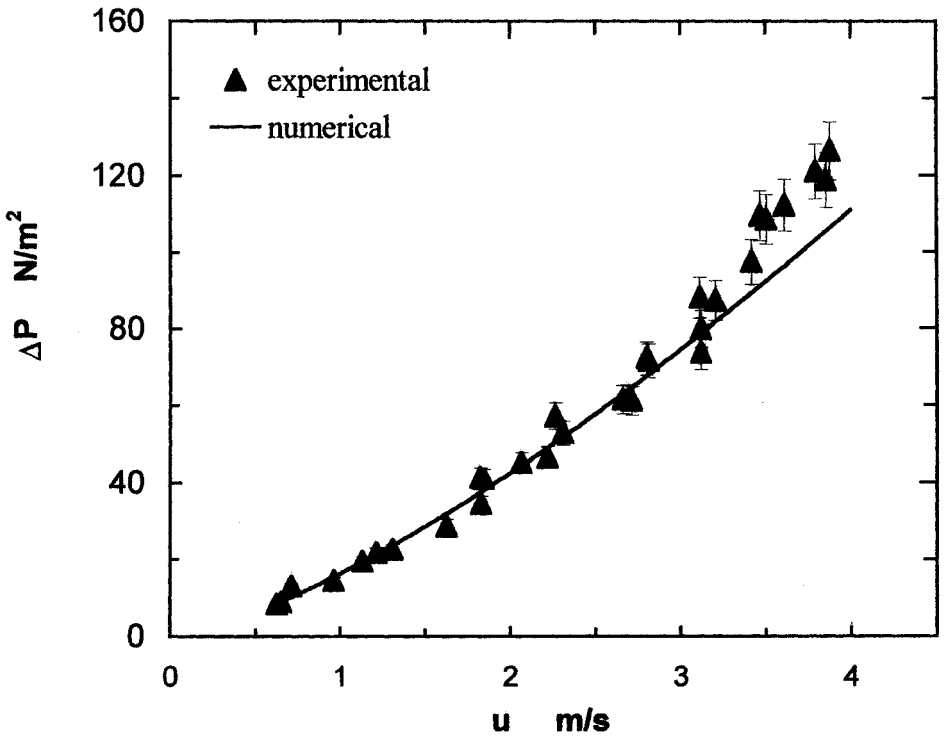

Fig. (6.35) Pressure drop of the flat fin cooling coil

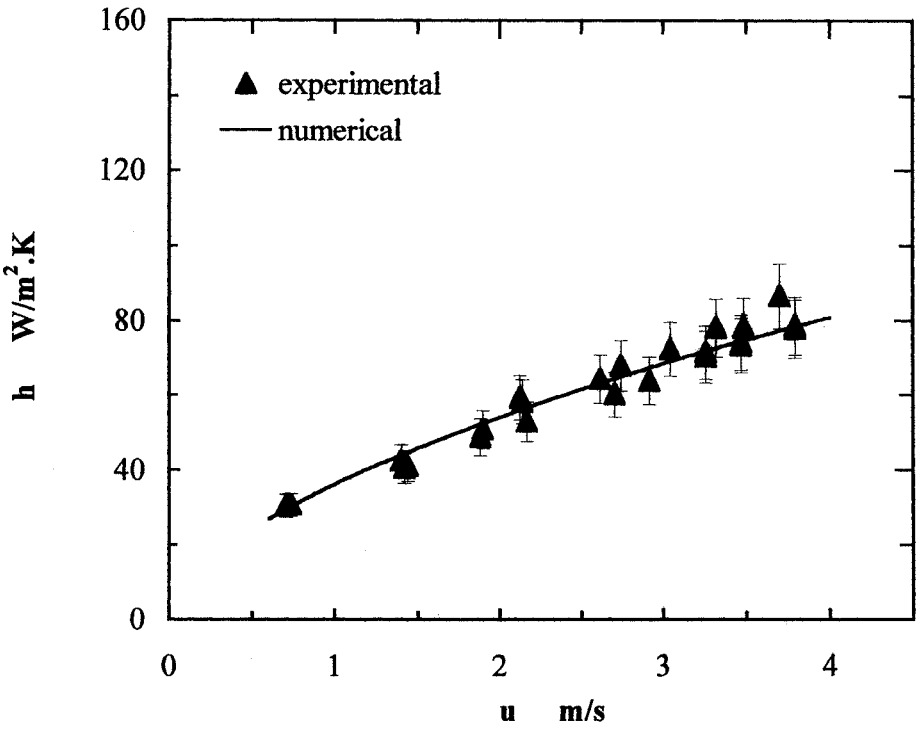

Fig. (6.36) Heat transfer coefficient of the corrugated fin cooling coil

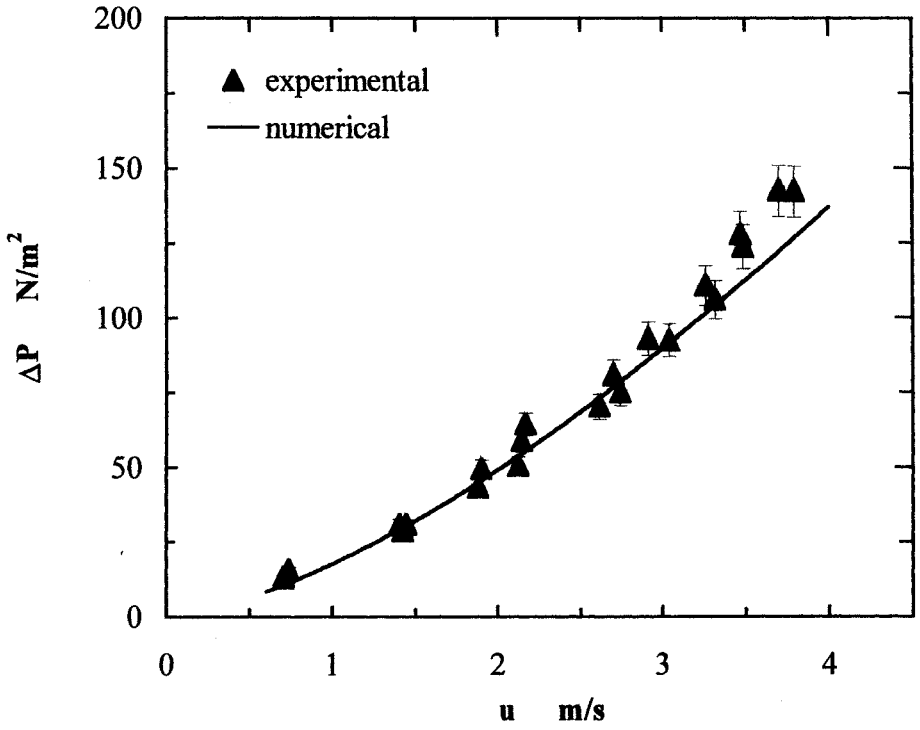

Fig. (6.37) Pressure drop of the corrugated fin cooling coil

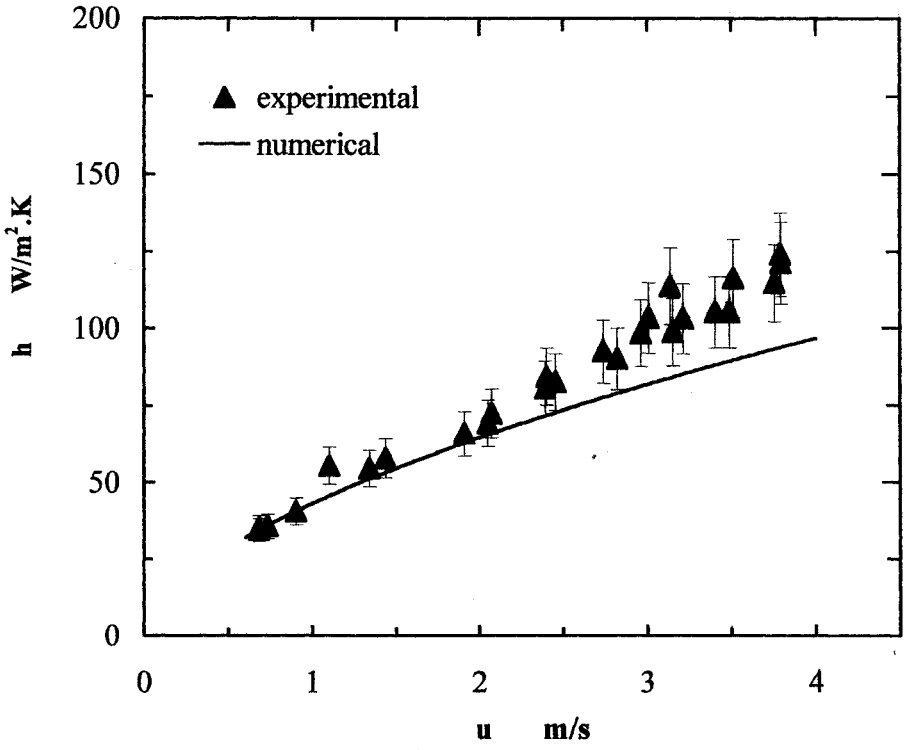

Fig. (6.38) Heat transfer coefficient of the turbulated fin cooling coil

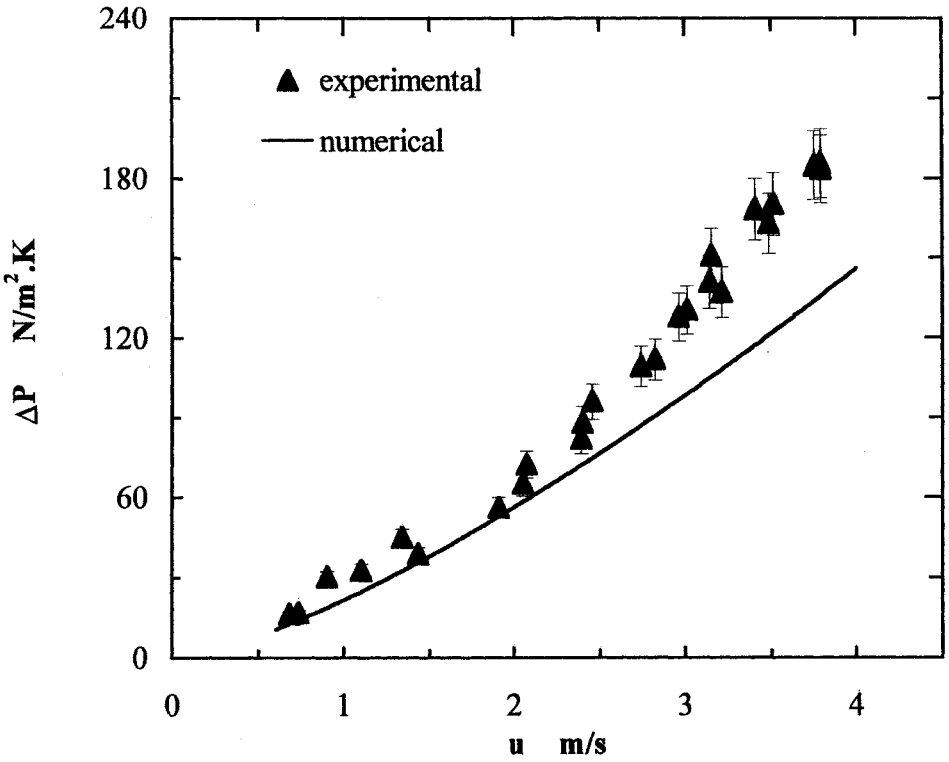

Fig. (6.39) Pressure drop of the turbulated fin cooling coil

6.8.1 Fin efficiency

A prediction of the fin-efficiency of flat, corrugated and turbulated fin-geometries is conducted based on the validated results of the tube row temperature gradient model using equation (6.5).

$$\eta_f = 1-\frac{A_o}{A_f}\left(1-\frac{Q_{TRTG}}{Q_{iso}}\right) \tag{6.5}$$

A validation between the fin efficiency predicted from the CFD results of TRTG model and the fin efficiency based on the approximation method of Schmidt is illustrated in Fig. (6.40), (the method of Schmidt was originally generated for the circular fin case and then extended to apply to a flat fin case [McQuiston and Parker, 1994]). This figure indicates that the fin efficiency decreases as the air velocity increases which is due to the increase of the heat transfer coefficient. Good agreement has been obtained between the flat fin-efficiency predicted from the present work and that obtained from the method of Schmidt. While in the case of corrugated and turbulated fins, the deviation in the Schmidt method was between 3 % to 8 % corresponding to 1 m/s $\leq u_{ai} \leq$ 4 m/s.

6.9 Performance evaluation criteria

A variety of methods exist for comparing the performance of various heat transfer surfaces. Three methods was presented here, which are helpful to resort a metric that expresses heat transfer performance against friction loss performance whilst incorporating an economic indicator which are:

1. Direct comparison between heat transfer coefficient and pressure drop.
2. Scope of possible reduction of the heat exchanger core volume.
3. Overall performance factor "OPF" of air-conditioning plant.

A direct comparison of the heat transfer versus pressure drop at the same inlet conditions is illustrated in Fig. (6.41).

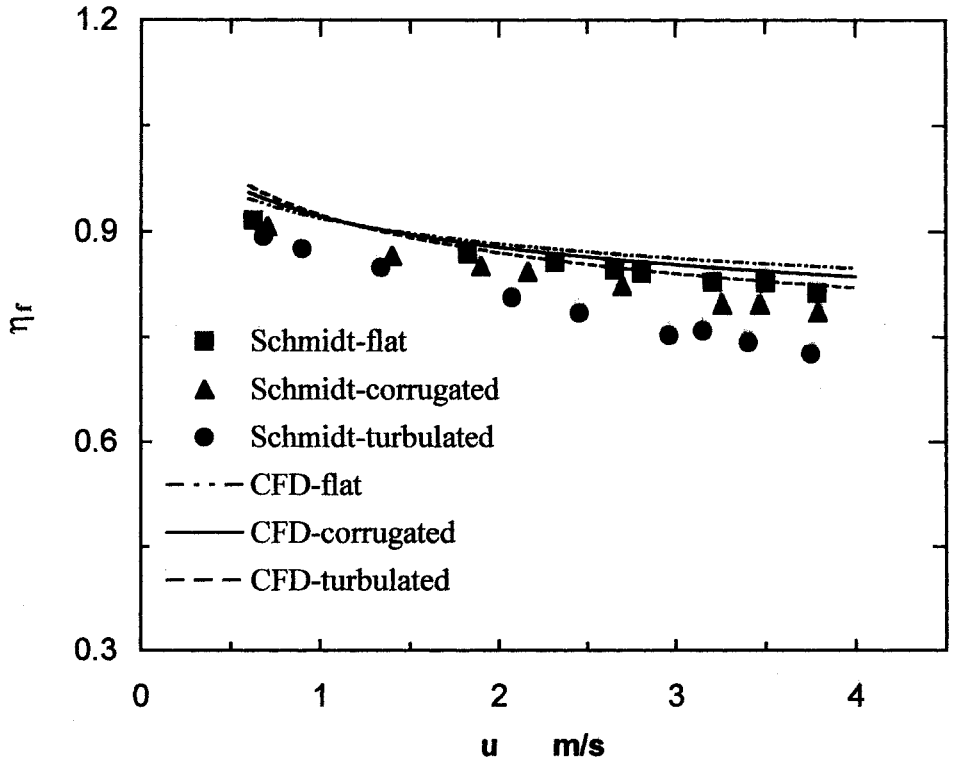

Fig. (6.40) Fin efficiency validation

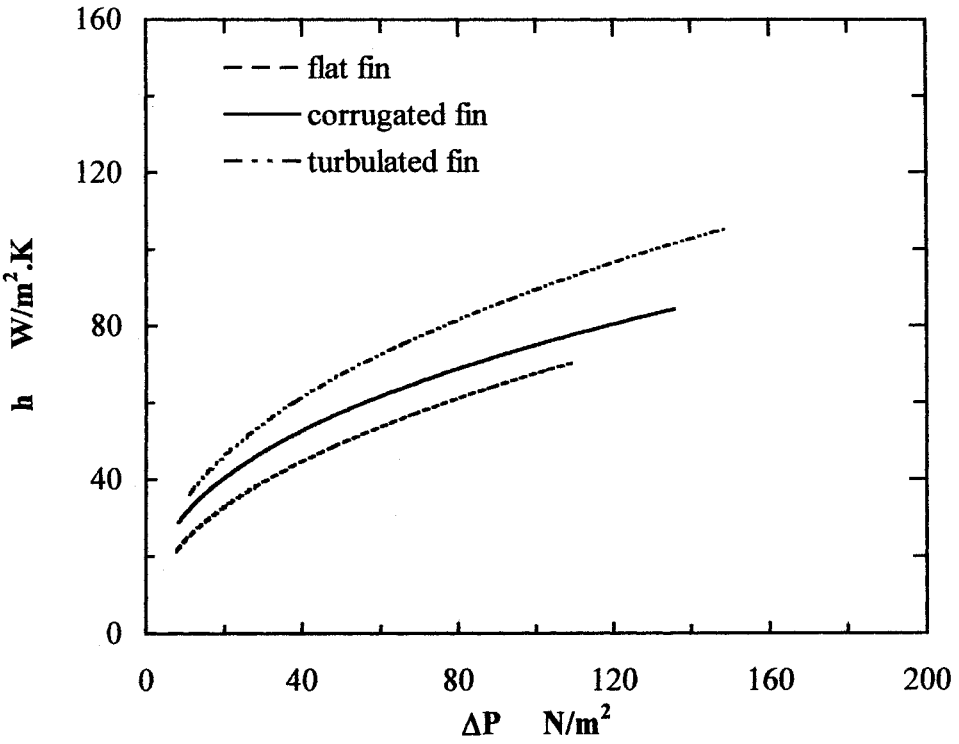

Fig. (6.41) Heat transfer coefficient vs pressure drop of all fin types

It is clear that the corrugated and turbulated fin enhance the heat transfer for the same pressure drop. At a given pressure drop ΔP = 52 N/m^2 (corresponding to u_{ai} = 2.3 m/s) the heat transfer coefficient of the corrugated and turbulated fin coils was higher than that of flat fin by 16 % and 36 % respectively.

The heat transfer per unit core volume per unit temperature difference ($h\alpha$) versus the friction power expenditure per unit core volume ($E_p\alpha$) is illustrated in Fig. (6.42). For the same value of friction power ($E_p\alpha$ = 1047 W/m^3 corresponding to u_{ai} = 2.3 m/s) the corrugated and turbulated fin coils required core volume of 19 % and 40 % lower than that of flat fin coil respectively at the same performance.

The enhancement of the cooling capacity achieved by using corrugated and turbulated coils at the same friction power leading to an improvement of the overall performance of the air conditioning plant. Thus the overall performance factor "OPF" is introduced here as an overall performance index of indirect expansion refrigeration plant (such as chilled water plant) to interpret how different fin geometries of cooling coil could affect the rate of cooling per unit pumping power. It is similar in some how as the coefficient of performance of the direct expansion refrigeration plant. A possible increase in the overall performance factor ratio "OPF_{ratio}" of the air conditioning plant is examined for the corrugated and turbulated fin cooling coils with respect to flat fin coil:

$$OPF = \frac{\text{cooling coil capacity}}{\text{fan friction power} + \text{total power input to the chiller}} \quad (6.8)$$

$$OPF_{ratio} = \frac{OPF}{OPF_{flat\text{-}fin}} \quad (6.7)$$

The cooling effect of the cooling coil ($m\ C_p\ \Delta T$) and the fan friction power ($m\ \Delta P/\rho$) are based on the validated results of TRTG model, whilst the total power input to the chiller is considered a constant between all fin cases at a manufacturer nominal value of 6400 W. Fig. (6.43) shows the variation of the OPF_{ratio} versus the inlet air velocity.

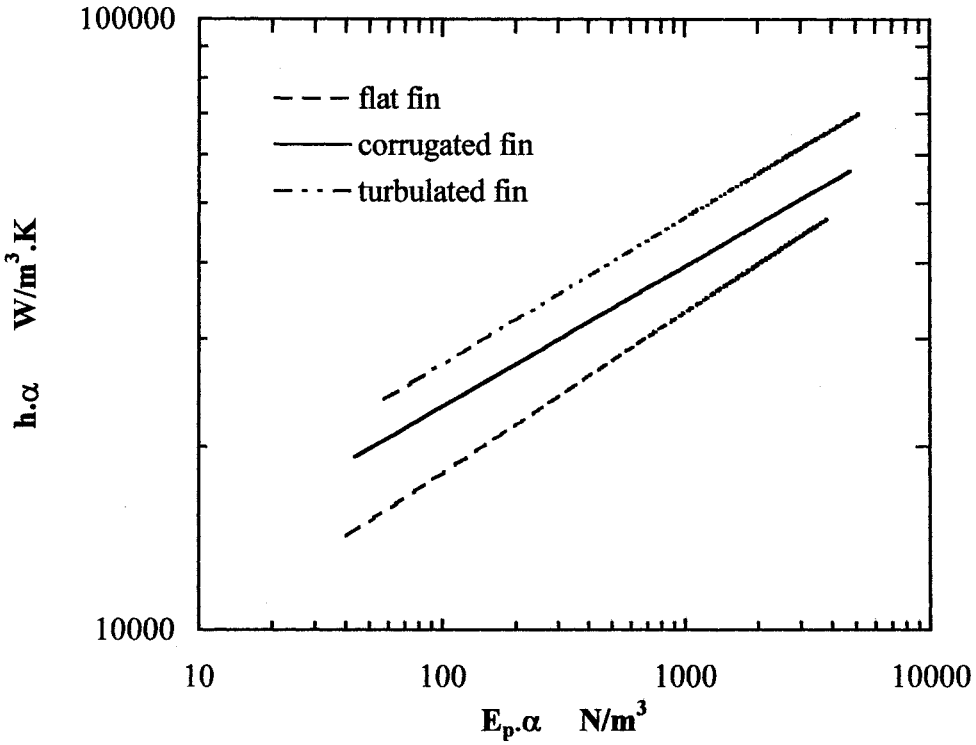

Fig. (6.42) Volume goodness factor for all fin types

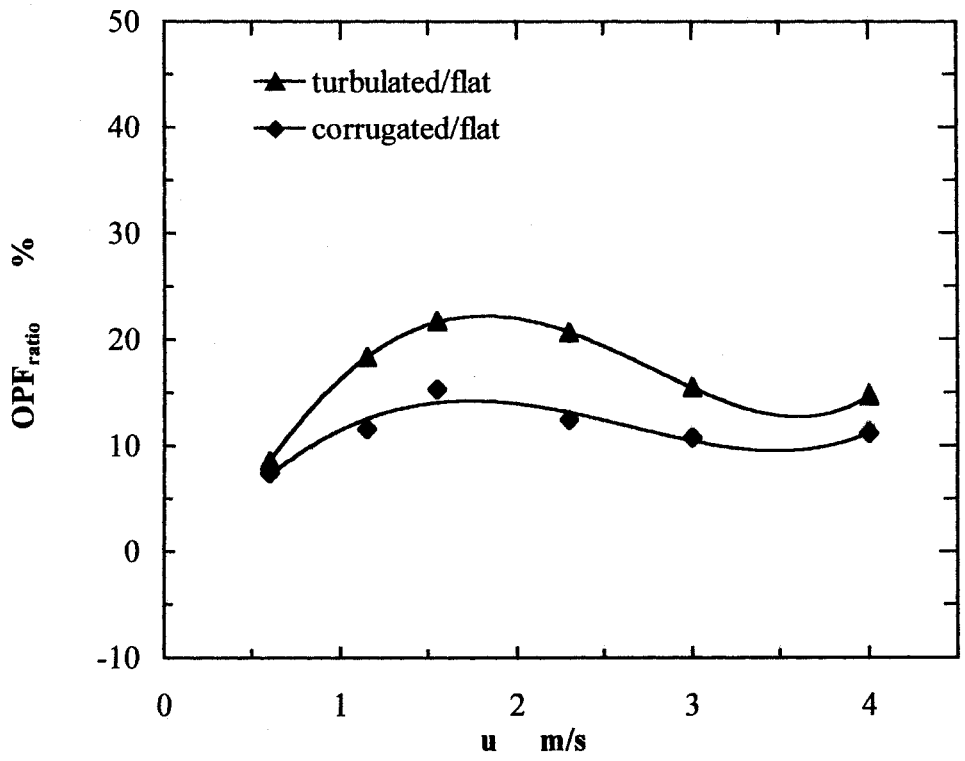

Fig. (6.43) Overall performance factor with respect to flat fin

For the same power input to chiller, it is evident that the using of corrugated and turbulated fin coils improve the overall performance of the air conditioning plant by 11.5 % and 16.5 % respectively compared with the flat fin coil. The maximum values of the OPF_{ratio} was obtained in the range of 1.2 m/s $\leq u_{ai} \leq$ 3 m/s. This improvement in the overall performance can be increased when the same strategy of the enhanced-fin surfaces are applied to the condenser-coil of the refrigeration plant.

6.10 Discussion

In the developing flow regime the velocity, pressure and temperature fields are varied with the axial flow-path length of the cooling coil. Unlike the case of the fully developed flow where the velocity, pressure and temperature fields are periodically repeatable. The wake zone at the rear of each of the tube row was largest in the case of flat fin which reduced for the corrugated fin case, while it was relatively small in the case of turbulated fin. The larger the wake zone, the poorer the heat exchanges.

The negative pressure at the rear of the last tube-row means that there were reverse flow induced by drag force caused by tubes which may be confirmed that an sufficient downstream length needs to be modelled for a good solution accuracy. A check is therefore carried out on the effectiveness of the downstream length used as illustrated in Fig. (6.44). The downstream length of fourteen tube-radius has been considered sufficient satisfactory.

In the case of flat fin, a laminar boundary layer grows along the flow direction from the leading edge, which reduces the heat exchange between the fin surface and air stream. While, the corrugated fin lengthens the flow path, inducing secondary flow and hence producing flow mixing. In the case of the turbulated fin the slits on the fin surface interrupt the growth of the boundary layer which produces a lower overall thermal resistance. The good flow mixing induced by the effect of turbulated fin can be inferred from the flow pattern shown in Figs (6.45) and (6.46).

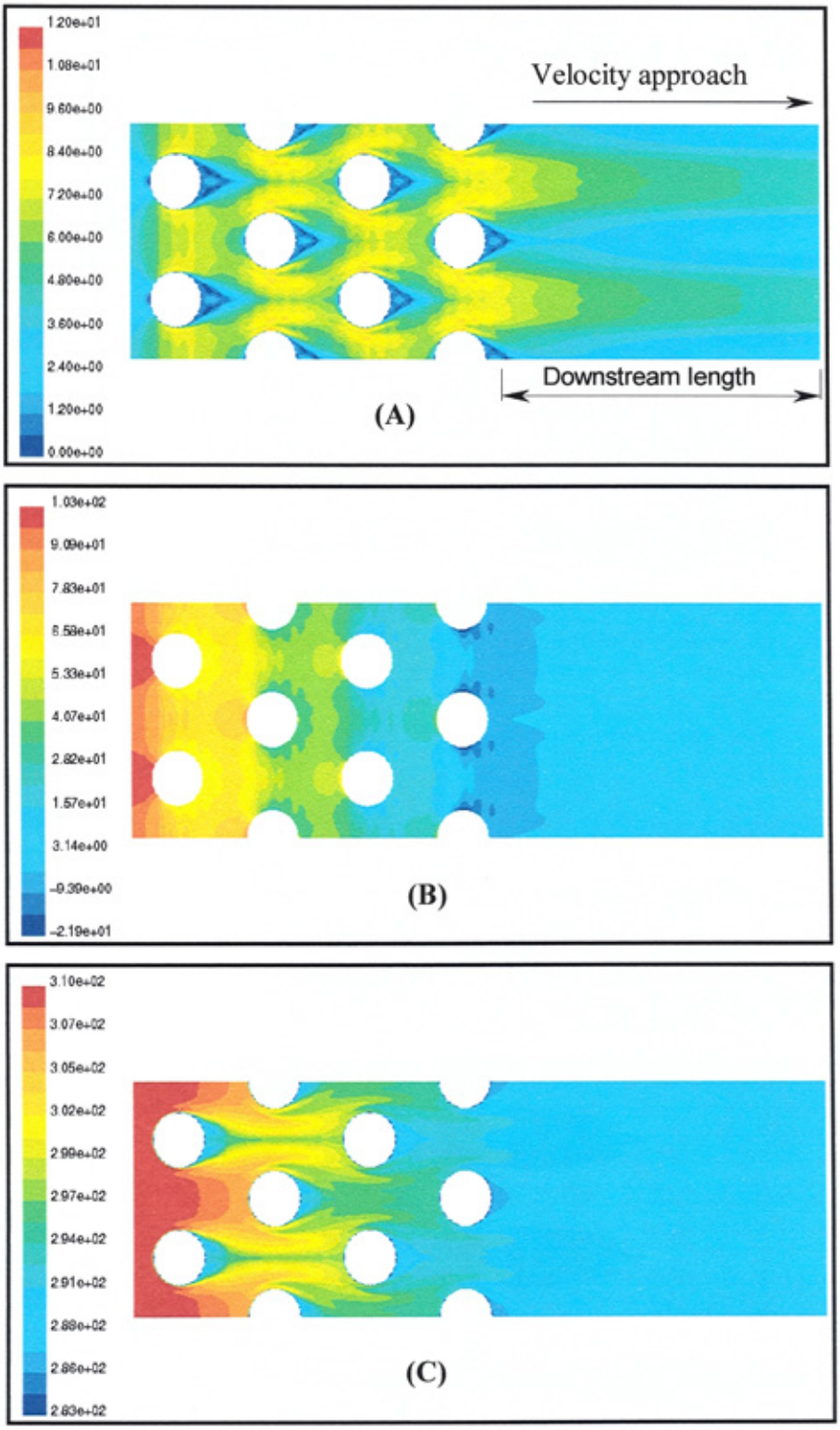

Fig. (6.44) Velocity, pressure, and temperature approach at u_{ai} = 3 m/s

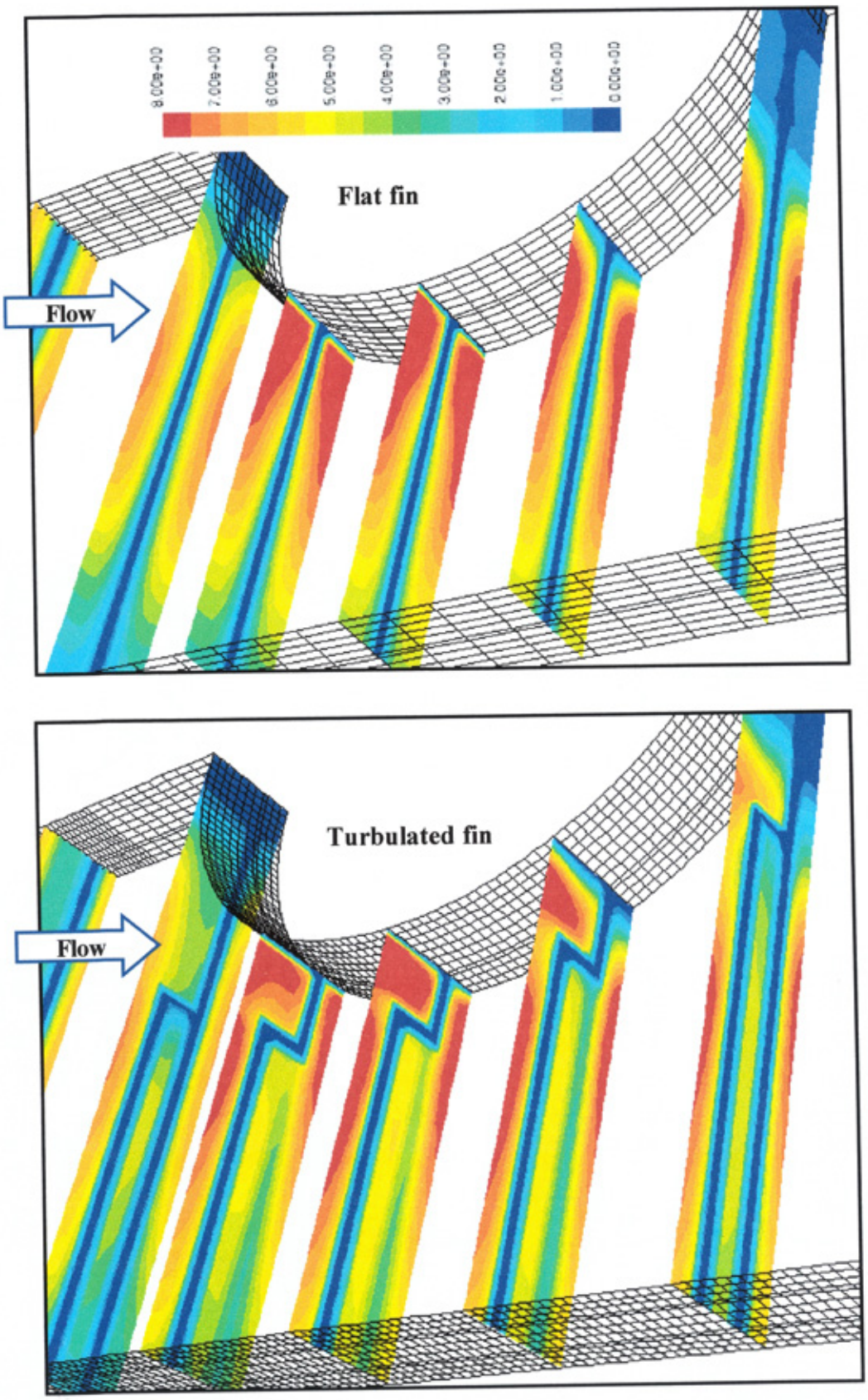

Fig. (6.45) Velocity contours of individual cross-section planes

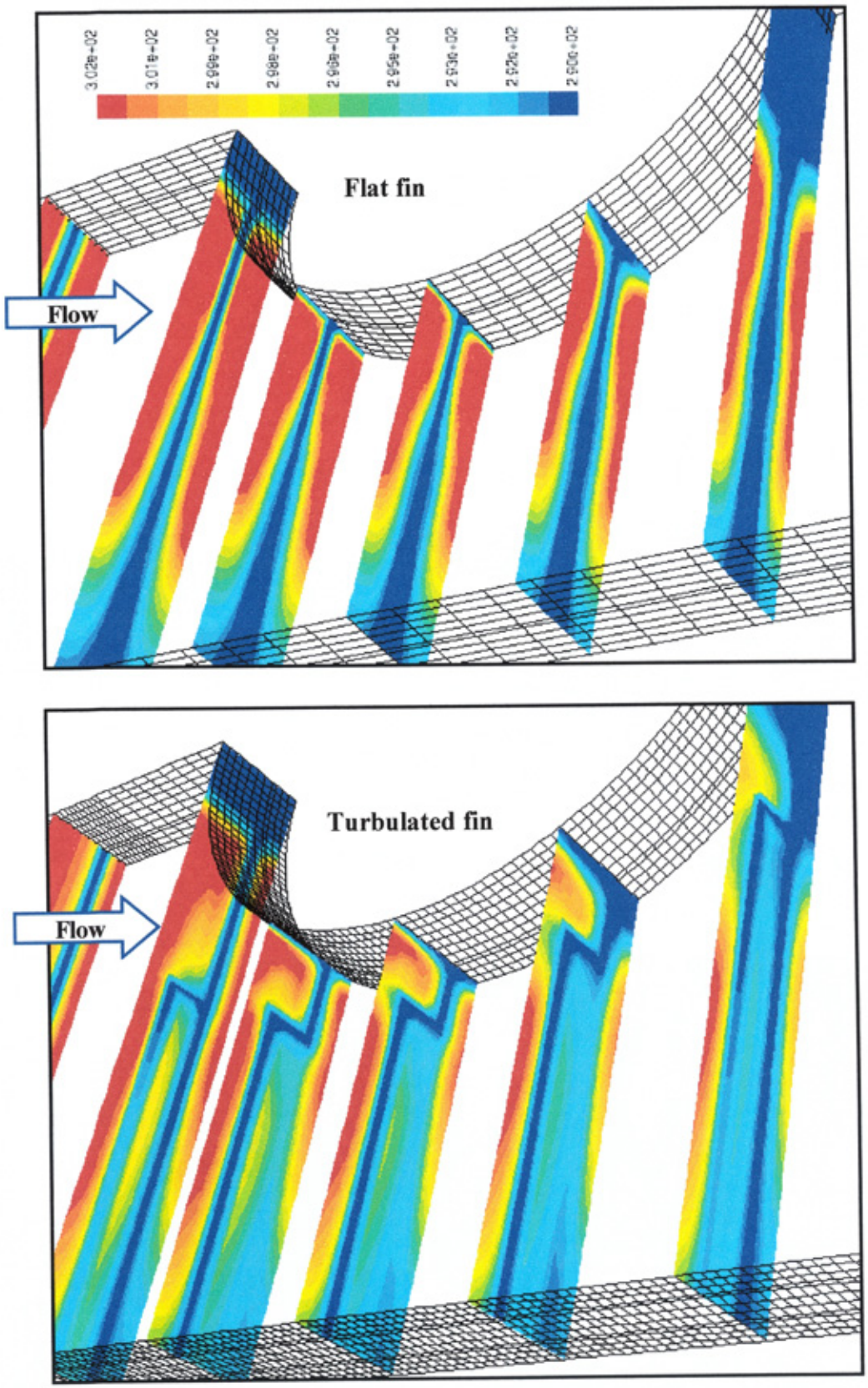

Fig. (6.46) Temperature contours of individual cross-section planes

An increase of the pressure drop is evident for the corrugated fin case due to the increased flow resistance of the airflow along the lengthened undulating path of peaks and valleys. In the case of turbulated fin the increase on the flow resistance produced by interrupted fin surfaces and the flow friction loss due to the effect of leading and trailing edges of fin slits this may be explained the highest pressure drop.

The modelling assumption of an isothermal fin would require the thermal conductivity of the fin material to be infinity or the thermal resistance of the fin material to be equal to zero. This overpredicted the Nusselt number by the range of 8.5 % to 43 % compared with the conjugate heat transfer, confirming that the isothermal fin over-predicts the heat transfer coefficient by 5 % to 35 %, [Jang *et al*, 1998].

The fin efficiency is depending upon the heat transfer coefficient, this may be explained the decrease of fin efficiency with the increase of air velocity and the flat-fin efficiency was higher than that of turbulated fin ($\eta_{flat} > \eta_{turbulated}$). In the case of flat fin, there is good agreement between the fin efficiency predicted using the results of TRTG model and that obtained from the approximation method of Schmidt. In the case of corrugated and turbulated fin geometries, the mean deviation was 3 % for u_{ai} = 1 m/s and 8 % for u_{ai} = 4 m/s.

6.11 Conclusion

In this chapter the three-dimensional CFD modelling of the fin-and-tube cooling coils having flat, corrugated and turbulated fin geometries have been investigated in developing flow regime. A finite volume discretization method was used for Reynolds number ranging from 285 to 1880. Multi-block hexahedral mesh technique with a body-fitted coordinates system was applied for all computational domains. Five types of modelling approaches were adapted for each fin type including isothermal fin-and-tube, conjugate heat transfer, periodic boundaries, tube-row temperature gradient and the effect of edge-burrs. The conjugate heat transfer model with variable row-on-row temperature including

periodic boundaries (tube-row temperature gradient model) was considered as a basic model, which was validated against the experimental results. The performance evaluation criteria of the cooling coils having various fin geometries were also investigated. The prediction of the fin efficiency for these fin geometries using the validated-model results was also presented.

The main conclusions are:

- The isothermal fin-and-tube approximation over-predicted the heat transfer coefficient up to 42 % when compared with conjugate heat transfer model.
- The assumption of symmetrical boundaries was showed to be inappropriate for the corrugated and turbulated fin models.
- Good agreement was obtained between the CFD modelling results and the corresponding experimental results of the heat transfer coefficient and pressure drop within experimental uncertainties of ± 10 % and ± 6 % respectively.
- At a given pressure drop (ΔP = 52 N/m^2 corresponding to u_{ai} = 2.3 m/s), the heat transfer coefficient of the corrugated and turbulated fin coils was higher than that of flat fin by 16 % and 36 % respectively.
- For typical operating conditions, the corrugated and turbulated fin coils required core volumes of 19 % and 40 % less than that of flat fin coil respectively for the same coil performance.
- The use of corrugated and turbulated-fin coils would improve the overall performance factor (OPF) of the air conditioning plant by 11.5 % and 16.5 % respectively compared with the flat fin coil at the same chiller-power.
- The prediction of the flat-fin efficiency was in good agreement with that obtained from the method of Schmidt. In the case of corrugated and turbulated fin geometries, the Schmidt method was deviated within 3 % to 8 % from the present prediction.

CHAPTER –VII-

Parametric modelling of fin-and-tube cooling coils

7.1 Introduction

In this chapter, the influence of the major geometrical parameters on cooling coils performance was investigated for the flat, corrugated and turbulated fin types. These parameters may be viewed as design degree-of-freedom in practice and hence merit analysis using the model validated in the previous chapter. These parameters are:

- Fin pitch
- Fin material
- Fin thickness

The aim was to obtain an insight into the influence of these parameters on the thermo-fluid characteristics of the flat, corrugated and turbulated fin cooling coils. The performance characteristics of the cooling coils with fin pitch of (2.08 mm, 2.5 mm and 3.125 mm), fin materials of (copper, Aluminium, Stainless Steel, Copper-Nickel alloy) and fin thickness of (0.12 mm, 0.25 mm) which was commonly used according to design consideration of the air conditioning plant are investigated.

In the CFD modelling of these parameters, the multi-blocks hexahedral mesh technique, Conjugate heat transfer and periodic boundaries are adapted for all models except the mesh density (number of nodes) which is varied according to fin pitch and fin thickness. The mesh generation are similar to that described in the pervious chapter for the original conjugate model with fin pitch of 2.5 mm and fin thickness of 0.12 mm (i.e. all models are adapted with approximately constant cell size).

7.2 Effect of fin pitch

Since the fin pitch and the inlet air velocity may be varied, the performance characteristics of the cooling coils are evaluated based on a constant mass flow rate and fin surface area. All the CFD models have the same specifications except fin geometry (flat, corrugated and turbulated), fin pitch (2.08 mm, 2.5 mm and 3.125 mm) and mesh density. Fig. (7.1) shows the variation of the heat transfer coefficient versus the air mass flow rate for the flat fin case. The increase of the heat transfer coefficient with decreasing of the fin pitch is obtained at the expense of the pressure drop as illustrated in Fig. (7.2). The airflow resistance increase with a smaller fin spacing. At a given mass flow of 0.58 kg/s (corresponding to u_{ai} = 2.3 m/s for f_p = 2.5 mm), the increase in heat transfer coefficient and pressure drop for the f_p = 2.08 mm compared to f_p = 2.5 mm were 11.3 % and 45 % respectively while these values decreased by 17 % and 43 % respectively for f_p = 3.125 mm.

A similar pattern of results was obtained for the corrugated and turbulated fin coils as illustrated in Figs. (7.3)-(7.6) respectively.

The smaller fin pitch, the higher transfer surface area for a given core volume however, better heat transfer performance is obtained at the expense of higher pressure drop. In order to quantify the effectiveness of fin pitch, a compromise is needed between the heat transfer coefficient and the pressure drop. For this purpose, the heat transfer per unit temperature difference per unit core volume versus the friction power per unit core volume (volume goodness factor) was compared at various fin pitch as illustrated in Figs. (7.7)-(7.9). This reveals that the higher volume goodness factor for all cases occur at the higher fin pitch (f_p = 3.125 mm).

7.3 Effect of fin materials

The choice of fin material is governed by consideration of thermal conductivity, corrosion properties, manufacturing costs, and the material density.

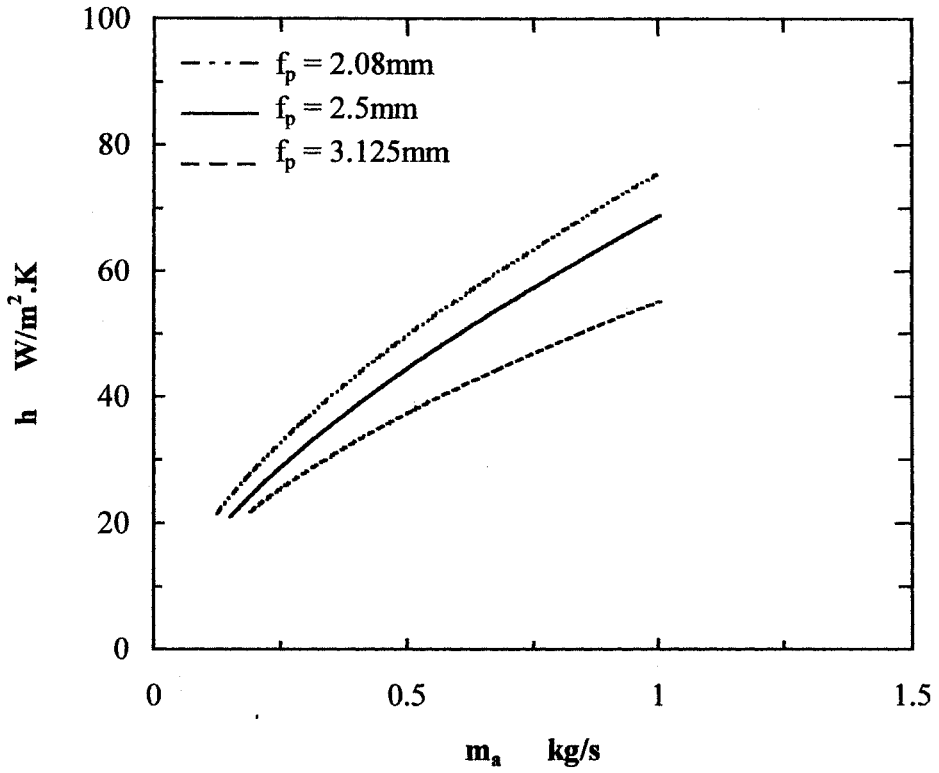

Fig. (7.1) Heat transfer coefficient of the flat fin case

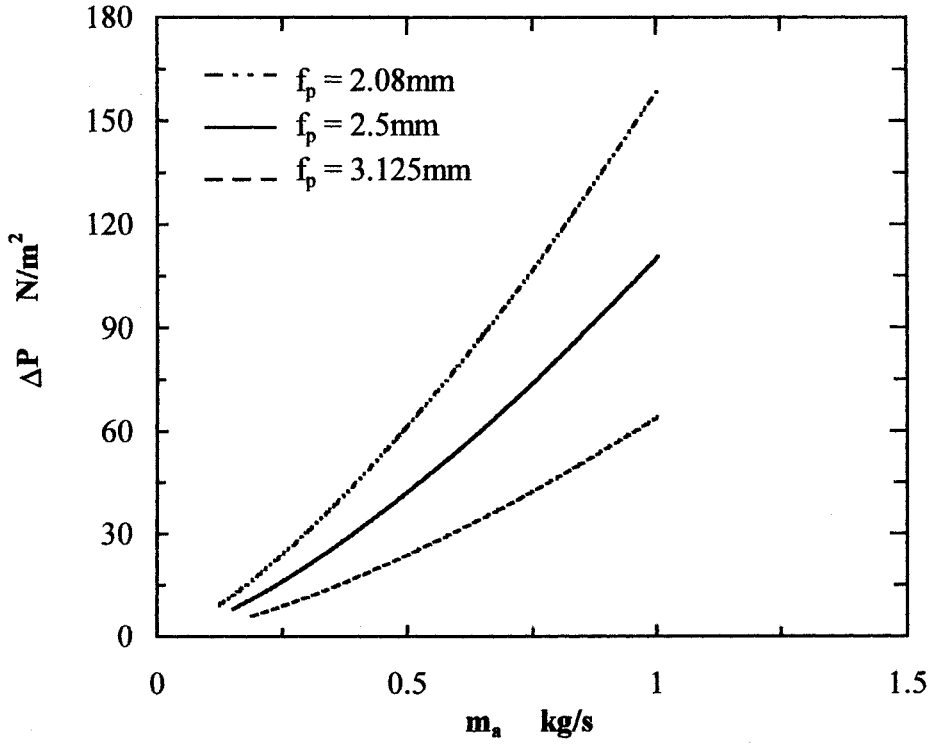

Fig. (7.2) Pressure drop of the flat fin case

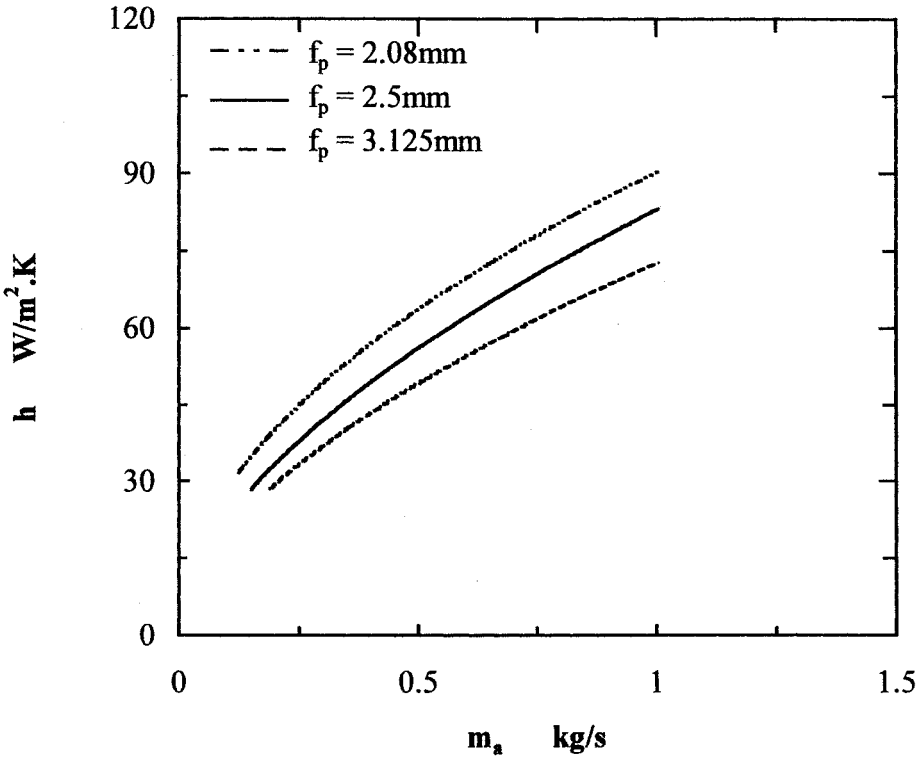

Fig. (7.3) Heat transfer coefficient of the corrugated fin case

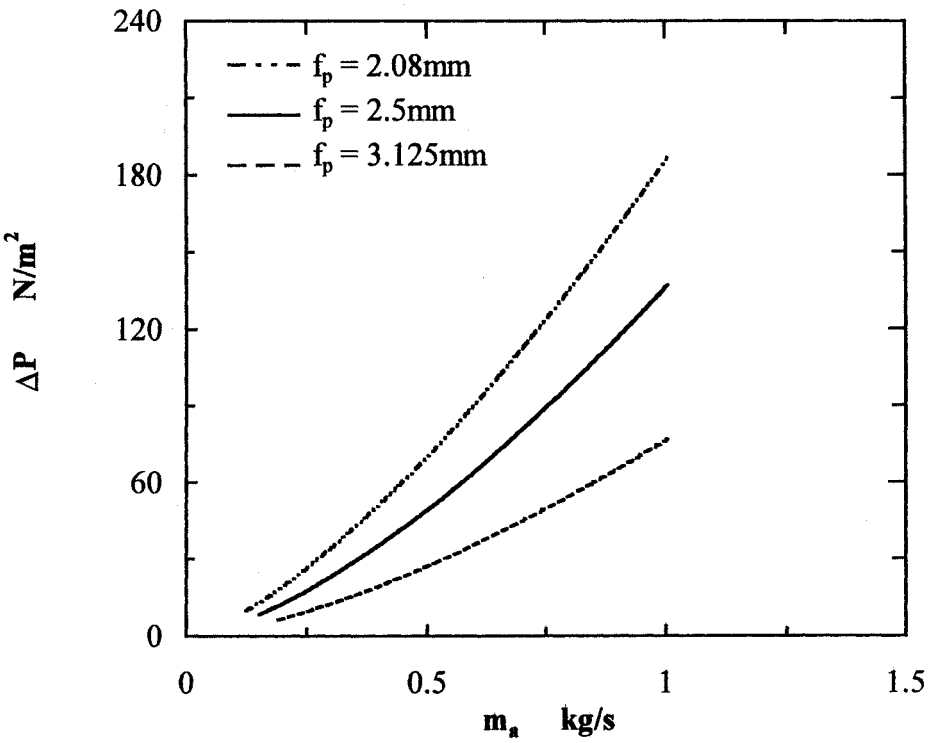

Fig. (7.4) Pressure drop of the corrugated fin case

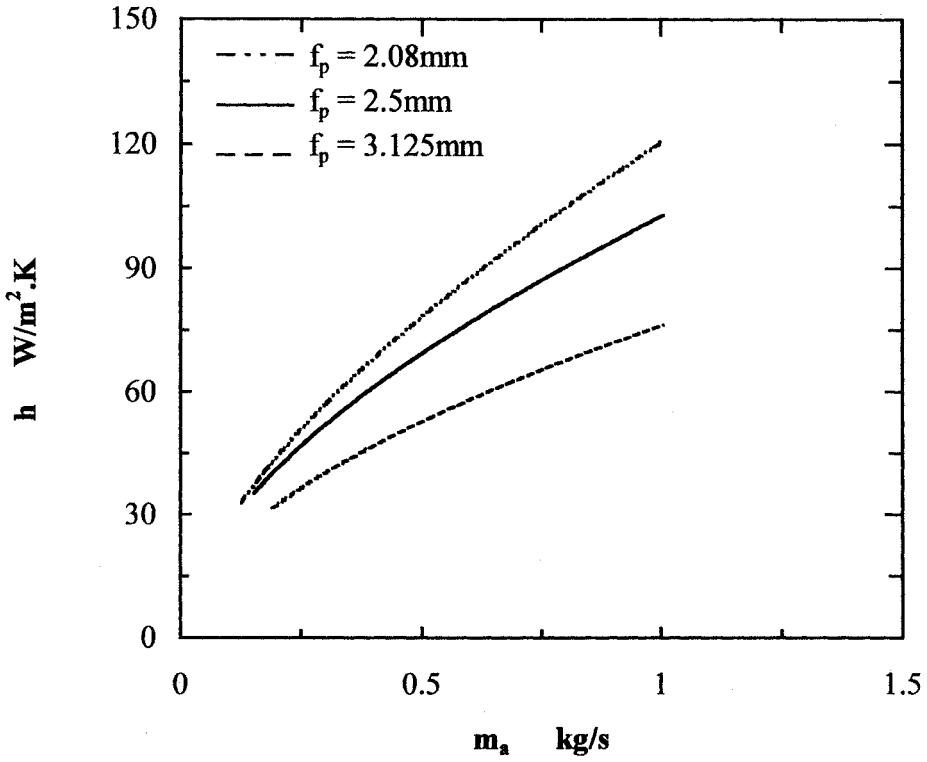

Fig. (7.5) Heat transfer coefficient of the turbulated fin case

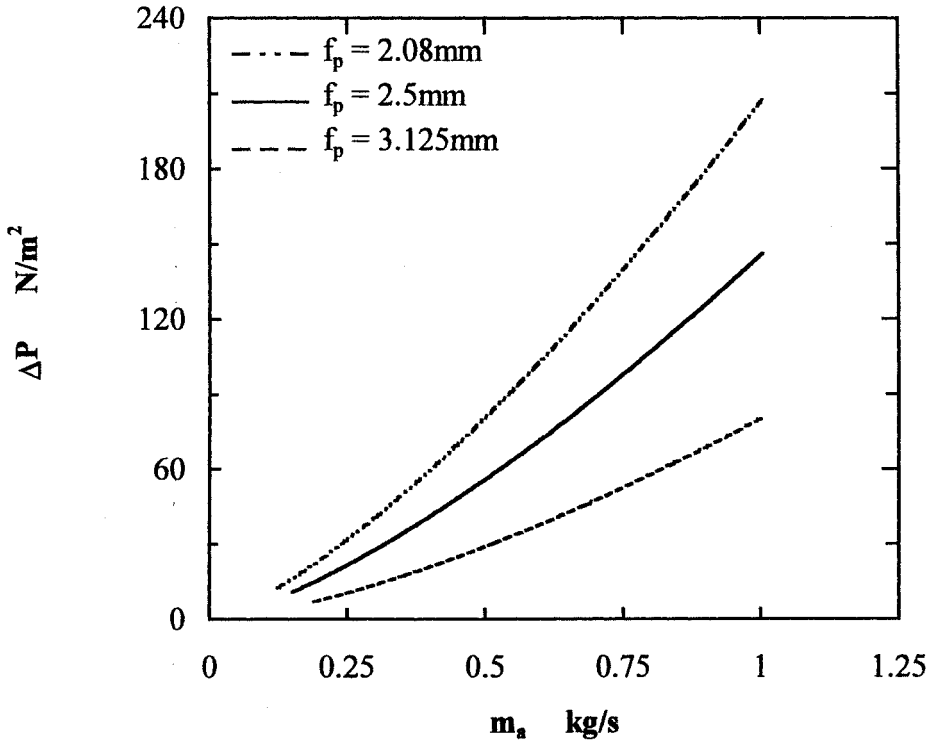

Fig. (7.6) Pressure drop of the turbulated fin case

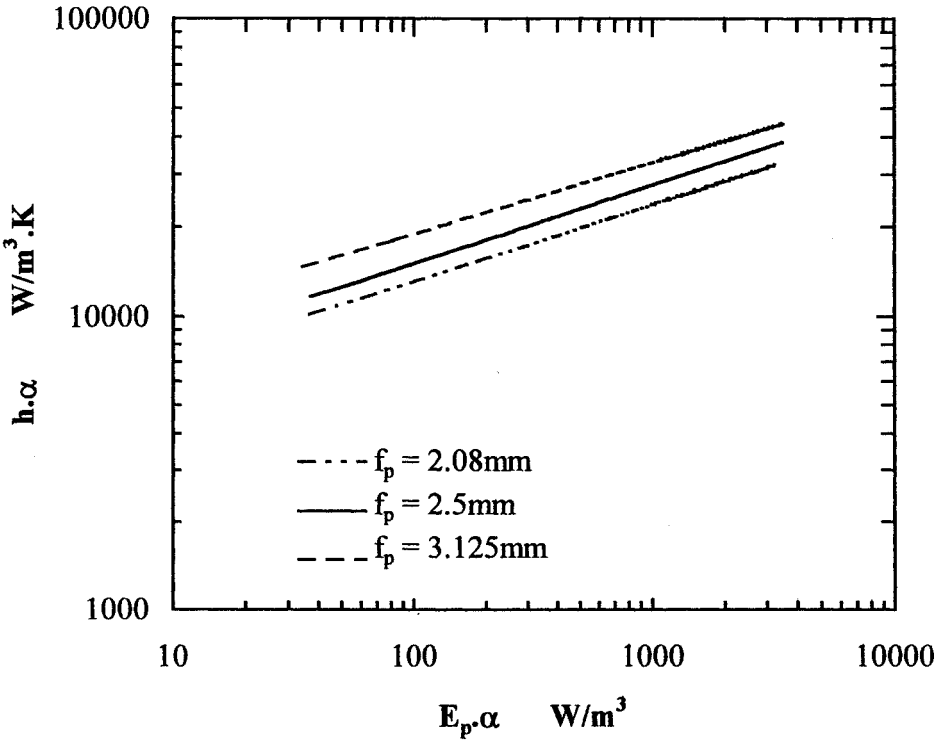

Fig. (7.7) Volume goodness factor of the flat fin case

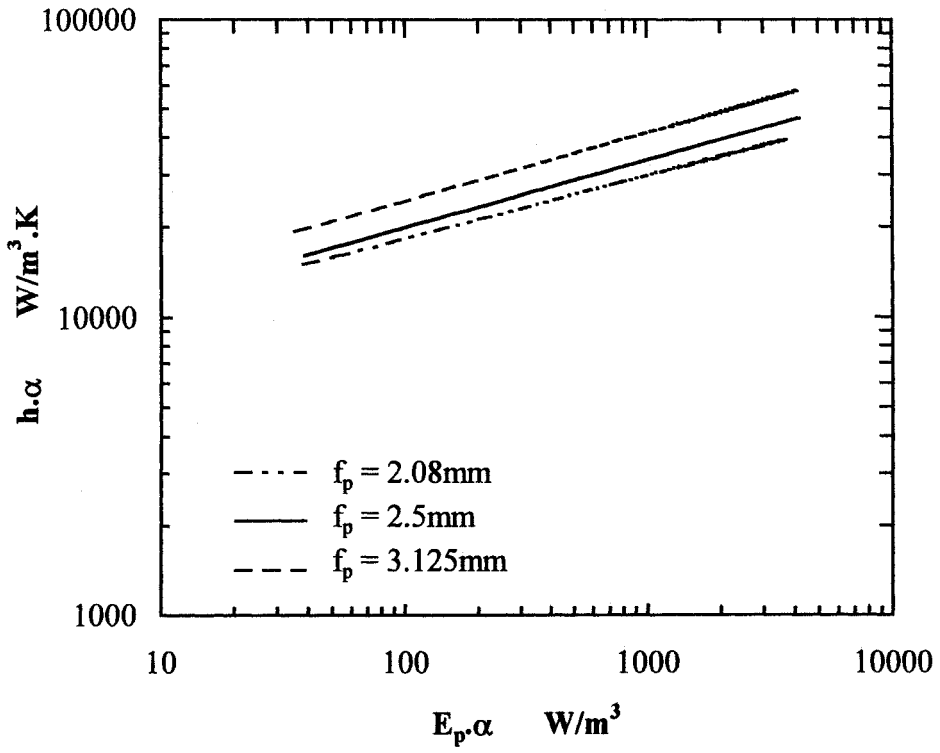

Fig. (7.8) Volume goodness factor of the corrugated fin case

The effectiveness of a fin material is given directly by the ratio of its thermal conductivity to its density (k/ρ) [Walker 1982]. Four CFD models were adapted for each fin type according to the materials of copper, aluminium, stainless steel (AISI 302) and copper-nickel alloy (cupro-nickel). The fin pitch and the thickness were fixed at the base values of 2.5 mm, 0.12 mm respectively and in all other respects the models hade the same specification as described in chapter –VI-. The thermal specifications of the fin material are given in Table (7.1).

The use of the copper-nickel alloy as a fin material in the case of corrosive environment (chemical industries, sea-houses) has been investigated and compared with a common material in such cases of stainless steel. The copper-nickel alloy has not reported as a fin material of such fin-and-tube cooling coils.

The Nusselt number of the flat fin coil with various fin materials is illustrated in Fig. (7.10). The fin material of copper has the highest value of the Nusselt number followed by aluminium while the fin material of stainless steel has the lowest value. At the practical air velocity of 2.3 m/s (Re = 1080), the Nusselt number of the copper fin material was 2.5 % greater than that of aluminium, while the stainless steel and copper-nickel were 26 % and 21 % lower than that of aluminium fin respectively. The prediction of the fin efficiency of the flat fin coil based on equation (7.1) is illustrated in Fig. (7.11). Again, the copper fin material has the highest fin efficiency followed by aluminium while the lowest fin efficiency was with stainless steel.

A similar pattern of results was also obtained for the corrugated and turbulated fin coils with various fin materials as illustrated in Figs. (7.12)-(7.15) respectively.

Table (7.1) Thermal properties of the fin materials [Fluent database, 1999]

Items		**Copper**	**Aluminium**	**Stainless steel** [Incropera,1996]	**Copper-Nickel** [Powell, 1990]
ρ,	kg/m^3	8978	2719	8055	8900
Cp,	J/kg.K	381	871	480	377
K	W/m.K	387.6	202.4	15.1	50

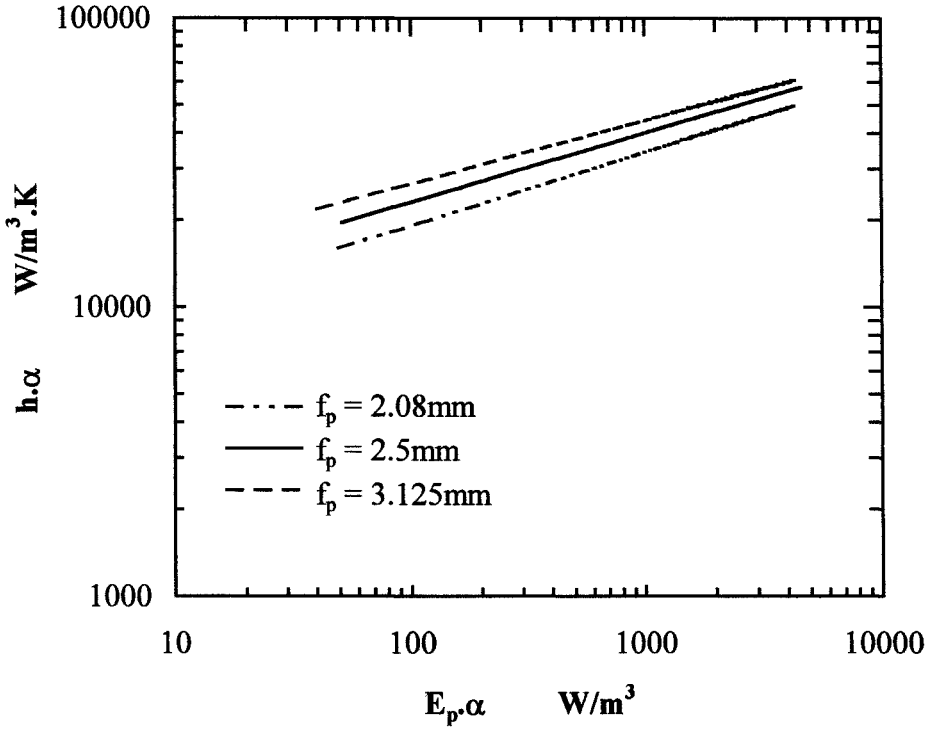

Fig. (7.9) Volume goodness factor of the turbulated fin case

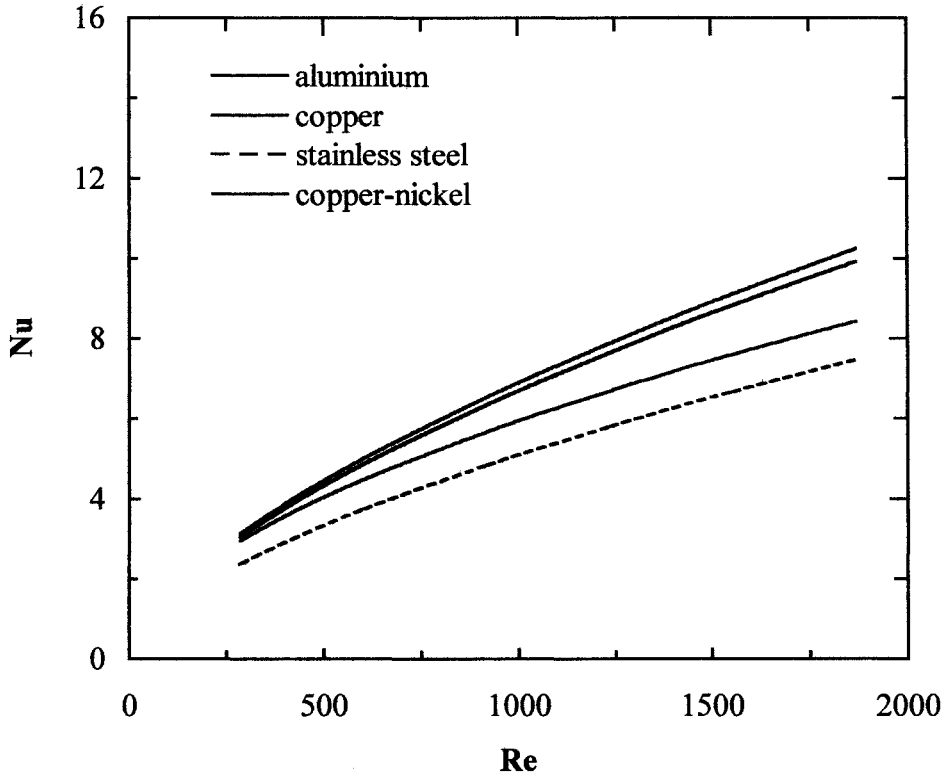

Fig. (7.10) Effect of fin material on the Nusselt number of the flat fin

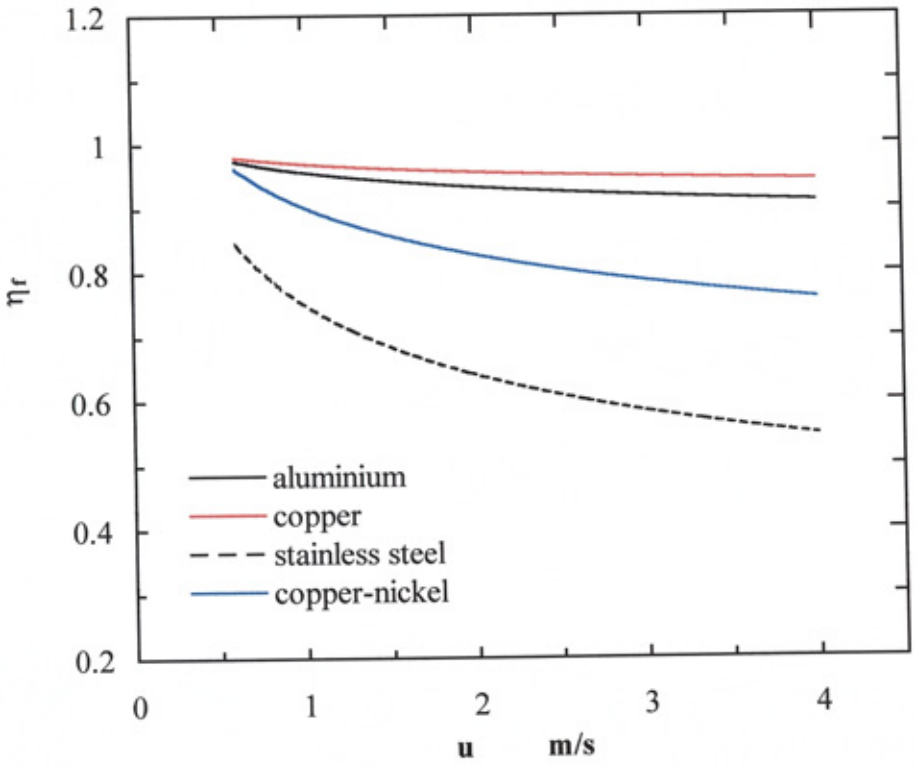

Fig. (7.11) Fin efficiency (flat fin)

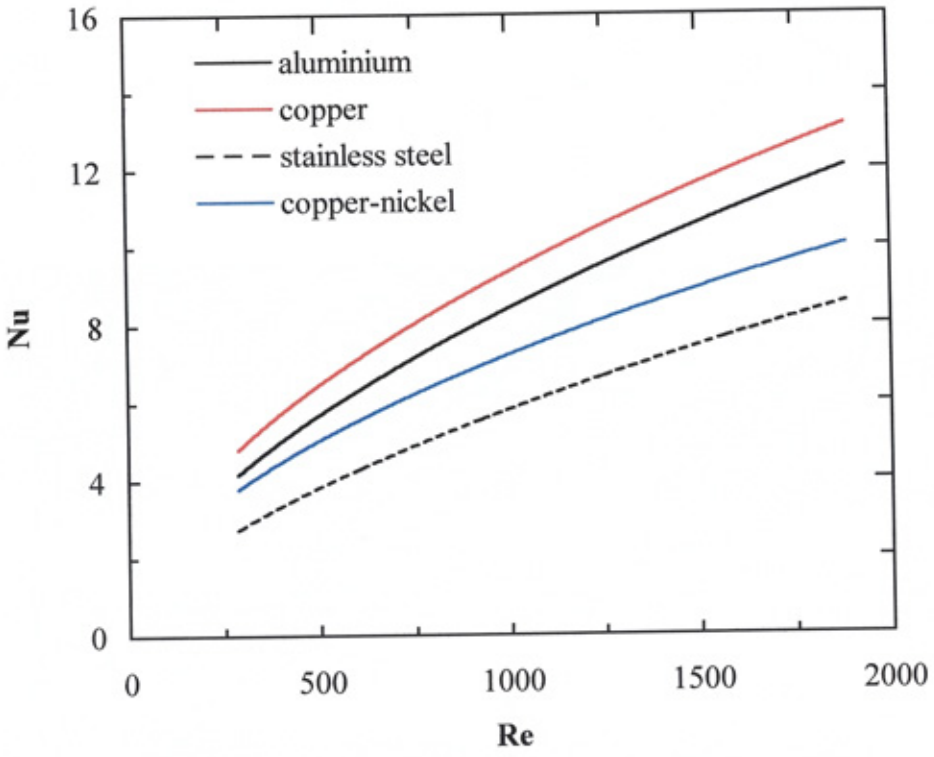

Fig. (7.12) Effect of fin material on the Nusselt number (corrugated fin)

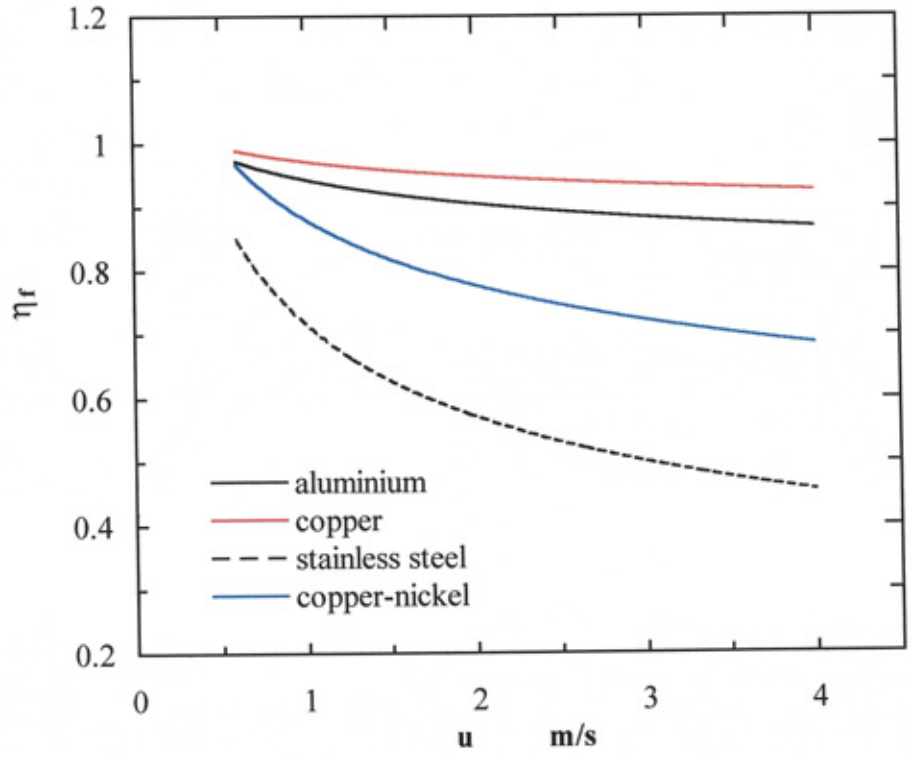

Fig. (7.13) Fin efficiency (corrugated fin)

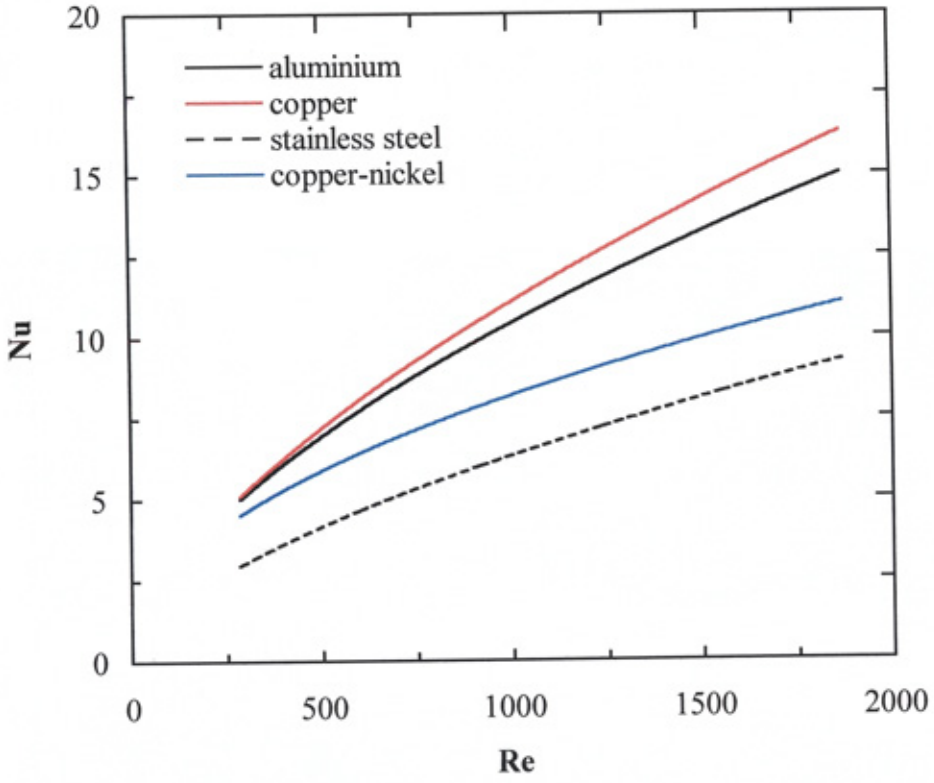

Fig. (7.14) Nusselt number of the turbulated fin case

$$\eta_f = 1 - \frac{A_o}{A_f}\left(1 - \frac{Q_{conj}}{Q_{iso}}\right) \tag{7.1}$$

These figures show that the fin efficiency is strongly dependent on the fin material as well as air velocity. The thermal characteristics of the copper-nickel alloy as fin material is better than that of stainless steel.

7.4 Effect of fin thickness

The fin thickness is a parameter that is governed mainly by the strength of the fin material and its conductivity. Conjugate heat transfer models were adapted for each fin type with a fin thickness of 0.25 mm and compared with the original model of fin thickness of 0.12 mm. The Nusselt number and the friction factor of the flat fin coil for this case are illustrated in Figs. (7.16) and (7.17) respectively.

It is noted that, the increase of fin thickness led to a small decrease in Nusselt number and a small increase in friction factor. This is also evident for the corrugated fin as illustrated in Figs. (7.18) and (7.19). In the case of the turbulated fin geometry a significant decrease in Nusselt number and increase in friction factor was noted as illustrated in Figs. (7.20) and (7.21) respectively.

The effect of the fin thickness (0.12 mm $\leq t \leq$ 0.25 mm) on the flat and corrugated fin coils was relatively small. The present results agree with those of Abu Madi *et al* (1998). They concluded that for both flat and corrugated fins, an increase in the heat transfer coefficient with smaller fin thickness while, the effect of fin thickness of 0.13 mm $\leq t \leq$ 0.2 mm on the friction was very small [Abu Madi *et al*, 1998]. However, Wang *et al* (1996) concluded that the fin thickness of 0.13 mm $\leq t \leq$ 0.2 mm have a negligible effect on the thermal hydraulic characteristics of the flat fin heat exchanger.

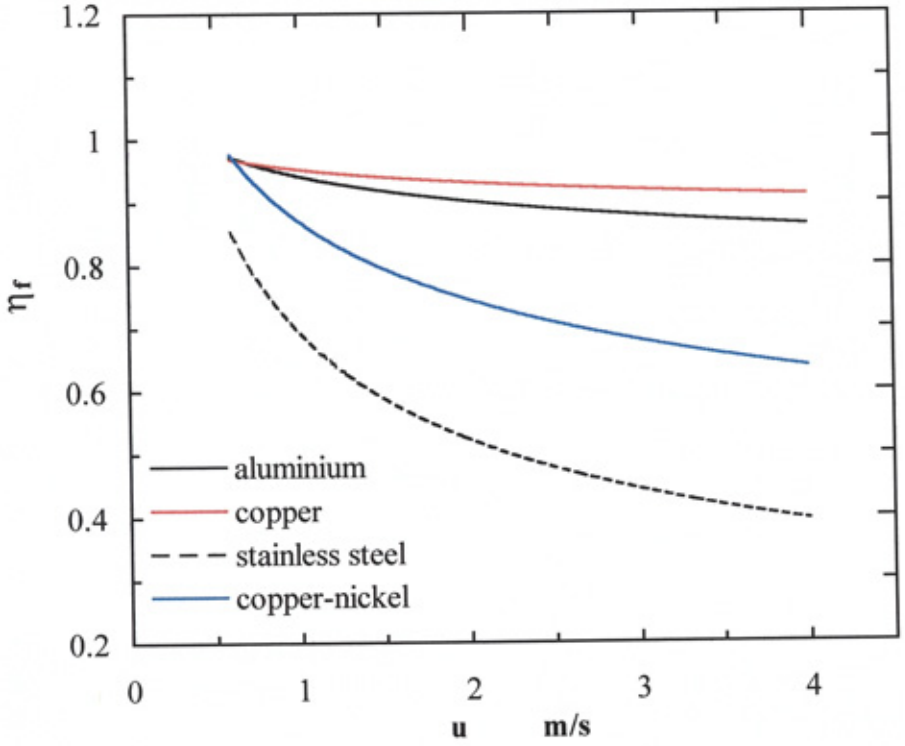

Fig. (7.15) Fin efficiency (turbulated fin)

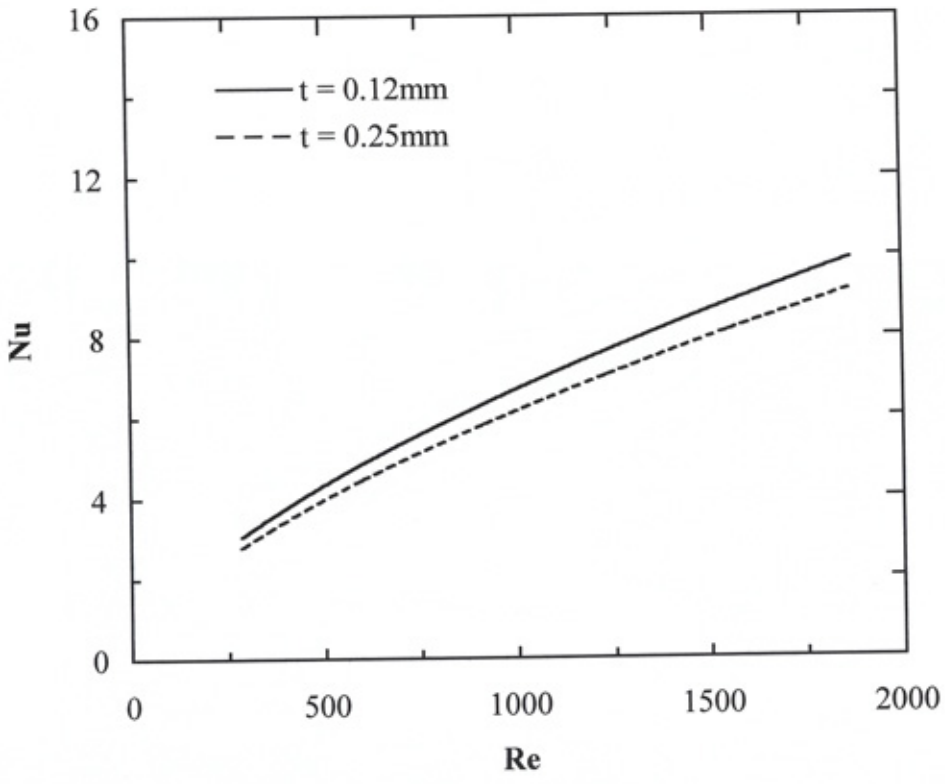

Fig. (7.16) Effect of fin thickness on the Nusselt number (flat fin)

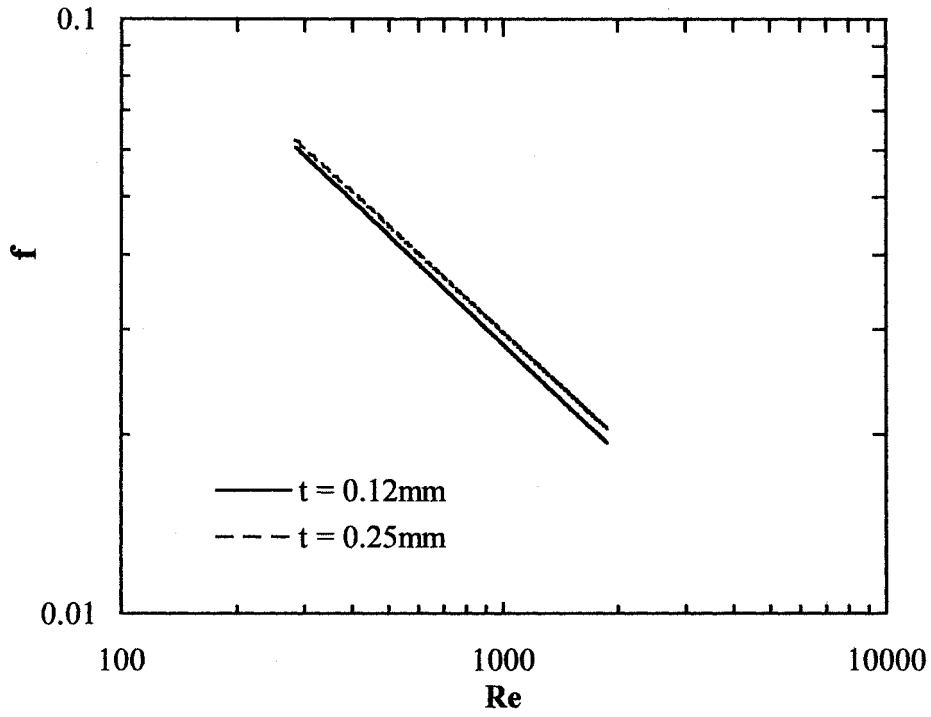

Fig. (7.17) Effect of fin thickness on the friction factor (flat fin)

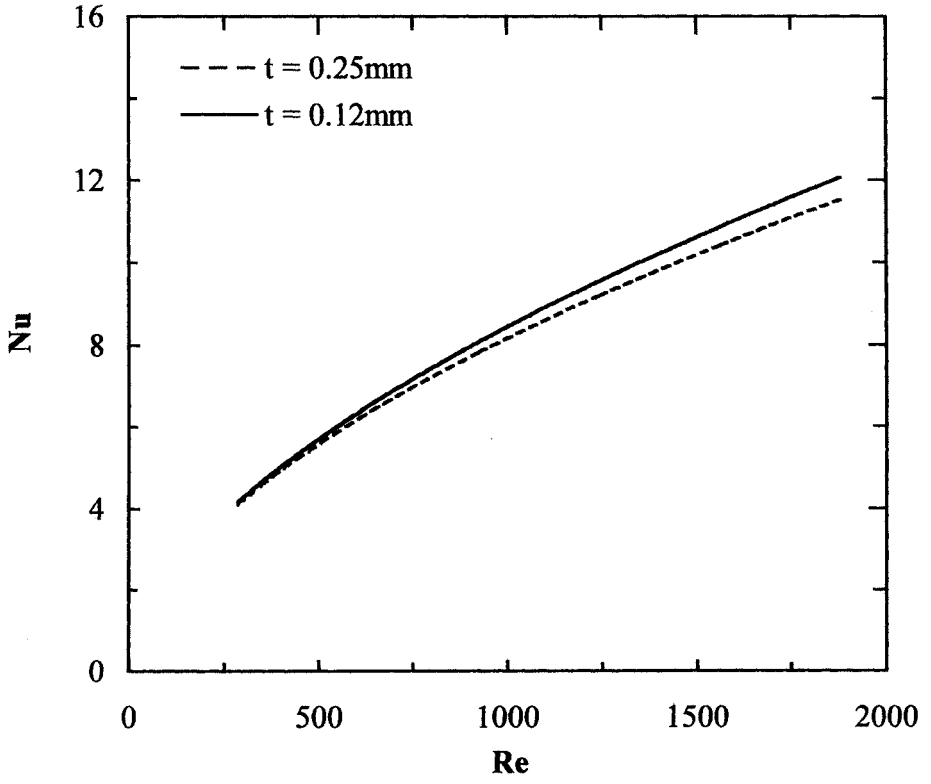

Fig. (7.18) Effect of fin thickness on the Nusselt number (corrugated fin)

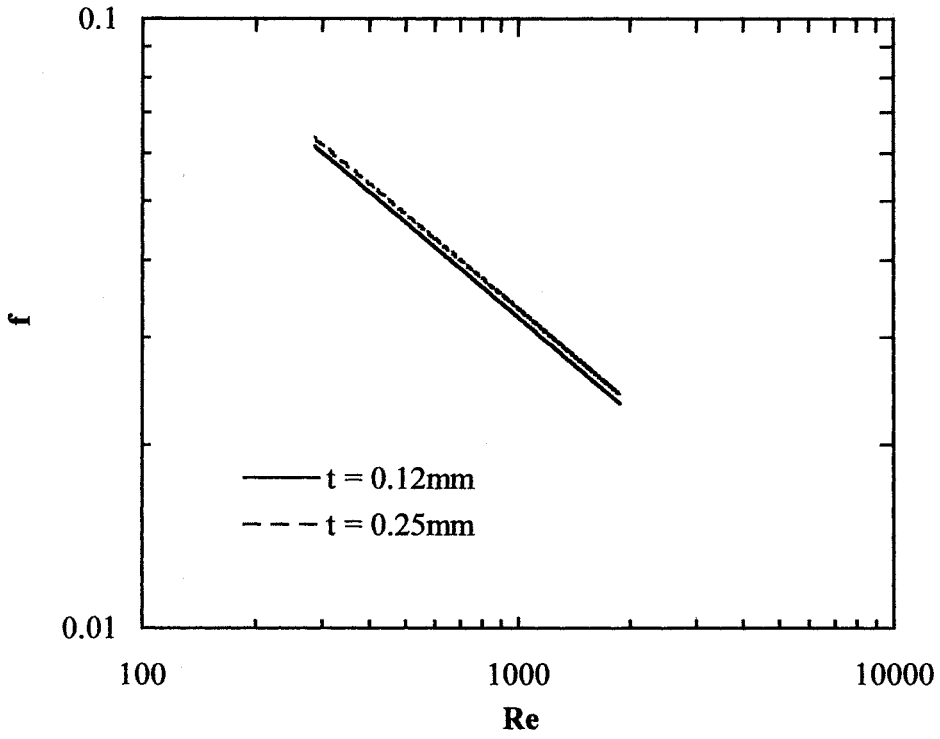

Fig. (7.19) Effect of fin thickness on friction factor (corrugated fin)

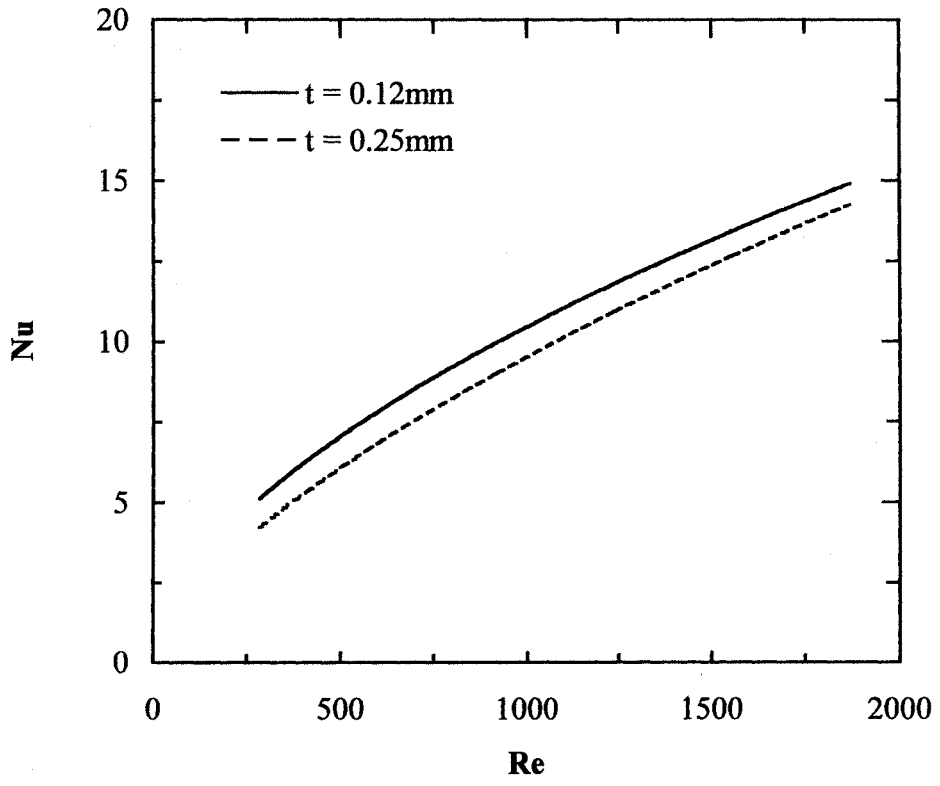

Fig. (7.20) Effect of fin thickness on the Nusselt number (turbulated fin)

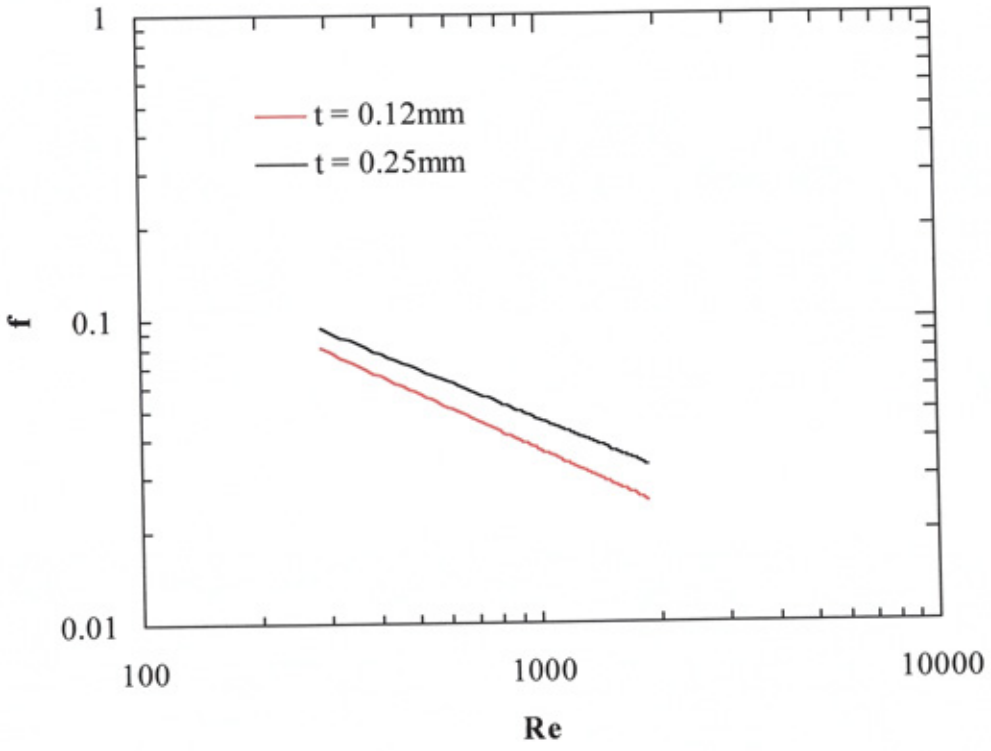

Fig. (7.21) Effect of fin thickness on the friction factor (turbulated fin)

7.5 Discussion

In general, the performance evaluation of the fin-and-tube cooling coils required a fixed datum to make a direct comparison possible. Since the fin pitch and the inlet air velocity are varied according to fin pitch and inlet velocity, therefore the performance characteristics of the cooling coils are evaluated under a constant mass flow rate. In some of the previous studies such as Rich (1973), Wang *et al* (1996, 1997a, 1998b & 1999c) and Wang and Chi (2000), the evaluation characteristics of the fin-and-tube heat exchangers were conducted under constant Reynolds number which is showed to be inappropriate (in such

case, the mass flow rate and the hydraulic diameter are varied according to fin pitch and inlet velocity, and hence the Reynolds number was not the fixed datum to compare from).

The mechanism of using a smaller fin pitch is used to obtain a large surface area for heat transfer; however, this is obtained at the expense of higher-pressure drop. As the fin pitch decreases, the flow acceleration through the fin passages increases and the ability to form a vortex upstream of the tube increases, which reduces the boundary layer thickness. This may be explained the increased of heat transfer coefficient with smaller fin pitch.

In order to qualify the increase in both heat transfer and friction with smaller fin pitch, the volume goodness factor criteria is used. The direct comparison of the heat transfer coefficient with the pressure drop is not helpful here, since the mass flow rate changes with the fin pitch at a given inlet velocity.

Although the heat transfer coefficient and pressure drop increase with decreased fin pitch, an improved volume goodness factor is obtained with increased fin spacing. Hence, the selection of the cooling coils fin-pitch not only depends on the heat transfer and pressure drop characteristics but also consideration of fouling, cost, weight, and noise have to sought.

The fin efficiency varies as the inverse of the heat transfer coefficient, which in turn is strongly dependent on the air velocity (hence, a decrease in fin efficiency with air velocity). The thermal resistance of the fin is mainly dependent on its thermal conductivity (the higher thermal conductivity the lower thermal resistance for a given thickness), thus the copper fin material has the highest values of Nusselt number and fin efficiency while stainless steel has the lowest values. Although copper is the best from the standpoint of thermal conductivity, aluminium is more common choice due to the additional benefits related to low cost and weight. The Nusselt number of copper material was 1% to 14 % higher than that of aluminium however, it was 2.9 times the aluminium price [CES, 1999] at the same sheet volume.

Another possibility is the use of copper-nickel alloy (Cu = 87.5 % Ni = 10%, Fe = 1.5% and Mn = 0.7 %) which, through common in other types of heat exchanger (e.g. shell and tube). It has not reported as a fin material of the fin-and-

tube cooling coils. Copper-nickel alloy is very corrosion resistant and thermally stable. It is virtually immune to stress corrosion cracking and exhibits high oxidation resistance in steam and moist air as well as air stream containing seawater vapour, [Powell, 1990]. The effectiveness (k/ρ) and the material price of the copper-nickel alloy is approximately three times and 1.1 times that of stainless steel respectively. At the practical air velocity (u = 2.3 m/s), the Nusselt number and fin efficiency using copper-nickel alloy were higher than that of Stainless Steel by (22 % to 28 %) and (29 % to 48 %) respectively.

Finally the fin thickness was considered. Although the thermal resistance of the fin decreases with increase of fin thickness, the Nusselt number decreases, this may be explained by the global increase of the thermal resistance of the conduction-convection coupling (convection from primary surface and conduction to secondary surface) rather than the smaller hydraulic diameter.

A scope of the conduction-convection coupling can be clearly explained using the fin effectiveness. The fin effectiveness was referred to the total heat transfer (conduction-convection) of the finned surface to the convection heat transfer form the same surface without fins. The maximum fin effectiveness ε_f may be expressed as, [Heggs, 1996]:

$$\varepsilon_f = \sqrt{\frac{k.p_i}{h.A_c}} \quad \text{or} \quad \varepsilon_f = \sqrt{\frac{2k}{h}\left(\frac{1}{t}+\frac{1}{\pi D}\right)} \tag{7.2}$$

Where A_c and p_i are the cross-section area and perimeter of the fin at the fin-root respectively. It is clear that, the fin effectiveness enhance by using smaller fin thickness for a given material and tube diameter. For this reason the use of thin fin is preferred from heat transfer point of view.

As the fin thickness increases, the pressure drop increases for which the same reasons as in the case with smaller fin pitch. In the turbulated fin case, the increase in fin thickness led to a significant increase in form drag rather than an increase in flow resistance throughout the turbulated fin passages.

7.5 Conclusion

In this chapter the influence of key design parameters of fin-and-tube cooling coils have been investigated. The characteristics of the cooling coils having various fin geometries, fin pitches, fin materials, and fin thickness were analysed numerically based on a validated models of these cooling coils. Multi-block hexahedral mesh techniques with conjugate heat transfer, periodic boundaries were applied for all computational domains while the mesh density was varied according to fin pitch and fin thickness.

The main conclusions are:

- The heat transfer coefficient and pressure drop increased with decreased fin pitch, but an improved volume goodness factor was obtained with increased fin pitch.
- For applications requiring resistance to corrosion, the thermal characteristic of the copper-nickel alloy is better than that of the stainless steel (25 % and 38 % higher in both Nusselt number and fin efficiency respectively) while the price is only 10 % higher.
- Best thermal performance was achieved with smaller fin thickness.
- The selection of fin material and thickness has to be considered all design parameters such as material effectiveness (k/ρ), material strength, corrosion problems, cost, and the importance of weight.
- The thermofluid engineer has to be considered all the different situations encountered in the cooling coil selection such as; inside and outside design conditions, the allowable friction resistance through the air and watersides, Space limitation, presence of corrosive and dust in the atmosphere.

CHAPTER-VIII-

Conclusions and recommended further work

8.1 Conclusion

In this research the heat transfer and friction characteristics of fin-and-tube cooling coils having turbulated, corrugated and flat fin geometries have been investigated. The influences of fin geometries, inlet-air conditions and inlet-chilled water temperatures on the performance of the cooling coils were investigated with particular reference to the developing flow region. Both experimental and CFD modelling approaches were applied. The main objectives of the work were:

I. Two-dimensional CFD modelling of a corrugated wall channel and a staggered tube bundle using finite element and finite volume methods. The purpose was to obtain key insights into required modelling strategies needed for the more complex three-dimensional problem of the composite fin-and-tube heat exchanger.

II. Experimental measurements on a family of air-conditioning cooling coils having flat, corrugated and turbulated-fin geometries to support later model validation.

III. Three-dimensional CFD modelling of fin-and-tube cooling coils with various fin details.

IV. Performance evaluation of the corrugated and turbulated fin cooling coils compared with the conventional flat fin coil.

V. Further parametric studies of these cooling coils based on the three-dimensional validated model.

The main conclusions of the work are introduced according to these objectives:

I. Three-dimensional CFD modelling and its experimental validation.

Initially two-dimensional CFD modelling of the corrugated fin-and-tube heat exchanger-components were investigated to establish the scope of the three-dimensional modelling work. An experimental analysis was then carried out on the fin-and-tube cooling coils having flat, corrugated and turbulated-fin geometries in order to generate modelling boundary conditions as well as data for three-dimensional model validation. Three-dimensional CFD modelling of these cooling coil types were then developed:

1. Good agreement was obtained between the CFD modelling results and the corresponding experimental results of heat transfer coefficient and pressure drop within measurement uncertainties of ± 10 % and ± 6 % respectively.

2. The Nusselt number and the friction factor were found to be practically independent of both inlet air and chilled-water temperatures.

3. At a nominal face velocity of 2 m/s the Nusselt number and the friction factor of the turbulated fin coil was higher than that of the flat fin coil by 57 % and 60 % respectively, while the corrugated fin coil was higher by 19 % and 16.4 % respectively.

4. At a given pressure drop (ΔP = 52 N/m^2 corresponding to u_{ai} = 2.3 m/s), the heat transfer coefficient of the corrugated and turbulated fin coils was higher than that of flat fin coil by 16 % and 36 % respectively contributing to significant energy saving of the air conditioning plant.

5. At a typical operating condition (2 m/s ≤ u_{ai} ≤ 2.5 m/s) and for the same fan power and heat transfer, the corrugated and turbulated-fin coils

required fin surface area of 16 % and 35 % less than that of flat fin respectively.

6. At a typical operating condition (2 m/s ≤ u_{ai} ≤ 2.5 m/s), the corrugated and turbulated fin coils required core volumes of 19 % and 40 % less than that of flat fin coil respectively for the same heat transfer and friction power.

7. The use of corrugated and turbulated-fin coils improved the overall performance factor (OPF)* of the air conditioning plant by 11.5 % and 16.5 % respectively compared with the flat fin coil at the same chiller-power.

8. The prediction of the flat-fin efficiency was in good agreement with that obtained from the method of Schmidt. In the case of corrugated and turbulated fin geometries, the Schmidt method was deviated up to 8 % from the present prediction.

9. The assumption of an isothermal fin-and-tube overpredicted the heat transfer coefficient up to 42 % compared with the results of conjugate heat transfer model. The assumption of symmetrical boundaries was found inappropriate for the corrugated and turbulated fin modelling.

II. Application studies.

Based on the three-dimensional validated model, further parametric studies of fin pitch, fin material and fin thickness were conducted for these cooling coil types.

---

* The overall performance factor (OPF) was introduced as an overall performance index of indirect expansion refrigeration plant (such as chilled water plant) to interpret how different fin geometries of cooling coil could affect the rate of cooling per unit pumping power:

$$\text{OPF} = \frac{\text{cooling coil capacity}}{\text{fan friction power} + \text{total power input to the chiller}}$$

1. The heat transfer coefficient and pressure drop of these cooling coils increased with decreased fin pitch, however an improved volume goodness factor was obtained with increased fin pitch.

2. As to fin material, the thermal characteristic of the copper-nickel alloy is better than that of the stainless steel (25 % and 38 % higher in both Nusselt number and fin efficiency respectively).

3. Best thermal performance was achieved with smaller fin thickness.

8.2 Recommended further work

This research has provided the opportunity for a range of future work. It is suggested that the following topics would be suitable areas of investigation:

- Three-dimensional numerical modelling of the heat and mass transfer of the cooling coils under wet conditions (surface condensation).

- Three-dimensional CFD modelling and its validation of the key design parameters of the turbulated fin geometry such as slit length, slit width, slit height and number of slits per tube row under both steady and transient conditions.

- Development of an optimisation method for the design selection of fin-and-tube cooling coils parameters.

REFERENCES

Abu Madi M., Johns R. A. and Heikal M. R., 1998. Performance characteristics correlation for round tube and plate finned heat exchangers. *International Journal of Refrigeration* 21(7) 507-517.

ANSYS. 1997. *ANSYS CFD FLOTRAN analysis guide*. Ansys Inc., USA

Asako Y. and Faghri M. 1987. Finite-volume solutions for laminar flow and heat Transfer in a corrugated duct. *Journal of Heat Transfer, ASME Transaction*. 109, 627-634

ASHRAE Fundamental Handbook. 1997. American Society of Heating, Refrigeration and Air-Conditioning Engineers, Inc., Atlanta, USA, Inch-Pound Edition.

ASHRAE Handbook, HVAC Systems and Equipment. 2000. American Society of Heating, Refrigeration and Air-Conditioning Engineers, Inc., Atlanta, USA, SI Edition.

Atkinson K. N., Drakulic R., Heikal M. R., and Cowell T. A., 1998. Two-and three dimensional numerical methods of flow and heat transfer over louvered fin arrays in compact heat exchangers. *International Journal of Heat and Mass Transfer* 41, 4063-4080

Beecher D. T. and Fagan T. J. 1986. Effect of fin pattern on the air side heat transfer coefficient in plate-finned-tube heat exchangers. *ASHRAE Transaction* 92, (2) 1961-1984

Burmeister L. C. 1983. *Convective heat transfer*. John Wiley and Sons

Cambridge Engineering Selector (CES) database. 1999. Granta design Ltd, Cambridge

Chen C. J. and Wung T. S. 1989. Finite analytic solution of convective heat transfer for tube arrays in crossflow: part I, *Journal of heat transfer ASME transaction.* 111, 633-641

Chen C. J. and Wung T. S. 1989. Finite analytic solution of convective heat transfer for tube arrays in crossflow: part II. *Journal of heat transfer ASME transaction.* 111, 641-648

Drakulic R. 1997. *Numerical modelling of flow and heat transfer in louvered fins.* Ph.D thesis, University of Brighton, U.K.

FLUENT. 1999. *Fluent user's guide.* Lebanon, Fluent Inc., USA

Focke W.W., Zachariades J. and Olivier I. 1985. The effect of the corrugation inclination angle on the thermohydraulic performance of plate heat exchangers. *International Journal of Heat and Mass Transfer*, 28 (8) 1469-1479

GAMBIT. 1999. *Gambit-1.3- modelling guide.* Lebanon, Fluent Inc., USA

Garimella S. and Coleman J. W. 1998. Design of cross-flow condensers for ammonia-water absorption heat pumps. *ASHRAE Transaction.* 21 (2) 1553-1564

Ghanem A. G., El-Shazly K. M. and El-Asfouri A. S. 1996. *An experimental investigation for enhancement of heat transfer though fin-and-tube heat exchanger using corrugated fin.* M.Sc. Cairo University, Egypt.

Ghanem A. G., El-Shazly K. M. and El-Asfouri A. S. 1997. Enhancement of heat transfer though fin-and-tube heat exchanger using corrugated fins. *Journal of engineering and applied science,* Cairo University, Egypt, 44 (2), 309-324

Giovannoni F. and Mattarolo L. 1983. Experimental researches on the finned tube heat exchangers with corrugated fins. *XIV International Congress of Refrigeration,* B-1 (493), Paris, 215-220

Gnielinski, V. 1976. New equations for heat and mass transfer in turbulent pipe and channel flow. *International Chemical Engineering*. 16, 359-368

Gomaa A, LeFeuvre R, Underwood C and Bond T. 1999. Numerical analysis of developing laminar flow and heat transfer characteristics through corrugated wall channels. *IMechE Sixth UK National Conference on Heat Transfer*, Edinburgh, UK, PP. 205-214

Gomaa A, Underwood C, Bond T and Penlington R. 2001. Numerical analysis of the developing laminar fluid flow and heat transfer characteristics in a staggered tube bundle. *IChemE Seventh UK National Conference on Heat Transfer*, Nottingham, UK, F7

Griffin H. E. 1996. *Computational analysis of surfaces use in plate-fin heat exchangers*. PhD Thesis, Department of Chemical Engineering, University of Leeds.

Heggs P. J 1999. Fin effectiveness is a better performance indicator than fin efficiency. *Sixth UK National Conference on Heat Transfer*, IMechE, PP. 3-12

Hersch C. 1997. *Numerical computation of internal and external flows. Vol. 1. Fundamental of numerical discretization*. Jhon Wiley & Sons Ltd.

Holman J. P. 1994. *Experimental methods for engineers* McGrow Hill, Inc. Sixth Edition.

Incoropera F P. and DeWitt D P. 1996. *Fundamental of heat and mass transfer.* John Wiley & Sons, Inc., Forth Edition, 1996

Jang J., Wu M. and Chang W. 1996. Numerical and experimental studies of three-dimensional plate-fin and tube heat exchangers. *International journal of heat and mass transfer*. 39 (14) 3057-3066

Jang, J.Y. and Chen, L.K. 1997. Numerical analysis of heat transfer and fluid flow in a three-dimensional wavy-fin and tube heat exchanger. *International Journal of Heat and Mass Transfer*. 40 (16) 3981-3990

Jang J, Lai J, Liu L. 1998. The thermal-hydraulic characteristics of the staggered circular finned-tube heat exchangers under dry and dehumidifying conditions. *International Journal of Heat and Mass Transfer*. 41, 3321-3337

John F. W. 1996. *Computational fluid dynamics, an introduction.* 2nd Edition, Springer-Vrlag Berlin Heidelberg, New York

Kajino, M. and Hiramatsu, M. 1985. Research and development of automotive heat exchangers. *Hemisphere Publication* 1 Corp, New York, Ny, USA, pp. 20-32

Kang H. C. and Kim M. H. 1999. Effect of strip location on the air-side pressure drop and heat transfer in strip fin-and-tube heat exchanger. *Intentional Journal of Refrigeration*. 22, 302-312

Kay W. M. and London A. L. 1984. *Compact heat exchangers.* McGrow Hill, Inc. Third Edition, New York.

Kim N. H., Yun J. H. and Web R. L. 1997. Heat transfer and friction correlations for wavy plate fin-and-tube heat exchangers. *Journal of Heat Transfer ASME Transaction.* 119, 560-567

Kim M-H., Youn B. and Bullard C. W. 2001. Effect of inclination on the air-side performance of a brazed aluminium heat exchanger under dry and wet conditions. *International Journal of Heat and Mass Transfer.* 44, 4613-4623

Knudsen J. G. and Katz D. L. 1958. *Fluid dynamics and heat transfer.* McGraw-Hill, INC

Launder B. E. and Massey T. H. 1978. The numerical prediction of viscous flow and heat transfer in tube banks. *Journal of Heat Transfer ASME Transaction.*100, 565-571

Lin T. R. 2000. Experimental study of burr formation and tool chipping in the face milling of stainless steel. *Journal of Material Processing Technology.*108, 12-20

Lozza G. and Merlo U. 2001. An experimental investigation of heat transfer and friction losses of interrupted and wavy fins for fin-and-tube heat exchangers. *International Journal of Refrigeration.* 24, 409-416

Longtenberg S. A. and Dixon A. G. 1998. Computational fluid dynamics studies of fixed bed heat transfer. *Chemical Engineering and Processing.* 37, 7-21.

Maltson, J.D. 1990. *The performance of rippled fin heat exchangers.* PhD Thesis, Department of Mechanical Engineering and Manufacturing System, Coventry Polytechnic, Coventry.

McQuiston, F.C. 1978. Correlation of heat, mass and momentum transport coefficients for plate-fin-tube heat transfer surfaces with staggered tubes. *ASHRAE Transaction.* 84, (1) 294-309

McQusiton F C. and Parker J D. 1994. *Heating, ventilation, air-conditioning-analysis and design.* John Wiley & Sons, Inc., Forth Edition.

Metwally M. N., AbouZiyan H. Z. and ElLeathy A. M. 1997. Performance of advanced corrugated-duct solar air collector compared with five conventional designs. *Renewable Energy.*10 (4) 519-537

Mirth D. R. and Ramadhyani S. 1993. Comparison of methods of modelling the air-side heat and mass transfer in chilled-water cooling coils. *ASHRAE Transaction.* 99 (2) 285-299.

Mirth D R and Ramadhyani S 1994. Correlations for predicting the air-side Nusselt numbers and friction factors in chilled-water cooling coils. *Experimental Heat Transfer,* 7, 143-162

Mirth D. R. and Ramadhyani S. 1995. Performance of chilled-water cooling coils *HVAC&R Research.* 1 (2) 160-172

Molki, M. and Yuen, C.M. 1986. Effect of interwall spacing on heat transfer and pressure drop in a corrugated-wall duct. *International Journal of Heat and Mass Transfer*, 29 (7) 987-997.

Patankar S. V. 1980. *Numerical heat transfer and fluid flow.* Hemisphere Publishing Corporation.

Patankar S. V. and Spalding D. B. 1972. A calculation procedure for heat, mass and momentum transfer in three-dimensional parabolic flows. *International of Heat and Mass Transfer.* 15, 1787

Polley, R.K. 1992. *Optimisation of compact heat exchanger* Department of Chemical Engineering, U.M.I.S.T, 2, *Compact Heat Exchanger; Techniques of Size Reduction.* Foumeny E.A. and P. J. Heggs P. J.

Powell C. A. 1990. *Copper Nickel 90-10 and 70-30 Alloys* TN 31. Copper Development Association Inc., USA.

Rich D. G. 1973. The effect t of fin spacing on the heat transfer and friction performance of multirow, smooth plate fin-and-tube heat exchangers. *ASHRAE Transaction.* 79 (2) 135-145

Rush T. A., Newell T. A. and Jacobi A. M. 1999. An experimental study of flow and heat transfer in sinusoidal wavy passages. *International Journal of Heat and Mass Transfer*, 42, 1541-1553

Saber, K. 1975. *Louver fin heat exchanger.* Techigi works, Hitachi, LTD. 800, Ohira-machi, Shimot Suga-gun, Tochigi, Japan.

Saniei, N. and Dini, S. 1993. Heat transfer characteristics in a wavy-walled channel. *Journal of Heat Transfer, ASME Transaction.* 115, 788-792

Sauer H. J. and Ganesh, R 1988. Finned tube heat exchangers - an improved coil model for microcomputer simulation. *American Society of Mechanical Engineers, Heat Transfer Division,(Publication) HTD*, PY- 96, 489-498

Springer M. E. and Thole K. A. 1998. Experimental design for flowfield studies of louvered fins. *Experimental Thermal and Fluid Science*, 18, 258-269

Srinivas G. and John W. C. 1998. Design of cross-flow condensers for ammonia-water absorption heat pumps. *ASHRAE Transaction*, 21 (2) 1553-1564

Sunden, B. and Skoldheden 1985. Heat transfer and pressure drop in a new type of corrugated channels. *International Communications in Heat and Mass Transfer*, 12 (5), 559-566

Thermal Transfer Technology Limited (3T), Seaham, Co. Durham, SR7 OPW, UK

Vasudeviah M. and Malamurugan K. 2001. On forced convective heat transfer for a stokes flow in a wavy channel. *International Communication in Heat and Mass Transfer*, 28, 289-297

Versteeg H. K. and Malalasesekera W 1995. *An introduction to computational fluid dynamics, the finite volume method.* Longman Group LTD, UK

Walker G. 1982. *Industrial heat exchangers, a basic guide*. Mc-Graw-Hill publications Co., New York.

Wang C., Chang Y.H. and Lin Y. 1996. Sensible heat transfer and friction characteristics of plate fin-and-tube heat exchangers having plane fins. *International Journal of Refrigeration*, 19 (4) 223-230

Wang C. C., Fu W. L. and Chang C. T. 1997a. Heat transfer and friction characteristics of typical wavy fin-and-tube heat exchangers. *Experimental Thermal and Fluid Science*, 14, (2) 174-186

Wang C., Tsai Y. and Lu D. 1998b. Comprehensive study of convex-louver and wavy fin-and-tube heat exchangers. *Journal of Thermophysics and Heat Transfer*, 12 (3) 423-430

Wang C. C., Jang J. Y. and Chiou N. F. 1999b. A heat transfer and friction correlation for wavy fin-and-tube heat exchangers. "Technical notes", *International Journal of Heat and Mass Transfer,* 42, 1919-1924

Wang C. C., Tao W. H., and Chang C. J. 1999c. An investigation of the airside performance of the slit fin-and-tube heat exchangers. *International Journal of refrigeration,* 22, 595-603

Wang C. C., Lee C-J., Lin S-P. 1999d. Heat transfer and friction correlation compact louvered fin-and-tube heat exchangers. *International Journal of Heat and Mass Transfer*, 42, 1945-1956

Wang C. C., Chi K-Y. 2000. Heat transfer and friction characteristics of plain fin-and-tube heat exchanger, part I: New experimental data. *International Journal of Heat and Mass Transfer*, 43, 2693-2700

Wang C. C., Chi K-Y. 2000. Heat transfer and friction characteristics of plain fin-and-tube heat exchanger, part II: Correlation. *International Journal of Heat and Mass Transfer*, 2000, 43, 2681-2691

Wang C. C., Lee W. S., and Sheu W. J. 2001. A comparative study of compact enhanced fin-and-tube heat exchangers. *International Journal of Heat and Mass Transfer*, 44, 3565-3573

Wang C. C., Lin Y. and Lee C. 2000a. Heat and momentum transfer for compact louvered fin-and-tube heat exchangers in wet conditions. *International Journal of Heat and Mass Transfer*, 43, 3443-3452

Wang C. C., Webb R. L. and Chi K-Y. 2000. Data reduction for air-side performance of fin-and-tube heat exchangers. *Experimental Thermal and Fluid Science*, 21, 218-226

Wang G., and Vanka S. P. 1995. Convective heat transfer in periodic wavy passages. *International Journal of Heat and Mass Transfer*, 38, (17) 3219-3230

Webb R. L. 1990. Air-side heat transfer correlations for flat and wavy plate fin-and-tube geometries. *ASHRAE Transaction*, 96 (20) 445-449

Webb R. L. 1994. *Principles of enhanced heat transfer*. John Willy & Sons, Inc, New York.

Yan W-M. and Sheen P-J. 2000. Heat transfer and friction characteristics of fin-and-tube heat exchangers. *International Journal of Heat and Mass Transfer*, 43, 1651-1659.

Yang, L., Asako, Y., Yamaguchi, Y. and Faghri, M. 1995. Numerical prediction of transitional characteristics of flow and heat transfer in a corrugated duct. *Journal of American Society of Mechanical Engineering HTD*, 318, 145-152

Yik F. H., Underwood C. P. and Chow W. K. 1997. Chilled-water cooling and dehumidifying coils with corrugated plate fins: modelling method. *Building Services Engineering Research & Technology*, 18 (1) 47-58

Young D. F., Munson B. R. and Okiishi T. H. 2001. *A brief introduction to fluid mechanics.* John Wiley & Sons, Inc., USA

Yun J. Y. and Lee K. S. 1999. Investigation of heat transfer characteristics on various kind of fin-and-tube heat exchangers with interrupted surfaces. *International Journal of Heat and Mass Transfer*, 42, 2375-2385.

Yun J. Y. and Lee K. S. 2000. Influence of design parameters on the heat transfer and flow friction characteristics of the heat exchanger with slit fins. *International Journal of Heat and Mass Transfer*, 43 2529-2539.

Zdravistch F., Fletcher C. and Behnia M. 1994. Laminar and turbulent heat transfer predictions in tube banks in cross flow. *Proceedings of international conference on fluid and thermal energy* conversion, Kutta, Indonesia, PP. 29-34

Zdravistch F., Fletcher C. and Behnia M. 1995. Numerical laminar and turbulent fluid flow and heat transfer predictions in tube banks. *International journal of numerical methods in heat and fluid flow*, 5, 717-733

Zukaukas A. A., Ulinskas R. V. and Sipavicius S. J. 1978. Average heat transfer and pressure drop in cross flow of viscous fluids over tube bundles. *Journal of heat transfer-soviet research,* 10 (6) 90-101

Zukaukas A. A. 1987. Heat transfer form tubes in crossflow. *Advances in heat transfer, Academic press*, 18, 87-159

APPENDIX -A-

Measurements observation

A.1 Observation of the flat fin cooling coil

Flat fin coil			Nominal T_{ai} = 42 °C, T_{wi} = 10 °C						Date	28-2-01
Velocity m/s			Air side temperature						ΔP_a	8.90
0.47	1.06	0.79	T_{ai}			T_{ao}			T_{wi}	9.83
0.4	0.77	0.56	66.21	42.26	37.70	18.47	17.46	15.06	T_{wo}	14.12
0.46	1.08	0.69	60.55	51.39	47.16	18.26	17.71	14.87	$\dot{V}$	6E-04
0.55	0.6	0.57	71.67	63.78	58.98	18.30	16.95	14.41	T_{db}	24.1
average = 0.667			average = 55.52			average = 16.83			T_{wb}	13.8

Flat fin coil			Nominal T_{ai} = 42 °C, T_{wi} = 10 °C						Date	28-2-01
Velocity m/s			Air side temperature						ΔP_a	14.34
0.35	1.18	0.94	T_{ai}			T_{ao}			T_{wi}	9.92
0.6	1.32	1.38	35.58	33.98	33.40	19.79	18.34	17.16	T_{wo}	14.23
0.92	0.85	1.06	55.34	35.58	43.00	19.61	18.43	16.40	$\dot{V}$	6E-04
1.06	1.04	0.85	62.21	55.38	52.40	19.07	16.28	15.42	T_{db}	22.8
average = 0.963			average = 45.21			average = 17.83			T_{wb}	12.9

Flat fin coil			Nominal T_{ai} = 42 °C, T_{wi} = 10 °C						Date	28-2-01
Velocity m/s			Air side temperature						ΔP_a	22.48
0.91	0.97	1.06	T_{ai}			T_{ao}			T_{wi}	9.83
1.24	1.39	1.42	52.75	39.78	31.81	19.81	18.50	17.18	T_{wo}	14.17
1.15	1.49	1.62	57.81	37.11	27.35	20.77	19.15	15.33	$\dot{V}$	6E-04
1.46	1.49	1.51	47.05	47.37	38.46	21.56	18.02	15.44	T_{db}	22
average = 1.309			**average = 42.17**			**average = 18.42**			T_{wb}	12.4

Flat fin coil			Nominal T_{ai} = 42 °C, T_{wi} = 10 °C						Date	28-2-01
Velocity m/s			Air side temperature						ΔP_a	40.94
1.57	1.66	1.75	T_{ai}			T_{ao}			T_{wi}	10.07
1.75	1.89	1.83	42.76	49.11	38.26	20.72	19.00	17.80	T_{wo}	15.12
1.82	1.88	1.87	50.31	50.65	38.00	21.93	22.85	19.00	$\dot{V}$	6E-04
1.95	2.18	1.95	40.24	41.06	32.42	23.26	23.15	19.47	T_{db}	24.5
average = 1.842			**average = 42.53**			**average = 20.8**			T_{wb}	14.8

Flat fin coil			Nominal T_{ai} = 42 °C, T_{wi} = 10 °C						Date	28-2-01
Velocity m/s			Air side temperature						ΔP_a	46.52
2.09	1.94	2.1	T_{ai}			T_{ao}			T_{wi}	10.05
2.26	2.22	2.45	37.85	43.87	35.09	19.85	18.51	17.66	T_{wo}	14.82
2.18	2.16	2.38	44.80	45.14	35.87	20.64	22.24	18.74	$\dot{V}$	6E-04
2.26	2.28	2.31	35.95	38.32	31.39	22.35	22.19	18.90	T_{db}	22.8
average = 2.219			**average = 38.7**			**average = 20.12**			T_{wb}	12.9

Flat fin coil			Nominal T_{ai} = 42 °C, T_{wi} = 10 °C						Date	28-2-01
Velocity m/s			Air side temperature						ΔP_a	59.21
2.06	2.1	2.19	T_{ai}			T_{ao}			T_{wi}	9.78
2.2	2.22	2.35	37.53	44.57	36.74	20.17	18.95	18.50	T_{wo}	14.83
2.32	2.29	2.4	44.43	45.12	37.61	20.86	22.17	19.54	$\dot{V}$	6E-04
2.3	2.35	2.4	36.46	38.75	33.67	22.54	22.69	19.77	T_{db}	24.6
average = 2.265			average = 39.43			average = 20.58			T_{wb}	14.6

Flat fin coil			Nominal T_{ai} = 42 °C, T_{wi} = 10 °C						Date	28-2-01
Velocity m/s			Air side temperature						ΔP_a	72.22
2.65	2.65	2.83	T_{ai}			T_{ao}			T_{wi}	9.84
2.75	2.8	2.75	35.79	42.90	36.13	20.35	19.46	19.21	T_{wo}	15.02
2.71	2.85	2.95	41.53	42.91	37.33	20.82	22.98	20.23	$\dot{V}$	6E-04
2.78	2.8	3.03	35.30	37.51	33.86	22.45	22.85	20.32	T_{db}	24.6
average = 2.796			average = 38.14			average = 20.96			T_{wb}	14.6

Flat fin coil			Nominal T_{ai} = 42 °C, T_{wi} = 10 °C						Date	28-2-01
Velocity m/s			Air side temperature						ΔP_a	88.04
2.93	2.85	2.99	T_{ai}			T_{ao}			T_{wi}	9.79
3.08	3.11	3.12	35.48	42.74	36.76	20.87	20.18	20.49	T_{wo}	15.42
3.12	3.19	3.21	41.55	42.25	38.81	21.36	23.58	21.34	$\dot{V}$	6E-04
3.26	3.15	3.35	34.58	36.81	35.81	23.12	23.66	21.32	T_{db}	25
average = 3.113			average = 38.31			average = 21.77			T_{wb}	14.9

Flat fin coil			Nominal T_{ai} = 42 °C, T_{wi} = 10 °C						Date	28-2-01
Velocity m/s			Air side temperature						ΔP_a	109.3
3.32	3.3	3.43	T_{ai}			T_{ao}			T_{wi}	10.05
3.45	3.38	3.39	34.26	40.75	35.36	21.00	20.14	20.73	T_{wo}	15.61
3.49	3.46	3.68	39.09	40.19	36.82	21.50	23.41	21.56	$\dot{V}$	6E-04
3.59	3.6	3.51	33.41	34.95	34.53	22.99	23.68	21.52	T_{db}	24
average = 3.467			average = 36.6			average = 21.84			T_{wb}	14.5

Flat fin coil			Nominal T_{ai} = 42 °C, T_{wi} = 10 °C						Date	28-2-01
Velocity m/s			Air side temperature						ΔP_a	118.6
3.42	3.64	3.97	T_{ai}			T_{ao}			T_{wi}	9.79
3.7	4.08	4.01	32.50	38.63	33.93	20.52	19.88	20.38	T_{wo}	15.14
3.64	4.08	4	36.51	37.88	35.12	20.99	23.06	21.16	$\dot{V}$	6E-04
3.9	3.92	3.9	31.85	33.54	32.96	22.29	23.12	21.09	T_{db}	21
average = 3.855			average = 34.77			average = 21.39			T_{wb}	12.8

A.2 Observation of the corrugated fin cooling coil

Corrugated fin coil			Nominal T_{ai} = 33 °C, T_{wi} = 10 °C						Date	9-3-01
Velocity m/s			Air side temperature						ΔP_a	12.91
0.5	0.9	0.86	T_{ai}			T_{ao}			T_{wi}	10.39
0.53	0.9	0.92	46.48	28.88	24.62	14.97	14.46	14.07	T_{wo}	13.11
0.6	0.66	0.76	42.48	28.14	25.78	14.72	15.18	13.38	$\dot{V}$	6E-04
0.66	0.62	0.52	46.58	40.27	35.33	14.37	13.03	12.65	T_{db}	23.7
average = 0.703			average = 35.4			average = 14.09			T_{wb}	15.4

Corrugated fin coil			Nominal T_{ai} = 33 °C, T_{wi} = 10 °C						Date	9-3-01
Velocity m/s			Air side temperature						ΔP_a	30.92
0.96	0.96	1.17	T_{ai}			T_{ao}			T_{wi}	9.68
1.27	1.38	1.7	40.21	36.07	27.07	15.79	15.03	14.16	T_{wo}	13.07
1.65	1.36	1.55	41.42	35.61	26.75	16.44	16.76	14.07	$\dot{V}$	6E-04
1.35	1.72	1.73	38.30	32.12	25.70	16.62	15.62	13.94	T_{db}	23.7
average = 1.4			average = 33.69			average = 15.38			T_{wb}	15.4

Corrugated fin coil			Nominal T_{ai} = 33 °C, T_{wi} = 10 °C						Date	9-3-01
Velocity m/s			Air side temperature						ΔP_a	49.63
1.34	1.52	2.01	T_{ai}			T_{ao}			T_{wi}	9.95
2.02	1.81	1.96	35.64	35.97	28.76	16.45	15.71	15.73	T_{wo}	13.92
1.96	1.97	2.16	38.27	37.55	29.71	17.36	18.77	15.97	$\dot{V}$	6E-04
2.08	2.09	1.84	34.16	31.94	28.02	17.76	17.45	15.85	T_{db}	22
average = 1.897			average = 33.34			average = 16.78			T_{wb}	15.2

Corrugated fin coil			Nominal T_{ai} = 33 °C, T_{wi} = 10 °C						Date	9-3-01
Velocity m/s			Air side temperature						ΔP_a	64.34
1.92	1.98	2.18	T_{ai}			T_{ao}			T_{wi}	9.93
2.19	2.18	2.39	34.30	35.47	29.29	16.43	15.87	16.19	T_{wo}	13.85
2.18	2.17	2.35	37.08	37.18	30.49	17.36	19.13	16.56	$\dot{V}$	6E-04
2.08	2.13	2.23	33.12	32.10	29.18	17.83	17.77	16.40	T_{db}	22
average = 2.165			average = 33.13			average = 17.06			T_{wb}	15.2

Corrugated fin coil			Nominal T_{ai} = 33 °C, T_{wi} = 10 °C						Date	9-3-01
Velocity m/s			Air side temperature						ΔP_a	80.87
2.24	2.37	2.95	T_{ai}			T_{ao}			T_{wi}	9.7
2.36	2.62	2.93	33.42	34.62	29.27	16.71	16.30	16.66	T_{wo}	13.82
2.54	2.69	2.98	35.91	36.20	30.94	17.69	19.58	17.11	$\dot{V}$	6E-04
2.83	2.84	3.05	32.62	32.03	29.78	18.10	18.07	16.91	T_{db}	21.7
average = 2.7			average = 32.75			average = 17.46			T_{wb}	13

Corrugated fin coil			Nominal T_{ai} = 33 °C, T_{wi} = 10 °C						Date	9-3-01
Velocity m/s			Air side temperature						ΔP_a	110.8
2.98	2.92	3.27	T_{ai}			T_{ao}			T_{wi}	10.01
3.35	3.31	3.42	32.91	33.80	29.49	17.63	17.35	17.68	T_{wo}	14.57
3.26	3.27	3.51	34.92	34.95	30.85	18.73	20.67	18.28	$\dot{V}$	6E-04
3.33	3.23		31.87	31.57	30.06	19.12	19.09	17.98	T_{db}	26
average = 3.259			average = 32.27			average = 18.5			T_{wb}	17.3

Corrugated fin coil			Nominal T_{ai} = 33 °C, T_{wi} = 10 °C						Date	9-3-01
Velocity m/s			Air side temperature						ΔP_a	127.9
3.16	3.12	3.61	T_{ai}			T_{ao}			T_{wi}	9.84
3.44	3.62	3.72	31.76	32.57	28.48	17.57	17.30	17.82	T_{wo}	14.50
3.43	3.38	3.71	33.85	33.65	29.89	18.62	20.54	18.23	$\dot{V}$	6E-04
3.46	3.43	3.57	30.76	30.60	29.33	19.06	18.99	17.72	T_{db}	26
average = 3.471			average = 31.21			average = 18.43			T_{wb}	17.5

Corrugated fin coil			Nominal T_{ai} = 33 °C, T_{wi} = 10 °C						Date	9-3-01
Velocity m/s			Air side temperature						ΔP_a	142.2
3.46	3.57	3.9	T_{ai}			T_{ao}			T_{wi}	9.94
3.64	4.09	3.9	32.53	33.74	30.15	18.13	17.93	18.58	T_{wo}	14.86
3.71	3.93	3.89	34.44	34.37	31.19	19.15	21.10	18.92	$\dot{V}$	6E-04
3.8	3.84	3.79	31.37	31.40	30.20	19.60	19.66	18.56	T_{db}	26
average = 3.793			average = 32.15			average = 19.07			T_{wb}	17.5

Corrugated fin coil			Nominal T_{ai} = 42 °C, T_{wi} = 10 °C						Date	8-3-01
Velocity m/s			Air side temperature						ΔP_a	15.70
0.48	0.85	0.99	T_{ai}			T_{ao}			T_{wi}	9.78
0.5	0.98	0.98	63.88	35.82	37.08	17.16	13.31	15.77	T_{wo}	14.18
0.62	0.64	0.72	54.30	40.65	47.58	16.54	16.58	15.19	$\dot{V}$	6E-04
0.62	0.66	0.79	68.22	59.54	56.01	15.77	13.90	14.28	T_{db}	21.7
average = 0.736			average = 51.45			average = 15.39			T_{wb}	15.1

Corrugated fin coil			Nominal T_{ai} = 42 °C, T_{wi} = 10 °C						Date	8-3-01
Velocity m/s			Air side temperature						ΔP_a	28.58
0.93	0.9	1.3	T_{ai}			T_{ao}			T_{wi}	9.91
1.56	1.33	1.65	55.26	45.56	36.70	17.91	17.62	16.89	T_{wo}	14.62
1.38	1.45	1.86	61.50	43.03	32.34	19.11	19.16	15.91	$\dot{V}$	6E-04
1.57	1.51	1.56	50.48	51.03	39.27	19.80	17.38	15.38	T_{db}	26.3
average = 1.417			average = 46.13			average = 17.68			T_{wb}	16.7

Corrugated fin coil			Nominal T_{ai} = 42 °C, T_{wi} = 10 °C						Date	8-3-01
Velocity m/s			Air side temperature						ΔP_a	43.22
1.52	1.55	2.1	T_{ai}			T_{ao}			T_{wi}	9.37
1.76	1.68	2.2	44.29	50.40	37.87	16.91	16.70	16.05	T_{wo}	14.31
1.78	1.71	2.11	50.51	51.22	36.67	18.55	20.08	16.09	$\dot{V}$	6E-04
2.02	1.87	2.26	41.23	42.09	32.03	19.44	19.54	16.66	T_{db}	24.3
average = 1.88			average = 42.92			average = 17.78			T_{wb}	15.8

Corrugated fin coil			Nominal T_{ai} = 42 °C, T_{wi} = 10 °C						Date	8-3-01
Velocity m/s			Air side temperature						ΔP_a	58.75
1.92	1.85	2.11	T_{ai}			T_{ao}			T_{wi}	10.11
2.17	1.92	2.15	39.90	46.95	38.00	17.61	17.41	17.35	T_{wo}	15.21
2.16	2.02	2.51	46.42	47.82	38.57	19.02	21.14	17.95	$\dot{V}$	6E-04
2.21	2.13	2.55	37.06	39.47	34.14	20.09	20.46	18.38	T_{db}	21.1
average = 2.142			average = 40.93			average = 18.82			T_{wb}	14.2

Corrugated fin coil			Nominal T_{ai} = 42 °C, T_{wi} = 10 °C						Date 8-3-01	
Velocity m/s			Air side temperature						ΔP_a	74.91
3.03	2.33	2.88	T_{ai}			T_{ao}			T_{wi}	9.59
2.35	2.7	2.81	36.28	43.64	36.28	17.40	17.45	17.38	T_{wo}	14.8
2.45	2.78	2.74	42.25	44.23	37.74	18.79	21.18	18.46	$\dot{V}$	6E-04
2.89	2.89	3.03	35.00	37.18	33.78	19.74	20.44	18.70	T_{db}	24.3
average = 2.74			average = 38.49			average = 18.84			T_{wb}	15.8

Corrugated fin coil			Nominal T_{ai} = 42 °C, T_{wi} = 10 °C						Date 8-3-01	
Velocity m/s			Air side temperature						ΔP_a	92.32
2.79	2.77	3.15	T_{ai}			T_{ao}			T_{wi}	10.02
2.9	2.99	3.28	37.40	44.25	37.91	18.73	18.90	19.11	T_{wo}	15.78
3.03	3.11	3.21	42.19	44.82	39.80	20.29	22.73	20.28	$\dot{V}$	6E-04
3.03	3.17	3.08	36.11	38.14	36.05	21.00	21.89	20.42	T_{db}	21.7
average = 3.043			average = 39.63			average = 20.37			T_{wb}	15.1

Corrugated fin coil			Nominal T_{ai} = 42 °C, T_{wi} = 10 °C						Date 8-3-01	
Velocity m/s			Air side temperature						ΔP_a	106.0
2.82	3.3	3.37	T_{ai}			T_{ao}			T_{wi}	10.05
3.17	3.5	3.47	36.56	43.59	37.27	19.08	19.15	19.31	T_{wo}	16
3.21	3.31	3.45	41.61	43.12	38.89	20.67	23.25	20.79	$\dot{V}$	6E-04
3.35	3.46	3.44	35.12	36.68	35.76	21.59	22.42	20.88	T_{db}	26
average = 3.321			average = 38.73			average = 20.79			T_{wb}	17

Corrugated fin coil			Nominal T_{ai} = 42 °C, T_{wi} = 10 °C						Date 8-3-01	
Velocity m/s			Air side temperature						ΔP_a	123.8
2.94	3.22	3.62	T_{ai}			T_{ao}			T_{wi}	8.69
3.33	3.58	3.65	34.40	41.16	35.72	17.78	18.06	18.24	T_{wo}	14.64
3.31	3.61	3.78	38.98	40.93	37.19	19.28	21.78	19.70	$\dot{V}$	6E-04
3.6	3.58	3.62	33.15	34.90	34.59	20.21	21.14	19.72	T_{db}	26
average = 3.487			average = 36.78			average = 19.55			T_{wb}	17.1

Corrugated fin coil			Nominal T_{ai} = 42 °C, T_{wi} = 10 °C						Date 8-3-01	
Velocity m/s			Air side temperature						ΔP_a	142.4
3.54	3.46	3.3	T_{ai}			T_{ao}			T_{wi}	10.05
3.7	3.82	3.89	36.60	37.49	37.45	19.94	19.91	20.24	T_{wo}	16.04
3.94	3.9	3.76	37.89	36.74	36.56	20.39	21.67	20.32	$\dot{V}$	6E-04
3.56	3.95	3.56	34.91	35.01	35.33	20.81	20.79	20.36	T_{db}	26
average = 3.698			average = 36.44			average = 20.49			T_{wb}	17

A.3 Observation of the turbulated fin cooling coil

Turbulated fin coil			Nominal T_{ai} = 33 °C, T_{wi} = 10 °C						Date	19-3-01
Velocity m/s			Air side temperature						ΔP_a	16.84
0.59	0.92	0.97	T_{ai}			T_{ao}			T_{wi}	9.5
0.56	0.9	0.91	55.49	33.21	27.66	12.35	11.87	11.29	T_{wo}	12.62
0.57	0.7	0.85	49.22	40.55	30.22	13.02	13.02	11.85	$\dot{V}$	6E-04
0.63	0.61	0.57	55.54	47.52	39.38	13.41	12.35	11.55	T_{db}	26.1
average = 0.732			average = 42.09			average = 12.3			T_{wb}	13.1

Turbulated fin coil			Nominal T_{ai} = 33 °C, T_{wi} = 10 °C						Date	19-3-01
Velocity m/s			Air side temperature						ΔP_a	38.60
1.07	1.26	1.72	T_{ai}			T_{ao}			T_{wi}	10.22
1.18	1.37	1.71	44.38	35.99	28.00	14.07	13.53	12.76	T_{wo}	13.72
1.48	1.59	1.65	46.50	33.54	27.39	15.25	14.07	13.34	$\dot{V}$	6E-04
1.08	1.37	1.73	42.09	35.87	29.46	16.00	14.44	13.11	T_{db}	26.1
average = 1.434			average = 35.91			average = 14.06			T_{wb}	13.1

Turbulated fin coil			Nominal T_{ai} = 33 °C, T_{wi} = 10 °C						Date	19-3-01
Velocity m/s			Air side temperature						ΔP_a	64.97
1.81	1.75	2.09	T_{ai}			T_{ao}			T_{wi}	10.19
2.12	1.97	2.2	37.19	35.73	28.00	14.70	13.93	13.40	T_{wo}	14.06
1.97	2.03	2.27	39.45	38.06	28.87	16.10	16.10	14.72	$\dot{V}$	6E-04
2.05	2.2	2.19	34.66	31.75	27.15	16.96	16.22	14.25	T_{db}	26.1
average = 2.054			average = 33.43			average = 15.15			T_{wb}	13.1

Turbulated fin coil			Nominal T_{ai} = 33 °C, T_{wi} = 10 °C						Date	19-3-01
Velocity m/s			Air side temperature						ΔP_a	88.02
2.15	2.12	2.34	T_{ai}			T_{ao}			T_{wi}	9.97
2.39	2.3	2.55	34.36	35.59	29.37	15.04	14.40	14.14	T_{wo}	14.25
2.33	2.55	2.65	36.72	37.20	30.12	16.43	16.43	15.71	$\dot{V}$	6E-04
2.48	2.55		32.36	32.01	28.27	17.38	17.20	15.18	T_{db}	26.1
average = 2.401			average = 32.89			average = 15.77			T_{wb}	13.1

Turbulated fin coil			Nominal T_{ai} = 33 °C, T_{wi} = 10 °C						Date	19-3-01
Velocity m/s			Air side temperature						ΔP_a	109.2
2.44	2.43	2.81	T_{ai}			T_{ao}			T_{wi}	9.75
2.6	2.69	2.84	34.89	35.57	29.81	15.55	14.95	14.77	T_{wo}	14.46
2.57	3.04	3.02	37.36	37.49	31.67	16.85	16.85	16.36	$\dot{V}$	6E-04
2.6	3.12		33.33	33.40	30.35	17.88	17.54	15.57	T_{db}	26.1
average = 2.742			average = 33.76			average = 16.26			T_{wb}	13.1

Turbulated fin coil			Nominal T_{ai} = 33 °C, T_{wi} = 10 °C						Date	19-3-01
Velocity m/s			Air side temperature						ΔP_a	130.3
2.63	2.66	2.97	T_{ai}			T_{ao}			T_{wi}	9.85
2.81	2.9	3.4	34.54	35.79	30.86	16.03	15.48	15.39	T_{wo}	14.85
2.87	3.22	3.31	36.68	37.06	31.68	17.36	17.36	17.00	$\dot{V}$	6E-04
2.99	3.31		32.65	32.95	30.62	18.37	18.24	16.33	T_{db}	26.1
average = 3.006			average = 33.65			average = 16.84			T_{wb}	13.1

Turbulated fin coil			Nominal T_{ai} = 33 °C, T_{wi} = 10 °C						Date	19-3-01
Velocity m/s			Air side temperature						ΔP_a	140.8
2.82	3.13	3.26	T_{ai}			T_{ao}			T_{wi}	9.55
2.9	3.15	3.3	31.21	32.67	28.24	16.12	15.91	15.53	T_{wo}	14.90
3.05	3.19	3.35	33.16	33.62	29.60	17.65	16.85	16.85	$\dot{V}$	6E-04
3.1	3.07	3	29.84	30.44	29.03	17.12	16.86	15.87	T_{db}	26
average = 3.11			average = 30.87			average = 16.53			T_{wb}	13.5

Turbulated fin coil			Nominal T_{ai} = 33 °C, T_{wi} = 10 °C						Date	19-3-01
Velocity m/s			Air side temperature						ΔP_a	170.2
3.13	3.24	3.53	T_{ai}			T_{ao}			T_{wi}	9.59
3.35	3.5	3.7	30.57	31.52	27.37	16.03	15.87	15.36	T_{wo}	14.38
3.33	3.6	3.75	32.52	32.75	28.58	17.57	16.61	16.61	$\dot{V}$	6E-04
3.56	3.8	3.65	28.73	29.72	28.20	17.10	16.70	15.69	T_{db}	26
average = 3.512			average = 30			average = 16.39			T_{wb}	13.5

Turbulated fin coil			Nominal T_{ai} = 33 °C, T_{wi} = 10 °C						Date	19-3-01
Velocity m/s			Air side temperature						ΔP_a	185.5
2.59	3.55	3.64	3.61			T_{ao}			T_{wi}	9.72
2.84	3.69	3.84	3.87	30.60	31.07	27.31	16.28	15.85	15.86	15.27
3.18	3.66	4	3.86	32.30	32.31	28.67	17.58	17.58	17.29	6E-04
3.41	3.71	4	4	28.73	29.57	28.18	18.43	18.23	16.52	26
average = 3.509			average = 21.81			average = 20.9			T_{wb}	13.5

Turbulated fin coil			Nominal T_{ai} = 42 °C, T_{wi} = 10 °C						Date	20-3-01
Velocity m/s			Air side temperature						ΔP_a	16.36
0.57	0.9	0.57	T_{ai}			T_{ao}			T_{wi}	9.79
0.69	1.1	0.58	66.01	42.43	42.78	13.41	12.76	12.33	T_{wo}	14.10
0.75	0.55	0.77	62.48	51.45	49.99	13.56	13.62	12.81	$\dot{V}$	6E-04
0.5	0.52		73.73	63.70	61.89	14.86	13.51	12.95	T_{db}	26.3
average = 0.682			average = 57.16			average = 13.31			T_{wb}	16.7

Turbulated fin coil			Nominal T_{ai} = 42 °C, T_{wi} = 10 °C						Date	20-3-01
Velocity m/s			Air side temperature						ΔP_a	30.21
0.4	0.85	0.86	T_{ai}			T_{ao}			T_{wi}	9.72
0.96	1.24	1.33	61.88	37.46	32.42	14.60	13.78	13.53	T_{wo}	14.34
0.76	1.04	1.25	59.21	36.38	40.45	15.33	14.94	14.40	$\dot{V}$	6E-04
0.69	0.69	0.75	58.95	52.31	50.20	16.28	13.94	13.98	T_{db}	25
average = 0.902			average = 47.7			average = 14.53			T_{wb}	16

Turbulated fin coil			Nominal T_{ai} = 42 °C, T_{wi} = 10 °C						Date	20-3-01
Velocity m/s			Air side temperature						ΔP_a	50.20
0.82	1.3	1.7	T_{ai}			T_{ao}			T_{wi}	9.91
1.01	1.28	1.65	51.22	45.72	35.60	14.93	14.66	14.11	T_{wo}	14.81
1.18	1.27	1.85	56.92	45.60	31.48	16.58	16.78	14.10	$\dot{V}$	6E-04
1.05	1.42	1.55	42.61	46.83	34.88	18.98	16.80	14.52	T_{db}	25
average = 1.34			average = 43.43			average = 15.72			T_{wb}	16

Turbulated fin coil			Nominal T_{ai} = 42 °C, T_{wi} = 10 °C						Date	20-3-01
Velocity m/s			Air side temperature						ΔP_a	72.30
1.5	1.69	1.86	T_{ai}			T_{ao}			T_{wi}	10.07
1.82	2.25	2.18	43.52	49.31	39.15	15.65	15.27	14.42	T_{wo}	15.39
2.11	2.11	2.5	50.78	50.51	38.07	17.08	18.05	15.73	$\dot{V}$	6E-04
1.62	2.55	2.71	37.88	41.92	32.16	19.65	19.39	16.63	T_{db}	24.5
average = 2.075			average = 42.59			average = 16.87			T_{wb}	15.5

Turbulated fin coil			Nominal T_{ai} = 42 °C, T_{wi} = 10 °C						Date	20-3-01
Velocity m/s			Air side temperature						ΔP_a	95.96
2.03	2.05	2.64	T_{ai}			T_{ao}			T_{wi}	9.93
2.42	2.51	2.62	38.08	45.69	37.40	15.79	15.40	14.85	T_{wo}	15.36
2.34	2.69	2.52	44.27	46.05	38.50	17.00	18.61	16.63	$\dot{V}$	6E-04
2.42	2.77		35.36	39.36	33.50	19.30	19.59	17.21	T_{db}	24.5
average = 2.455			average = 39.8			average = 17.15			T_{wb}	15.5

Turbulated fin coil			Nominal T_{ai} = 42 °C, T_{wi} = 10 °C						Date	20-3-01
Velocity m/s			Air side temperature						ΔP_a	127.7
2.52	2.58	2.94	T_{ai}			T_{ao}			T_{wi}	9.97
2.77	2.91	3.17	34.28	42.03	35.67	15.87	15.67	15.26	T_{wo}	15.34
2.88	3.13	3.3	39.76	41.96	37.49	16.99	18.76	17.31	$\dot{V}$	6E-04
2.89	3.5		32.50	36.34	32.87	19.05	19.72	17.77	T_{db}	24.5
average = 2.963			average = 36.99			average = 17.38			T_{wb}	15.5

Turbulated fin coil			Nominal T_{ai} = 42 °C, T_{wi} = 10 °C						Date	20-3-01
Velocity m/s			Air side temperature						ΔP_a	153.7
2.79	2.8	3.35	T_{ai}			T_{ao}			T_{wi}	9.99
2.18	3.16	3.45	34.80	42.27	36.50	16.97	16.67	16.98	T_{wo}	16.14
3.11	3.32	3.4	40.02	41.52	37.82	18.42	19.61	19.44	$\dot{V}$	6E-04
2.85	3.83	3.6	32.77	36.06	34.46	20.18	20.81	18.68	T_{db}	26.5
average = 3.153			average = 37.36			average = 18.64			T_{wb}	16.8

Turbulated fin coil			Nominal T_{ai} = 42 °C, T_{wi} = 10 °C						Date	20-3-01
Velocity m/s			Air side temperature						ΔP_a	171.2
3.2	3.19	3.54	T_{ai}			T_{ao}			T_{wi}	9.71
3.42	3.45	3.58	32.23	38.93	33.83	15.94	15.81	15.68	T_{wo}	15.19
3.44	3.67	3.57	36.84	38.50	35.30	17.07	18.76	17.68	$\dot{V}$	6E-04
2.55	3.7	3.56	30.22	33.48	32.04	19.08	19.76	18.08	T_{db}	26.5
average = 3.406			average = 34.6			average = 17.54			T_{wb}	16.8

Turbulated fin coil			Nominal T_{ai} = 42 °C, T_{wi} = 10 °C						Date	20-3-01
Velocity m/s			Air side temperature						ΔP_a	184.7
3.42	3.38	3.73	T_{ai}			T_{ao}			T_{wi}	9.78
3.47	3.85	3.72	33.24	40.57	35.60	16.60	16.60	16.49	T_{wo}	15.74
3.65	3.9	3.98	37.72	39.24	36.57	17.78	19.66	18.53	$\dot{V}$	6E-04
3.83	4	4.1	31.25	35.08	33.84	19.78	20.62	18.98	T_{db}	25.5
average = 3.753			average = 35.9			average = 18.34			T_{wb}	15

APPENDIX (B)

Experimental results

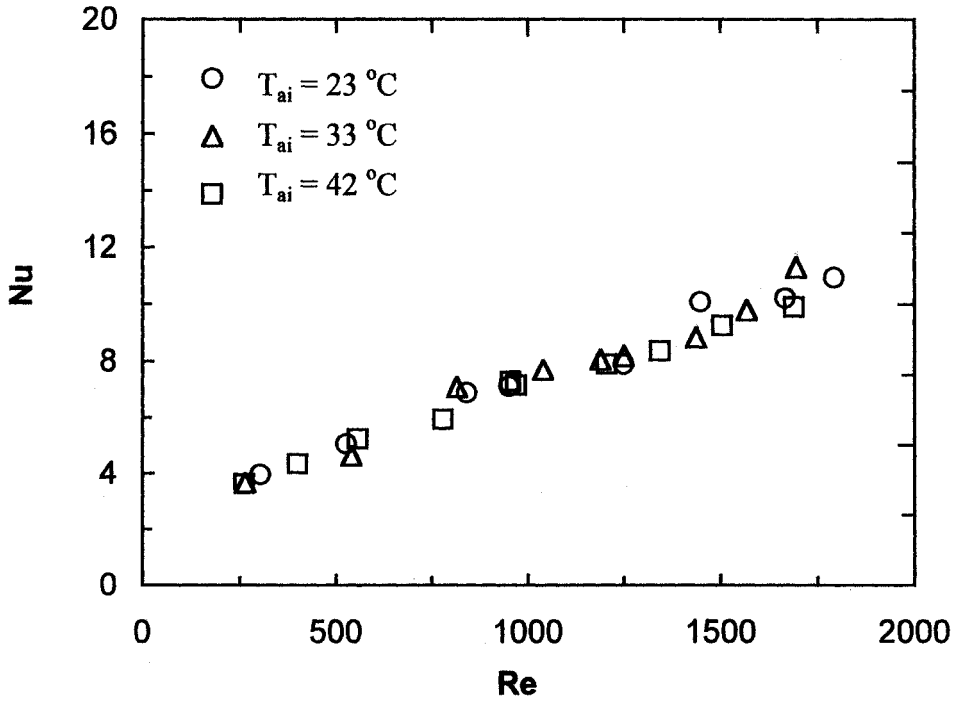

Fig. (B-1) Nusselt number of the flat fin coil for T_{wi} = 5 °C

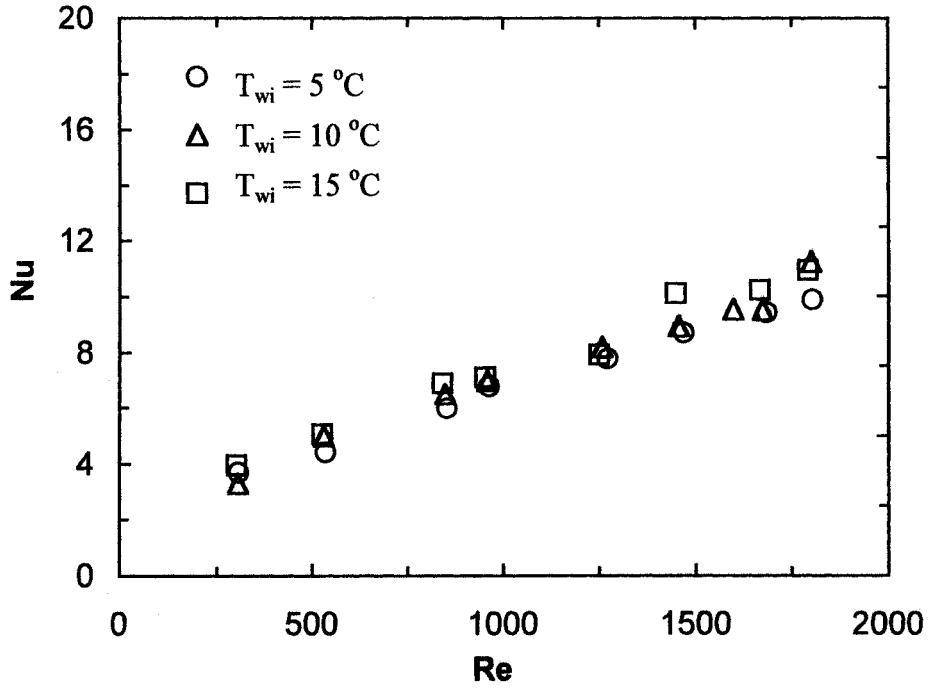

Fig. (B-2) Nusselt number of the flat fin coil for T_{ai} = 23 °C

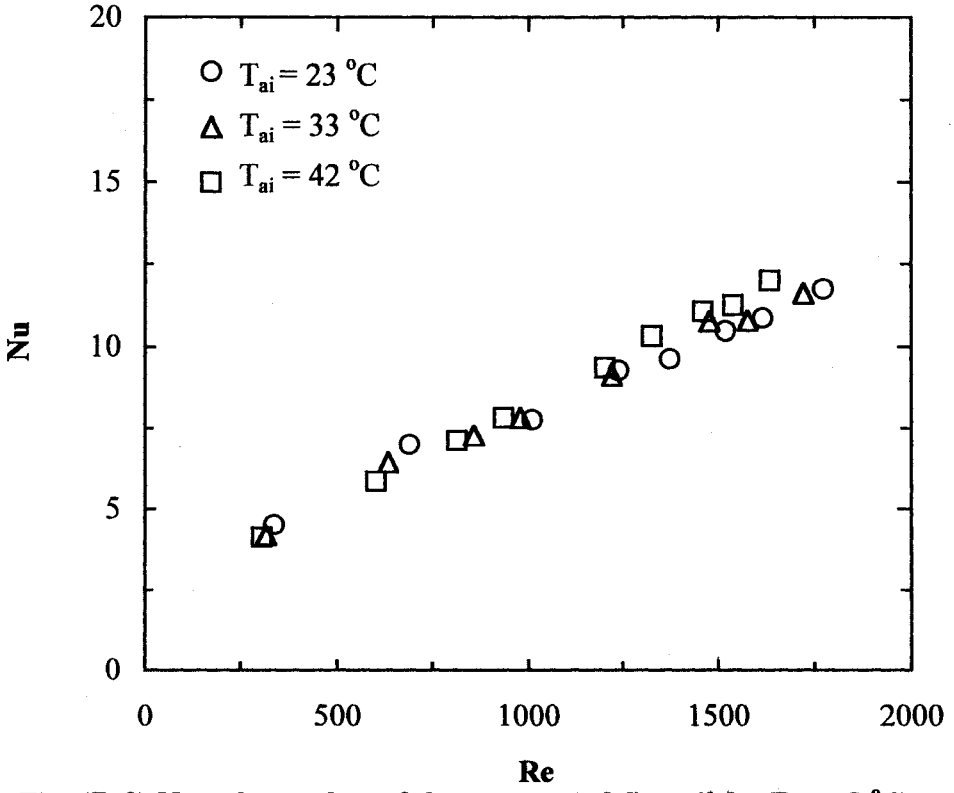

Fig. (B-3) Nusselt number of the corrugated fin coil for T_{wi} = 5 °C

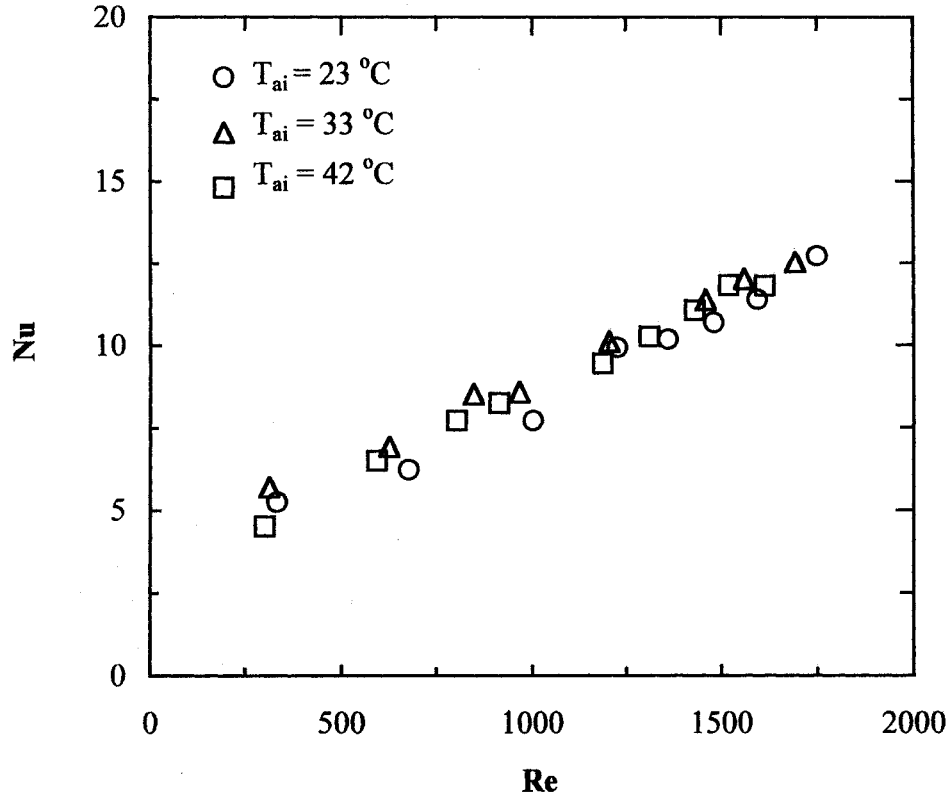

Fig. (B-4) Nusselt number of the corrugated fin coil for T_{wi} = 15 °C

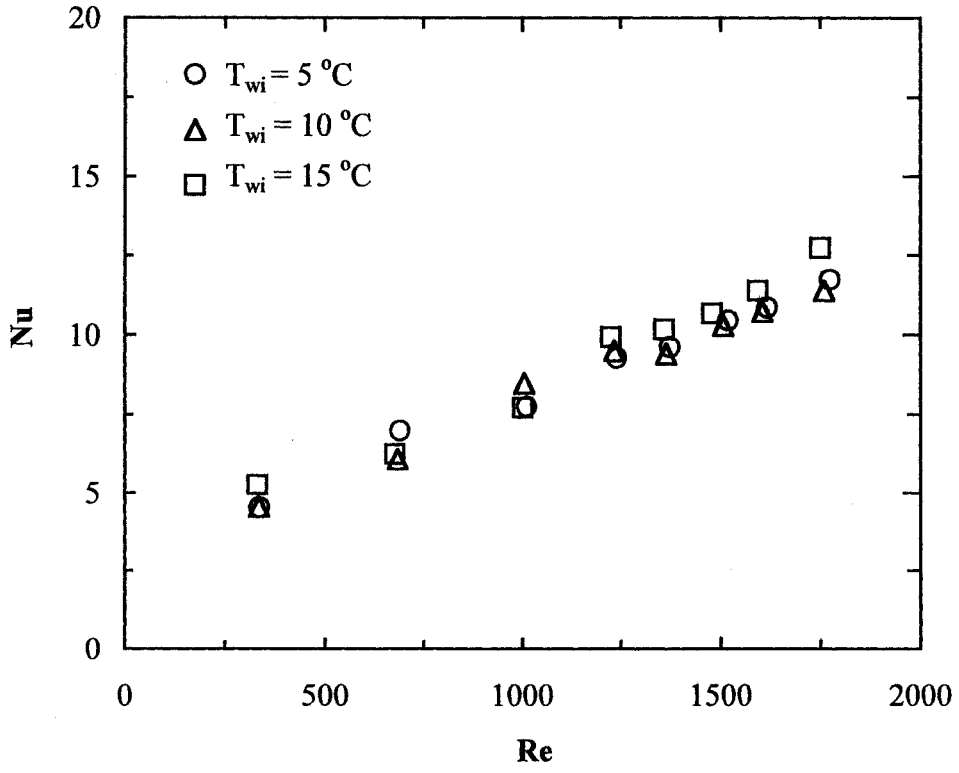

Fig. (B-5) Nusselt number of the corrugated fin coil for T_{ai} = 23 °C

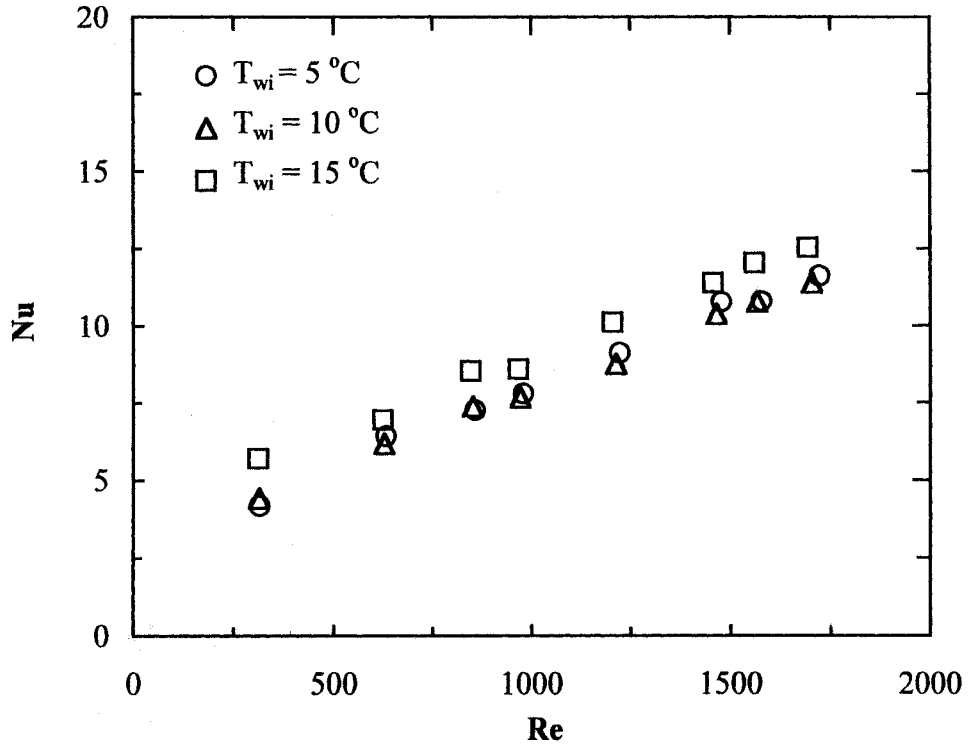

Fig. (B-6) Nusselt number of the corrugated fin coil for T_{ai} = 33 °C

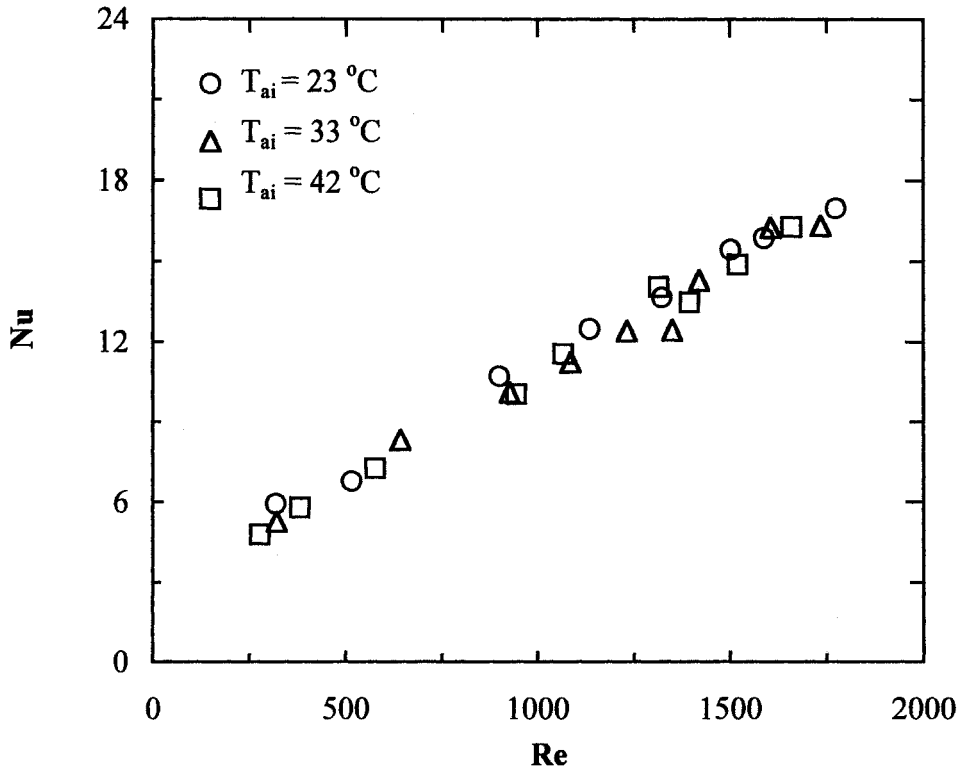

Fig. (B-7) Nusselt number of the turbulated fin coil for T_{wi} = 5 °C

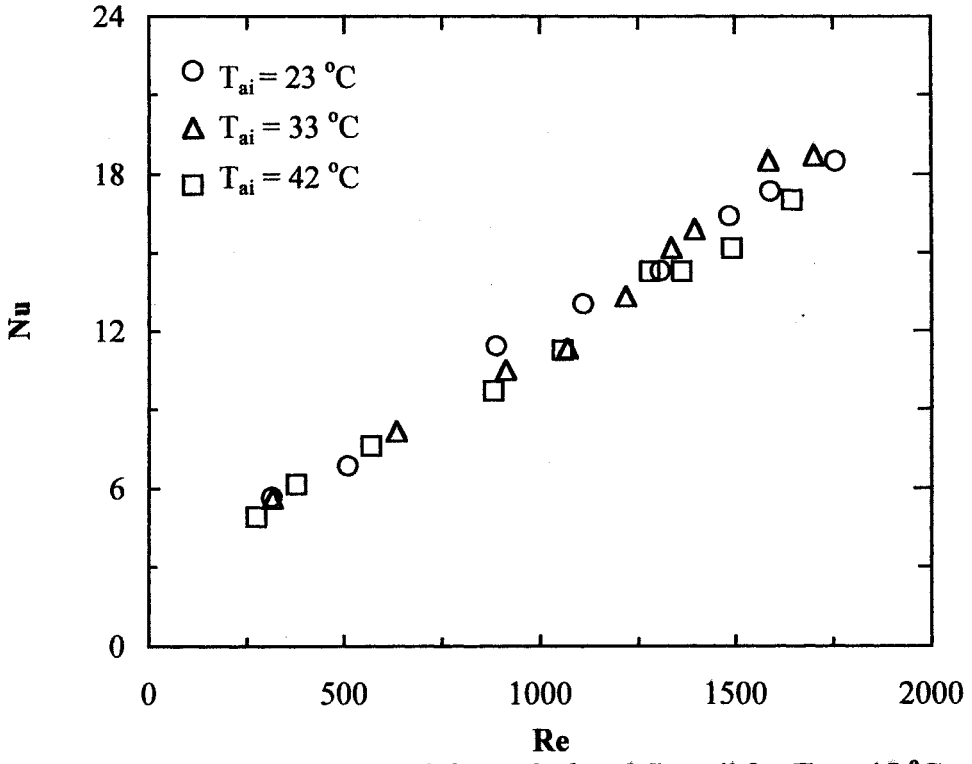

Fig. (B-8) Nusselt number of the turbulated fin coil for T_{wi} = 15 °C

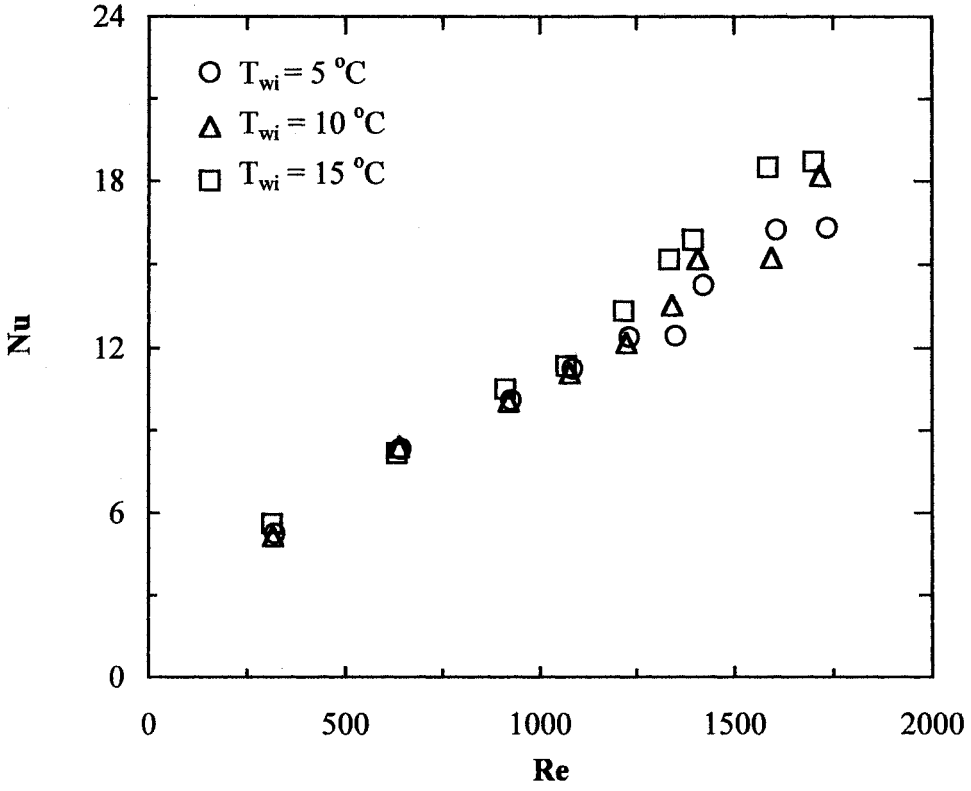

Fig. (B-9) Nusselt number of the turbulated fin coil for T_{ai} = 33 °C

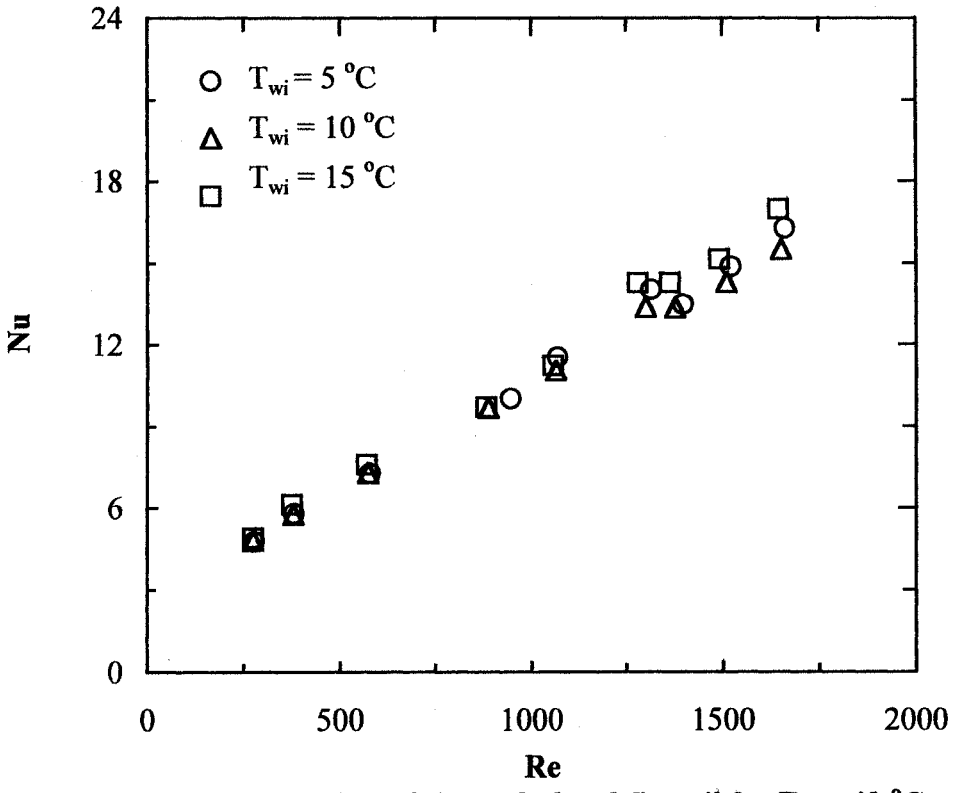

Fig. (B-10) Nusselt number of the turbulated fin coil for T_{ai} = 42 °C

APPENDIX -C-

Error analysis

In this appendix, the calculation of the error, precision, and the general validity of the experimental measurements are carried out. The probable errors in the experimental data are those values that have some uncertainty. This uncertainty varies a great deal depending upon the circumstances of experiment. In fact, the magnitude of the experimental error is always uncertain.

The different types of experimental errors are as follows;

1. Errors in the apparatus construction and in the measurement.
2. Permanent error, which will cause repeated readings to be in error by approximately the same amount (sometimes called systematic errors)
3. Random errors, which may be caused by observation, round up and interpolation.

C.1. Uncertainties approximation by the differential method

In fact, the measurements should be combined to calculate particular results, which are desired. Therefore, it should be to know the uncertainty in the final result due to the uncertainties in the measurements. The accuracy of the results obtained from experimental measurements is governed by the accuracy of an instrument and its limited by its sensitivity.

In the present work the differential approximation method was considered to evaluate the uncertainty in a result R_s that is a function of the independent parameters;

$X_1, X_2, X_3, ..., X_n$, i.e.

$$R_s = R_s(X_1, X_2, X_3, ..., X_n) \qquad \text{(C-1)}$$

At the same time it may perturb the variables by ΔX_1, ΔX_2, ΔX_3, .., ΔX_n and then;

$$R_s (X_1 + \Delta X_1) = R_s (X_1 + \Delta X_1, X_2, X_3, \ldots, X_n),$$

$$R_s (X_n + \Delta X_n) = Rs (X_1, X_2, X_3, \ldots, X_n + \Delta X_n) \qquad \text{(C-2)}$$

Therefore, for small enough values of the quantities ΔX_1, ΔX_2, ΔX_3, $\ldots\ldots \Delta X_n$, the partial derivatives can be well approximated by

$$\frac{\partial R_s}{\partial X_i} \approx \frac{R_s(X_i + \Delta X_i) - R_s(X_i)}{\Delta X_i}, \; i = 1, 2, 3, \ldots, n \qquad \text{(C-3)}$$

If there are uncertainties W_1, W_2, W_3, ..., W_n in the independent variables and W_R is the uncertainty in the result on the same odds, then the uncertainty in the result can be given as; [Holman, 1994]

$$W_R = \left[\left(\frac{\partial R_s}{\partial X_1} W_1 \right)^2 + \left(\frac{\partial R_s}{\partial X_2} W_2 \right)^2 + \left(\frac{\partial R_s}{\partial X_3} W_3 \right)^2 + \ldots\ldots + \left(\frac{\partial R_s}{\partial X_n} W_n \right)^2 \right]^{\frac{1}{2}} \qquad \text{(C-4)}$$

Since the values of the partial derivative and the errors in the measuring parameters may be positive or negative, then the absolute values are considered to obtain the maximum absolute uncertainty in the result W_R [Ghanim et al, 1996]

C.1.1 Uncertainty involved in determining of airside heat transfer rate

The airside heat transfer rate is given by;

$$Q_a = \rho \, A \, u_i \, Cp \, \Delta T$$

Each of the uncertainties W_u and W_T contribute in the uncertainty of the airside heat transfer rate by its relative order. Thus, the uncertainty in the airside heat transfer rate is due to the following;

1. Uncertainty in determination of u_i measurements
2. Uncertainty in temperature measurements

From equation (C-4) the uncertainty in determining of the rate of heat transfer in airside W_{Qa} can be obtain by;

$$\frac{\partial Q_a}{\partial u} = \rho\, A\, C_p\, \Delta T \tag{1.1.a}$$

$$\frac{\partial Q_a}{\partial T_{ai}} = \rho\, A\, C_p\, u \tag{1.1.b}$$

$$\frac{\partial Q_a}{\partial T_{ao}} = -\rho\, A\, C_p\, u \tag{1.1.c}$$

Substituting in equation (C.4), then the maximum absolute uncertainty in determining the rate of heat transfer in airside W_{Qa} is given as;

$$W_{Qa} = \left[\left(\frac{\partial Q_a}{\partial u_i} W_u \right)^2 + 2 \left(\frac{\partial Q_a}{\partial T_a} W_T \right)^2 \right]^{\frac{1}{2}} \tag{1.1.d}$$

C.1.2 Uncertainty involved in determining of heat transfer in the waterside

The waterside heat transfer rate is given by;

$$Q_w\ V_W\ \rho_W\ Cp_w\ (T_{wo} - T_{wi})$$

By the same manner in section (C.1.1) the maximum absolute uncertainty in determining of rate of heat transfer in waterside W_{Qw} is given by;

$$W_{Qw} = \left[\left(\frac{\partial Q_w}{\partial V} W_V \right)^2 + 2 \left(\frac{\partial Q_w}{\partial T_w} W_T \right)^2 \right]^{\frac{1}{2}} \qquad (1.2.a)$$

C.1.3 Uncertainty involved in determining of the average heat transfer

The average rate of heat transfer is given by;

$$Q_{av} = \frac{Q_w + Q_a}{2}$$

By the same way in section (C.1.1) the maximum absolute uncertainty in determining of the average rate of heat transfer is given by;

$$W_{Qav} = \left[\left(\frac{\partial Q_{av}}{\partial Q_w} W_{Qw} \right)^2 + \left(\frac{\partial Q_{av}}{\partial Q_a} W_{Qa} \right)^2 \right]^{\frac{1}{2}} \qquad (1.3.a)$$

The values of the maximum percentage uncertainty in the average rate of heat transfer W_{Qav} for the flat, corrugated and turbulated fin cooling coils is given in tables [(C.3.1.1) to (C.3.3.3)].

C.1.4 Uncertainty involved in determining of *LMTD*

The log-mean temperature is given by;

$$\theta = \frac{(T_{ao} - T_{wi}) - (T_{ai} - T_{wo})}{\ln \frac{(T_{ao} - T_{wi})}{(T_{ai} - T_{wo})}}$$

$$\frac{\partial \theta}{\partial T_{ao}} = \frac{\ln \frac{(T_{ao} - T_{wi})}{(T_{ai} - T_{wo})} - [(T_{ao} - T_{wi}) - (T_{ai} - T_{wo})] \frac{1}{(T_{ao} - T_{wi})}}{\left(\ln \frac{(T_{ao} - T_{wi})}{(T_{ai} - T_{wo})}\right)^2} \quad (1.4.a)$$

$$\frac{\partial \theta}{\partial T_{wi}} = \frac{-\ln \frac{(T_{ao} - T_{wi})}{(T_{ai} - T_{wo})} + [(T_{ao} - T_{wi}) - (T_{ai} - T_{wo})] \frac{1}{(T_{ao} - T_{wi})}}{\left(\ln \frac{(T_{ao} - T_{wi})}{(T_{ai} - T_{wo})}\right)^2} \quad (1.4.b)$$

Since the T_{ai}, T_{ao} in same order of uncertainty and also T_{wi}, T_{wo}, then, the value of uncertainty in both T_{ao}, T_{wi} will multiply by 2. Substituting in equation (C.4), then the maximum absolute uncertainty in determining of log-mean temperature difference is given as;

$$W_\theta = \left[2\left(\frac{\partial \theta}{\partial T_{ao}} W_{Ta}\right)^2 + 2\left(\frac{\partial \theta}{\partial T_{wi}} W_{Tw}\right)^2\right]^{\frac{1}{2}} \quad (1.4.c)$$

The values of the maximum percentage uncertainty in the log mean temperature difference for the flat, corrugated and turbulated fin cooling coils is given in tables [(C.3.1.1) to (C.3.3.3)].

C.1.5 Uncertainty involved in the overall heat transfer coefficient

In the present work the overall heat transfer coefficient was calculated based on the log mean temperature difference;

$$U = \frac{Q_{av}}{A\,\theta}$$

Where

Q_{av} Average rate of heat transfer, W

A Heat transfer surface area, m^2

θ Cross flow log-mean temperature difference, °C

Each of the uncertainties W_Q, and W_θ contribute in the uncertainty of the overall heat transfer by its relative order. Thus, the uncertainty in the overall heat transfer coefficient is due to the following;

1. Uncertainty in determination of average rate of heat transfer
2. Uncertainty in determination of log mean temperature difference

From equation (C-4) the uncertainty in determining of the overall heat transfer coefficient W_U can be given as:

$$\frac{\partial U}{\partial Q_{av}} = \frac{1}{A\,\theta} \tag{1.5.a}$$

$$\frac{\partial U}{\partial \theta} = \frac{-Q_{av}}{A\,\theta^2} \tag{1.5.b}$$

Substituting in equation (C.4), then the maximum absolute uncertainty in determining the overall heat transfer coefficient W_U is given as:

$$W_U = \left[\left(\frac{\partial U}{\partial Q_{av}} W_{Qav} \right)^2 + \left(\frac{\partial U}{\partial \theta} W_\theta \right)^2 \right]^{\frac{1}{2}} \tag{1.5.c}$$

The values of the maximum percentage uncertainty in the overall heat transfer coefficient W_U for the flat, corrugated and turbulated fin cooling coils is given in tables [(C.3.1.1) to (C.3.3.3)].

C.1.6 Uncertainty involved in the air-side heat transfer coefficient

The airside heat transfer coefficient is given as;

$$h_o = \frac{1}{A_o\,\eta_o\left[\frac{1}{A_o U_o} - \frac{\ln(D_o/D_i)}{2\pi L k} - \frac{1}{h_i A_i}\right]} \tag{1.6.a}$$

$$\frac{\partial h_o}{\partial U_o} = \frac{\eta_o}{U_o^{\,2}\left[A_o\eta_o\left(\frac{1}{A_o U_o} - \frac{\ln(D_o/D_i)}{2\pi L k} - \frac{1}{A_i h_i}\right)\right]^2} \tag{1.6.b}$$

$$\frac{\partial h_o}{\partial h_i} = \frac{A_o\,\eta_o}{h_i^{\,2} A_i\left[A_o\eta_o\left(\frac{1}{A_o U_o} - \frac{\ln(D_o/D_i)}{2\pi L k} - \frac{1}{A_i h_i}\right)\right]^2} \tag{1.6.c}$$

Substituting in equation (C.4), then the maximum percentage uncertainty in the airside heat transfer coefficient W_{ho} is given as;

$$W_{ho} = \frac{100}{h_o}\left[\left(\frac{\partial h_o}{\partial U_o} W_{Uo}\right)^2 + \left(\frac{\partial h_o}{\partial h_i} W_{hi}\right)^2\right]^{\frac{1}{2}} \% \tag{1.6.d}$$

C.1.7 Uncertainty involved in determining the Nusselt number

The Nusselt number is defined as;

$$Nu = \frac{h\,D_h}{k} \tag{1.7.a}$$

$$\frac{\partial Nu}{\partial h_o} = \frac{D_h}{k} \tag{1.7.b}$$

Substituting in equation (C.4), then the maximum relative uncertainty in determining the airside heat transfer Nusselt number W_{Nu} is given as;

$$W_{Nu} = \frac{100}{Nu}\left[\left(\frac{\partial Nu}{\partial h_o} W_{ho}\right)^2\right]^{\frac{1}{2}} \% \tag{1.7.c}$$

The values of the maximum percentage uncertainty in the airside heat transfer Nusselt number W_{Nu} for the flat, corrugated and turbulated fin cooling coils is given in tables [(C.3.1.1) to (C.3.3.3)].

C.2.1 Uncertainty involved in determining the friction factor

The friction factor is defined according to Kay and London definition [Kay and London,1984] as;

$$f = \frac{A_{ff}\,\rho_m}{A\,\rho_i}\left[\frac{2\Delta P\,\rho_i}{G^2} - \left(1+\sigma^2\right)\left(\frac{\rho_i}{\rho_o} - 1\right)\right]$$

$$\frac{\partial f}{\partial \Delta P} = \frac{2A_{ff}\,\sigma^2}{A\,\rho_m\,u^2} \tag{2.1.a}$$

$$\frac{\partial f}{\partial \bar{u}} = \frac{-4A_{ff}\,\Delta P\,\sigma^2}{A\,\rho_m\,u^3} \tag{2.1.b}$$

Substituting in equation (C.4), then the maximum percentage uncertainty in the friction factor W_f is given as;

$$W_f = \frac{100}{f}\left[\left(\frac{\partial f}{\partial \Delta P} W_{\Delta P}\right)^2 + \left(\frac{\partial f}{\partial u} W_{\bar{u}}\right)^2\right]^{\frac{1}{2}} \quad \% \qquad (2.1.c)$$

The values of the maximum percentage uncertainty in the friction factor W_f for the flat, corrugated and turbulated fin cooling coils is given in tables [(C.3.1.1) to (C.3.3.3)].

C.3 Summary

The summary of the percentage maximum relative uncertainty in the average heat transfer W_{Qav}, log-mean temperature difference W_{Θ}, overall heat transfer coefficient W_U, Nusselt number W_{Nu}, and friction factor W_f for flat, corrugated and turbulated fin cooling are given as the following;

C.3.1. Flat fin cooling coil

Table (C.3.1.1) Maximum percentage uncertainty for $T_{ai} = 42\,^{\circ}C$, $T_{wi} = 10\,^{\circ}C$

u	W_{Qav}	W_{Θ}	W_U	W_{Nu}	W_f
0.649	8.69	2.43	9.03	10.48	13.4
0.963	8.22	2.34	8.54	10.18	11.3
1.309	7.71	2.23	8.02	9.78	10.2
1.842	6.77	1.81	7.01	8.87	9.3
2.219	6.68	1.93	6.95	9.13	9
2.265	6.56	1.76	6.79	8.92	9
2.796	6.26	1.71	6.49	8.84	8.6
3.113	6.01	1.56	6.21	8.68	8.5
3.467	5.99	1.69	6.23	8.82	8.4
3.855	6	1.72	6.24	8.97	8.3

Table (C.3.1.2) Maximum percentage uncertainty for $T_{ai} = 33\,^{\circ}C$, $T_{wi} = 10\,^{\circ}C$

u	W_{Qav}	W_{Θ}	W_U	W_{Nu}	W_f
0.625	10.98	4.23	11.76	13.65	13.7
0.712	10.07	3.28	10.56	12.38	12.9
1.216	9.08	3.12	9.61	11.83	10.5
1.822	8.11	2.48	8.48	11.03	9.4
2.307	7.22	2.45	7.63	10.24	8.9
2.657	7.35	2.22	7.68	10.28	8.7
2.808	7.05	2.1	7.36	9.95	8.7
3.121	6.74	2.09	7.06	9.99	8.5
3.207	6.9	2.1	7.21	10.03	8.5
3.502	6.62	2.01	6.92	9.87	8.4
3.743	6.63	2	6.92	10.13	8.4

Table (C.3.1.3) Maximum percentage uncertainty for T_{ai} = 23 °C, T_{wi} = 10 °C

u	W_{Qav}	W_{Θ}	W_U	W_{Nu}	W_f
0.649	17	6.2	17.54	20.01	13.6
1.132	14.11	4.84	14.91	17.98	10.8
1.826	10.41	3.51	10.98	13.98	9.4
2.063	9.95	3.12	10.42	13.54	9.2
2.710	8.73	2.83	9.17	12.4	8.8
3.122	8.95	3.04	9.45	13	8.6
3.416	8.58	2.92	9.07	12.69	8.5
3.608	8.08	2.65	8.51	11.98	8.5
3.877	7.66	2.54	8.07	11.9	8.4

C.3.2. Corrugated fin cooling coil

Table (C.3.2.1) Maximum percentage uncertainty for T_{ai} = 42 °C , T_{wi} = 10 °C

u	W_{Qav}	W_{Θ}	W_U	W_{Nu}	W_f
0.736	8.44	2.97	8.94	10.54	13
1.417	7.11	2.36	7.49	9.29	10.2
1.88	6.6	2.26	6.98	9.03	9.5
2.142	6.45	2.11	6.78	9.18	9.3
2.74	6.12	2.03	6.45	9.16	8.9
3.043	5.84	1.83	6.12	8.9	8.7
3.321	5.71	1.81	5.99	8.96	8.6
3.487	5.71	1.8	5.99	8.96	8.6
3.698	5.7	1.87	6	9.3	8.6

Table (C.3.2.2) Maximum percentage uncertainty for T_{ai} = 23 °C, T_{wi} = 10 °C

u	W_{Qav}	W_{θ}	W_U	W_{Nu}	W_f
0.703	11.66	4.59	12.53	14.69	13.4
1.4	8.68	3.29	9.29	11.56	10.3
1.897	7.67	2.72	8.14	10.70	9.6
2.165	7.45	2.62	7.89	10.5	9.3
2.7	6.92	2.48	7.35	10.11	8.9
3.259	6.47	2.18	6.82	10.05	8.7
3.471	6.46	2.21	6.83	10.11	8.7
3.793	6.18	2.11	6.53	9.88	8.4

Table (C.3.2.3) Maximum percentage uncertainty for T_{ai} = 23 °C, T_{wi} = 10 °C

u	W_{Qav}	W_{θ}	W_U	W_{Nu}	W_f
0.703	19.6	7.55	21	21.56	13.4
1.443	13.85	5.57	14.93	18.3	10.3
2.123	10.65	4.12	11.42	15.43	9.4
2.613	9.2	3.65	9.9	13.67	9
2.914	8.87	3.33	9.47	13.11	8.9
3.259	7.5	2.79	8	11.43	8.7
3.471	7.45	2.79	7.95	11.49	8.7
3.793	7.36	2.81	7.88	11.56	8.6

C.3.3. Turbulated fin cooling coil

Table (C.3.3.1) Maximum percentage uncertainty for $T_{ai} = 42\,^{\circ}C$, $T_{wi} = 10\,^{\circ}C$

u	W_{Qav}	W_{Θ}	W_U	W_{Nu}	W_f
0.682	8.54	4.18	9.51	11.49	13.2
0.902	7.91	3.43	8.63	10.65	11.7
1.34	7.14	2.94	7.72	10.20	10.2
2.075	6.27	2.61	6.79	9.77	9.1
2.455	6.08	2.52	6.58	9.91	8.9
2.963	5.91	2.54	6.43	10.33	8.6
3.153	5.72	2.22	6.14	9.96	8.6
3.406	5.86	2.45	6.35	10.49	8.5
3.753	5.59	2.25	6.02	10.41	8.4

Table (C.3.3.2) Maximum percentage uncertainty for $T_{ai} = 33\,^{\circ}C$, $T_{wi} = 10\,^{\circ}C$

u	W_{Qav}	W_{Θ}	W_U	W_{Nu}	W_f
0.732	10.1	5.42	11.46	13.78	12.8
1.434	8.15	4.45	9.29	12.34	10
2.054	7.37	3.73	8.25	11.54	9.2
2.401	6.89	3.10	7.56	11.28	8.9
2.742	6.42	2.8	7	10.15	8.7
3.006	6.16	2.63	6.7	10.9	8.6
3.11	6.24	2.71	6.8	11.45	8.6
3.512	6.29	2.73	6.85	11.62	8.5
3.786	6.01	2.59	6.55	12.02	8.4